AD-A035 716 PURDUE UNIV LAFAYETTE IND THERMAL SCIENCES AND PROPU--ETC F/G 21/5
STAGNATION REGION GAS FILM COOLING SPANWISE ANGLED COOLANT INJE--ETC(U)
DEC 76 D W LUCKEY, M R L'ECUYER N00014-75-C-0873
UNCLASSIFIED TSPC-TR-76-2 NL

1 OF 4
AD A035716

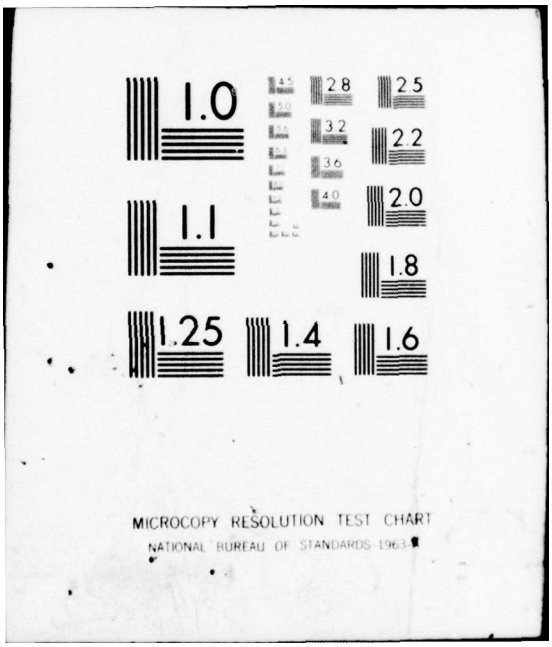
1.0
1.1
1.25
1.4
1.6
1.8
2.0
2.2
2.5
2.8
3.2
3.6
4.0
MICROCOPY RESOLUTION TEST CHART
NATIONAL BUREAU OF STANDARDS-1963-A

STAGNATION REGION GAS FILM COOLING -SPANWISE ANGLED COOLANT INJECTION-

by

David W. Luckey and Mel R. L'Ecuyer

SCHOOL OF MECHANICAL ENGINEERING
THERMAL SCIENCES & PROPULSION CENTER
PURDUE UNIVERSITY
WEST LAFAYETTE, INDIANA 47907

Technical Report TSPC-TR-76-2
December 1976

SUPPORTED BY
OFFICE OF NAVAL RESEARCH
POWER PROGRAM
CONTRACT NO. N00014-75-C-0873

UNCLASSIFIED

SECURITY CLASSIFICATION OF THIS PAGE (When Data Entered)

REPORT DOCUMENTATION PAGE

READ INSTRUCTIONS BEFORE COMPLETING FORM

1. REPORT NUMBER: TSPC-TR-76-2
2. GOVT ACCESSION NO.:
3. RECIPIENT'S CATALOG NUMBER:

4. TITLE (and Subtitle): STAGNATION REGION GAS FILM COOLING -SPANWISE ANGLED COOLANT INJECTION.

5. TYPE OF REPORT & PERIOD COVERED: Technical Report. May 1974 — Oct. 1976.

6. PERFORMING ORG. REPORT NUMBER:

7. AUTHOR(s): David W. Luckey and Mel R. L'Ecuyer

8. CONTRACT OR GRANT NUMBER(s): N00014-75-C-0873, NGR-15-005-147

9. PERFORMING ORGANIZATION NAME AND ADDRESS:
School of Mechanical Engineering
Thermal Sciences & Propulsion Center
Purdue University, W. Lafayette, IN 47907

10. PROGRAM ELEMENT, PROJECT, TASK AREA & WORK UNIT NUMBERS: NR 094-372

11. CONTROLLING OFFICE NAME AND ADDRESS:
Mr. James B. Patton, Jr., Office of Naval Research
Power Program, Code 473, 800 North Quincy Street
Arlington, VA 22217

12. REPORT DATE: Dec. 1976

13. NUMBER OF PAGES: 335

14. MONITORING AGENCY NAME & ADDRESS (if different from Controlling Office): 357p.

15. SECURITY CLASS. (of this report): Unclassified

15a. DECLASSIFICATION/DOWNGRADING SCHEDULE:

16. DISTRIBUTION STATEMENT (of this Report)

Approved for public release; distribution unlimited.

17. DISTRIBUTION STATEMENT (of the abstract entered in Block 20, if different from Report)

18. SUPPLEMENTARY NOTES

19. KEY WORDS (Continue on reverse side if necessary and identify by block number)

Film Cooling
Turbine Blade Cooling
Gas Turbine
Turbine Engine

20. ABSTRACT (Continue on reverse side if necessary and identify by block number)

This experimental investigation involved the study of gas film cooling from a single row of spanwise angled holes using the stagnation region of a cylinder in cross flow to model the leading edge of a turbine vane. The objective was to obtain data for the local convective heat transfer rates to a highly cooled, curved surface exposed to a turbulent hot mainstream flow and a secondary, film coolant flow. Since the leading edge of the first stage, inlet turbine vane experiences some of the most severe thermal loads found in

Over

DD FORM 1 JAN 73 1473 EDITION OF 1 NOV 65 IS OBSOLETE
S/N 0102-014-6601 |

SECURITY CLASSIFICATION OF THIS PAGE (When Data Entered)

20. (continued)

the turbine engine, effective film cooling is most important in this area. Film cooling of the leading edge area was modeled by making heat transfer measurements on the front stagnation region of a cylinder in cross flow.

Experiments were conducted in a rectangular duct using a film cooled cylindrical test surface normal to a two-dimensional freestream flow. A gas turbine combustor provided heated air flow to simulate a Reynolds number typical of a high pressure, high temperature turbine vane. Internal convection cooling of the cylinder allowed a gas-to-wall temperature ratio of 2.1 to be achieved while using a moderate freestream gas temperature (~1000°R; 555K). The film coolant was chilled to obtain a coolant-to-freestream density ratio of 2.2, representative of the gas turbine environment. The cylindrical test surface was instrumented with miniature heat flux gages, and wall thermocouples to determine the influence of the film coolant blowing ratio and the injection hole geometry on the film cooling performance.

Local heat flux measurements were made at three different locations downstream from the row of coolant injection holes. At each specific downstream location studied, the heat flux measurements were taken for three different spanwise locations of the coolant hole with respect to the heat flux gage. This provided an indication of the film coolant uniformity in the spanwise direction and its deterioration in the downstream direction. Experiments were conducted to study the influence of the spanwise coolant hole angle, β, and the location of the row of holes relative to the stagnation line on the cylinder, θ_i. Data were obtained for injection angles of β = 25°, 35°, and 45°, and three locations θ_i = 20°, 30°, and 40° as a function of the coolant blowing ratio (mass flux of the coolant/mass flux of the freestream).

The results are presented showing both the downstream and spanwise variations of the film cooling performance, and the influence of the spanwise coolant hole angle and of the location of the row of holes relative to stagnation on the Stanton Number Reduction due to film cooling. The results enabled the identification of an optimum coolant blowing ratio. Correlations were developed to show the relationship of the coolant hole angle, β, with the blowing ratio that produced the maximum film cooling performance and with the spanwise variation of the film cooling performance.

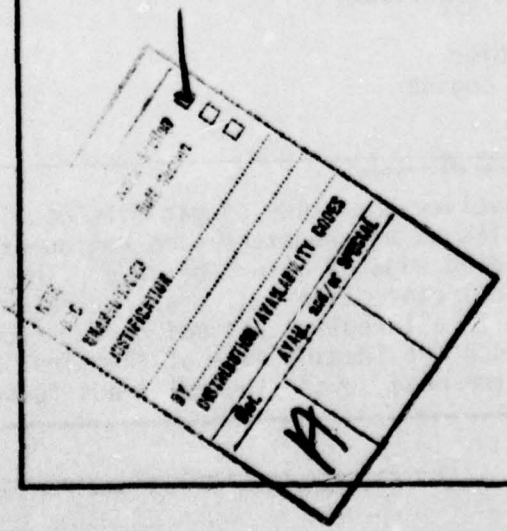

STAGNATION REGION GAS FILM COOLING

-SPANWISE ANGLED COOLANT INJECTION-

by

David W. Luckey and Mel R. L'Ecuyer

Supported by

Office of Naval Research
Power Program
Contract N00014-75-C-0873

Thermal Sciences and Propulsion Center
School of Mechanical Engineering
Purdue University
West Lafayette, Indiana 47907

Technical Report No. TSPC-TR-76-2

December 1976

ACKNOWLEDGEMENTS

The study reported herein was conducted under the sponsorship of the Office of Naval Research, Power Program, Contract No. N00014-75-C-0873. The experimental apparatus used was fabricated with support from the NASA Lewis Research Center under Grant No. NGR-15-005-147. The authors wish to express their sincere appreciation for the support provided by the aforementioned agencies.

The authors are indebted to Dr. Gary J. Hanus for his assistance in the design, fabrication, and instrumentation of the test cylinder and to Mr. David K. Winstanley for his assistance in the conduct of this phase of the investigation. The authors also wish to acknowledge Professors B.A. Reese and S.N.B. Murthy, Purdue University, for their advice during the investigation. Finally, special recognition is given to Ms. Bonnie Thomas for her expert typing and invaluable assistance in the preparation of this report.

The results of this investigation were published in an abbreviated form as AIAA Paper No. 76-728, AIAA/SAE 12th Propulsion Conference, July 1976 and will appear in a forthcoming issue of the AIAA Journal of Aircraft.

TABLE OF CONTENTS

	Page
LIST OF TABLES	v
LIST OF FIGURES	vi
NOMENCLATURE	xv
I. INTRODUCTION	1
I.A. General Discussion	1
I.B. Introduction to Film Cooling Parameters	5
I.C. Review of the Literature	11
I.C.1. Film Cooling Performance Parameters	12
I.C.2. Flow Visualization	25
I.C.3. Mass Flux Ratio, Velocity Ratio, Momentum Ratio, and Angle of Injection	33
I.C.4. Hole Spacing	51
I.C.5. Freestream Conditions	61
I.C.6. Film Cooling Correlations	70
I.D. Scope of Investigation	71
II. EXPERIMENTAL INVESTIGATION	73
II.A. Modeling of Gas Turbine Environment	73
II.B. General Description of Experimental Apparatus	77
II.B.1. Flow System	77
II.B.2. Test Cylinder	81
II.B.3. Instrumentation and Measurements	88
II.C. Experimental Conditions	93
II.D. Data Reduction	97
III. RESULTS AND DISCUSSION	101
III.A. Preliminary Experiments	101
III.A.1. Freestream Flow Conditions	101

Page

III.A.2. Cylinder and Coolant Conditions 107
III.A.3. Cylinder Pressure Distribution. 110

III.B. Heat Transfer Without Film Cooling. 122

III.C. Film Cooling Results. 151

III.D. Analysis of Film Cooling Data 171
III.D.1. Data for Spanwise Maximum Stanton Number Reduction. 175
III.D.2. Data for Spanwise Averaged Stanton Number Reduction. 190

III.E. Correlation of the Film Cooling Data. 196
III.E.1. Linear Film Cooling Range 197
III.E.2. Correlation of M^*_{opt} 198
III.E.3. Correlation of $(z/s)^*$ 203
III.E.4. Comparison of Correlation Results with Previous Studies. 216

IV. CONCLUSIONS 223

BIBLIOGRAPHY. 227

APPENDICES

I. Models and Correlations from Previous Investigations. . . . 233
I.A. Analytical Models 233
I.B. Experimental Correlations 239

II. Description of the Experimental Investigation 243
II.A. Experimental Apparatus 243
II.A.1. Flow System 243
II.A.2. Cylinder. 249
II.A.3. Measurements and Instruments. 255
II.B. Experimental Procedure 260
II.C. Data Reduction 264

III. Heat Flux Gage Theory and Operation 285

IV. Correlation for the Temperature Rise of Film Coolant Flowing Through the Injection Plate Holes 245

V. The Influence of a Stepwise Change in the Wall Temperature on the Heat Transfer Coefficient. 303

VI. Spanwise Distributions of the Film Cooling Data 313

LIST OF TABLES

Table		Page
1.	Heat Flux Gage Location	91
2.	Experimental Flow Conditions	94
3.	Film Coolant Injection Parameters	96
4.	Summary of Film Cooling Configurations	152
5.	The Influence of the Injection Angle, β, on M^*_{opt} and $[1-(St_{FC}/St_o)]^*$	182
6.	The Influence of Row Location, θ_i, on M^*_{opt} and $[1-(St_{FC}/St_o)]^*_{MAX}$ $(x/d_o = 8.0)$	189
7.	The Spanwise Averaged Stanton Number Reduction Results $(x/d_o = 8.0)$	195
8.	The Slope of the Stanton Number Reduction for Low Blowing Ratios	199
9.	The Influence of the Injection Angle, β, on the Optimum Blowing Ratio	201
10.	Blowing Ratios and $(z/s)^*$ Coolant Locations for Constant Values of the Spanwise Momentum Component, I_y, at $x/d_o = 8.0$	207

Appendix Table

A1.	The Density Ratio and θ_c Values for Different Film Cooling Configurations	301

LIST OF FIGURES

Figure		Page
1.	Film Cooling Configurations	3
2.	Coordinate Axes along Film Cooled Surface	6
3.	Definition of Coolant Injection Angles	8
4.	Leading Edge Cooling Configurations on a Turbine Vane .	10
5.	Heat Transfer Coefficient Downstream of Tangential Slot Injection (Hartnett, Birkebak, and Eckert[4])	15
6.	Heat Transfer Coefficient Downstream of Injection through a Slot and through a Single Row of Holes (Metzger and Fletcher[5])	16
7.	Heat Transfer Coefficient Downstream of Injection through a Single Row of Holes (Eriksen and Goldstein[6])	18
8.	Heat Transfer Coefficient Downstream of Hole Injection on a Film Cooled Turbine Vane Surface (Lander, Fish, and Suo[7])	19
9.	Heat Transfer Coefficient with Film Cooling versus the Dimensionless Coolant Temperature Ratio, Θ_c (Choe, Kays, and Moffat[10])	23
10.	"Horseshoe" Shape of Coolant Jet as It Interacts with the Freestream (Goldstein, Eckert, and Ramsey[16]) . . .	26
11.	Constant Temperature Profiles for a Heated Jet Interacting with the Freestream (Ramsey and Goldstein[12]) .	28
12.	Interaction of a Jet with the Freestream (Ramsey and Goldstein[12])	30
13.	The Influence of the Mass Flux Ratio on the Film Cooling Effectiveness (Wieghardt[17])	35
14.	The Influence of the Density Ratio on the Film Cooling Effectiveness for Tangential Slot Injection (Burns and Stollery[20])	36

Figure		Page
15.	The Influence of the Blowing Ratio on Film Cooling Effectiveness for Hole Injection (Goldstein, Eckert, Eriksen and Ramsey[21])	38
16.	The Influence of the Blowing Ratio on Film Cooling Effectiveness for a Spanwise Angled Hole (Goldstein, Eckert, Eriksen, and Ramsey[21])	39
17.	The Influence of the Density Ratio on Film Cooling Effectiveness for a Row of Streamwise Angled Holes (Pedersen[22])	41
18.	The Influence of the Velocity Ratio on Film Cooling Effectiveness for a Row of Streamwise Angled Holes (Pedersen[22])	42
19.	Centerline Effectiveness as a Function of the Momentum Flux Ratio (Goldstein, Eckert, and Burggraf[23])	44
20.	The Influence of the Slot Injection Angle of Film Cooling Effectiveness (Papell[25])	46
21.	The Influence of the Hole Angle on Film Cooling Effectiveness (Goldstein, Eckert, and Ramsey[16]) . . .	47
22.	Spanwise Spreading of the Coolant Jet as It Flows Downstream (Goldstein, Eckert, and Ramsey[16])	49
23.	The Influence of the Coolant Hole Angle on the Spanwise Spreading of the Coolant Jet (Goldstein, Eckert, and Ramsey[16])	50
24.	Lines of Constant Film Cooling Effectiveness for Single Hole Injection (Goldstein, Eckert, Eriksen, and Ramsey[21])	52
25.	Comparison between Slot and Hole Film Cooling (Metzger and Fletcher[5])	54
26.	Comparison of the Film Cooling Effectiveness with Injection from One Hole and a Row of Holes (Goldstein, Eckert, Eriksen, and Ramsey[26])	56
27.	Lateral Variation of the Film Cooling Effectiveness for Injection from a Row of Holes (Goldstein, Eckert, and Burggraf[23])	58
28.	The Influence of Hole Spacing on Film Cooling Effectiveness (Liess and Carnel[27])	59

Figure		Page
29.	The Effect of the Boundary Layer Displacement Thickness on the Centerline Film Cooling Effectiveness (Goldstein, Eckert, and Burggraf[23])	62
30.	The Effect of the Boundary Layer Displacement Thickness on the Laterally Averaged Film Cooling Effectiveness (Liess[14])	64
31.	The Influence of the Mach Number on the Film Cooling Effectiveness for Tangential Slot Injection (Papell and Trout[29])	66
32.	The Influence of the Mach Number on the Laterally Averaged Film Cooling Effectiveness for Injection through a Row of Holes (Liess[14])	67
33.	The Influence of the Freestream Turbulence on the Film Cooling Effectiveness (Carlson and Talmor[30])	68
34.	Schematic of Flow System	78
35.	Photograph of the Flow Channel	79
36.	Photograph of the Turbulence Section	80
37.	Photograph of the Cylinder in the Test Section	82
38.	Photograph of Test Cylinder with Plenum Covered by an Injection Plate	83
39.	Photograph of the Test Cylinder after Removing the Injection Plate	84
40.	Photograph of the Injection Plate with a Single Row of Spanwise Angled Holes	86
41.	Schematic of the Film Coolant Flow System	87
42.	Photograph of the Test Cylinder Mounted in the Flow Channel	89
43.	Vertical Velocity Profile (without the Flow Straightener)	102
44.	Horizontal Velocity Profile (without the Flow Straightener)	102
45.	Vertical Velocity Profile (with the Flow Straightener) .	105
46.	Horizontal Velocity Profile (with the Flow Straightener)	105

Figure		Page
47.	Vertical Total Temperature Profile (with the Flow Straightener)	106
48.	Horizontal Total Temperature Profile (with the Flow Straightener)	106
49.	Wall Temperature Distribution	108
50.	Variation of the Coolant Temperature with Coolant Flow Rate	111
51.	Variation of Cylindrical Drag with Reynolds Number (Schlicting[39])	113
52.	The Pressure Distribution for a Cylinder in Cross Flow (Flachshart[42])	115
53.	The Pressure Distribution for a Cylinder in Cross Flow (Schmidt and Wenner[45])	117
54.	The Influence of Freestream Turbulence on the Pressure Distribution for a Cylinder in Cross Flow (Giedt[46])	119
55.	The Influence of Freestream Turbulence on the Pressure Distribution for a Cylinder in Cross Flow (Seban[47])	121
56.	The Pressure Distribution for the Test Cylinder in Cross Flow	123
57.	Heat Transfer Distribution around a Cylinder in Cross Flow (Schmidt and Wenner[45])	125
58.	The Influence of Freestream Turbulence on the Heat Transfer Distribution around a Cylinder in Cross Flow (Giedt[46])	127
59.	The Influence of Freestream Turbulence on the Heat Transfer Distribution around a Cylinder in Cross Flow (Seban[47])	129
60.	Dry Wall Heat Transfer Data along a Smooth Test Cylinder (Injection Plate Downstream, Gages#0, 1, 4)	132
61.	The Correspondnece between Heat Flux Gage Identification Numbers and Angular Position on the Cylinder	133
62.	Dry Wall Heat Transfer Data along a Smooth Test Cylinder (Injection Plate Downstream, Gage#2)	134

Figure		Page
63.	Angular Location of the Heat Flux Gages Relative to the Coolant Holes and the Plate-Cylinder Seam	136
64.	Dry Wall Heat Transfer Distribution around the Test Cylinder as Measured by Gage #4 ($\Delta\theta$=66°)	138
65.	Local Freestream Velocity Distribution With and Without Flow Blockage	140
66.	Dry Wall Heat Transfer Distribution around the Test Cylinder as Measured by Gage #2 ($\Delta\theta$=40°)	141
67.	Dry Wall Heat Transfer Distribution around the Test Cylinder as Measured by Gage #0 ($\Delta\theta$=14°)	142
68.	Dry Wall Heat Transfer Distribution around the Test Cylinder as Measured by Gage #1 ($\Delta\theta$=8°)	144
69.	The Influence of the Cylinder-Injection Plate Seam on the Downstream Heat Transfer	146
70.	Comparison of Dry Wall Heat Transfer Results	150
71.	Variation of the Stanton Number Reduction with the Blowing Ratio, M	154
72.	Variation of the Stanton Number Reduction with the Blowing Ratio, Case I	157
73.	Variation of the Stanton Number Reduction with the Blowing Ratio, Case II	160
74.	Variation of the Stanton Number Reduction with the Blowing Ratio, Case III	162
75.	Variation of the Stanton Number Reduction with the Blowing Ratio, Case IV	164
76.	Variation of the Stanton Number Reduction with the Blowing Ratio, Case V	166
77.	Variation of the Stanton Number Reduction with the Blowing Ratio, Case VI	168
78.	Variation of the Stanton Number Reduction with the Blowing Ratio, Case VII	169
79.	Spanwise Variation of the Stanton Number Reduction (β=25°, θ_i=40°, x/d_o=8.0)	172

Figure		Page
80.	Spanwise Variation of the Stanton Number Reduction (β=35°, Θ_i=40°, x/d_o=8.0)	174
81.	Variation of the Spanwise Maximum Stanton Number Reduction with the Blowing Ratio (x/d_o=8.0)	176
82.	Spanwise Variation of the Stanton Number Reduction (Θ_i=20°, x/d_o=8.0)	179
83.	Variation of the Spanwise Maximum Stanton Number Reduction with the Blowing Ratio (x/d_o=6.4)	181
84.	The Influence of the Injection Angle, β, on the Location of the Spanwise Maximum Stanton Number Reduction	185
85.	The Influence of the Injection Location, Θ_i, on the Spanwise Maximum Stanton Number Reduction (x/d_o=8.0) . .	187
86.	Variation of the Spanwise Averaged Stanton Number Reduction with the Blowing Ratio (β=25°)	191
87.	Variation of the Spanwise Averaged Stanton Number Reduction with the Blowing Ratio (β=35°)	192
88.	Variation of the Spanwise Averaged Stanton Number Reduction with the Blowing Ratio (β=45°)	194
89.	Variation of the Stanton Number Reduction with the Vertical Component of the Velocity Ratio	204
90.	Test Surface Location of the Maximum Film Cooling Performance	205
91.	The Identification of the Stanton Number Reduction at Intermediate Blowing Ratios	210
92.	The Variation of $(z/s)^*$ with the Momentum Parameter, $I_z^{0.9}/I_y^{0.8}$ (Θ_i=40°, x/d_o=8.0)	212
93.	The Variation of $(z/s)^*$ with the Momentum Parameter, $I_z^{0.9}/I_y^{0.8}$ (x/d_o=8.0)	213
94.	The Variation of $(z/s)^*$ with the Momentum Parameter, $I_z^{0.9}/I_y^{0.8}$ (Θ_i=40°, x/d_o=6.4)	215
95.	The Variation of the z/s Locations Representing a 25% Reduction in the Spanwise Maximum Stanton Number Reduction with the Momentum Parameter, $I_z^{0.9}/I_y^{0.8}$	217

Figure Page

96. Comparison of the $(z/s)^*$ Correlation (Eq. 43) with the Data of Goldstein, et al.[21] 221

Appendix
Figure

A1. Comparison of Film Cooling Models 236

A2. Schematic of the Flow System 244

A3. Photograph of the Flow Channel 246

A4. Photograph of the Test Cylinder in the Flow Channel . . 248

A5. Photograph of the Test Cylinder without the Injection Plate over the Plenum Chamber 250

A6. Schematics of the Alcohol Coolant Loops 252

A7. Schematic of the Film Coolant Flow System 254

A8. Planar View of the Instrumented Cylinder Surface Downstream of the Row of Injection Holes 256

A9. Schematic of the Heat Flux Gage Circuit 259

A10. Heat Flux Gage Operation 286

A11. Calibration Curve for the Heat FLux Gages 293

A12. Heat Addition to the Film Coolant as It Passes Through the Holes in the Injection Plate 298

A13. The Influence of the Injection Plate Temperature on the Downstream Heat Transfer Coefficient (Θ_i=40°) 308

A14. The Influence of the Injection Plate Temperature on the Downstream Heat Transfer Coefficient (Θ_i=30°) 309

A15. The Influence of the Injection Plate Temperature on the Downstream Heat Transfer Coefficient (Θ_i=20°) 310

A16. Spanwise Variation of the Stanton Number Reduction (β=25°, Θ_i=40°, x/d_o=6.4) 315

A17. Spanwise Variation of the Stanton Number Reduction (β=25°, Θ_i=40°, x/d_o=8.0) 316

A18. Spanwise Variation of the Stanton Number Reduction (β=25°, Θ_i=40°, x/d_o=15.2) 317

Figure		Page
A19.	Spanwise Variation of the Stanton Number Reduction (β=25°, Θ_i=30°, x/d_o=6.4)	318
A20.	Spanwise Variation of the Stanton Number Reduction (β=25°, Θ_i=30°, x/d_o=8.0)	319
A21.	Spanwise Variation of the Stanton Number Reduction (β=25°, Θ_i=30°, x/d_o=15.2)	320
A22.	Spanwise Variation of the Stanton Number Reduction (β=25°, Θ_i=20°, x/d_o=6.4)	321
A23.	Spanwise Variation of the Stanton Number Reduction (β=25°, Θ_i=20°, x/d_o=8.0)	322
A24.	Spanwise Variation of the Stanton Number Reduction (β=25°, Θ_i=20°, x/d_o=15.2)	323
A25.	Spanwise Variation of the Stanton Number Reduction (β=35°, Θ_i=40°, x/d_o=6.4)	324
A26.	Spanwise Variation of the Stanton Number Reduction (β=35°, Θ_i=40°, x/d_o=8.0)	325
A27.	Spanwise Variation of the Stanton Number Reduction (β=35°, Θ_i=40°, x/d_o=15.2)	326
A28.	Spanwise Variation of the Stanton Number Reduction (β=35°, Θ_i=30°, x/d_o=6.4)	327
A29.	Spanwise Variation of the Stanton Number Reduction (β=35°, Θ_i=30°, x/d_o=8.0)	328
A30.	Spanwise Variation of the Stanton Number Reduction (β=35°, Θ_i=30°, x/d_o=15.2)	329
A31.	Spanwise Variation of the Stanton Number Reduction (β=35°, Θ_i=20°, x/d_o=6.4)	330
A32.	Spanwise Variation of the Stanton Number Reduction (β=35°, Θ_i=20°, x/d_o=8.0)	331
A33.	Spanwise Variation of the Stanton Number Reduction (β=35°, Θ_i=20°, x/d_o=15.2)	332
A34.	Spanwise Variation of the Stanton Number Reduction (β=45°, Θ_i=40°, x/d_o=6.4)	333
A35.	Spanwsie Variation of the Stanton Number Reduction (β=45°, Θ_i=40°, x/d_o=8.0)	334

Figure Page

A36. Spanwise Variation of the Stanton Number Reduction (β=45°, Θ_i=40°, x/d_o=15.2) 335

NOMENCLATURE

C_p	pressure coefficient, $P_w - P_{\infty_o} / P_{T_{\infty_o}} - P_{\infty_o}$
c_p	specific heat at constant pressure
D	test cylinder diameter
d_o	coolant hole diameter
Ec	Eckert number, $V_\infty^2 / c_p (T_\infty - T_w)$
g	local acceleration of gravity
h	local heat transfer coefficient
h'	local heat transfer coefficient with film cooling, $q''_{FC} / (T_{adw} - T_{w,FC})$
$\overline{h'}$	laterally averaged heat transfer coefficient
h	rectangular duct height
H	enthalpy
I	momentum flux ratio, $\rho_c V_c^2 / \rho_\infty V_\infty^2$
k	thermal conductivity
K	acceleration parameter, $\frac{\nu_\infty}{V_\infty^2} \frac{dV_\infty}{dx}$
ℓ	length of test surface
L	length of coolant hole
M	blowing or mass flux ratio, $\rho_c V_c / \rho_\infty V_\infty$
Ma	Mach number
$\dot{m}$	mass flow rate
n	direction normal to the surface
Nu	Nusselt number

NOMENCLATURE (Cont'd)

P,p	pressure
Pr	Prandtl number
q"	local heat flux
Re	Reynolds number
R	gas constant
s	coolant hole centerline-to-centerline spacing on the surface
St	Stanton number
s_o	coolant slot height or width
T,t	temperature
u	x-component of velocity
V	velocity
v	y-component of velocity
VR	normal component of velocity ratio, $\frac{V_c}{V_\infty} \sin\beta$
w	rectangular duct width
x	distance in streamwise direction downstream of coolant holes
x/d_o	dimensionless distance in streamwise direction downstream of coolant holes
x^+	non-dimensional coolant tube length, $L/d_o/RePr$
y	vertical distance from surface
z	spanwise or lateral distance
z/s, z/d_o	dimensionless spanwise distance
$1 - \frac{St_{FC}}{St_o}$	film cooling performance parameter, Stanton Number Reduction

NOMENCLATURE (Cont'd)

GREEK

α	coolant injection angle measured along the test surface relative to the x-axis
β	coolant injection angle measured vertically from the test surface
δ	boundary layer thickness
δ^*	boundary layer displacement thickness
η	film cooling effectiveness parameter
θ	angular position along a cylinder relative to stagnation
θ'	dimensionless temperature, $\frac{T - T_\infty}{T_w - T_\infty}$
θ_c	dimensionless coolant temperature ratio, $\frac{T_\infty - T_c}{T_\infty - T_w}$
θ_i	angular position of coolant injection along a cylinder relative to stagnation
θ_{mom}	boundary layer momentum thickness
ρ	density
τ	time
μ	dynamic viscosity
ν	kinematic viscosity
Φ	heat flux ratio, q''_{FC}/q''_o

SUBSCRIPTS

adw	adiabatic wall condition
ave	averaged
AVG	spanwise averaged Stanton Number Reduction, $[1-(St_{FC}/St_o)]_{AVG}$
c	coolant
D	cylinder diameter

NOMENCLATURE (Cont'd)

FC	film cooling condition
i	at injection
limit	deviating from linear trend
MAX	maximum Stanton Number Reduction, $[1-(St_{FC}/St_o)]_{MAX}$
o	without film cooling
opt	optimum blowing ratio condition
PL	film coolant plenum
T	total or stagnation condition
w	wall
y	component normal to the surface
z	component parallel to the surface in the spanwise direction
∞	freestream conditions
∞_o	freestream condition upstream of the test cylinder

SUPERSCRIPT

*	spanwise maximum of the Stanton Number Reduction, $[1-(St_{FC}/St_o)]^*$

I. INTRODUCTION

I.A. General Discussion

A thermodynamic cycle analysis shows that the performance of the gas turbine engine is strongly influenced by the maximum temperature of the thermodynamic cycle, i.e. the turbine (gas) inlet temperature. Therefore, advances in gas turbine engine performance are severely limited by the material properties of the turbine vane and the cooling techniques utilized in maintaining acceptable material temperatures. With the maximum allowable vane temperature being on the order of 2350°R (1305K) for available materials [1],† operation at higher turbine inlet temperatures has been made possible by significant advances in vane cooling techniques. Forced convection cooling within the vane, using compressor bleed air, has proven adequate for turbine inlet temperatures up to 3150°R (1750K) [1]. Although the capabilities of internal convective cooling schemes have been enhanced by the use of impingement flow, the high temperature and pressure conditions found in current and future advanced engines require that additional thermal protection (such as film or transpiration cooling) be provided to supplement the internal blade cooling.

Transpiration and film cooling are two ways that a coolant can be injected through a turbine vane surface to provide the extra thermal

†Numbers in [ ] refer to references in the Bibliography.

protection needed. With transpiration cooling, the coolant is injected uniformly through a porous wall, resulting in the formation of a thin layer of coolant along the surface. With the coolant traveling through many tortuous internal passages in the porous wall, the coolant temperature as it emerges at the surface is approximately the same as the external wall temperature. Thus the porous wall serves as an effective heat exchanger. Although transpiration cooling has been found to be a very effective way of providing the extra thermal protection needed, the fabrication of a porous turbine vane poses a very complex and expensive problem. Also, problems of oxidation within the porous material have forced the operating material temperature to be lowered, thus hampering the utilization of this scheme in turbine engines.

Film cooling is similar to transpiration in that it protects the surface from the influence of a hot gas stream by the injection of a coolant through the vane wall onto the surface. However, for film cooling, the coolant passes through discrete slots or holes machined in the vane which are generally easier and less costly to fabricate. The coolant acts as a heat sink, providing a protective layer of cool fluid along the surface. However, as the film flows downstream from the point of injection, it deteriorates due to mixing with the free-stream. Therefore, an efficient application of film cooling on a turbine vane surface requires a thorough understanding of the film coolant behavior after injection.

There are a variety of ways to film cool a surface. A cool, secondary fluid may be injected onto a surface exposed to a hot primary flow through slots, holes or a combination of both as illustrated in Fig. 1. Numerous studies have shown that a continuous slot will

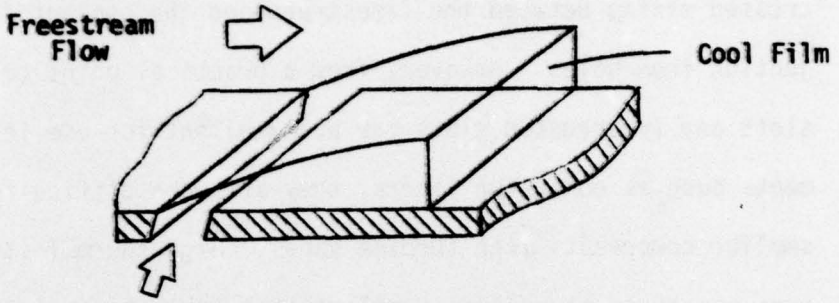

SLOT COOLING

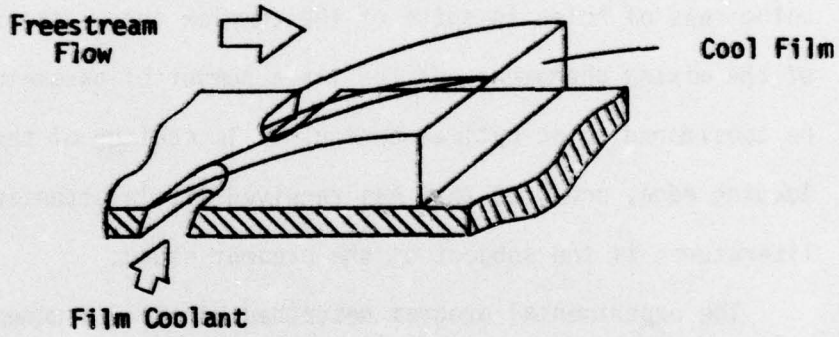

INTERRUPTED SLOT COOLING

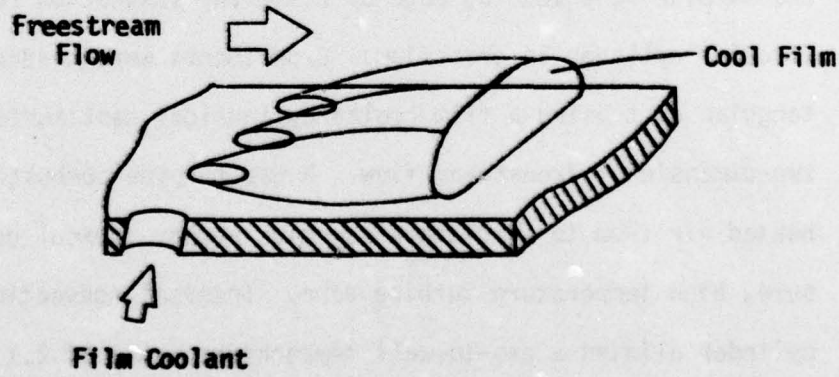

HOLE COOLING

Figure 1 Film Cooling Configurations

provide more efficient cooling than a row of holes, due to the increased mixing between the freestream and the coolant jets for injection from holes. However, from a practical point of view, while slots and interrupted slots may be excellent for use in large components such as combustor liners, they are more difficult to use in smaller components like turbine vanes. High thermal stresses in the vane can cause structural problems that make the use of slots difficult to incorporate, except perhaps in the trailing edge region. Therefore, most applications of film cooling on a turbine vane are accomplished using rows of holes in spite of the complex three-dimensional nature of the mixing phenomena and the large number of parameters which must be considered in an optimal design. Film cooling of the turbine vane leading edge, one area that has received little attention in the open literature, is the subject of the present study.

The experimental program described herein was undertaken to investigate the film cooling performance for a single row of holes in the turbine vane leading edge by using the stagnation region of a circular cylinder in crossflow. Experiments were conducted in a rectangular duct using a film cooled cylindrical test surface normal to a two-dimensional freestream flow. A gas turbine combustor provided heated air flow to simulate a Reynolds number typical of a high pressure, high temperature turbine vane. Internal convection cooling of the cylinder allowed a gas-to-wall temperature ratio of 2.1 to be achieved while using a moderate freestream gas temperature (~1000°R, 555K). The film coolant was chilled to obtain a coolant-to-freestream density ratio of 2.2, representative of the gas turbine environment. The cylindrical test surface was instrumented with miniature heat flux gages and wall

thermocouples to determine the influence of the film coolant blowing ratio and the injection hole geometry on the film cooling performance. Data were obtained to show the reduction in local heat flux due to film cooling as a function of streamwise location downstream from the row of holes and spanwise location between the holes.

I.B. Introduction to Film Cooling Parameters

This section provides a general overview of the film cooling process and introduces the terminology and parameters commonly employed in the literature. The statements are made in a general context with appropriate justification provided in the following section dealing with the literature survey.

Film cooling is the process whereby a cool fluid is injected onto a surface to protect it from a hot external freestream. The protective film serves as a heat sink, reducing the level of the heat flux to the surface. Figure 2 illustrates the coordinate system used to characterize the effect of film coolant injection through holes or a slot. Injection through a slot tends to provide a film that is uniform in the lateral direction. For injection through holes, the coolant jets flow downstream in the freestream (x) direction while at the same time spreading laterally across the surface in the z direction. If the coolant jets coalesce, they tend to reinforce each other, improving the uniformity of the protective film across the surface. The origin of the coordinate system is located at the center of the hole (or slot) of interest (see Fig. 2), and the hole diameter, d_o, slot width, s_o, or the center-to-center hole spacing, s, are frequently used to nondimensionalize the x and z coordinates.

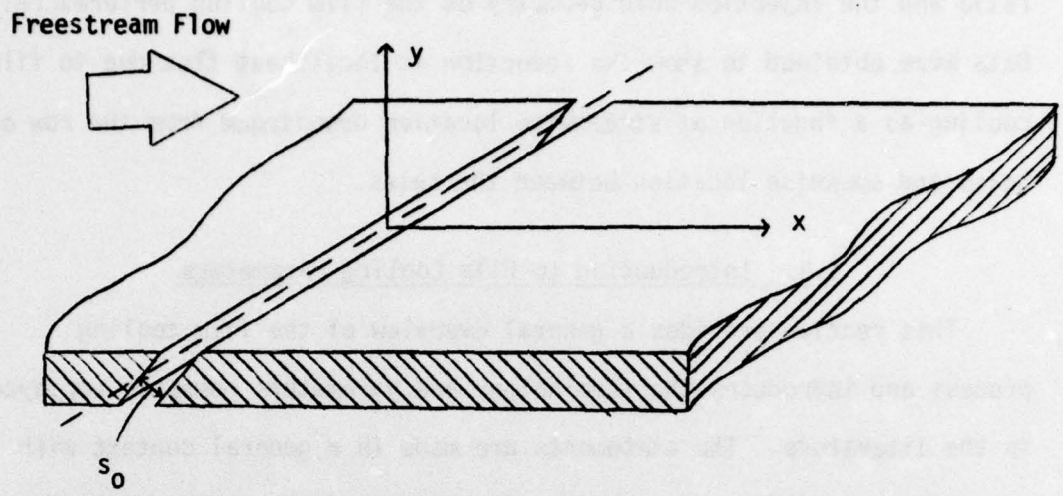

Injection through a Slot

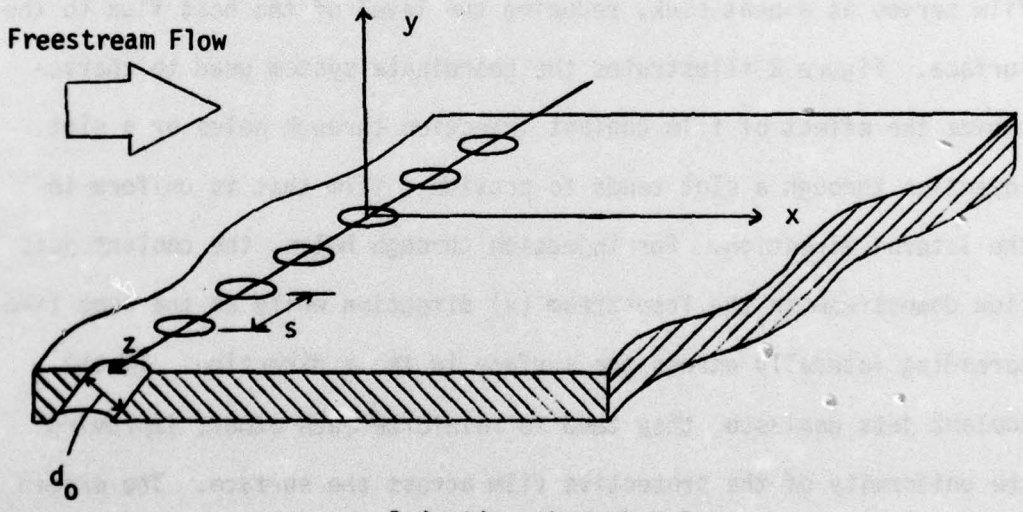

Injection through Holes

Figure 2 Coordinate Axes along Film Cooled Surface

With the film coolant acting as a heat sink, the magnitude of the reduction of the surface heat flux depends strongly on the amount of coolant injected (i.e. thermal capacity) which is commonly represented by a dimensionless mass flux ratio defined as[†]

$$M = \text{the blowing ratio} = \frac{\rho_c V_c}{\rho_\infty V_\infty} \tag{1}$$

As the coolant is blown onto the surface, mixing with the hot freestream results in a deterioration of the coolant film. The extent of this interaction depends on the penetration of the coolant jet away from the surface, into the freestream. Two hydrodynamic parameters frequently employed to characterize the jet penetration and mixing phenomena are the velocity ratio, V_c/V_∞, and the momentum flux ratio,

$$I = \frac{\rho_c V_c^2}{\rho_\infty V_\infty^2} \tag{2}$$

As can be seen, the magnitudes of the blowing ratio, the velocity ratio, the momentum flux ratio and the coolant-to-freestream density ratio are strongly interdependent. Therefore, while an increase in the blowing ratio will enhance the thermal capacity of the coolant, excessive coolant blowing can promote mixing and coolant jet penetration to the extent that the net effect is a deterioration of the coolant's ability to protect the surface.

Of equal importance in characterizing the penetration of the coolant jet is the injection hole angle which is defined in Fig. 3.

[†]The symbols are defined in the Nomenclature.

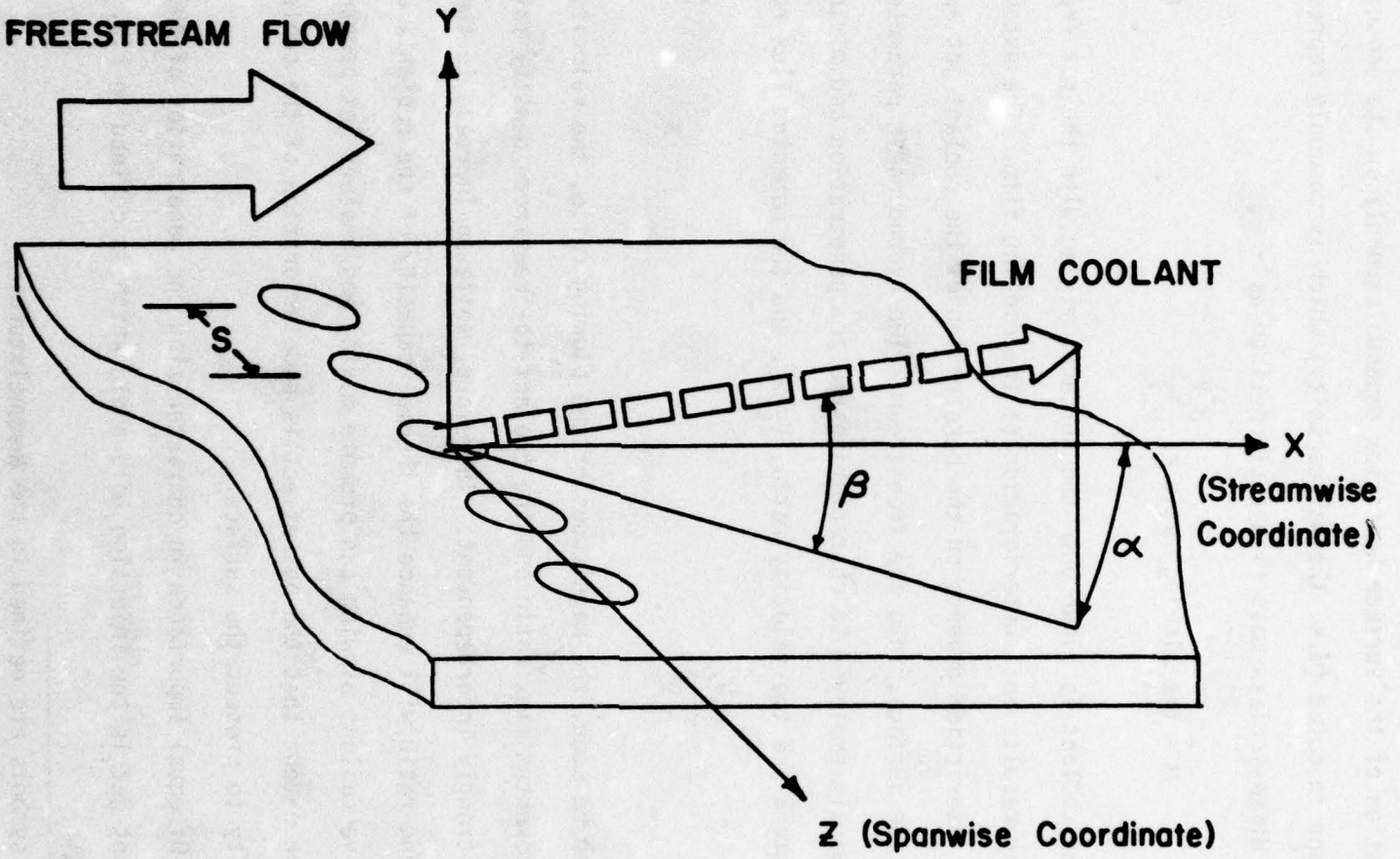

Figure 3 Definition of Coolant Injection Angles

The β angle represents the angle made with respect to the surface and the α angle represents the angular position relative to the x-axis. Thus, a hole angled at 35° in the streamwise direction would be represented by $\alpha = 0°$, $\beta = 35°$, while a similar hole in the spanwise direction would be represented by $\alpha = 90°$, $\beta = 35°$. To minimize penetration of the coolant, it is desirable to maintain the β angle as shallow as possible.

When one considers the application of film cooling near the leading edge of a turbine vane, the surface curvature complicates the problem of maintaining a shallow injection angle, β, as illustrated in Fig. 4. For streamwise angled holes ($\alpha = 0°$), the minimum injection angle is limited by the vane wall thickness. To resolve this problem, coolant holes angled in the spanwise direction ($\alpha = 90°$) are frequently employed. This permits the use of a shallow injection angle, β, although it does place some restrictions on the closeness of the hole spacing.

The hole spacing, s, is an important geometrical parameter relative to the uniformity of the film in the spanwise direction, z. The coolant jets interact with the freestream and spread in the spanwise direction attempting to coalesce. By reducing the hole spacing ratio, s/d_o, the lateral spreading before coalescence is decreased, helping to create a more uniform film across the surface. Furthermore, the reduction of the hole spacing ratio also decreases the area between the coolant jets exposed to freestream interaction, subsequently retarding the free-stream-coolant mixing process. When using spanwise angled holes, a compromise must be made between the advantages of a shallow injection hole angle and a small hole spacing ratio.

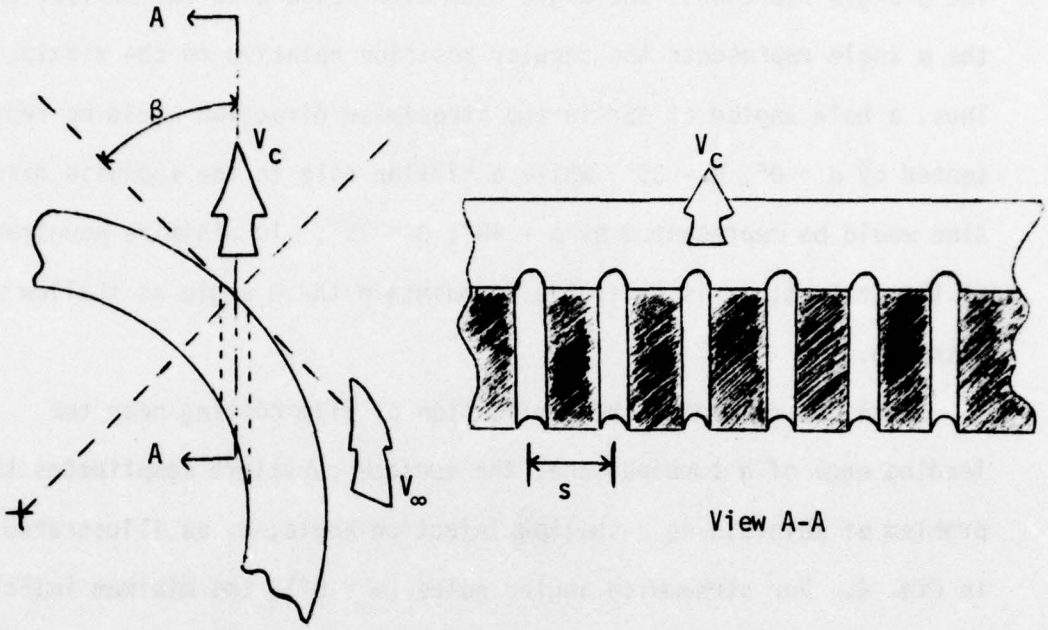

Streamwise Injection (α=0°)

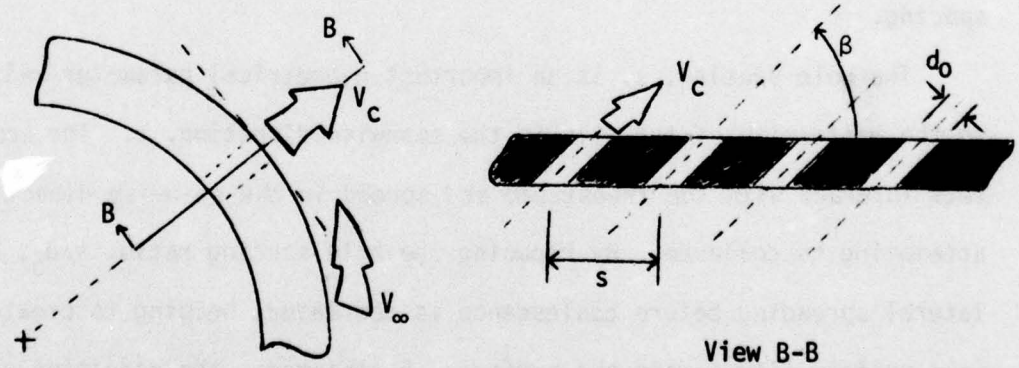

Spanwise Injection (α=90°)

Figure 4 Leading Edge Cooling Configurations on a Turbine Vane

In view of the importance of the injection hole angle in minimizing the coolant jet penetration and mixing with the freestream one can expect that the freestream boundary layer conditions at injection can also have a significant influence on the mixing process and the film cooling performance. A thin freestream boundary layer improves the performance due to the ability of the freestream to more readily deflect the coolant along the surface,thus reducing penetration. This is frequently characterized by the displacement thickness-to-hole diameter ratio, δ^*/d_o, at the point of injection. Other parameters influencing the coolant penetration into the freestream and/or the mixing process are the freestream acceleration and the freestream turbulence. These parameters have particular significance when applying film cooling to the leading edge of a turbine vane.

The foregoing discussion has provided a brief introduction of the film cooling process and important parameters which are employed in discussion of the film cooling literature presented in the following section.

I.C. Review of the Literature

A comprehensive review of the extensive film cooling literature has been prepared by Goldstein [2]. Those areas which are of specific interest to the application of film cooling to a turbine vane leading edge are reviewed herein, including literature that has been published since the Goldstein review.

I.C.1. Film Cooling Performance Parameters

As with all convective heat transfer analysis, film cooling requires a knowledge of the heat transfer rate at the solid surface for points downstream from the point of coolant injection. The two different approaches which have been developed for the correlation of film cooling heat transfer data are discussed and compared in this section.

In early investigations of film cooling, it was found convenient, experimentally, to use a "heated" coolant jet in a cold freestream flow to model the film cooling process. This is justified by an examination of the governing conservation equations which show [2], assuming constant property flows for small temperature differences, the analogy between film heating and film cooling. Investigations using a heated film also have shown the similarity of the temperature profile found in a boundary layer exposed to film heating compared to that found in high speed flow where kinetic effects and viscous dissipation combine to heat the fluid layers close to the surface. In high speed flow, if similarity of the velocity and temperature profiles is assumed, the heat transfer rate can be expressed [3] in terms of the heat transfer coefficient found for low velocity flow (h_o) and a driving potential between the wall temperature and the adiabatic wall temperature. Drawing on the resemblance of the temperature profiles for film heating and high speed flow, it has become conventional to express the heat flux to a film cooled surface as

$$q''_{w,FC} = h'(T_{adw,FC} - T_{w,FC}) \qquad (3)$$

where $T_{adw,FC}$ - adiabatic wall temperature with film cooling

$T_{w,FC}$ - wall temperature with film cooling

$q''_{w,FC}$ - heat flux at the wall with film cooling

h' - heat transfer coefficient with film cooling, defined by Eq. (3)

The adiabatic wall temperature reflects the extent that the freestream gas temperature near the wall has been changed by the addition of a cool (or hot) film. Film cooling experiments are conducted with an adiabatic surface for selected temperatures of the freestream (T_∞) and the coolant (T_c) to measure $T_{adw,FC}$. The adiabatic wall temperature is commonly presented in terms of the dimensionless adiabatic film cooling effectiveness

$$\eta_{adw} = \frac{T_\infty - T_{adw,FC}}{T_\infty - T_c} \tag{4}$$

with η_{adw} given as a function of the coolant blowing ratio (M), the location from injection (x/d_o, z/s), the injection angle (α,β), etc.

When the adiabatic film cooling effectiveness is known from previous experiments, the wall heat flux on a surface with film cooling can be determined from Eq. (3) provided that the heat transfer coefficient can be estimated. As a first approximation, it is frequently assumed that h' is approximately equal to h_o, the heat transfer coefficient with zero film coolant flow. This is found to be a good approximation for distances sufficiently far downstream from the point of injection. However, for application of Eq. (3) near the point of injection, it is necessary to know the value of h' more accurately because of the influence of the coolant mass addition on the hydrodynamic boundary layer.

Previous experiments have been conducted to determine both η_{adw} (under adiabatic wall conditions) and h' with a non-adiabatic wall. For the case in which film heating or cooling (with a small coolant-to-freestream temperature difference) has been employed to determine η_{adw}, it is possible to determine h' by using unheated coolant injection ($T_c=T_\infty$) on a non-adiabatic surface ($T_{w,FC} \neq T_\infty$). Then, the driving potential becomes ($T_\infty-T_{w,FC}$) since, for unheated injection, the adiabatic wall temperature equals the freestream temperature. Equation (3) can be employed to determine h' from the measured values of T_∞, $T_{w,FC}$, and $q''_{w,FC}$. Figure 5 illustrates the results of such an experiment using tangential slot injection [4] showing h'/h_o as a function of the downstream distance, x/d_o, for selected values of the blowing ratio, M. It can be seen that for a downstream distance, $x/s_o > 50$, and a blowing ratio, $M \lesssim 1.0$, the heat transfer coefficient with blowing (h') is equal to the "dry wall" heat transfer coefficient (i.e. without blowing), h_o. However, near the point of injection ($x/s_o < 50$) and/or with $M \gtrsim 1.0$, the value of h' can be substantially larger than h_o due to the hydrodynamic effects of coolant injection.

Metzger and Fletcher [5] have obtained similar results to compare the heat transfer coefficient for injection from a slot and a single row of holes as shown in Fig. 6.† While the values of h' and $\bar{h}'$ represent averaged values taken over the finite length of the test surface, the results show that, near injection, the hydrodynamic effects on h' (or $\bar{h}'$) can be significant. It does appear that the magnitude of the

†$\bar{h}'$ for the row of holes represents the laterally averaged value.

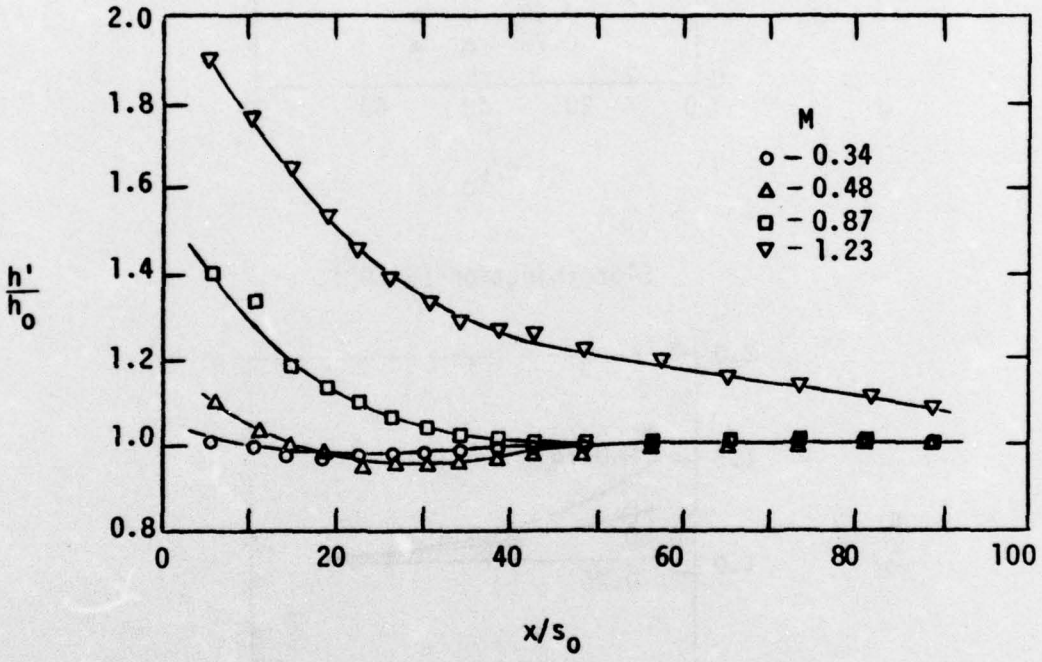

Figure 5 Heat Transfer Coefficient Downstream of Tangential Slot Injection (Hartnett, Birkebak, and Eckert [4])

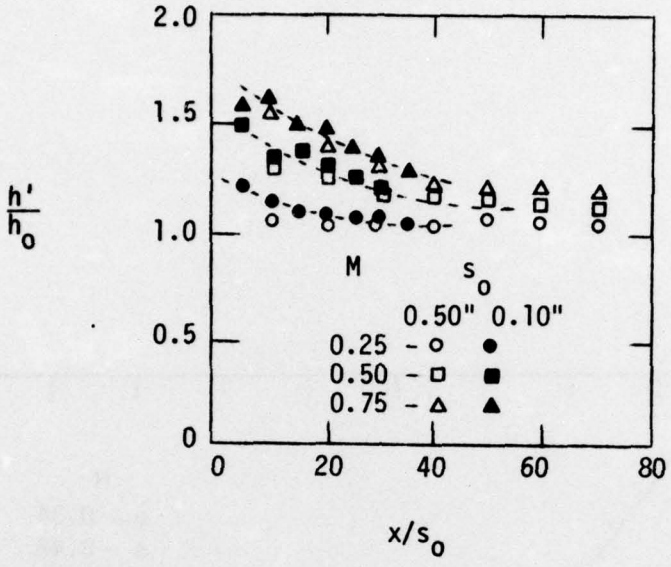

Slot Injection (β=60°)

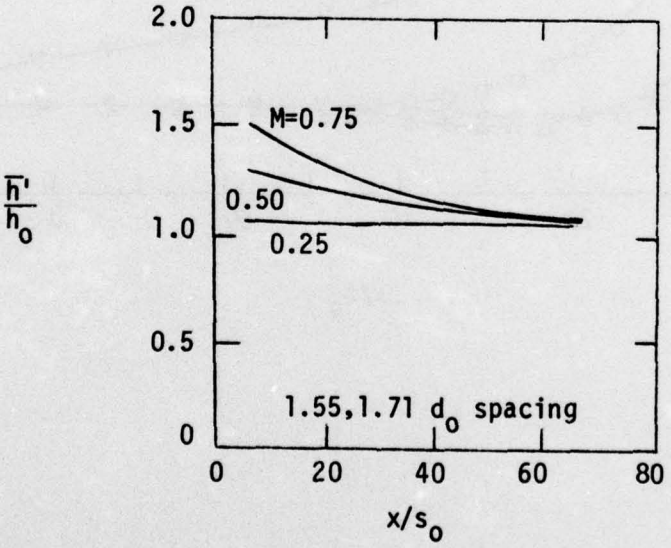

Single Row of Holes with
Streamwise Injection (β=60°)

Figure 6 Heat Transfer Coefficient Downstream of Injection through a Slot and through a Single Row of Holes (Metzger and Fletcher [5])

influence of coolant injection on h' may be strongly dependent on the injection geometry (β, s/d_o, . . .) as well as the blowing ratio. The results from detailed experiments with injection from a row of streamwise angled holes ($\beta = 35°$) [6], shown in Fig. 7, indicate that $\overline{h}'/h_o$ may not exceed 1.10 for values of $M \lesssim 1.0$.

It should be noted that the experiments in the foregoing references were conducted using small freestream-to-coolant temperature differences such that the effects of variations in the fluid properties are insignificant. To more closely model the film cooling conditions representative of turbine blade applications, Lander, Fish and Suo [7] conducted an experiment using film cooling injection from two staggered rows of holes on a turbine vane with a freestream-to-coolant temperature ratio of approximately 2.0. A transient measurement technique enabled the determination of h' under the same flow conditions used to measure $T_{adw,FC}$. The results shown in Fig. 8 again indicate that the hydrodynamic effects of coolant injection on h' are generally of such importance (or uncertainty) that the application of Eq. (3) near injection requires experiments to determine both $T_{adw,FC}$ and h'.

Although most film cooling effectiveness measurements have been made by measuring the adiabatic wall temperature distribution, the mass transfer analogy has also been employed. The film cooling process with an air freestream at T_∞ and an air coolant at T_c can be simulated by injecting a different coolant gas using the same film cooling geometry, but under isothermal conditions. Then, the mass fraction of the injected gas along the wall represents the impervious wall condition analogous to the adiabatic wall temperature. Measuremcnts of the wall

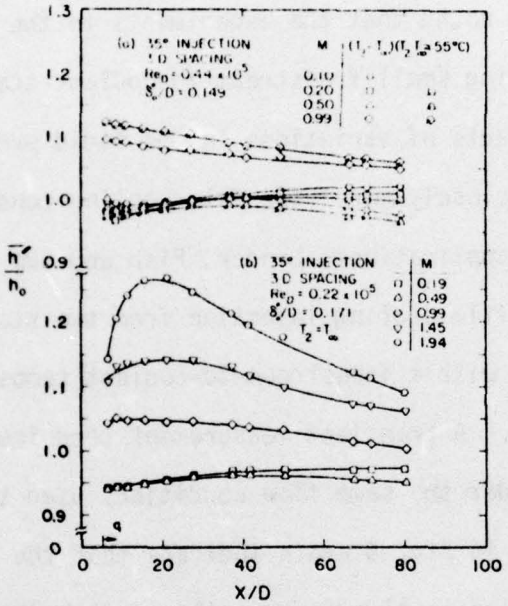

Figure 7 Heat Transfer Coefficient Downstream of Injection through a Single Row of Holes (Eriksen and Goldstein [6])

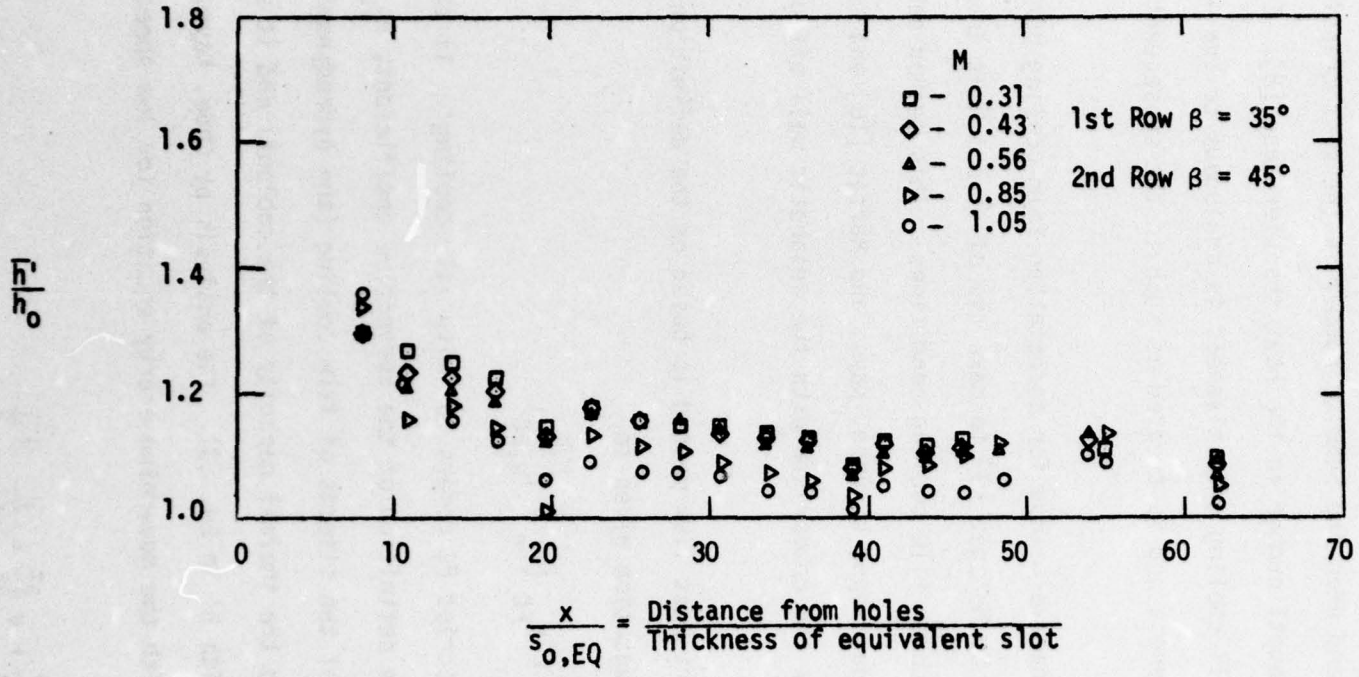

Figure 8 Heat Transfer Coefficient Downstream of Hole Injection on a Film Cooled Turbine Vane Surface (Lander, Fish and Suo [7])

mass fraction distribution are used to determine the film cooling effectiveness. This analogy becomes exact when the fluid properties are constant and when the Schmidt number in the mass transfer case equals the Prandtl number in the heat transfer case [8]. Then, the impervious wall cooling effectiveness is analogous to the adiabatic wall effectiveness and is treated as such in the subsequent discussion herein.

An alternative method for correlating film cooling performance was initiated by Metzger [9] to make use of direct heat transfer measurements under film cooling conditions. This method has subsequently been developed by Choe, Kays, and Moffat [10] and is reviewed herein to show the comparison with the adiabatic wall effectiveness method.

The direct heat flux method is based on the definition of a convective rate equation given as

$$q''_{FC} = h_{FC} (T_\infty - T_{w,FC}) \tag{5}$$

where the subscript FC refers to 'with film cooling'. It should be noted that the definition of the convection coefficient, h_{FC}, in Eq. (5) combines all of the effects of film cooling (the hydrodynamic effects of blowing and the thermal capacity of the coolant) and it should not be confused with h' in Eq. (3). The analysis by Choe, Kays, and Moffat [10] starts with the governing energy equation for low speed, constant property flow.

$$u \frac{\partial T}{\partial x} + v \frac{\partial T}{\partial y} = \frac{k}{\rho c_p} \frac{\partial^2 T}{\partial y^2} \tag{6}$$

The boundary conditions for two dimensional tangential slot injection over a constant temperature plate are

$$\begin{aligned} &\text{at } x = 0 \quad T = T_c && 0 \le y \le s_o \\ &\qquad\quad T = T_\infty && y > s_o \\ &\text{at } y = 0 \quad T = T_{w,FC} = \text{constant} \end{aligned} \tag{7}$$

The energy equation and the boundary conditions are non-dimensionalized, yielding the following

$$\text{RePr}\left[u' \frac{\partial \theta'}{\partial x'} + v' \frac{\partial \theta'}{\partial y'}\right] = \frac{\partial^2 \theta'}{\partial y'^2} \tag{8}$$

$$\text{at} \quad x' = 0 \qquad \theta' = \frac{T_c - T_\infty}{T_{w,FC} - T_\infty} = \theta_c \qquad 0 \le y' \le s_o/\ell$$

$$\theta' = 0 \qquad y' > s_o/\ell$$

$$y' = 0 \qquad \theta' = 1$$

where

$$\theta' = \frac{T - T_\infty}{T_{w,FC} - T_\infty}$$

It was noted [10] that the influence of changing the coolant temperature, i.e. θ_c, on the temperature in the boundary layer could be isolated since the energy equation was linear and θ_c appeared as a linear, non-homogeneous boundary condition. Therefore the temperature, T, was shown to be a function of x, y, z and θ_c.

Considering a given location on the test surface, and using the linearity of the system, the following equation was written to represent the temperature as a function of θ_c.

$$T(\theta_c) = T(0) + \theta_c * \Delta T \tag{9}$$

where $\Delta T = T(1) - T(0)$

with $\theta_c = 0$ for $T_c = T_\infty$, and $\theta_c = 1$ for $T_c = T_w$

An expression for the heat flux at the surface as a function of θ_c is obtained by applying the operator $-k \frac{\partial}{\partial y}$ to Eq. (9) and then considering the temperature gradient at $y = 0$. For a common driving potential $(T_\infty - T_{w,FC})$, the heat flux expression reduces to

$$h(\theta_c) = h(0) - \theta_c [h(0) - h(1)] \tag{10}$$

Equation (10) is the form originally suggested by Metzger [9] showing a linear relationship between the heat transfer coefficient with film cooling, $h(\theta_c)$[†], and the dimensionless coolant temperature, θ_c. Figure 9 illustrates a typical plot of the $h(\theta_c) - \theta_c$ variation. The point where the curve intersects the θ_c axis represents $h(\theta_c) = 0$, i.e. an adiabatic surface. Therefore, the intersection of the $h(\theta_c)$ line with the θ_c axis gives

$$\theta_{c,adw} = \frac{T_c - T_\infty}{T_{adw,FC} - T_\infty} = \frac{1}{\eta_{adw}} \tag{11}$$

An examination of Fig. 9 also shows that

$$\eta_{adw} = \frac{1}{\theta_{c,adw}} = \frac{h(0) - h(1)}{h(0)} \tag{12}$$

Thus, Choe, Kays, and Moffat [10] show that by substituting Eqs. (10) and (12) into (5), the heat flux with film cooling can be expressed as

---

[†]For clarification, it should be noted that the coefficient $h(\theta_c)$ is identical to h_{FC} previously defined by Eq. (5).

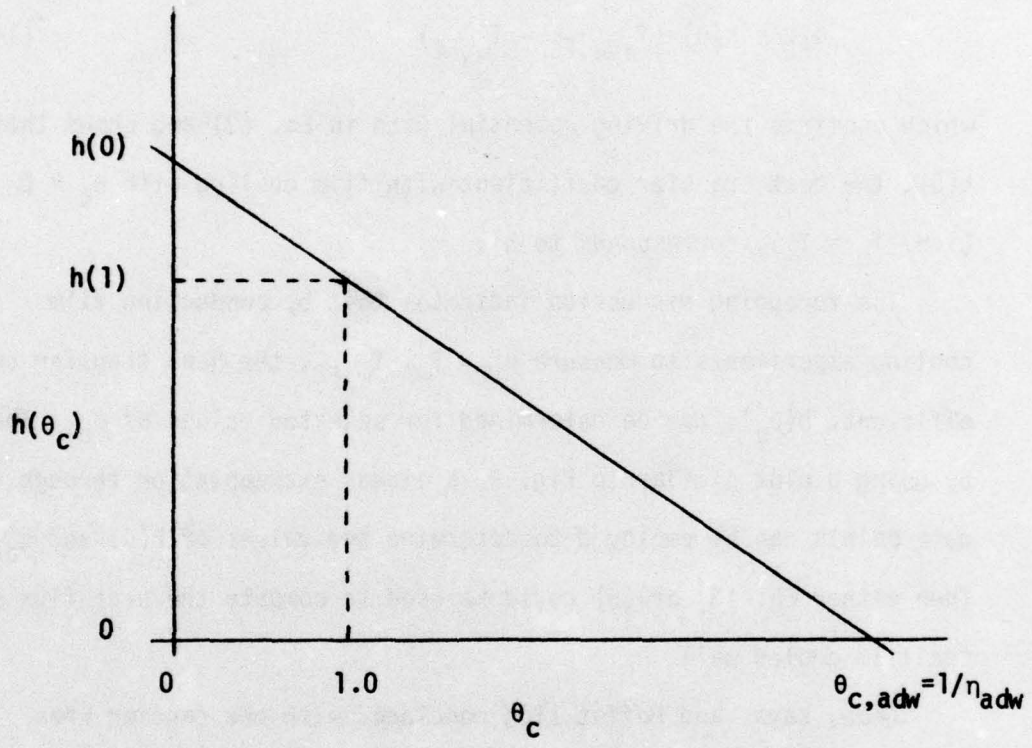

Figure 9 Heat Transfer Coefficient with Film Cooling versus the Dimensionless Coolant Temperature Ratio, θ_c (Choe, Kays, and Moffat [10])

$$q''_{FC} = h(0) \{1 - \theta_c * \eta_{adw}\} \{T_\infty - T_{w,FC}\} \quad (13)$$

By noting the definitions of θ_c and η_{adw}, Eq. (13) reduces to

$$q''_{FC} = h(0) (T_{adw,FC} - T_{w,FC}) \quad (14)$$

which confirms the driving potential used in Eq. (3) and shows that h(0), the heat transfer coefficient with film cooling with $\theta_c = 0$ (i.e. $T_c = T_\infty$), corresponds to h'.

The foregoing discussion indicates that by conducting film cooling experiments to measure q''_{FC}, T_∞, $T_{w,FC}$, the heat transfer coefficient, $h(\theta_c)$, can be determined for selected values of θ_c. Then by using a plot similar to Fig. 9, a linear extrapolation through the data points can be employed to determine the values of h(0) and η_{adw}. Then either Eq. (3) or (5) could be used to compute the heat flux at the film cooled wall.

Choe, Kays, and Moffat [10] concluded with one caution when comparing values for η_{adw} found by extrapolating the $h(\theta_c) - \theta_c$ curve with those obtained by measuring $T_{adw,FC}$ on an adiabatic surface. The linearity of the $h(\theta_c) - \theta_c$ curve was based on a constant wall temperature boundary condition, $T_{w,FC}$. However, for experiments to determine η_{adw} for a given value of T_c, the wall temperature ($T_{adw,FC}$) is allowed to vary. Thus, the derivative of the enthalpy thickness would not be the same in both cases and the h(0) values found from the $h(\theta_c) - \theta_c$ plot should not be used with the values of adiabatic effectiveness determined from an adiabatic test surface with a variable wall temperature.

An important fact to remember about the preceding analysis showing the relationship between the direct heat flux and the adiabatic wall effectiveness methods is that the $h(\theta_c) - \theta_c$ linearity is the result of the constant property assumption. This is the basis of the linearization of the energy equation, but once the temperature difference becomes large, the effect of property variations is uncertain.

I.C.2. Flow Visualization

Frequently, flow visualization has been employed to enhance the understanding of the film cooling process. The text of Abramvoich [11] and the papers by Ramsey and Goldstein [12], Eriksen [13], Liess [14] and most recently by Colladay and Russell [15] have provided an excellent picture of the interaction between the film coolant and the freestream for injection from discrete holes. Figure 10 provides a visual representation of a coolant jet injected into a freestream flow [16]. As the coolant jet leaves the surface, it retards the freestream flow along the upstream side of the jet causing an increased pressure there. Downstream of the jet, as the freestream flows around it, a reduced pressure occurs, providing the pressure difference necessary to deform and deflect the jet. Abramovich [11] explained that because of intense intermixing between the jet and the freestream, a turbulent layer quickly develops around the periphery of the jet. The slower peripheral particles are more forcefully bent in the direction of the freestream (moving along curved trajectories) than the higher velocity particles in the core of the jet. This creates the "horseshoe" shape and the circulatory motion within the jet shown in Fig. 10. This circulatory motion

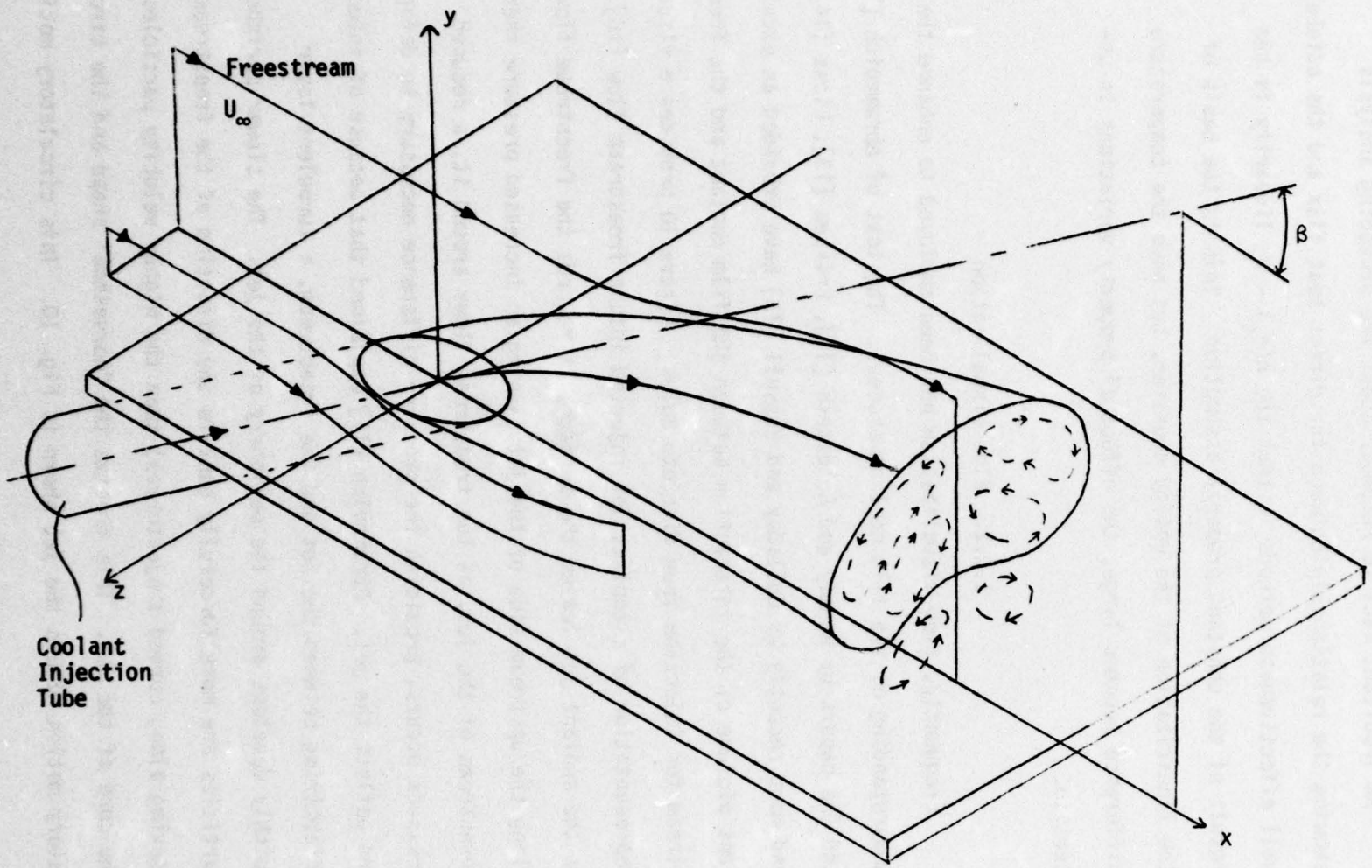

Figure 10 "Horseshoe" Shape of Coolant Jet as It Interacts with the Freestream (Goldstein, Eckert, Ramsey [16])

and the deflecting freestream flow causes the jet "legs" of the "horseshoe" to spread which only further enhances the vortex motion in the jet. The vortex motion increases the entrainment of fluid from the freestream, leading to large-scale mixing within the jet.

Ramsey and Goldstein [12] investigated the interaction of a heated jet injected normal to the freestream by making temperature measurements as a function of position normal to the surface (y/d_0), and downstream (x/d_0) and lateral (z/d_0) from the point of injection. Figure 11 presents contours of constant dimensionless temperature defined as

$$\frac{\theta}{\theta_2} = \frac{T - T_\infty}{T_c - T_\infty} \tag{15}$$

Data for three values of the blowing ratio are shown. Figure 11 clearly shows the "horseshoe" shape of the jet, especially at the downstream distance of $x/d_0 = 1.37$. For the smallest value of the blowing ratio ($M = 0.5$), Fig. 11 also shows a substantial influence of the coolant on the wall temperature (at $y/d_0 = 0$). The wall temperature approaches the freestream temperature (i.e. $\theta/\theta_2 \to 0$), as z/d_0 and x/d_0 increase, due to mixing of the coolant with the freestream. However, for the largest value of M (=2.0), the data show that the coolant has no influence on the wall temperature because of excessive penetration of the coolant jet into the freestream.

To investigate the jet penetration and mixing phenomena, Ramsey and Goldstein [12] did an extensive flow visualization study for the normal jet at a blowing ratio of 2.0. They observed that as the jet left the hole, a void was created immediately downstream of the hole as

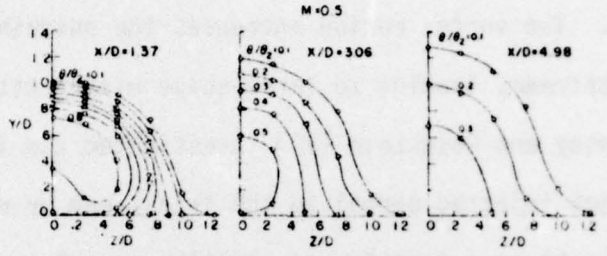

Constant-temperature contours for 90 deg injection angle, $M = 0.5$

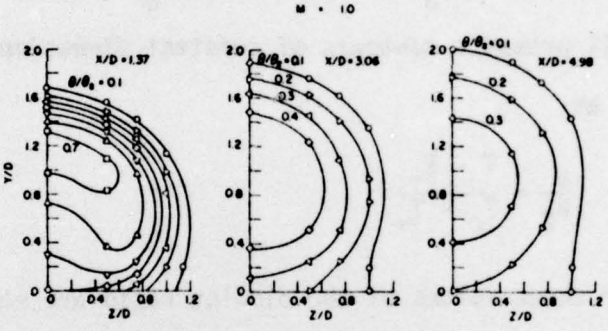

Constant-temperature contours for 90 deg injection angle, $M = 1.0$

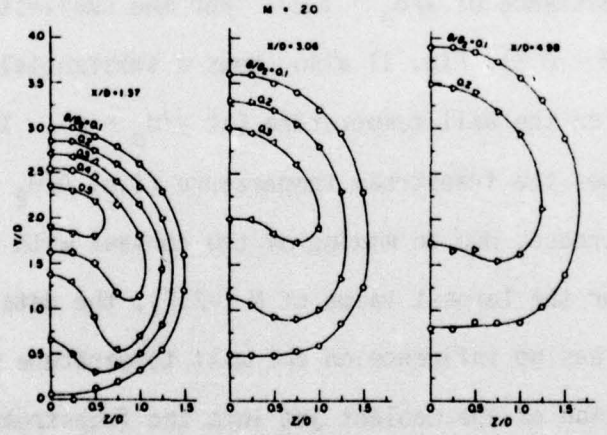

Constant-temperature contours for 90 deg injection angle, $M = 2.0$

Figure 11 Constant Temperature Profiles for a Heated Jet Interacting with the Freestream (Ramsey, Goldstein [12])

illustrated in Fig. 12. The void was filled as the freestream air moved around the jet toward the downstream side. From this location, the freestream moved upward, away from the wall, as it was entrained by the jet. At a distance, $x/d_0 = 1$, downstream, it was observed [12] that the freestream flowed upward away from the wall until it reached a height where it turned upstream and reverse flow existed. This flow of the freestream away from the wall was found to diminish with axial distance, until at a distance of $x/d_0 = 10$, it was no longer observable. However, due to the flow of the freestream away from the wall and the reverse flow above the wall, Ramsey and Goldstein [12] found that large eddies were created which enhanced the mixing between the freestream and the coolant. Ramsey and Goldstein [12] also conducted flow visualization studies at a blowing ratio of 1.0, and the trends were similar to those just discussed for M = 2.0. The difference in the two cases was that for the lower value of M, the vertical components of velocity in all regions were smaller.

For effective film cooling, it is desirable to minimize the penetration of the coolant jet in order to avoid the excessive coolant-freestream mixing that results from the large eddies generated when the freestream passes around and underneath the coolant jet. If the jet does not penetrate far into the freestream (for a moderate blowing ratio), it is possible for the jet to be deflected back toward the surface. A re-examination of the temperature profiles presented in Fig. 11, shows that as the blowing ratio is increased, the core of the jet (where θ/θ_2 is largest) moves farther away from the wall and the core temperature, $(\theta/\theta_2)_{max}$, decreases. Therefore the increased

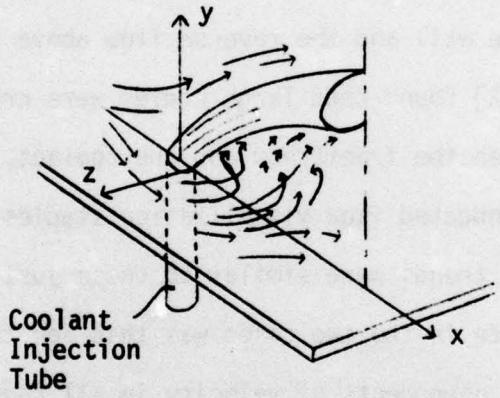

Figure 12 Interaction of a Jet with the Freestream (Ramsey and Goldstein [12])

blowing has caused the jet to penetrate farther into the freestream, and the increased mixing that accompanies the penetration of the jet has resulted in the core having lower values of θ/θ_2. For the downstream distance of $x/d_0 = 4.98$, it can be seen that, at M = 0.5, the core of the jet is attached to the surface while at a blowing ratio of 1.0, the core of the jet is slightly detached but the outer layers of the jet definitely influence the wall temperature. For a blowing ratio of M = 2.0, the jet is completely detached from the surface and has no influence on the wall temperature.

Liess [14] also studied the penetration of the coolant jet from the surface using a row of holes angled at 35° in the streamwise direction. His experiments showed that the jet was attached to the surface for a blowing ratio of 0.5, but for M = 1.0, it was slightly detached from the wall, and for M = 1.5 it was completely detached from the wall. The only possible benefit of a high blowing ratio, as observed by Eriksen [13], was that the increased mixing generated by the higher blowing ratio increased the lateral spreading of the jet.

Colladay and Russell [15] investigated the penetration of the coolant jet for three different coolant angles, with four holes arranged in a staggered array, $5d_0$ apart. For normal injection, they observed that the jet detached from the surface and penetrated into the freestream at a blowing ratio of 0.3. However, when the holes were angled at 30° with the freestream, the coolant jet did not begin to detach until the blowing ratio reached a value of 0.5. This indicates that shallower angles allow a higher blowing ratio to be used before the jet detaches from the surface. Their results for a compound

angle (α = 45°, β = 30°) showed that the lateral angle made by the jet entering the freestream tended to generate a single, strong vortex filament downstream that was observed to start at a blowing ratio of 0.3 and was most pronounced at the blowing ratios of 0.7 to 0.9. The strong vortex motion helped to keep the compound angled jet attached to the surface at a high blowing ratio. Even at an M value of 0.9, the jet remained attached to the surface.

While the penetration of the jet depends to a large part on the blowing ratio and the angle of injection, the boundary layer thickness of the freestream can also be expected to influence the deflection of the jet toward the surface. With a thinner boundary layer, the coolant encounters a higher freestream velocity closer to the surface which should reduce the penetration. Colladay and Russell [15] conducted tests on their 30° streamwise angled hole configuration for a boundary layer thickness 37% larger than previously tested. The film coolant was found to penetrate farther from the surface for the thicker boundary layer, but the penetration relative to the boundary layer thickness remained the same.

The foregoing flow visualization studies indicate that the best film cooling performance can be achieved when the coolant jet remains attached to the surface. Jet detachment from the wall and penetration into the freestream results in increased mixing with the freestream and reduced cooling effectiveness. Therefore it is important that the blowing ratio and the angle of injection be selected so that the coolant jet penetration is minimized.

I.C.3. Mass Flux Ratio, Velocity Ratio, Momentum Ratio and Angle of Injection

As the flow visualization studies have shown, the ability of the film coolant to protect the wall depends heavily on the penetration of the coolant, which determines whether the coolant jets remain attached to the surface. The penetration of the coolant is influenced by the mass flux ratio (M), the velocity ratio (V_c/V_∞), and the momentum flux ratio (I). Since these parameters and the density ratio (ρ_c/ρ_∞) are all interrelated, it has been difficult in previous experiments to isolate their individual influence on the condition of jet detachment from the surface. Furthermore, the flow visualization studies have shown that the angle of injection can have a significant influence on the jet penetration and subsequent detachment. It is expected that the component normal to the surface of the mass flux, velocity, and momentum flux ratios is instrumental in determining the condition for jet detachment from the surface.

Since the film coolant acts like a heat sink, the mass of coolant blown onto the surface is influential in the film coolant's ability to protect the wall. As long as the coolant remains attached to the surface, increasing the mass (i.e. thermal capacity) of the coolant leads to better film cooling performance. However, an increase in coolant mass by excessive blowing, resulting in coolant detachment from the surface, leads to large scale mixing with the freestream that overwhelms any benefit of the additional thermal capacity of the coolant.

Early investigations of film cooling with slots studied the influence of the blowing ratio on the film cooling effectiveness. However, for injection from a slot, a continuous film is formed across the

surface, in contrast to injection from holes where the freestream is able to pass between the coolant jets. When the coolant is injected from a slot, the mixing process between the coolant and the freestream is directly related to the coolant-freestream velocity ratio. Wieghardt [17], investigating film cooling with a slot, found that the adiabatic effectiveness reached a maximum for $M \approx 1.0$ as shown in Fig. 13. Since the density ratio was near unity, this value of M also corresponds to $V_c/V_\infty \approx 1.0$. As Figure 13 reveals, for a blowing ratio greater than 1.0, the beneficial effects of increasing the coolant thermal capacity were overwhelmed by the detrimental influence of the coolant-freestream mixing process. Other film cooling studies with tangential slots [18] [19] indicate similar trends with the mixing becoming a minimum when the coolant and freestream have the same velocity.

To isolate the influence of the blowing ratio on the thermal capacity of the coolant, Burns and Stollery [20] measured the effectiveness with injection from a tangential slot using different density ratios. The velocity ratio was held constant at 1.0 while different values of the density ratio were used to increase the mass flux ratio. Figure 14 shows that increasing the thermal capacity of the coolant (by increasing ρ_c/ρ_∞) resulted in an increase in the film cooling effectiveness.

For injection from discrete holes it is much more difficult to isolate the influence of the blowing ratio on the coolant-freestream mixing process. With injection from holes, the freestream flows between the coolant jets, causing the coolant to exhibit a three-dimensional behavior different from that observed for two-dimensional slot

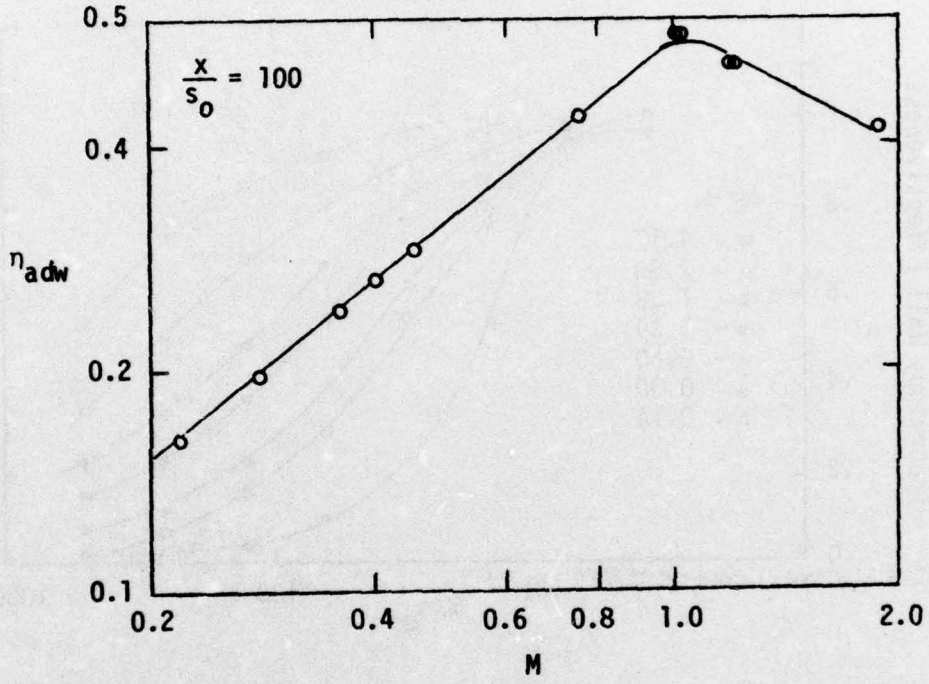

Figure 13. The Influence of the Mass Flux Ratio on the Film Cooling Effectiveness (Wieghardt [17])

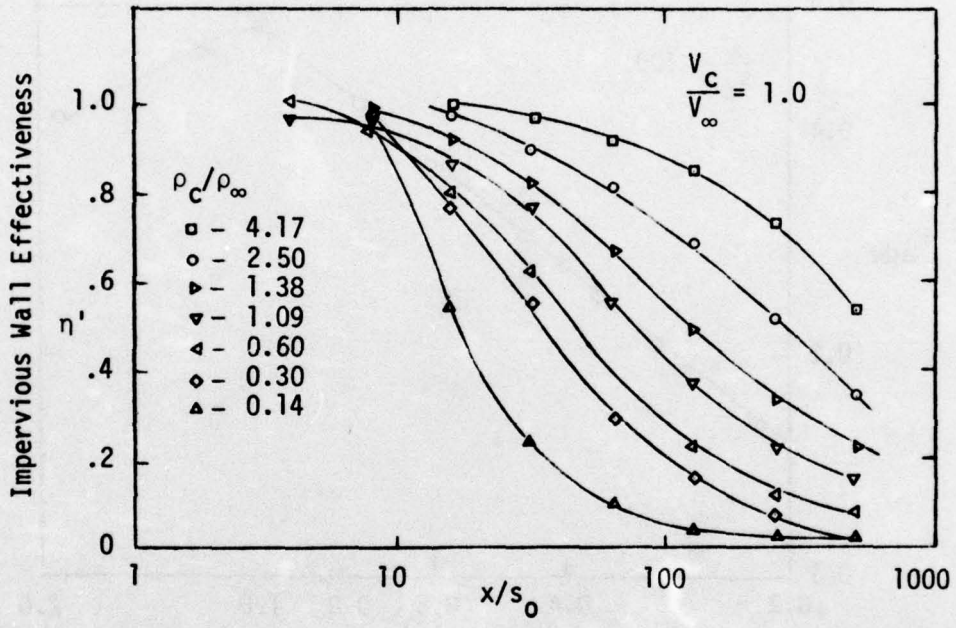

Figure 14. The Influence of the Density Ratio on the Film Cooling Effectiveness for Tangential Slot Injection (Burns and Stollery [20])

cooling. Numerous investigations have been conducted to determine the influence of the blowing ratio on the adiabatic effectiveness, including those by Liess [14], Goldstein, Eckert, and Ramsey [16], and Eriksen [13]. They observed that injection from a streamwise angled hole or row of holes (α=0°, β=35°) achieved an optimum cooling effectiveness for a blowing ratio of M $\approx$ 0.5. Since these investigations were conducted with $\rho_c/\rho_\infty \approx 1.0$, this corresponded to a velocity ratio of 0.5. Figure 15, from Goldstein, Eckert, Eriksen, and Ramsey [21], shows that close to injection (x/d_o = 5.2 and 11.1) the adiabatic effectiveness increased with blowing ratio for M $\leq$ 0.5, due to the increased thermal capacity of the coolant. However, as the blowing ratio was increased further, the effectiveness decreased markedly apparently as a result of the coolant penetration into the freestream and the enhanced freestream-coolant mixing. There was little difference between injection from a single hole or a row of holes. Further downstream the decrease in effectiveness for M > 0.5 was not as pronounced. In fact, for the row of holes, η_{adw} increased again as M was increased above approximately 1.0 to 1.5. Since the density ratio was near unity, these results again indicate an optimum cooling effectiveness for a velocity ratio of approximately 0.5.

While most previous studies have concentrated on streamwise injection, Goldstein, Eckert, Eriksen, and Ramsey [21] also investigated injection from a single spanwise angled hole (α=90°, β=35°), again with a negligible density variation. Figure 16 illustrates their results showing the adiabatic effectiveness as a function of spanwise location (z/d_o) for selected values of x/d_o and the blowing ratio. Close to

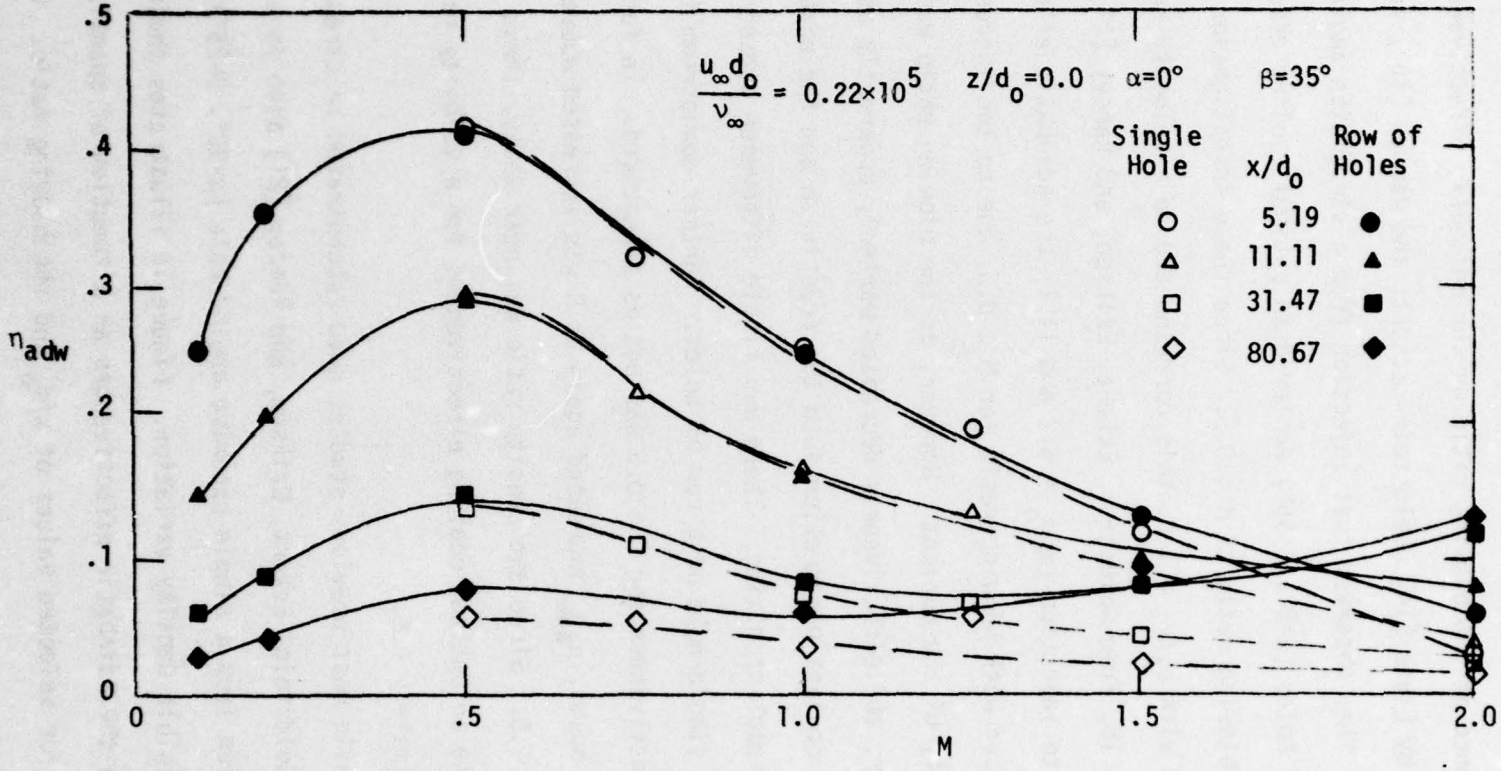

Figure 15. The Influence of the Blowing Ratio on Film Cooling Effectiveness for Hole Injection (Goldstein, Eckert, Eriksen and Ramsey [21])

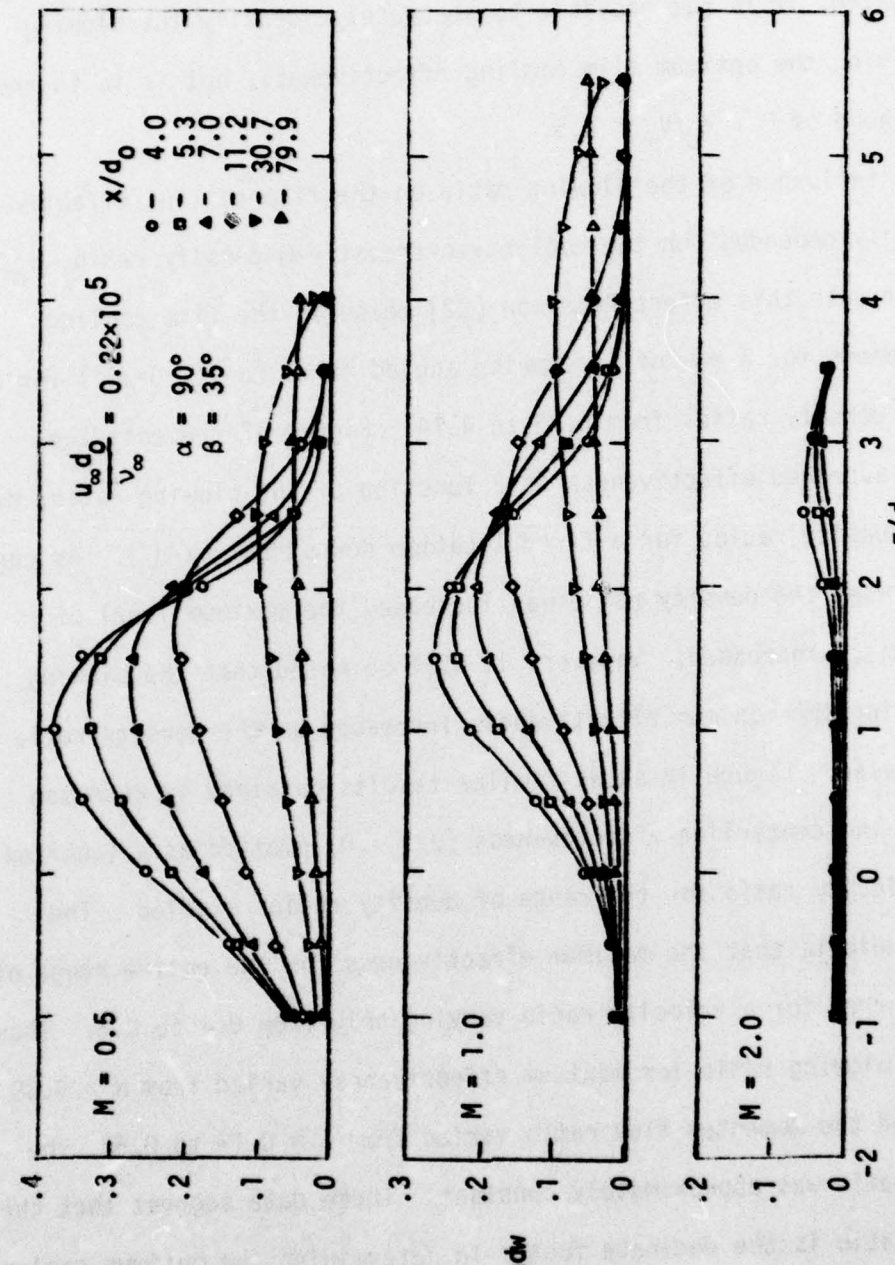

Figure 16. The Influence of the Blowing Ratio on Film Cooling Effectiveness for a Spanwise Angled Hole (Goldstein, Eckert, Eriksen and Ramsey [21])

injection ($x/d_o \leq 11.2$), the highest values of adiabatic effectiveness were achieved for the blowing ratio of 0.5, while η_{adw} decreased for higher values of the blowing ratio. Due to the limited values of M investigated, it is not possible to accurately identify the blowing ratio giving the optimum film cooling effectiveness, but it is in the neighborhood of $M \approx V_c/V_\infty \approx 0.5$.

The influence of the blowing ratio on the film cooling effectiveness is strongly dependent on the coolant-to-freestream density ratio, ρ_c/ρ_∞. To investigate this effect Pederson [22] measured the film cooling effectiveness for a row of streamwise angled holes (α=0°, β=35°) for a range of density ratios from 0.75 to 4.14. Figure 17 presents the spanwise averaged effectiveness as a function of the blowing ratio, M, and the density ratio, for a fixed location downstream (x/d_o). As can be seen, when the density ratio was increased the maximum level of effectiveness increased. However, it will be noted that the blowing ratio giving the maximum effectiveness increased as the density ratio was increased. Figure 18 shows similar results obtained by Pederson [22] with the centerline effectiveness (z/s = 0) plotted as a function of the velocity ratio for the range of density ratios studied. The results indicate that the maximum effectiveness for the entire range of ρ_c/ρ_∞ occurred for a velocity ratio varying only from 0.4 to 0.5. Thus, while the blowing ratio for maximum effectiveness varied from $M \approx 0.38$ to 1.67 and the momentum flux ratio varied from $I \approx 0.19$ to 0.67, the velocity ratio was approximately constant. These data suggest that the velocity ratio is the dominate factor in determining the optimum coolant blowing ratio.

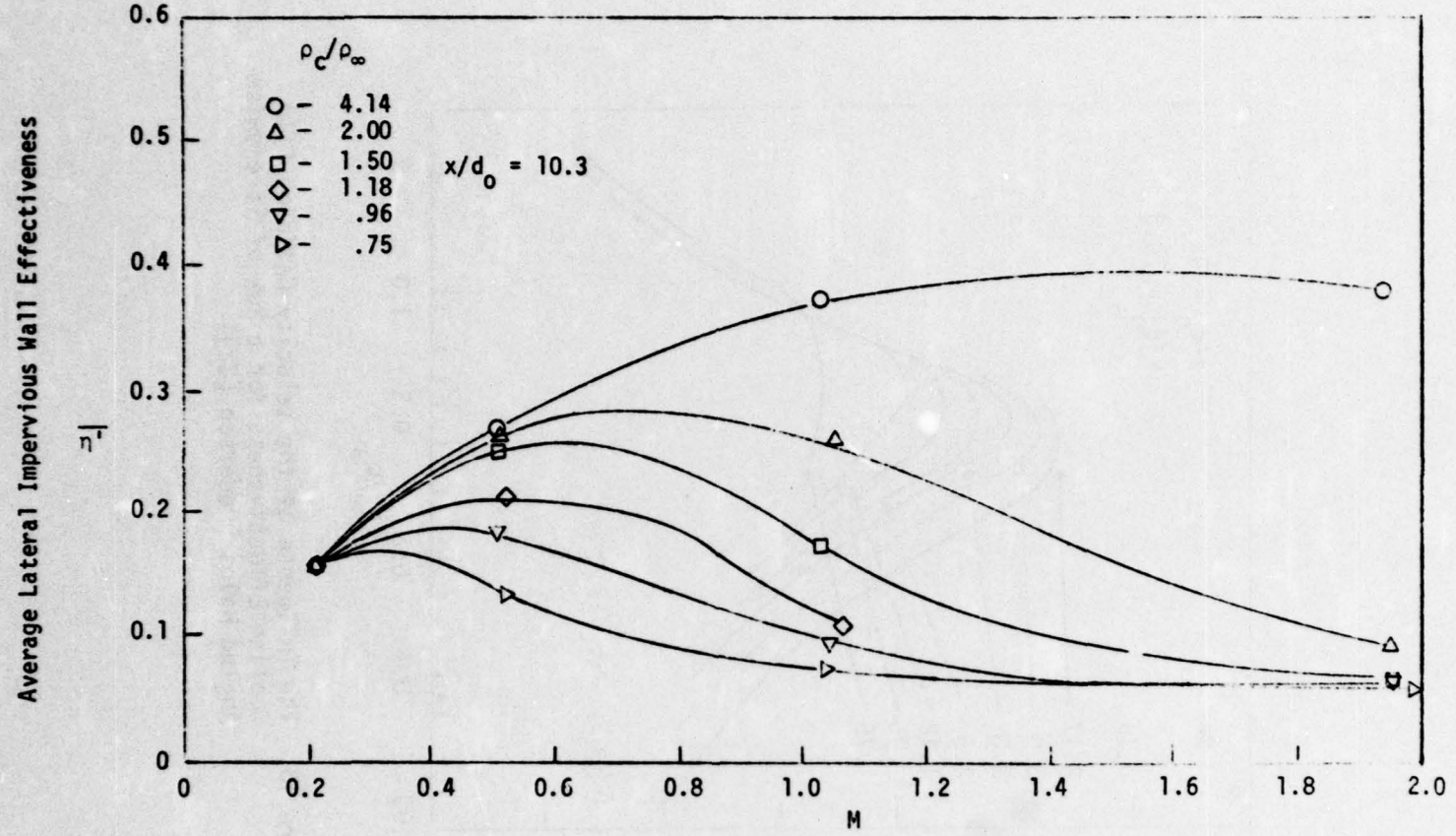

Figure 17. The Influence of the Density Ratio on Film Cooling Effectiveness for a Row of Streamwise Angled Holes (Pederson [22])

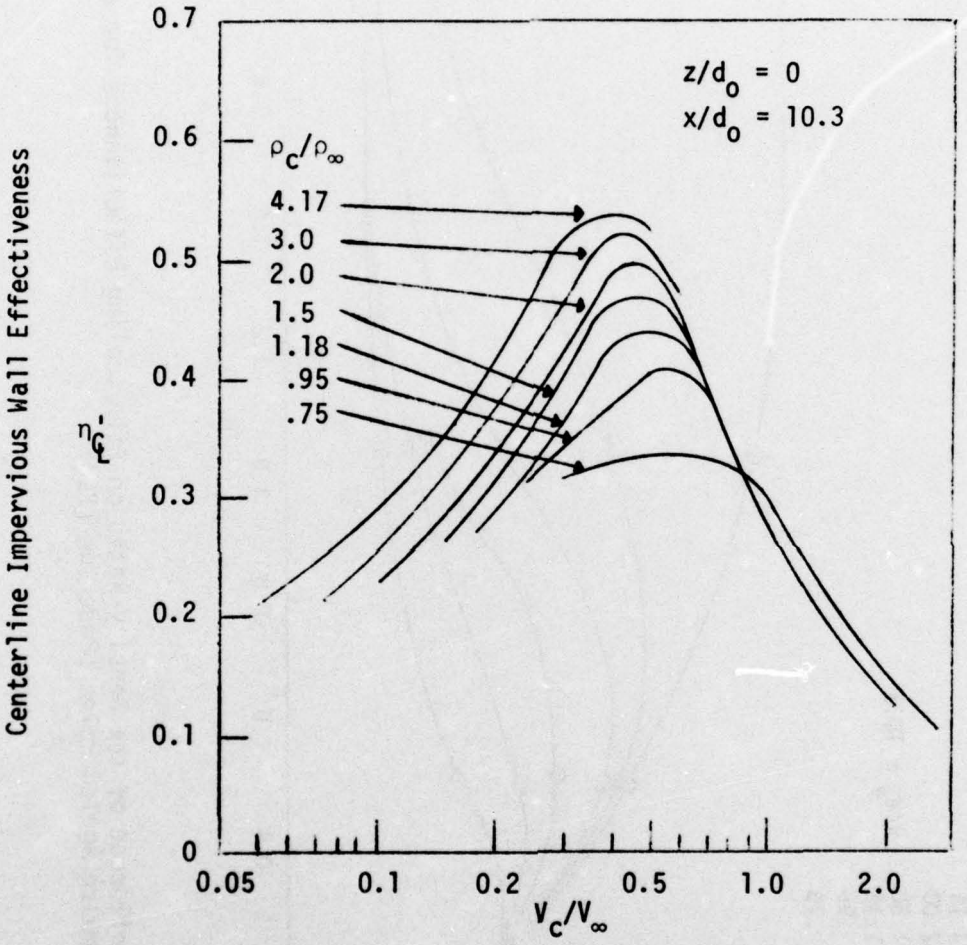

Figure 18. The Influence of the Velocity Ratio on Film Cooling Effectiveness for a Row of Streamwise Angled Holes (Pederson [22])

Goldstein, Eckert, and Burggraf [23] examined the use of the momentum flux ratio to correlate the maximum film cooling effectiveness for different values of the density ratio. Their results, for both a row of holes and a single hole (α=0°, β=35°), shown in Fig. 19 indicate that the maximum film cooling effectiveness (centerline value at x/d_0 = 6) was achieved for a momentum flux ratio that was approximately constant at a value of 0.2. For the values of density ratio investigated, this value of momentum flux ratio corresponds to V_c/V_∞ in the range of 0.24 to 0.48.

Foster and Lampard [24] also have investigated the influence of density ratio on the film cooling effectiveness for a row of normal holes (β=90°). They found that close to the hole (x/d_0 = 6.5), the effectiveness increased as ρ_c/ρ_∞ was increased (ρ_c/ρ_∞ = 1.50 to 3.50) for a constant value of V_c/V_∞. Furthermore, for a constant value of ρ_c/ρ_∞, the effectiveness increased as V_c/V_∞ was decreased (V_c/V_∞ = 1.06 to 0.38). For the condition, ρ_c/ρ_∞ = 2.0, their data indicate the maximum film cooling effectiveness occurs for V_c/V_∞ somewhat less than 0.38, although the data presented do not show how the optimum velocity ratio varies with ρ_c/ρ_∞. As Foster and Lampard [24] have concluded, the influence of the density ratio and the velocity ratio on the condition for optimum cooling effectiveness is too complex to be accounted for in terms of simple parameters such as the mass flux ratio, M, or the momentum flux ratio, I.

While the hydrodynamic parameters just discussed play an important role in the coolant jet penetration into the freestream and detachment from the surface, the angle of the coolant hole is also significant.

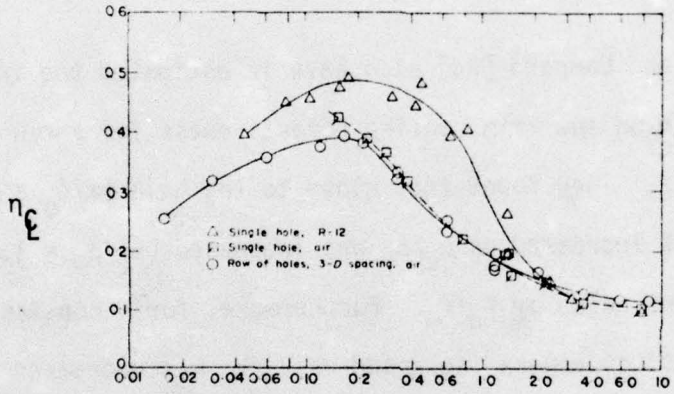

$\eta_{\mathcal{L}}$

I, Momentum Flux Ratio

Figure 19. Centerline Effectiveness as a Function of the Momentum Flux Ratio (Goldstein, Eckert, and Burggraf [23])

When investigating the jet detachment from the surface, the normal component of the jet velocity and/or momentum flux ratios is expected to be the predominant factor. Also, the tangential component of the momentum flux ratio probably has an influence on the coolant jet trajectory across the surface (especially when using non-streamwise injection).

One of the initial investigations into the influence of the angle of injection was conducted by Papell [25] using a slot ($\rho_c/\rho_\infty \approx 2$). His results, presented in Fig. 20, show that the adiabatic effectiveness decreased as the injection angle (β) increased. The sharpest drop in the effectiveness was seen when the angle was increased past 75°. The decrease in effectiveness with increasing angle increased as the blowing ratio increased.

For film coolant injection from holes, increasing the angle of injection would cause the jet to detach at a lower blowing ratio resulting in lower levels of effectiveness [15]. The data of Goldstein, Eckert, and Ramsey [16] shown in Fig. 21 compare the results for streamwise injection at an angle of β = 90° and 35°, illustrating the higher level of adiabatic effectiveness achieved with the shallower angle. For a blowing ratio of 0.5, the jet from the shallow angle probably remained attached to the surface, while the jet from the 90° angle most likely detached and penetrated into the freestream [15].

While injection with a steep angle causes the jet to detach at a lower blowing ratio, the increased mixing involved with the jet penetration into the freestream does have one advantage. The increased mixing causes the "legs" of the "horseshoe" of the jet to spread at a

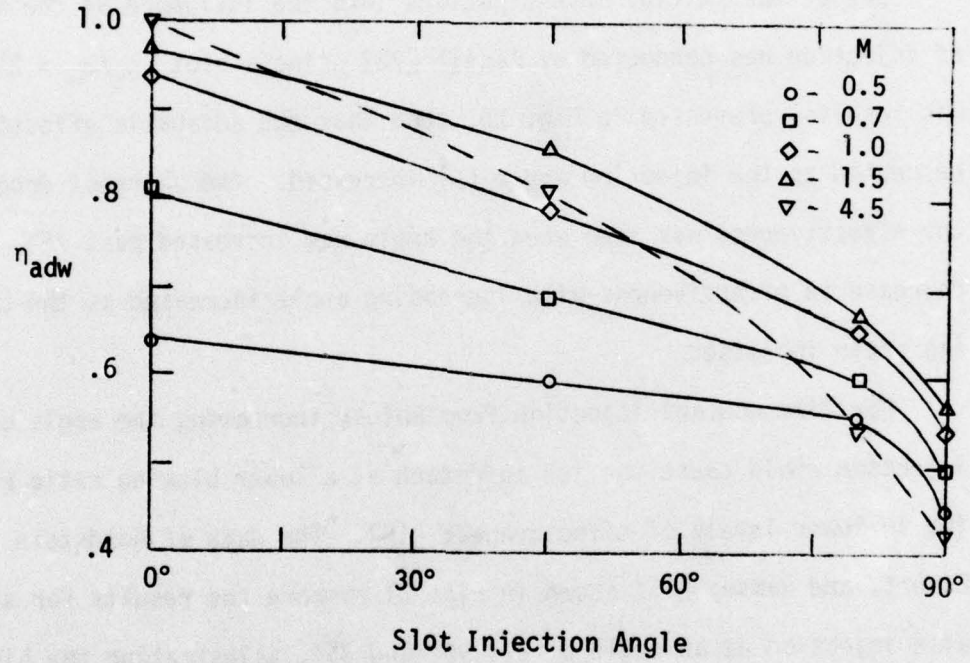

Figure 20. The Influence of the Slot Injection Angle on Film Cooling Effectiveness (Papell [25])

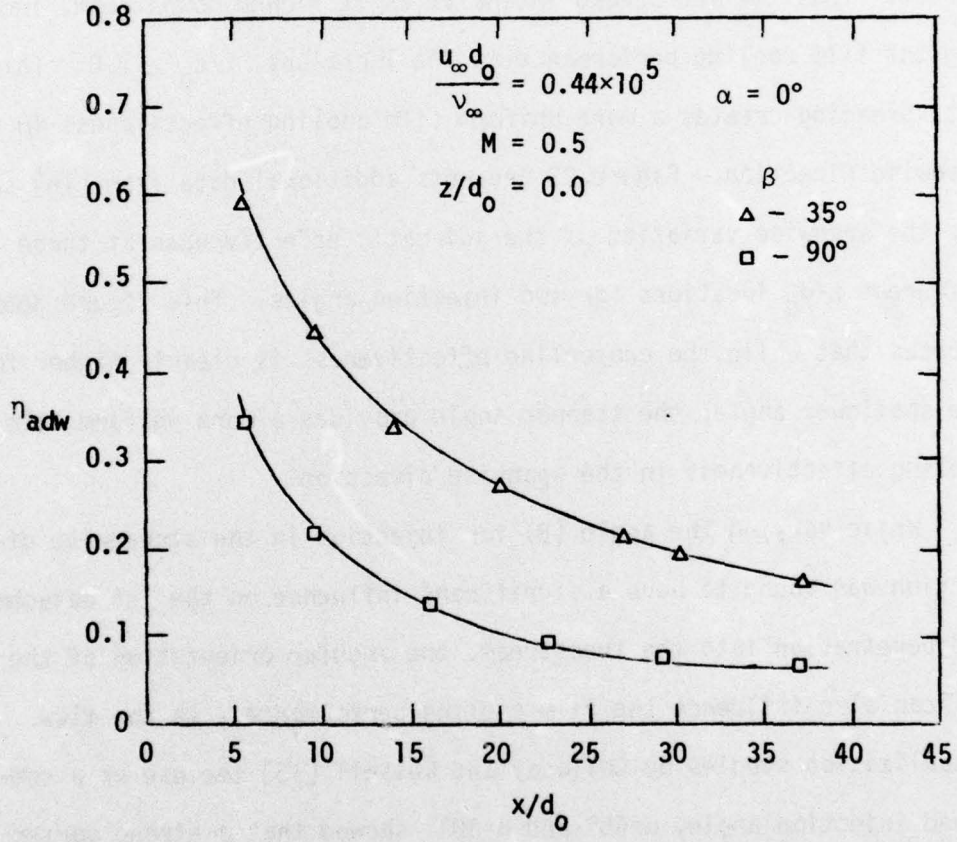

Figure 21. The Influence of the Hole Angle on Film Cooling Effectiveness (Goldstein, Eckert, and Ramsey [16])

faster rate, so that adjacent jets will coalesce closer to injection and reinforce each other. The ability of the jet to spread in the spanwise direction can be seen clearly in Figure 22. The data by Goldstein, Eckert, and Ramsey [16] show that for a single hole angled at 35° in the streamwise direction the adiabatic effectiveness for $z/d_o \geq 1.0$ increased (or remained constant) as the coolant flowed downstream. Thus the jet spread laterally as it flowed downstream, increasing the film cooling performance at the locations, $z/d_o \geq 1.0$. This jet spreading creates a more uniform film cooling effectiveness in the spanwise direction. Figure 23 presents additional data from [16] showing the spanwise variation of the adiabatic effectiveness at three different x/d_o locations for two injection angles. This figure demonstrates that while the centerline effectiveness is clearly higher for the shallower angle, the steeper angle provides a more uniform film cooling effectiveness in the spanwise direction.

While varying the angle (β) for injection in the streamwise direction was found to have a significant influence on the jet detachment and penetration into the freestream, the angular orientation of the jet (α) can also influence the film cooling performance. In the flow visualization studies by Colladay and Russell [15] the use of a compound injection angle, α=45° and β=30°, showed that a strong vortex filament generated by the jet entering the freestream enabled the jet to remain attached to the surface for a blowing ratio up to 0.9. Very few film cooling studies have been conducted for non-streamwise injection configurations, but Goldstein, Eckert, Eriksen, and Ramsey [21] did investigate a single hole angled at 35° in the spanwise direction

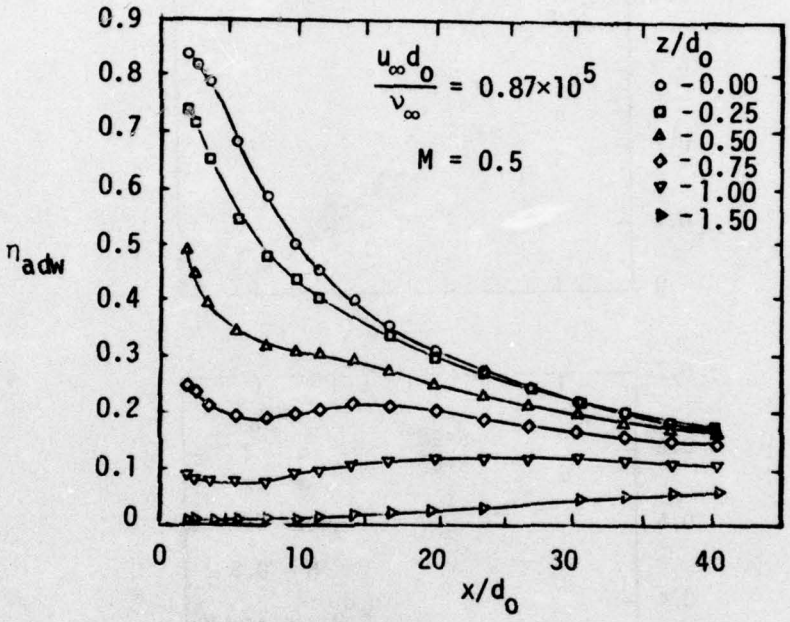

Figure 22. Spanwise Spreading of the Coolant Jet as It Flows Downstream (Goldstein, Eckert and Ramsey [16])

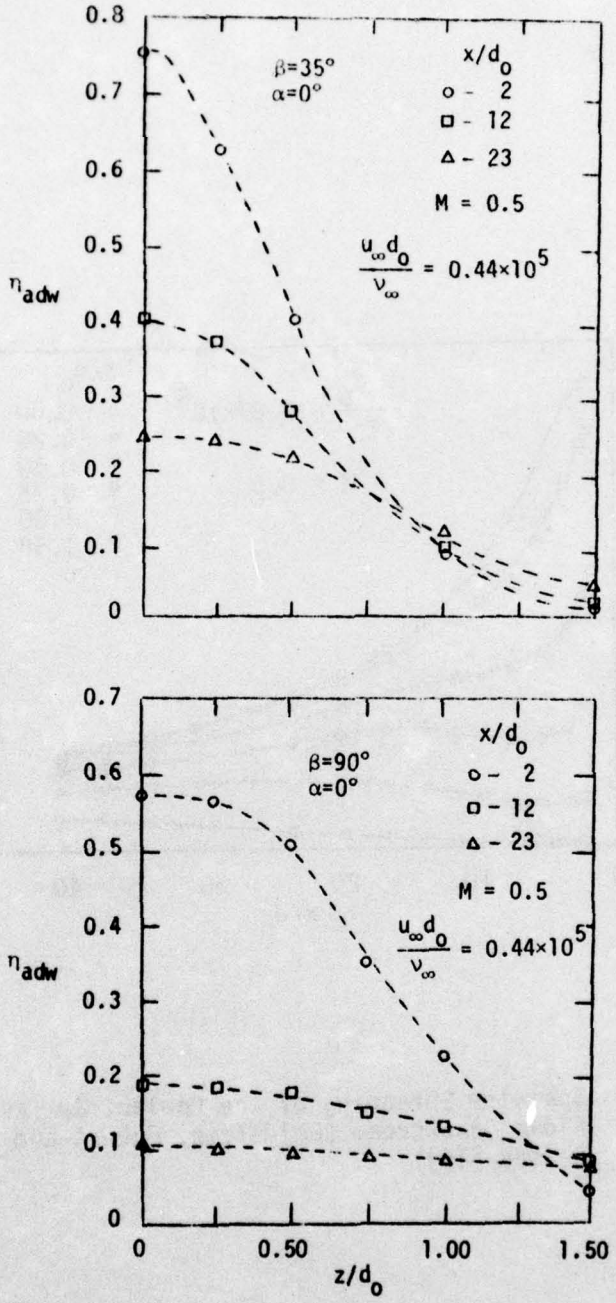

Figure 23. The Influence of the Coolant Hole Angle on the Spanwise Spreading of the Coolant Jet (Goldstein, Eckert, and Ramsey [16])

(β=35°, α=90°). The results presented in Fig. 24 show the contours of constant adiabatic effectiveness on the test surface, comparing the results with those obtained for a single hole angled at 35° in the streamwise direction (β=35°, α=0°). Data for two values of the blowing ratio are shown. At the value M = 0.5, the spanwise injection produced a wider field of film cooling coverage, but with a lower level of effectiveness. However, for the value of M = 1.0, the spanwise injection not only widened the field of coverage but achieved a higher level of adiabatic effectiveness. These results may reflect the observation of Colladay and Russell [15] that for a higher blowing ratio, the spanwise injection results in the jet remaining closer to the surface subsequently resulting in higher effectiveness values downstream from injection.

The foregoing discussion illustrates the complex interaction of the mass flux, velocity, momentum flux, and density ratios and the angle of injection in governing the film cooling performance. It appears that the choice of an optimum film cooling condition requires that all of these parameters be taken into consideration.

I.C.4. Hole Spacing

Although it is desirable to have the coolant jets remain attached to the surface to achieve high cooling effectiveness, it is also important to have the jets spread laterally across the surface to form a uniform protective layer. With jet detachment, the enhanced mixing between the coolant and freestream aids the lateral spreading of the jet. The parameter that directly influences how far the jets must

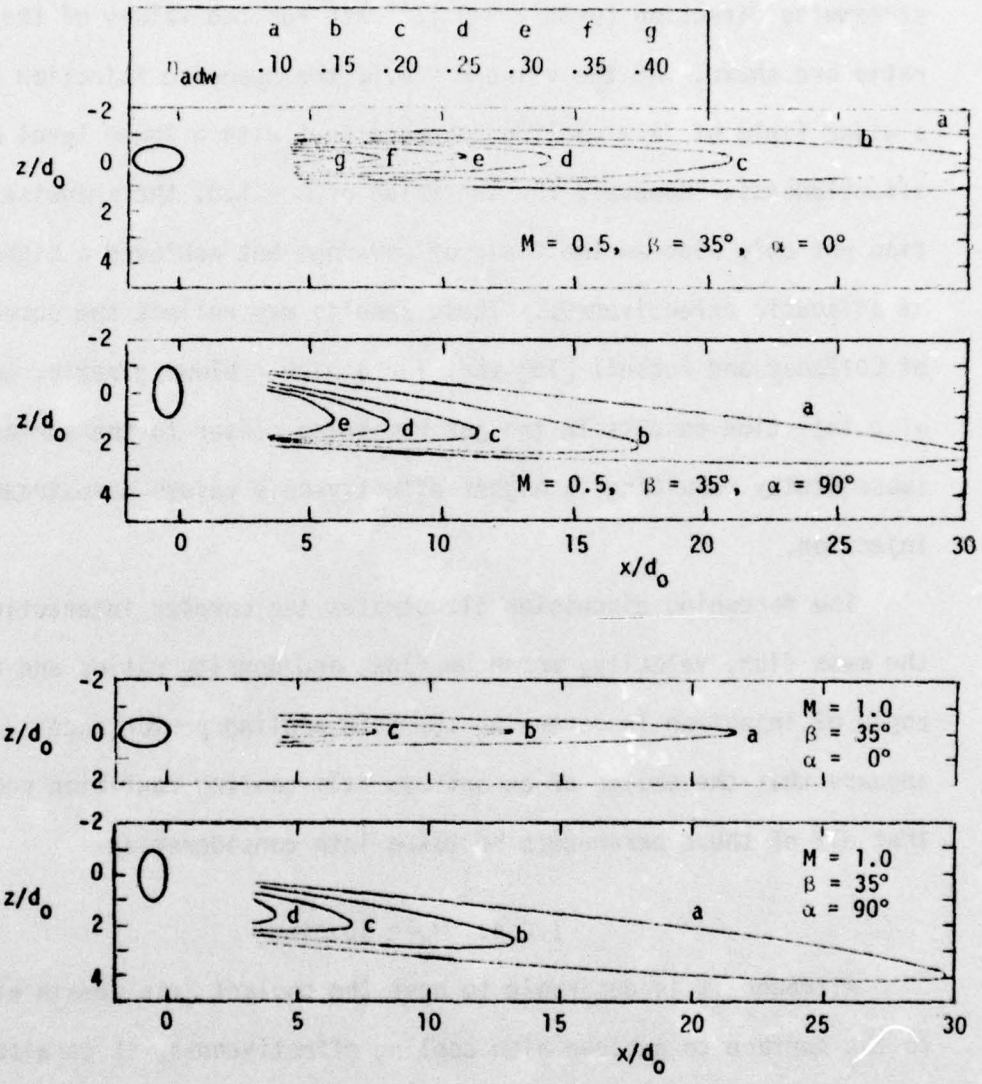

Figure 24. Lines of Constant Film Cooling Effectiveness for Single Hole Injection (Goldstein, Eckert, Eriksen, and Ramsey [21])

spread before they coalesce is the hole spacing-to-diameter ratio, s/d_o. If the holes are spaced close together, less mixing will be required to spread the coolant because the jets will have a shorter distance to spread before they coalesce. Therefore a small spacing ratio would enable the jets to be kept close to the surface (i.e. no detachment), while at the same time enhancing the formation of a spanwise uniform film coolant layer. A subsequent benefit of a close hole spacing is the smaller area available between the coolant holes for the freestream to flow. Therefore more of the freestream is forced to flow over the top of the coolant jets, providing a larger pressure difference to bend the jets toward the wall. The only negative influence of a small spacing ratio might be the possible interaction between jets. This could enhance the mixing process between the coolant and the freestream. Also, from the designer's viewpoint, it is desirable to avoid smaller values of s/d_o than necessary, in order to minimize the coolant flow rate (per unit area of coverage) requirements.

In the limit as the hole spacing ratio approaches unity, the hole configuration approaches that of a slot. Slot cooling has the advantage of the freestream always flowing over the top of the coolant, never underneath it. As expected, slot cooling has been found to provide better film cooling performance than a comparable hole configuration at the same blowing ratio. Figure 25 presents the results of Metzger and Fletcher [5] comparing film cooling with hole and slot injection. The data correspond to a blowing ratio of 0.25 for holes with two values of s/d_o. The data for two injection angles, β=20° and 60°, showed little influence of β since, at this low blowing ratio, the

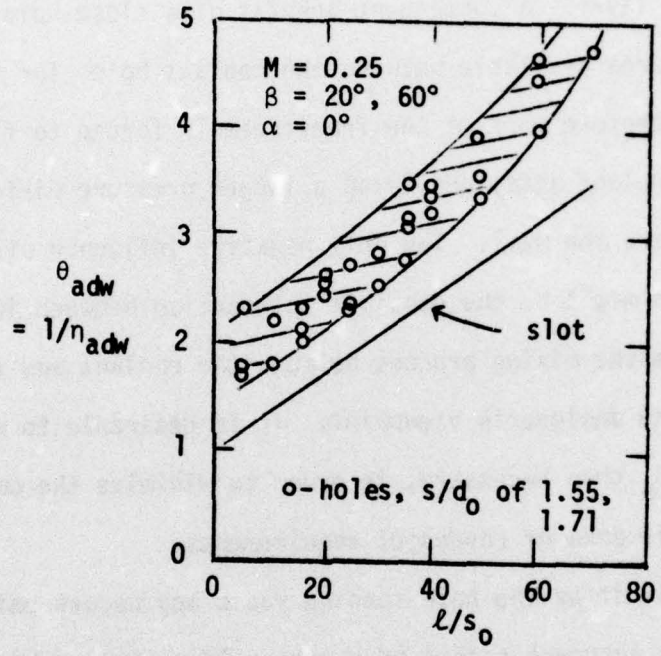

Figure 25. Comparison between Slot and Hole Film Cooling (Metzger and Fletcher [5])

coolant apparently remained attached to the surface. Figure 25 illustrates the higher adiabatic effectiveness for injection from a slot due to the ability of the freestream to pass between the coolant jets even for such small values of s/d_0.

To determine the influence of the freestream blockage on the film cooling performance, Goldstein, Eckert, Eriksen, and Ramsey [26] compared the downstream variation of the adiabatic effectiveness for coolant injection from a single hole and a row of holes spaced at $s/d_0 = 3.0$. Figure 26 shows the results for two values of z/d_0 and four values of the blowing ratio. At the low blowing ratio of 0.5, corresponding to an attached jet, the centerline effectiveness ($z/d_0 = 0.0$) was identical, while at $z/d_0 = 1.5$, the row of holes gave slightly higher values of effectiveness, indicating a reinforcement of the coolant from adjacent holes. However, as the blowing ratio was increased to a range where jet detachment is expected, the effectiveness values (at both $z/d_0 = 0.0$ and 1.5) for the row of holes were significantly higher than for the single hole, with the difference in effectiveness increasing as the jets flowed downstream. This is attributed to the lateral spreading of the jets until they eventually coalesced and reinforced each other. The increased centerline effectiveness ($z/d_0 = 0.0$) was probably the result of the increased freestream blockage by the multiple jets since increased blockage would inhibit the mixing at high values of M. Thus, for the two values of s/d_0 (0.0 and 1.50) studied, the row of holes shows a definite improvement in effectiveness over the single row especially for a high blowing ratio ($M > 0.5$).

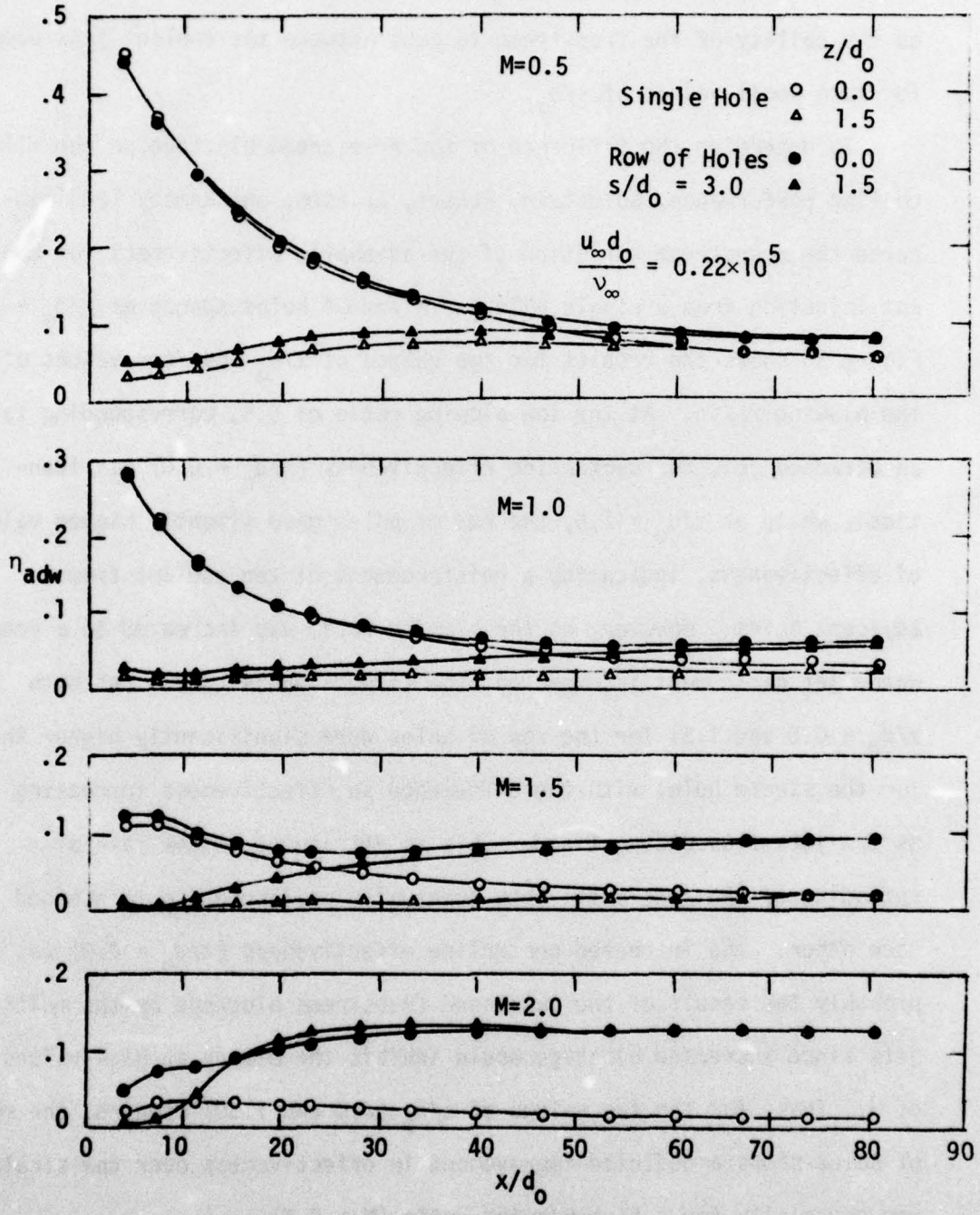

Figure 26. Comparison of the Film Cooling Effectiveness with Injection from One Hole and a Row of Holes (Goldstein, Eckert, Eriksen, and Ramsey [26])

For coolant injection from holes, there is a substantial spanwise variation in the film cooling effectiveness especially close to injection as indicated by Fig. 26. Goldstein, Eckert and Burggraf [23] investigated the spanwise variation of the adiabatic effectiveness for a row of streamwise angled holes at several downstream distances. Figure 27 shows their results for the three middle holes in a row of eleven holes, with $s/d_0 = 3.0$, using a blowing ratio of $M = 0.5$ (where the jets were presumably attached to the surface). At the locations close to injection ($x/d_0 = 2.7$, 6.7, and 16.7), there was a significant spanwise variation in the adiabatic effectiveness. Further downstream ($x/d_0 \geq 44.7$) the variation was insignificant. An important feature shown by the data that close to injection ($x/d_0 = 2.7$) is the hole-to-hole variation of the centerline effectiveness, which was as much as $\pm$ 11% (0.54 to 0.68) for adjacent holes.

The spanwise variation of the effectiveness has also been investigated by Liess and Carnel [27] using hole spacings of $s/d_0 = 2.22$, 3.33, and 4.0. The data for a row of streamwise angled holes (β=35°) and a blowing ratio of $M = 0.85$ are shown in Fig. 28. The results reveal that even for the smallest hole spacing ($s/d_0 = 2.22$), the spanwise variation close to injection ($x/d_0 < 5$) was significant. However, for $x/d_0 > 10$, the coolant jets apparently had coalesced to form a uniform effectiveness across the surface. For the two wider hole spacings, a spanwise variation in effectiveness persisted to $x/d_0 > 25$. A comparison of the centerline effectiveness ($z/s = 0$) close to injection ($x/d_0 = 2$) for all three values of s/d_0 shows that η_{adw} decreased as the hole spacing was increased. However, at $x/d_0 = 5$, the centerline effectiveness

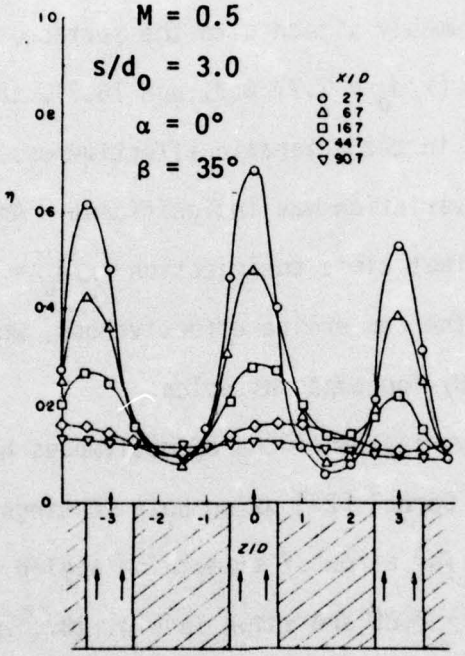

Figure 27. Lateral Variation of the Film Cooling Effectiveness for Injection from a Row of Holes (Goldstein, Eckert, and Burggraf [23])

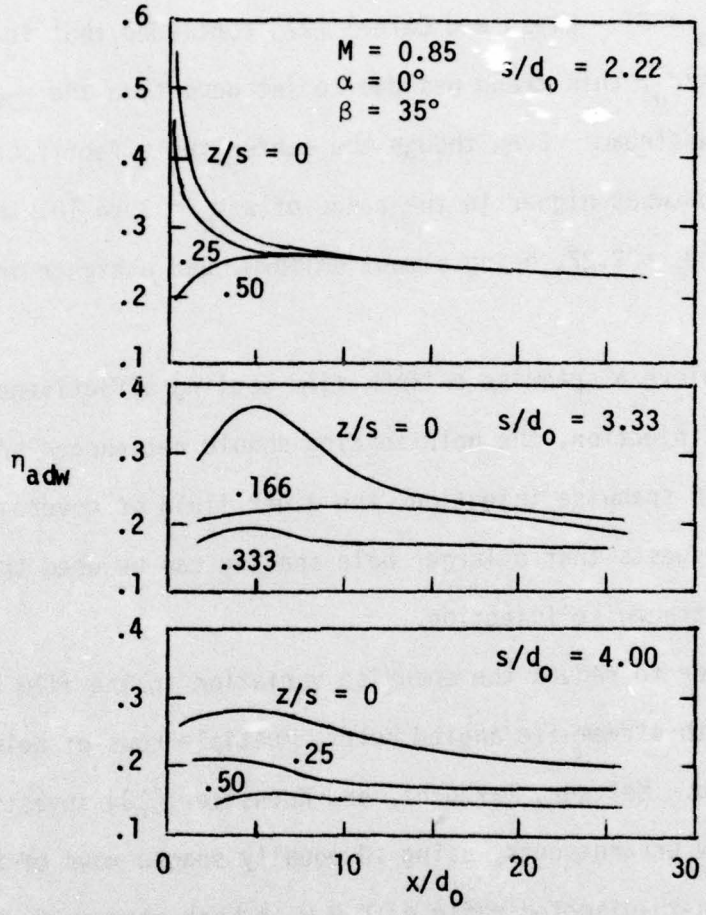

Figure 28. The Influence of Hole Spacing on Film Cooling Effectiveness (Liess and Carnel [27])

was highest for $s/d_o = 3.33$. While the centerline value for $s/d_o = 2.22$ continually decreased with increasing x/d_o, the centerline effectiveness for $s/d_o = 3.33$ and 4.0 showed an increase with downstream distance (up to $x/d_o \approx 5$). Liess and Carnel [27] concluded that for the larger values of s/d_o, this trend was due to jet departure and reattachment further downstream. Even though the centerline effectiveness for $s/d_o = 3.33$ was somewhat higher in the range of $x/d_o \approx 3$ to 10, the effectiveness for $s/d_o = 2.22$, being almost uniform, had a higher integrated value.

To achieve a spanwise uniform film cooling effectiveness with streamwise injection, the hole spacing should not exceed $s/d_o \approx 2.0$. However, for spanwise injection, the wider field of coverage shown in Fig. 24, suggests that a larger hole spacing can be used than that found for streamwise injection.

In order to reduce the spanwise variation in the film cooling performance with streamwise angled holes, multiple rows of holes have been investigated. Metzger, Takeuchi, and Kuenstler [28] investigated multiple row arrangements, using 10 equally spaced rows of holes (β=90°) with a pitch-to-diameter ratio of 4.8 with both staggered and in-line arrangements of the holes. The in-line arrangement proved to be inferior to the staggered array, because the cooling effect from an upstream hole was found to be negated after flowing over two holes in-line downstream. The staggered arrangement used the coolant from an upstream row to fill in the gaps between the holes of the downstream row thus allowing the coolant to pass four rows downstream before its cooling influence became negligible.

I.C.5. Freestream Conditions

While the hole geometry and the coolant blowing parameters obviously play a significant role in the film cooling process, the freestream conditions can also influence the film cooling performance. Flow visualization studies by Collady and Russell [15] have shown that the boundary layer thickness has a definite influence on the freestream's ability to bend the coolant jets to flow along the surface. With a thinner boundary layer, the coolant jets encounter a higher velocity closer to the wall which enhances the deflection of the coolant jets toward the wall and results in less penetration of the coolant into the freestream, less mixing and higher levels of film cooling performance downstream.

Goldstein, Eckert, Eriksen and Ramsey [21] investigated the influence of the boundary layer displacement thickness on the centerline adiabatic effectiveness downstream of a single streamwise angled hole (β=35°). Goldstein, Eckert, and Burggraf [23] also conducted a similar investigation, but with a row of streamwise angled holes (β=35°) with a hole spacing of s/d_o = 3.0. Figure 29 shows the influence of δ^*/d_o at three different downstream locations. The trends developed in each investigation seem to agree that the film cooling effectiveness decreases as the ratio of the boundary layer displacement thickness-to-hole diameter is increased, although the trend does seem to diminish for the higher values of δ^*/d_o investigated. Since the results for the single hole are compared with the results for a row of holes, the results far downstream (x/d_o = 30) differ as the jets from the row of holes begin to coalesce.

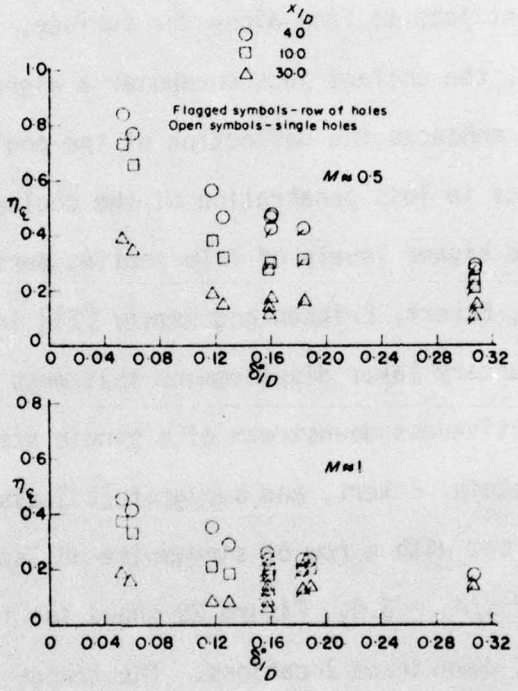

Flagged symbols from Goldstein, Eckert, Eriksen and Ramsey [21]

Open symbols from Goldstein, Eckert and Burggraf [23]

Figure 29. The Effect of the Boundary Layer Displacement Thickness on the Centerline Film Cooling Effectiveness (Goldstein, Eckert and Burggraf [23])

Liess [14] also conducted an investigation of the boundary layer thickness on the film cooling effectiveness, but his results were for a spanwise averaged adiabatic effectiveness, not a centerline value. The tests were made on a row of streamwise angled holes (β=35°) with s/d_o = 3. His results, presented in Fig. 30, show the spanwise averaged effectiveness at three different downstream locations. They show the same trend seen previously with the effectiveness decreasing as the ratio δ^*/d_o increases. However, the averaged effectiveness was approximately constant for δ^*/d_o less than 0.2, which is in sharp contrast to the trend of the centerline effectiveness (Fig. 29) that continues to increase for δ^*/d_o values as low as 0.05.

An important consideration when reviewing the effect of the boundary layer displacement thickness on the film cooling performance, is that all of the investigations were conducted with a turbulent boundary layer. On a blunt body like a turbine vane, the leading edge is covered by a laminar boundary layer. For a fixed value of δ^*/d_o, the laminar boundary layer thickness is about one third that of a turbulent boundary layer. Therefore the coolant jet will encounter higher velocities even closer to the surface with the laminar boundary layer, possibly resulting in a better deflection of the jet than with a turbulent boundary layer. This improvement in the jet deflection and the absence of turbulence in the boundary layer could result in higher levels of adiabatic effectiveness than those seen in Fig. 29, but with the thinner laminar boundary layer, the effectiveness would probably become even more sensitive to changes in δ^*/d_o than that already seen for the turbulent boundary layer.

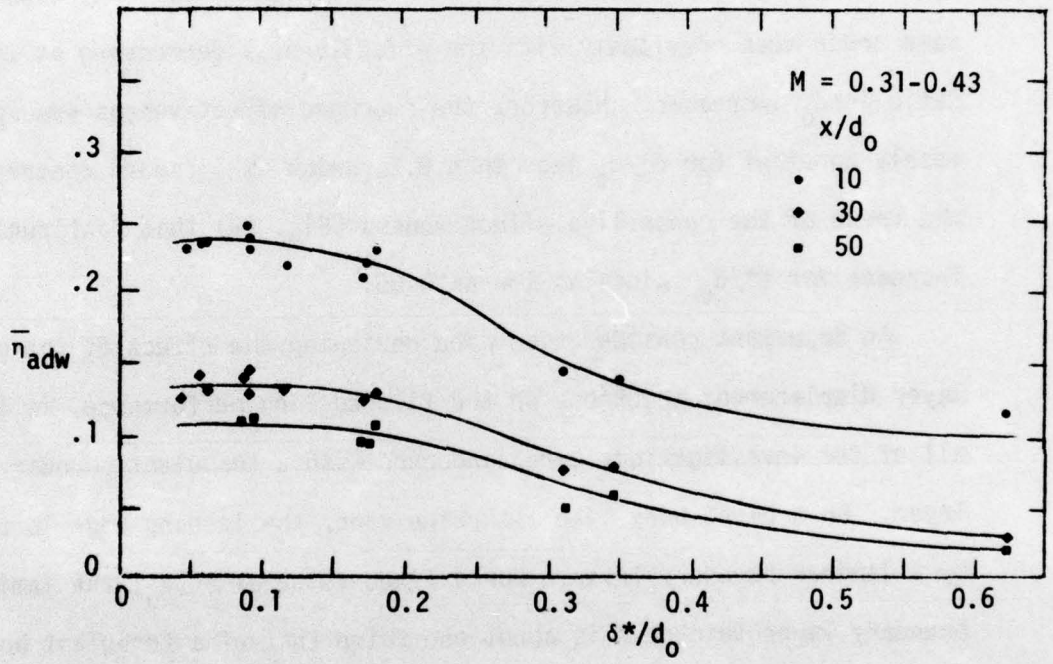

Figure 30. The Effect of the Boundary Layer Displacement Thickness on the Laterally Averaged Film Cooling Effectiveness (Liess [14])

The freestream Mach number has been shown to have little effect on the film cooling process in the subsonic region as verified by two investigations. Papell and Trout [29] investigated the influence of the Mach number on tangential slot cooling and their results are presented in Fig. 31. With a constant blowing ratio of 1.0, three different Mach numbers (0.20, 0.50, and 0.70) were investigated and found to have no influence on the film cooling effectiveness. Liess [14] also investigated the influence of the Mach number, using a row of streamwise angled holes (β=35°) with a blowing ratio of approximately 0.35. The results for three Mach numbers shown in Fig. 32 indicate no effect of the Mach number on the film cooling effectiveness.

The presence of large scale freestream turbulence can greatly enhance the mixing process between the coolant jet and freestream, decreasing the film cooling performance. Carlson and Talmor [30] investigated the effect of freestream turbulence on film cooling effectiveness for slot injection. Figure 33 shows their results with the adiabatic effectiveness plotted against a blowing parameter X, where

$$X = \frac{Re_\infty^{0.8}}{Re_c} \left(\frac{\mu_\infty}{\mu_c}\right)\left(\frac{c_{p_\infty}}{c_{p_c}}\right) \tag{16}$$

The figure shows that for all values of X investigated, as the turbulence intensity increased, the film cooling effectiveness decreased.

The freestream acceleration can also be expected to influence the film cooling performance. The parameter which identifies the freestream acceleration is K_1, where

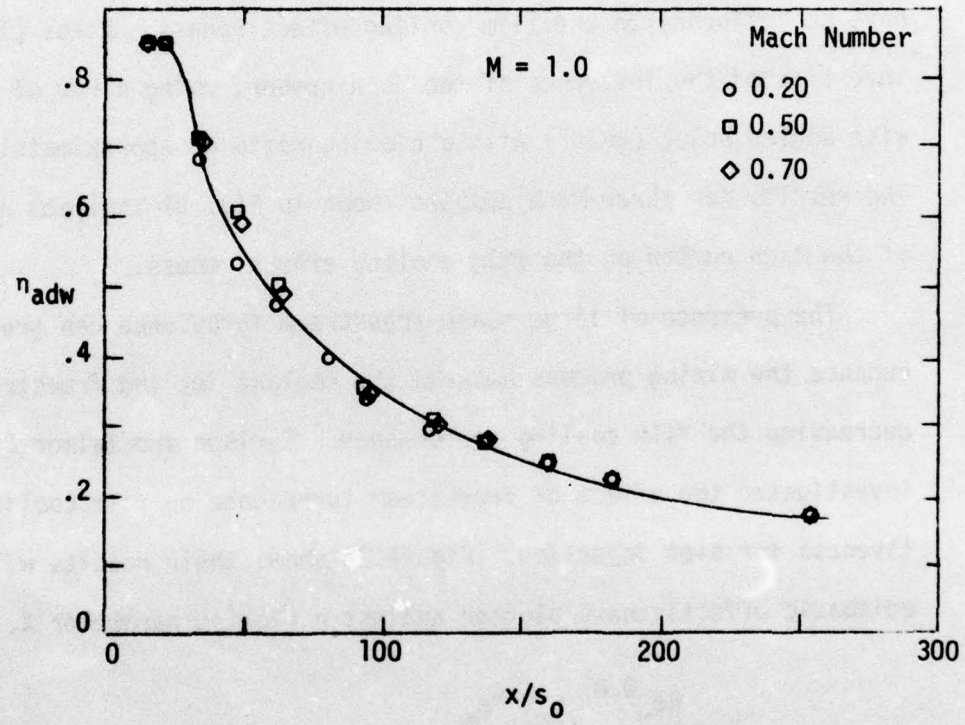

Figure 31. The Influence of the Mach Number on the Film Cooling Effectiveness for Tangential Slot Injection (Papell and Trout [29])

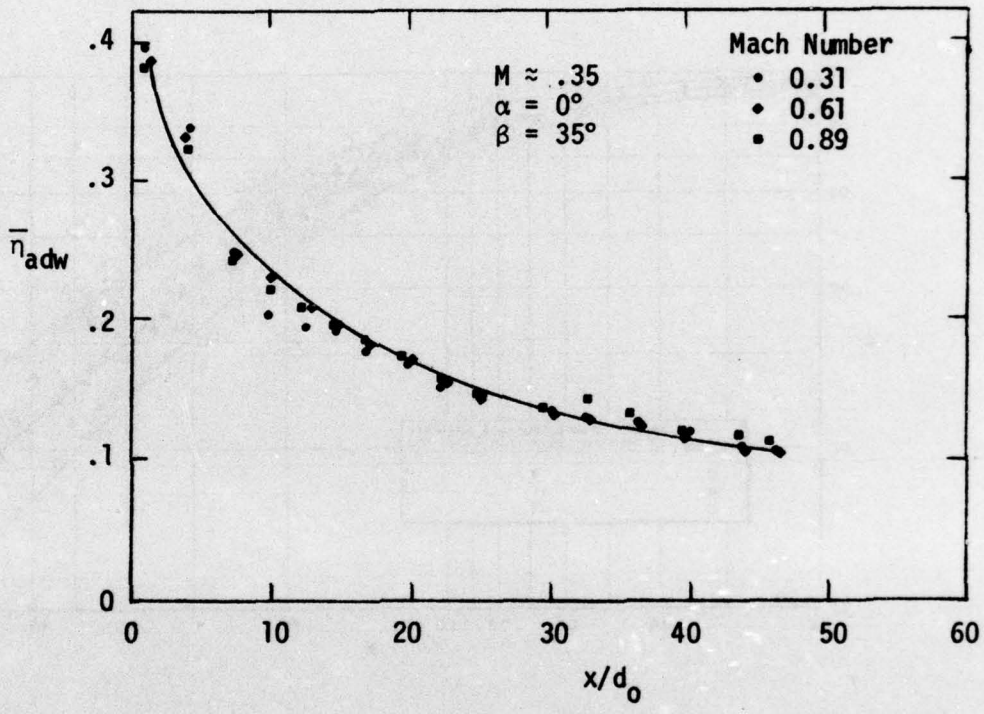

Figure 32. The Influence of the Mach Number on the Laterally Averaged Film Cooling Effectiveness for Injection through a Row of Holes (Liess [14])

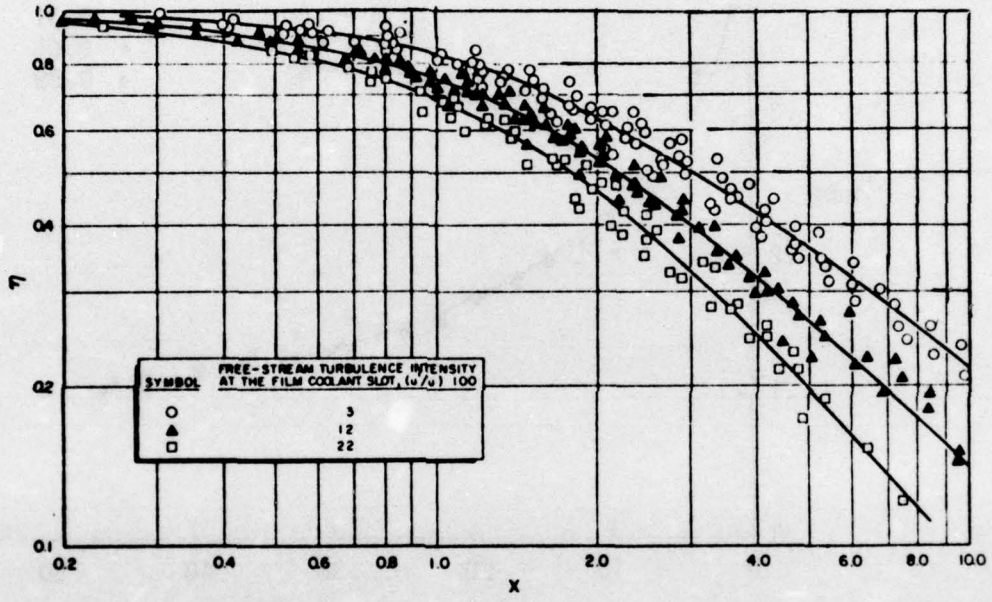

Figure 33. The Influence of the Freestream Turbulence on the Film Cooling Effectiveness (Carlson and Talmor [30])

$$K_i = \frac{\nu_\infty}{V_\infty^2} \frac{dV_\infty}{dx} \qquad (17)$$

Kays, Moffat, and Thielbahr [31] conducted experiments with transpiration cooling and showed that the influence of a favorable pressure gradient may increase or decrease the cooling performance depending on the magnitude of K_i and the coolant blowing ratio. For film cooling through a slot, Seban and Back [32] and Pai and Whitelaw [33] have shown that the influence of favorable pressure gradient is small for values of K_i up to approximately 1×10^{-6}, but values of $K_i = 3\times10^{-6}$ have produced a decrease of up to twenty percent in the film cooling effectiveness (compared to a zero pressure gradient case). Goldstein [34] and Liess [14] have shown similar results with injection through a row of streamwise angled holes ($\beta=35°$, $s/d_o \approx 3.0$). However there is some uncertainty as to the combined effects of discrete hole blowing and a favorable pressure gradient since Launder and York [35] and Nicolas and LeMeur [36] have reported finding an increase in the film cooling effectiveness with $K_i \approx 2\times10^{-6}$.

When freestream turbulence and acceleration are combined, Jones and Launder [37] found that the acceleration tended to reduce the turbulence level. This indicates that the suppression of the freestream turbulence level could lead to a reduction in the coolant-freestream mixing and to an improvement in the film cooling effectiveness. Liess [14] confirmed in his flow visualization studies of film cooling that the freestream acceleration suppressed the streamwise vortices in the flow, but as soon as the pressure gradient was removed, they suddenly

developed again. Therefore when freestream turbulence is present, a favorable pressure gradient may be beneficial to the film cooling process by suppressing the turbulent mixing.

I.C.6. Film Cooling Correlations

This literature survey has reviewed the influence of the coolant blowing parameters, the injection geometry, and the freestream conditions on the film cooling performance. While numerous investigations have been conducted to study these parameters, no correlation has been reported for hole film cooling which is probably a consequence of the complex three-dimensional nature of the problem. However, numerous correlations have been proposed from both analytical and experimental work with two-dimensional slot cooling. A majority of the analytical models proposed have been based on the heat sink model [2]. A discussion of some of the different analytical models developed can be found in Appendix I, but the general form of the adiabatic effectiveness for the heat sink model is

$$\eta_{adw} = \frac{C_1}{C_2 + C_3 \xi^{0.8}} \tag{18}$$

where

$$\xi = \left(\frac{x}{Ms_o}\right) \left(\frac{c_{p_c}}{c_{p_\infty}}\right) \left(\frac{\mu_c}{\mu_\infty} Re_c\right)^{-0.25}$$

and C_1, C_2, and C_3 are constants.

Even more correlations have been reported from experimental investigations conducted and some of them are described in Appendix I. The

correlations take the general form

$$\eta_{adw} = A(x/Ms_o)^B (Re_c)^C \qquad (19)$$

where A, B, and C are constants.

I.D. Scope of Investigation

As the literature survey has shown, there are numerous parameters that influence the film cooling process and many of them have been the object of thorough investigations. However the information available for the film cooling performance close to injection from a row of holes angled in the spanwise direction is limited. Since this hole configuration is directly applicable to use on a turbine vane leading edge, this investigation was conducted to provide detailed information regarding the influence of coolant injection on the local convective heat transfer rate downstream from a single row of spanwise angled coolant holes.

The leading edge of a turbine vane was modeled in the subject investigation using the front stagnation region of a circular cylinder in crossflow. Hot combustion gas flowing over the cylindrical, film cooled test surface was employed to simulate the Reynolds number representative of a high temperature, high pressure gas turbine. Internal cooling of the cylinder wall maintained the test surface at a temperature of ~261K (470°R), allowing the use of a moderate gas temperature (~555K, 1000°R) to simulate a gas-to-wall temperature ratio of ~2.1. Film cooling experiments were conducted to determine the local heat flux using spanwise injection hole angles of β = 25°, 35°, 45°; α = 0° with

different locations of the row of holes relative to stagnation (θ_i = 20°, 30°, and 40°).

The objectives of the experimental study were:

1) to measure the heat flux reduction on a film cooled cylindrical surface as a function of the downstream (x/d_o) and lateral (z/d_o) distance from the injection holes
2) to determine the influence of the spanwise injection angle, β
3) to determine the influence of the location of the rows of holes relative to stagnation
4) to determine the film coolant blowing condition that produces the optimum film cooling performance

The following chapters contain a detailed description of the experimental investigation, the results obtained, and the correlation of the data.

II. EXPERIMENTAL INVESTIGATION

II.A. Modeling of Gas Turbine Environment

The objective of this research program was to investigate film cooling under conditions characteristic of the leading edge region of a turbine vane. To model the leading edge region, geometric similarity was obtained using the front stagnation region of a circular cylinder in crossflow. Effective modeling of the convective heat transfer on a turbine vane requires the simulation of the important dimensionless parameters that govern the flow and heat transfer phenomena. A dimensional analysis procedure, following that by Eckert and Drake [3], is summarized herein to identify the dimensionless parameters that require modeling. Since we are only interested in the dimensional structure of the terms in the conservation equations, the continuity, x-momentum, and energy equations, shown below, are written in an abbreviated form.

Continuity:
$$\frac{\partial(\rho u)}{\partial x} + \frac{\partial(\rho v)}{\partial y} = 0 \tag{20}$$

x-Momentum:
$$\rho u \frac{\partial u}{\partial x} + \ldots = -\frac{\partial P}{\partial x} + \left[\frac{\partial}{\partial x}\left(\mu \frac{\partial u}{\partial x}\right) + \ldots\right] \tag{21}$$

Energy:
$$\rho c_p u \frac{\partial T}{\partial x} + \ldots = \left[u \frac{\partial P}{\partial x} + \ldots\right] + \left[\frac{\partial}{\partial x}\left(k \frac{\partial T}{\partial x}\right)\ldots\right] + \left[2\mu\left(\frac{\partial u}{\partial x}\right)^2 + \ldots\right] \tag{22}$$

Due to the large temperature differences characteristic of the turbine environment, it is of interest to include the temperature dependence of the physical properties. Generally, for the gas and temperature range

of interest, the property variations can be reasonably approximated by the following simplifying expressions [3]:

$$\rho = \frac{P}{RT} \qquad \mu = C_\mu T^\varepsilon \qquad k = C_k T^\varepsilon$$

$$c_p = \text{constant} \qquad Pr = \text{constant} \tag{23}$$

where C_μ, C_k are constants.

Since the Prandtl number and c_p are assumed to be constant, the exponents for the viscosity and the thermal conductivity will be the same.

The variables in Eqs. (20) through (22) are non-dimensionalized by defining the following quantities [3].

$$x' = x/D \qquad y' = y/D$$

$$u' = u/(V_{\infty_o}) \qquad v' = v/(V_{\infty_o})$$

$$P' = P/\rho_\infty(V_{\infty_o})^2 \qquad T' = T/T_{\infty_o} = T/T_\infty \,^\dagger$$

$$\rho' = \rho/\rho_\infty \qquad \mu' = \mu/\mu_\infty$$

$$k' = k/k_\infty \tag{24}$$

∞_o = designates the freestream condition upstream of the cylinder

D = cylinder diameter

V = freestream velocity

ρ = density

μ = dynamic viscosity

k = thermal conductivity

---

† T_{∞_o} is set equal to T_∞ because of the low flow velocity used in this investigation.

The non-dimensional form of the equations then becomes:

Continuity: $$\frac{\partial}{\partial x'}\left(\frac{P'}{T'}u'\right) + \frac{\partial}{\partial y'}\left(\frac{P'}{T'}v'\right) = 0 \tag{25}$$

x-Momentum: $$\frac{P'}{T'}\left(u'\frac{\partial u'}{\partial x'} + \ldots\right) = -\frac{\partial P'}{\partial x'} + \frac{1}{Re}\left[\frac{\partial}{\partial x'}\left(T'^{\varepsilon}\frac{\partial u'}{\partial x'}\right) + \ldots\right] \tag{26}$$

Energy: $$\frac{P'}{T'}\left(u'\frac{\partial T'}{\partial x'} + \ldots\right) = Ec\left(u'\frac{\partial P'}{\partial x'} + \ldots\right) + \frac{1}{RePr}\left[\frac{\partial}{\partial x'}\left(T'^{\varepsilon}\frac{\partial T'}{\partial x'}\right) + \ldots\right] + \frac{Ec}{Re}\left[2T'^{\varepsilon}\left(\frac{\partial u'}{\partial x'}\right)^2 + \ldots\right] \tag{27}$$

where $$Re = \frac{\rho_\infty (V_{\infty_0}) D}{\mu_\infty}$$

$$Pr = \frac{c_p \mu_\infty}{k_\infty}$$

$$Ec = \frac{(V_{\infty_0})^2}{c_p (T_\infty - T_w)}$$

The corresponding non-dimensional boundary conditions are:

In the freestream, upstream of the cylinder	$u' = 1$	$T' = 1$ $P' = 1$
At the cylinder surface	$u' = 0$	$T' = T_w/T_\infty$ (28)

The functional dependence of the solution of this system of equations with the boundary conditions can be expressed as:

$$u' = f(x', y', Re, Pr, Ec, \varepsilon, T_w/T_\infty) \tag{29a}$$

$$T' = f(x', y', Re, Pr, Ec, \varepsilon, T_w/T_\infty) \tag{29b}$$

Thus, if one considers the convective heat transfer coefficient defined as

AD-A035 716 PURDUE UNIV LAFAYETTE IND THERMAL SCIENCES AND PROPU--ETC F/G 21/5
STAGNATION REGION GAS FILM COOLING SPANWISE ANGLED COOLANT INJE--ETC(U)
DEC 76 D W LUCKEY, M R L'ECUYER N00014-75-C-0873
UNCLASSIFIED TSPC-TR-76-2 NL

2 OF 4
AD A035716

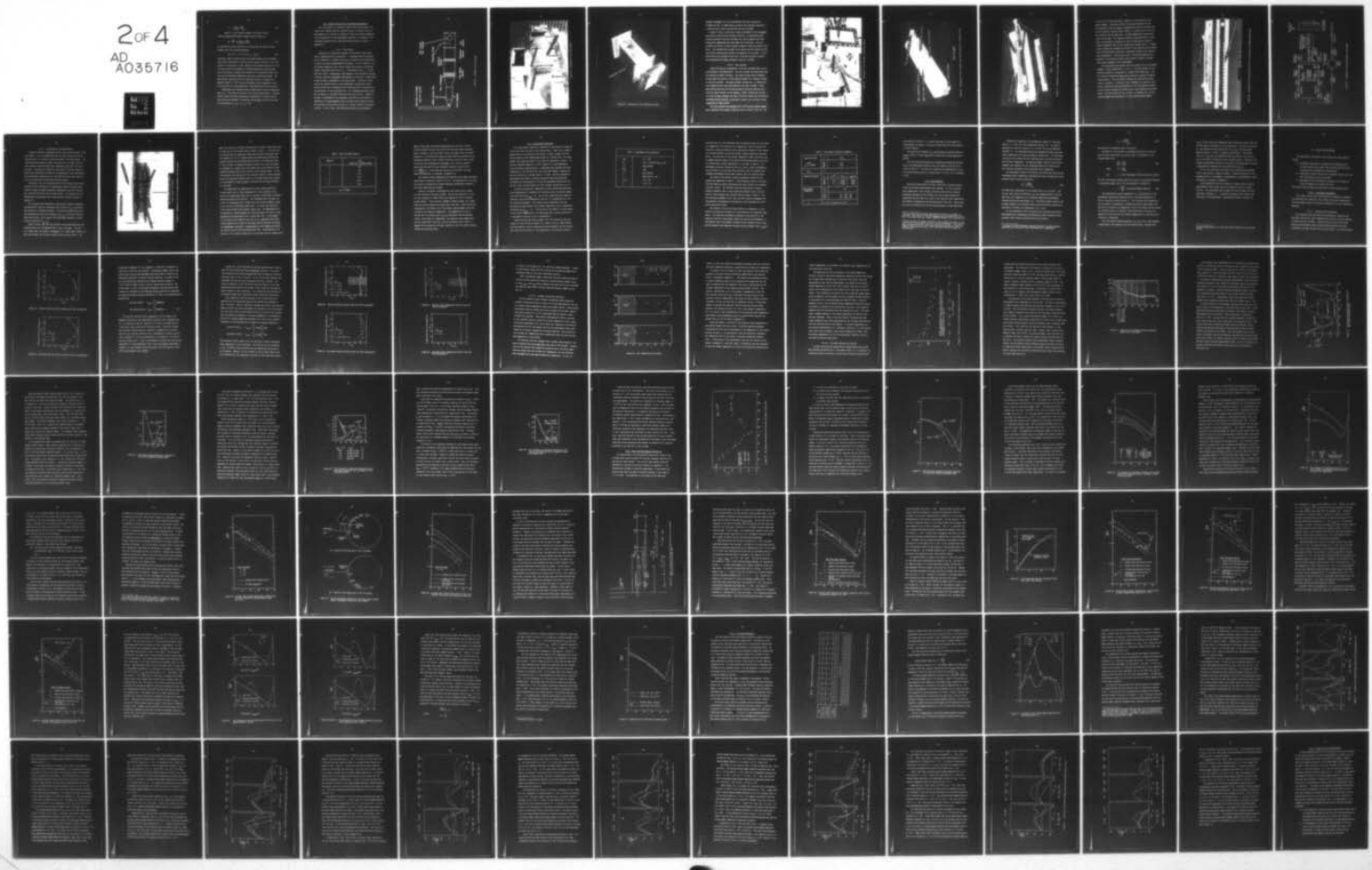

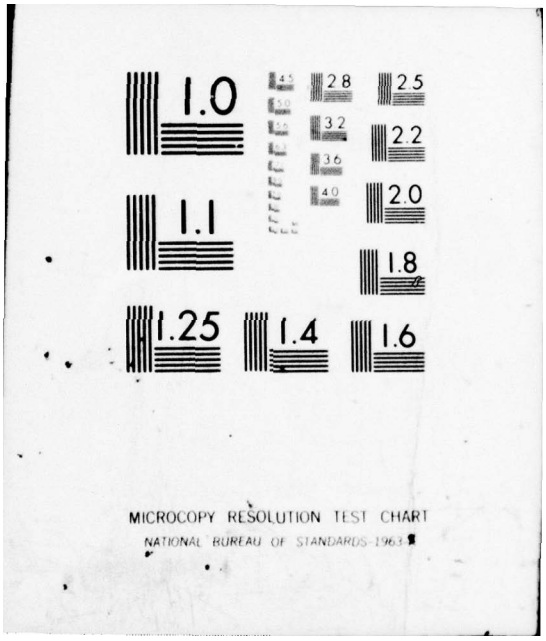
1.0
1.1
1.25
1.4
1.6
1.8
2.0
2.2
2.5
2.8
3.2
3.6
4.0
MICROCOPY RESOLUTION TEST CHART
NATIONAL BUREAU OF STANDARDS-1963-A

$$h = - \frac{k}{(T_w - T_\infty)} \left(\frac{\partial T}{\partial n}\right)_w \tag{30}$$

where n is the direction normal to the wall surface

then the dimensionless Nusselt number can be written as

$$Nu = \frac{hD}{k} = \frac{1}{(1 - T_w/T_\infty)} \left(\frac{\partial T'}{\partial n'}\right)_w \tag{31}$$

An examination of Eqs. (29b) and (31) shows that the Nusselt number depends upon the following parameters

$$Nu = f(x', y', Re, Pr, Ec, \varepsilon, T_w/T_\infty) \tag{32}$$

Therefore, under conditions where the Prandtl number and the exponent ε do not vary significantly, and the kinetic energy available in the free-stream for dissipation is small compared to the thermal energy ($Ec \ll 1.0$), the heat transfer environment at elevated temperatures and pressures can be simulated by reduced flow conditions if the Reynolds number and the wall-to-freestream temperature ratio are maintained constant. The experimental conditions for this study were chosen to simulate the Reynolds number (1.7×10^5) and the freestream-to-wall temperature ratio (~2.0) typical of a high temperature, high pressure gas turbine engine.

Experiments were conducted using a dimensionless coolant temperature ratio, $\theta_c \approx 1.03$, which is typical of gas turbine applications. Colladay [38] has shown that when considering a combination of internal convection cooling and external film cooling, the optimum cooling of the vane is achieved when $T_c = T_w$, i.e. $\theta_c = 1.0$.

II.B. General Description of Experimental Apparatus

The investigation of stagnation region film cooling typical of a turbine vane leading edge was conducted using a cylindrical test surface exposed to a crossflow of heated air from a gas turbine combustor. A brief description of the experimental apparatus is presented in the following sections, while a more detailed description is given in Appendix II.

II.B.1. Flow System

Figure 34 is a simplified schematic of the overall flow system used in conducting this investigation. A blow-down facility provided an air flowrate of ~4 lbm/sec with the air storage facility permitting a typical run time of approximately 30 minutes. The air entered a J-47 gas turbine combustor, where methyl alcohol was burned to provide the nominal freestream conditions of T_{T_∞} ~ 550K (990°R) and P_{T_∞} ~ 3.9×10^5 N/m^2 (56.7 psia). Downstream of the combustor, the flow passed through a diffuser into the rectangular flow channel (0.114m wide × 0.205m high). Figure 35 shows a photograph of the flow channel. Initially the combustion gas passed through a flow straightener (consisting of three drilled plates and a rectangular flow mixing section) to minimize the non-uniformity of the freestream flow. The straightener-mixing section was followed by a turbulence section and the test section. Figure 36 presents a photograph of the turbulence section which consisted of a combination of interchangeable ducts and square mesh screens to permit the variation of the screen grid and its location relative to the test cylinder. In this study, the freestream turbulence was maintained

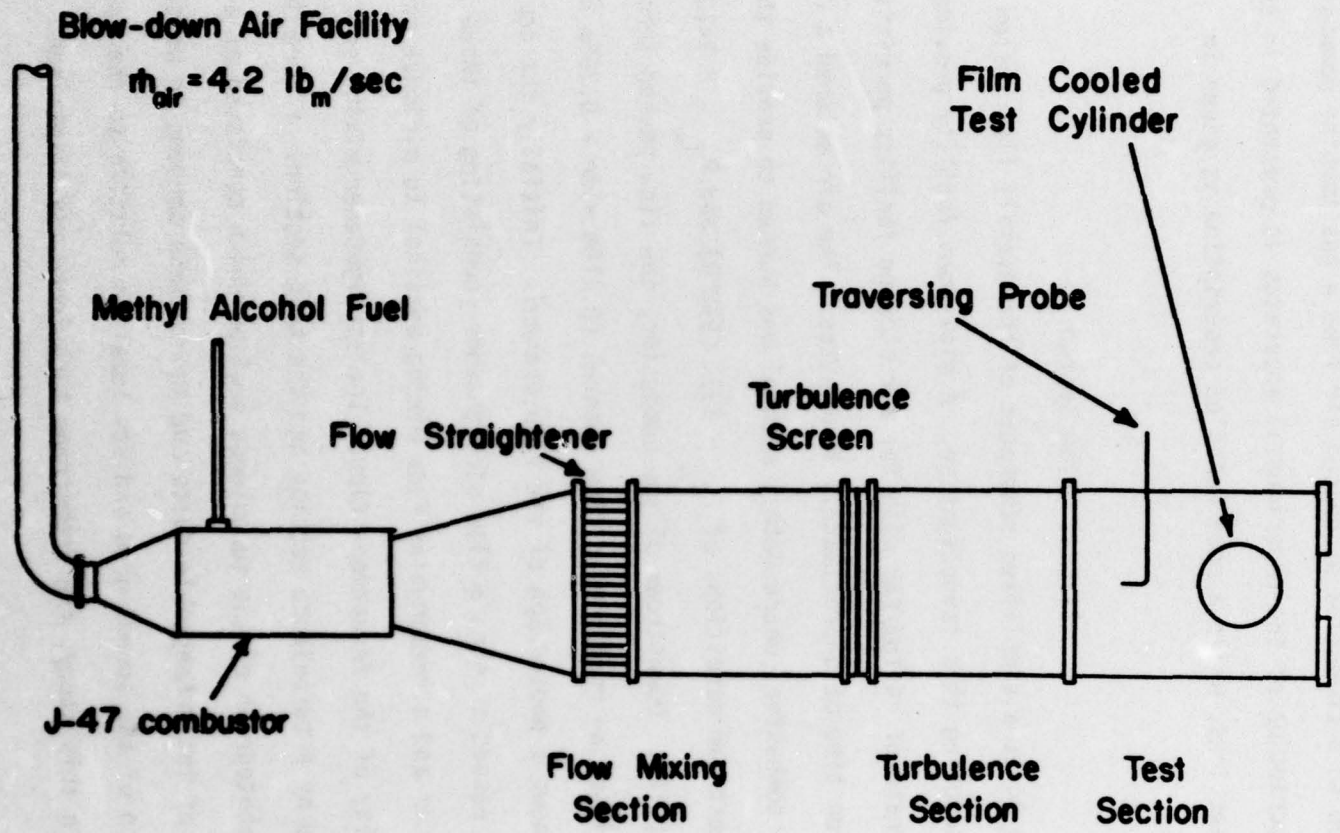

Figure 34. Schematic of Flow System

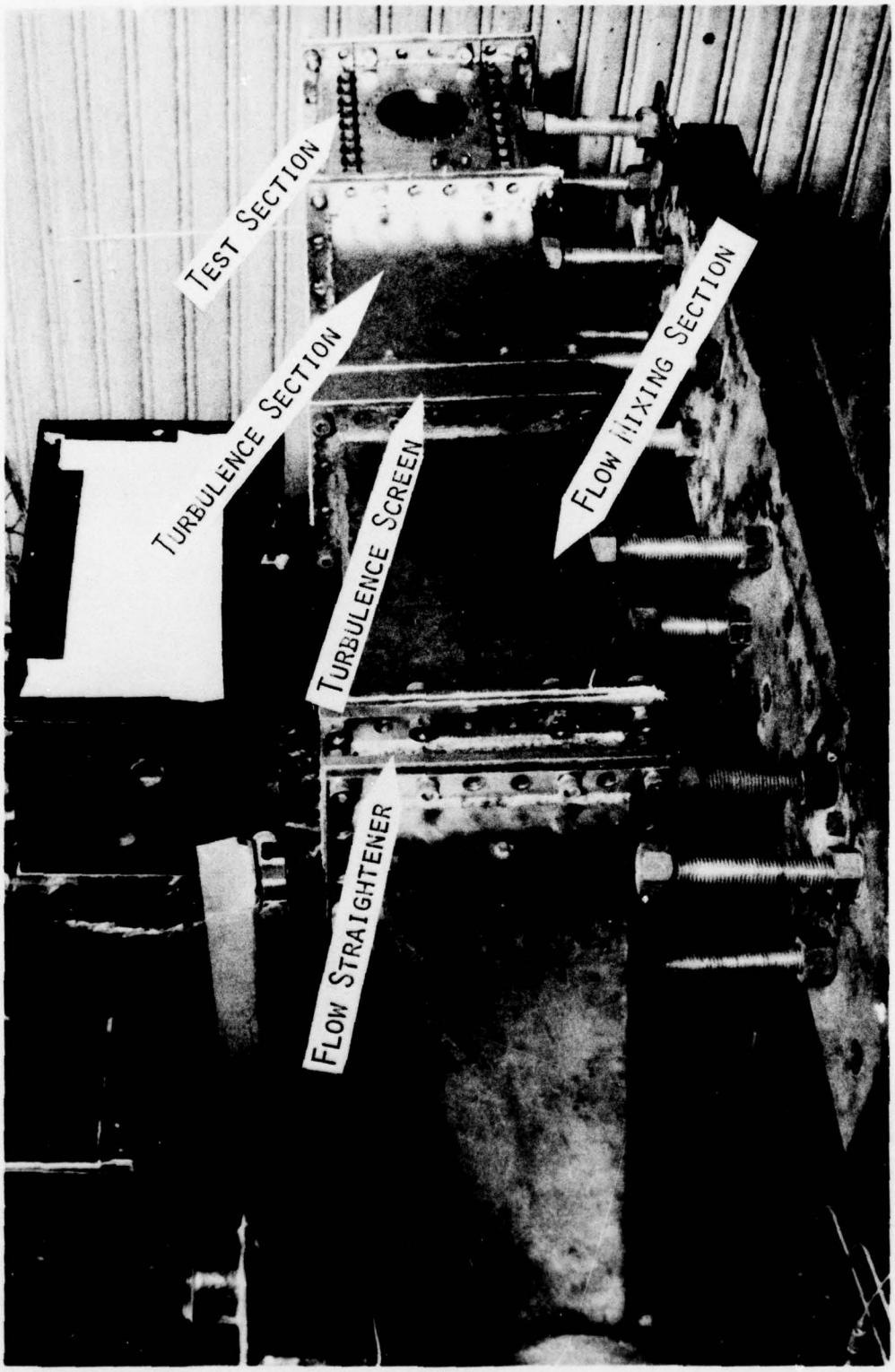

Figure 35. Photograph of the Flow Channel

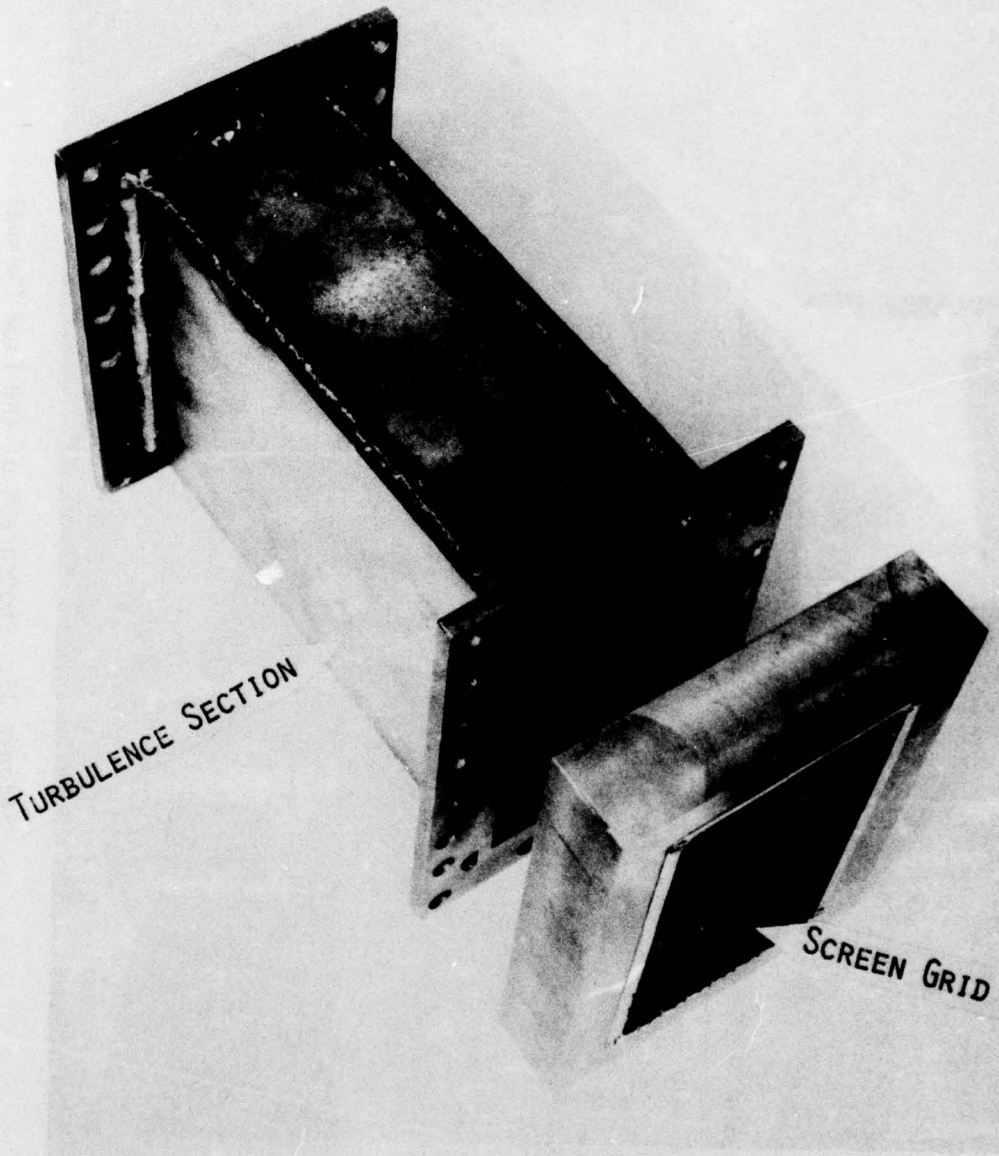

Figure 36 Photograph of the Turbulence Section

constant throughout all of the experiments with the screen grid (1.59mm wire dia. × 6.36mm center-to-center wire spacing) located at a fixed position (.49m) upstream from the test cylinder.

Figure 37 shows a photograph (viewing upstream) of the rectangular test section with the test cylinder installed. A traversing probe, located upstream of the test cylinder, was used to measure the free-stream total temperature and total and static pressures. The test cylinder was held by circular flanges attached to the test section side walls. This enabled the cylinder to be rotated and the location of the row of film cooling holes relative to stagnation to be varied. A flat plate nozzle was attached to the exit of the test section to control the freestream Mach number upstream of the test cylinder.

II.B.2. Test Cylinder

Figure 38 provides a photograph of the test cylinder prior to the installation of instrumentation. The test cylinder was fabricated from two concentric copper cylinders. The inner cylinder had 10 channels milled along the outside to form coolant channels for internal cooling of the test cylinder. The outer cylinder (5.02cm dia. × 0.159cm wall) was slipped over and then oven brazed to the inner cylinder. Holes were drilled into each end of the cylinder to provide inlet and exit ports for each internal coolant channel. Methyl alcohol was chilled in a dry ice heat exchanger and then circulated through the individually throttled coolant channels to maintain a nominal test cylinder surface temperature of 260K (470°R).

The test cylinder was equipped with a film coolant plenum chamber and a removable film coolant injection plate as shown in Fig. 39. Two

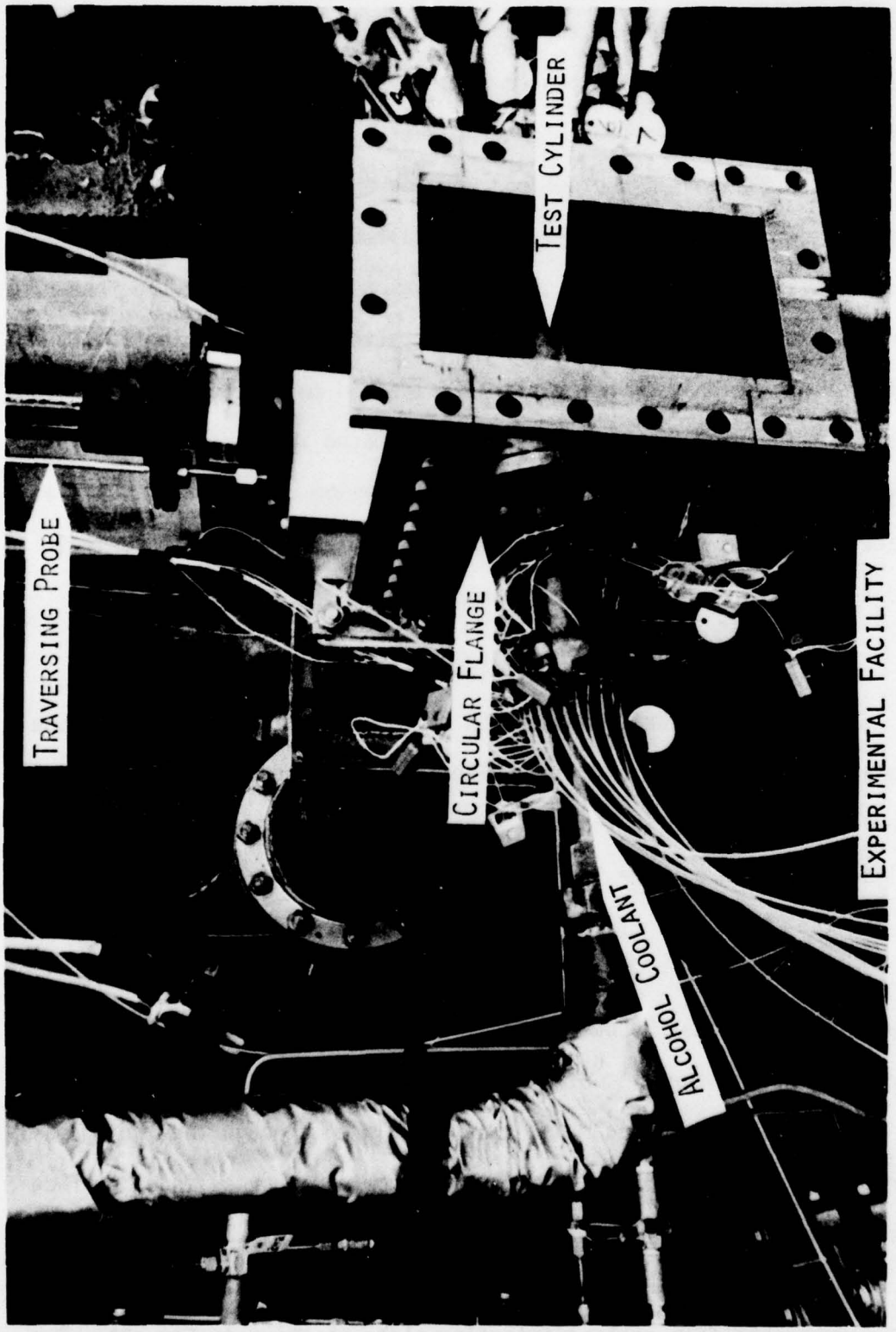

Figure 37. Photograph of the Cylinder in the Test Section

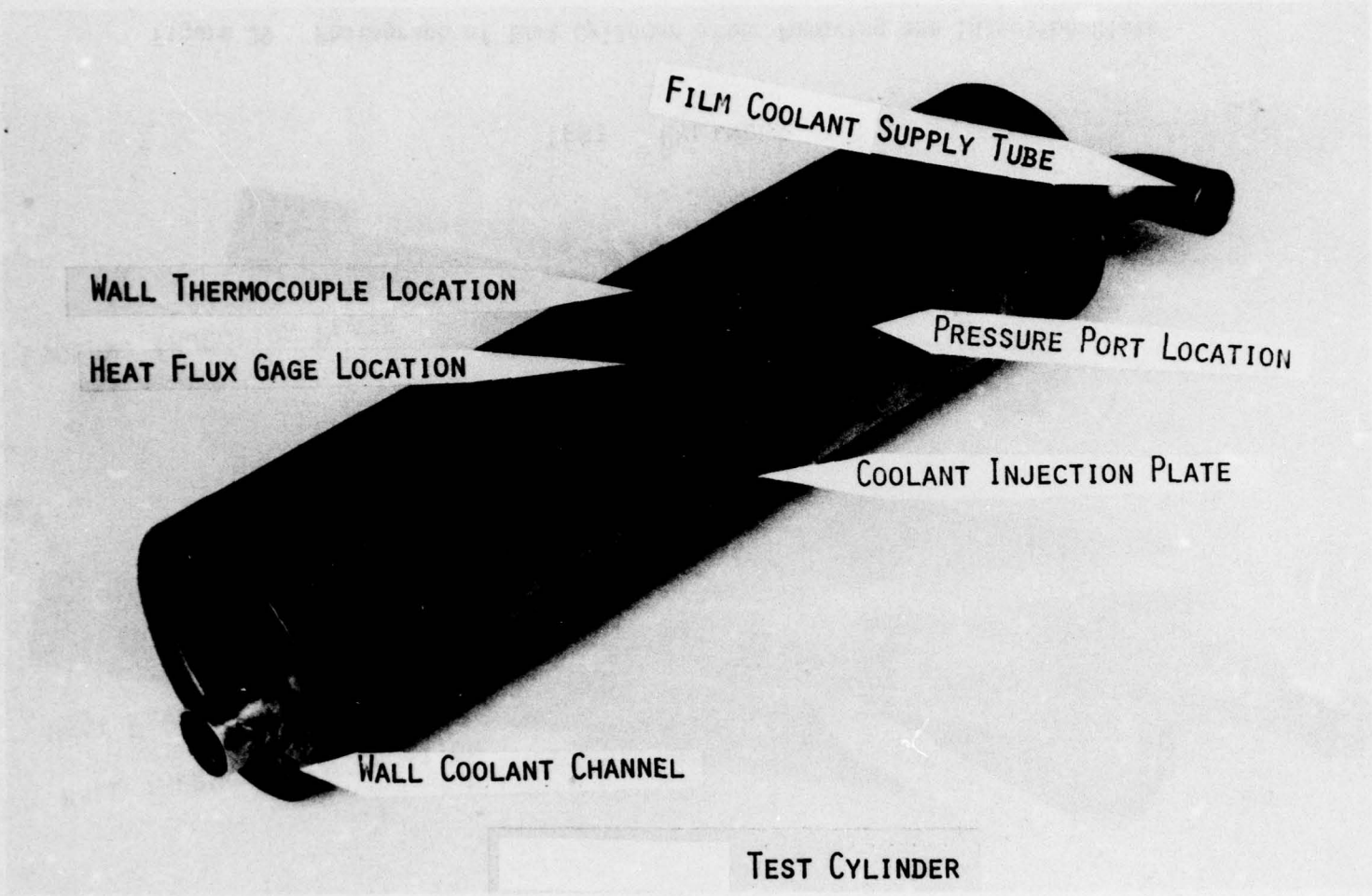

Figure 38 Photograph of Test Cylinder with Plenum Covered by an Injection Plate

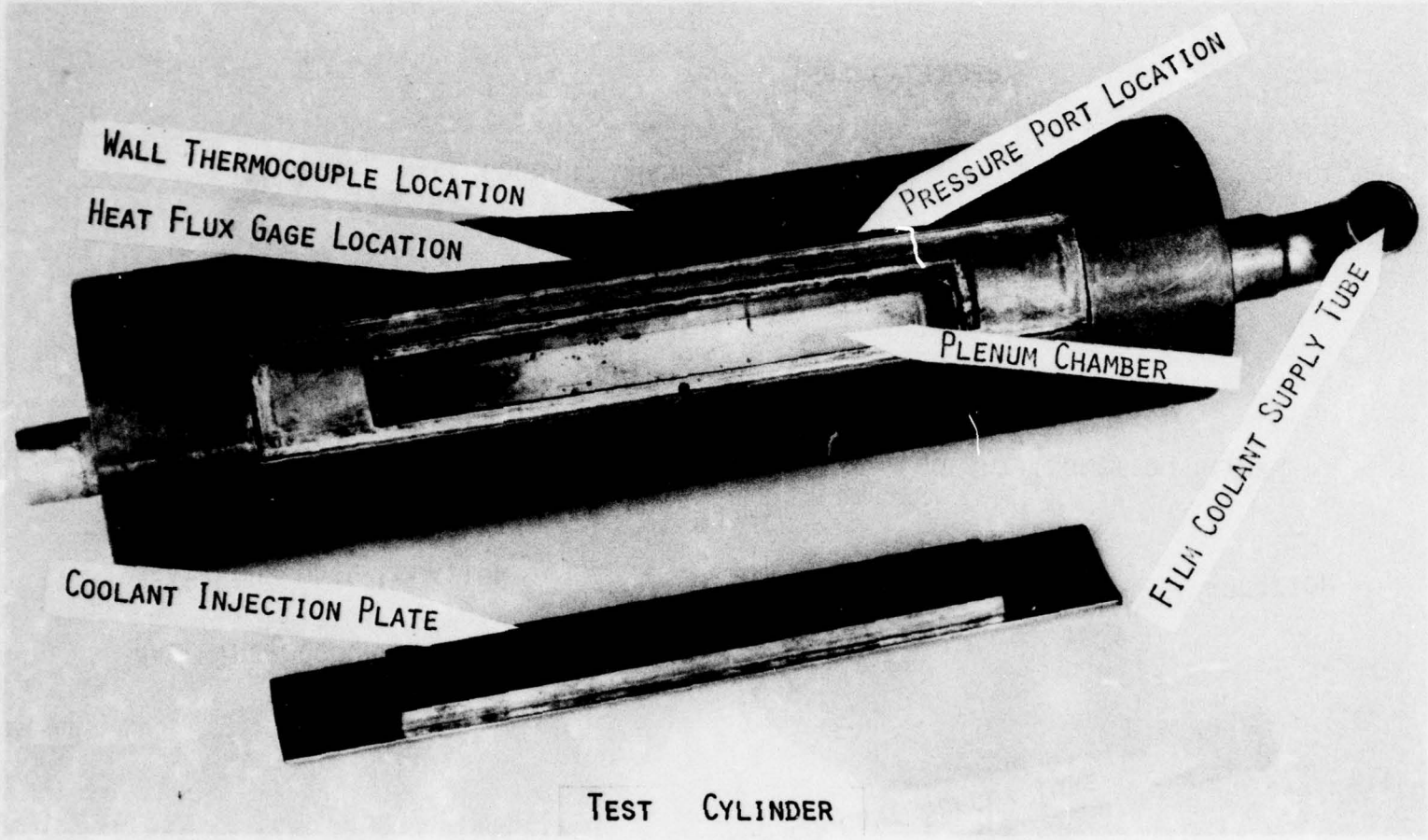

Figure 39 Photograph of Test Cylinder after Removing the Injection Plate

1.27cm (0.5 in) tubes were used to supply air film coolant to the plenum chamber. Holes were drilled at selected locations for the installation of heat flux gages, thermocouples, and wall pressure taps. The film coolant injection plate, shown in a close-up view in Fig. 40, was sealed to the cylinder with a silicone adhesive and secured with screws on the ends. The injection plate was fabricated from a 0.32cm thick plate bonded to the back of a thin, 0.16cm plate to obtain a length-to-diameter ratio of the coolant holes greater than 3. A copper coolant channel was attached to the back of the injection plate through which chilled alcohol coolant was circulated to control the injection plate temperature. Film coolant holes of the desired geometry were machined in the injection plate, with a series of plates allowing a wide range of geometry to be investigated.

The flow system used to meter the film coolant flow to the plenum chamber is shown schematically in Fig. 41. The film coolant air was initially stored in a surge tank at 1.03×10^7 N/m^2 (1500 psig). The air flow was filtered and regulated to maintain a constant flowmeter inlet pressure. The film coolant flowrate was controlled by three valves in parallel. Two hot wire mass flowmeters (in parallel) were used to provide an accurate measurement of the film coolant flowrate in both the low flowrate (0-5 SCFM) and the high flowrate (0-20 SCFM) range. The film coolant air was chilled in a methanol-dry ice bath heat exchanger just upstream of the film coolant plenum chamber.

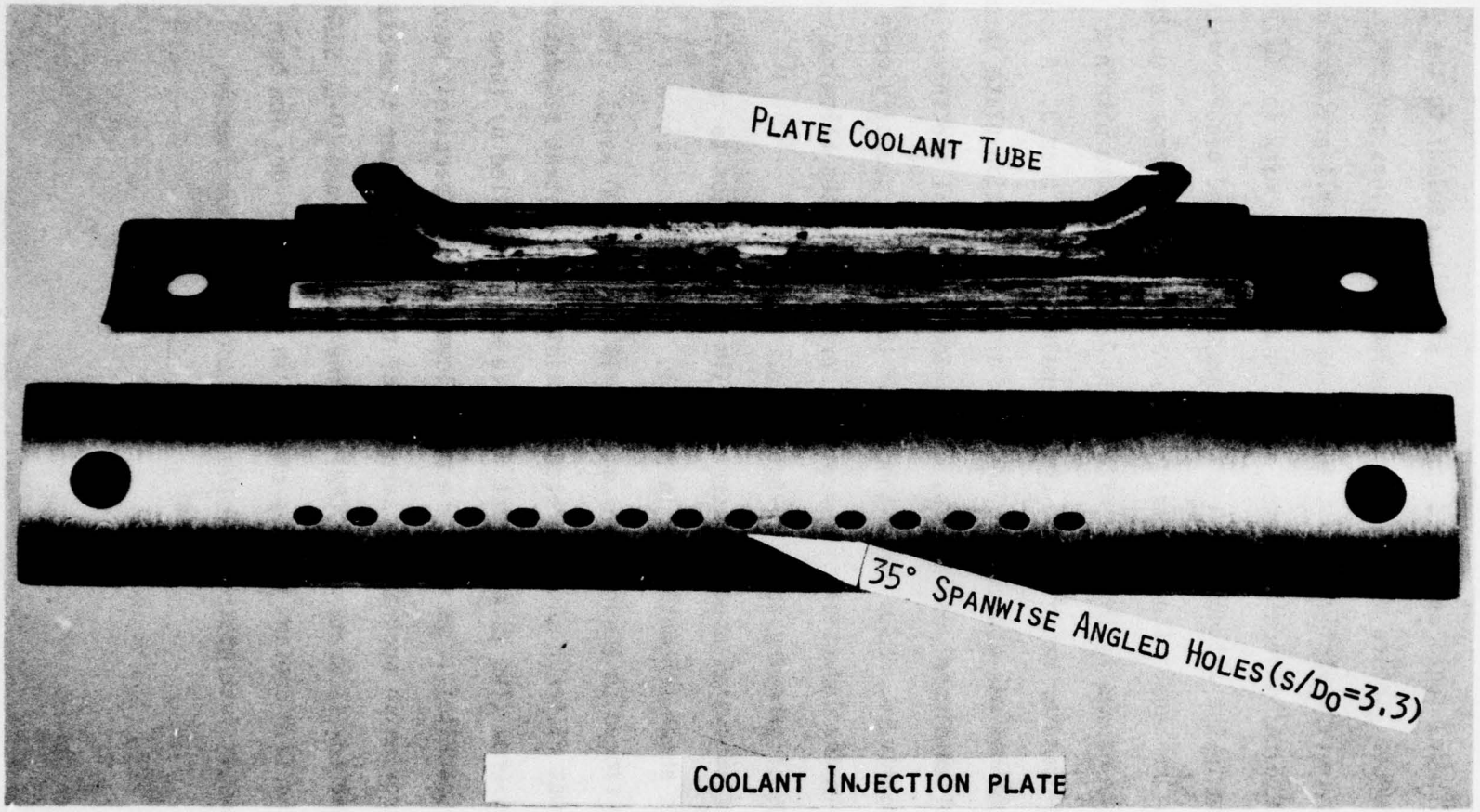

Figure 40 Photograph of the Injection Plate with a Single Row of Spanwise Angled Holes

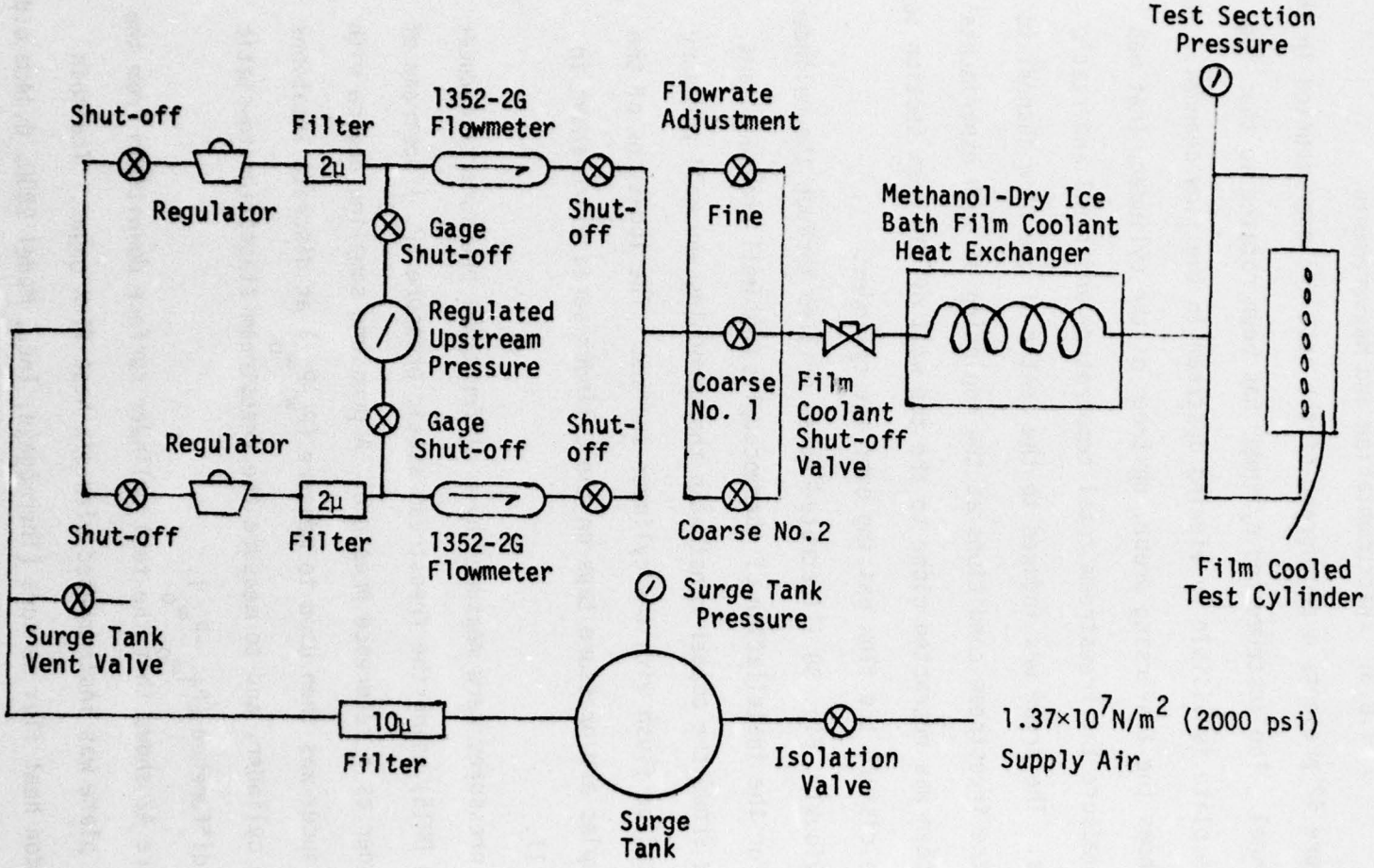

Figure 41. Schematic of the Film Coolant Flow System

II.B.3. Instrumentation and Measurements

Figure 42 presents a photograph of the test cylinder mounted in the flow channel. The instrumented cylinder has been rotated so that the injection plate is visible by viewing upstream in the flow channel. The figure shows the traversing probe, upstream of the cylinder, that was used to measure the freestream total temperature and total and static pressures. The probe was indexed to the center of the flow channel to measure the freestream conditions at the beginning of each experimental run and then was retracted close to the top wall of the test section so as not to disturb the flow passing over the cylinder.

Previously, Fig. 38 illustrated holes drilled through the cylinder surface for the installation of thermocouples and wall pressure taps. Figure 42 shows the copper-constantan thermocouples and wall pressure taps installed flush with the cylinder surface. The locations of the thermocouples and pressure taps on the cylinder surface are shown in Appendix II.

All pressures were measured by a differential pressure transducer (Validyne DP15) using the freestream static pressure (P_{∞_0}) upstream of the cylinder as a reference pressure. A pressure sampling device with one transducer was then used to measure ($P_w - P_{\infty_0}$) at discrete locations along the cylinder, and to measure the freestream stagnation-to-static pressure difference ($P_{T_{\infty_0}} - P_{\infty_0}$).

Figure 42 shows that the test cylinder surface downstream from the injection plate was instrumented with six heat flux gages. The thin foil, Gardon heat flux sensors (Thermogage, Inc., Model 2000, 0.44cm o.d.) were press fitted into the test cylinder flush with the surface. The

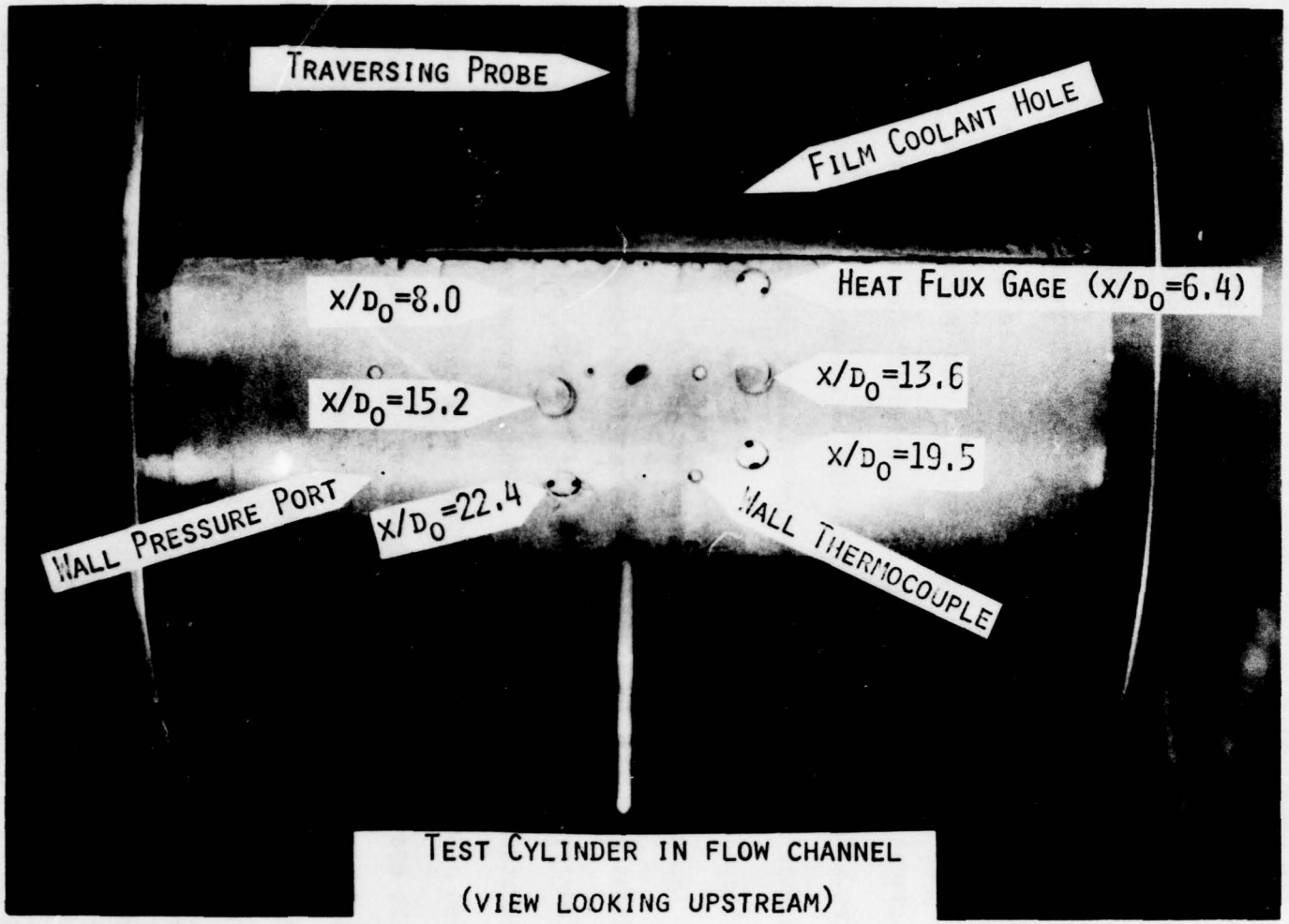

Figure 42 Photograph of the Test Cylinder Mounted in the Flow Channel

gages were mounted at different dimensionless distances downstream (x/d_o) from the row of film coolant holes as shown in Table 1. Since the location of the heat flux gages was fixed, the variation of the heat flux with respect to z/s (i.e. between holes) was measured by shifting the spanwise location of the coolant holes drilled in the injection plate. As Fig. 42 shows, to change the spanwise location of a heat flux gage with respect to a coolant hole, the coolant hole can be shifted in the spanwise direction with the drilling of a new injection plate. In this investigation, for each value of the injection angle, β, three injection plates with the holes shifted relative to the gages were used on successive experiments in order to measure the heat flux at three different z/s locations.

The Gardon heat flux gage operates on the principle that the incident heat flux on a thin constantan foil flows radially to the cylindrical copper body (heat sink) of the gage, establishing a parabolic temperature profile over the foil. The Thermogage heat flux gage consisted of a constantan foil, 0.025mm thick and 0.051cm diameter, bonded to the end of a cylindrical, copper tube. The sensor was then press fitted into a 0.44cm outer diameter copper plug. The temperature difference that is created between the center and edge of the foil is then dependent on the magnitude of the incident heat flux. A fine copper wire is fused to the center of the foil on its underneath side, while another copper wire is fused to the copper body and the emf from these two thermocouple junctions is representative of the temperature difference across the foil and the incident heat flux. Coincidentally, the variation of the thermal conductivity of constantan and the thermoelectric

Table 1 Heat Flux Gage Location

Gage No.	x/d_o (from row of coolant holes)
0	8.0
1	6.4
2	15.2
3	13.6
4	22.4
5	19.5
d_o = 0.159cm	

power of the copper-constantan thermocouple are such that a linear relation between the heat flux and the emf from the copper-constantan gage is produced. Due to the small size of the gages used, the signal produced is in the microvolt range, and each sensor was matched with an operational amplifier (gain ~1000) to provide a millivolt level signal. Each sensor was calibrated (by Thermogage, Inc.) using a radiation source with the amplifier gain adjusted to obtain a sensitivity of 115.7 $\frac{\text{joule}}{\text{m}^2\text{-sec}}$ mv. A more detailed discussion of the heat flux gage theory and operation is presented in Appendix III.

The cylinder surface temperature was measured using copper-constantan thermocouples installed as shown in Fig.42. The temperature of the injection plate was measured with copper-constantan thermocouples mounted in the plate 0.8mm below the surface.

Figure 41 previously illustrated the flow system used to supply air film coolant to the test cylinder. The air was precooled in a dry ice heat exchanger to ~228K (410°R) and supplied to the film coolant plenum chamber. A hot wire mass flowmeter (Thermo Systems, Inc., Model 1352) was used to measure the coolant mass flow rate. Copper-constantan thermocuples, positioned in the film coolant plenum chamber, were used to measure the plenum air temperature. The temperature of the air leaving the film coolant holes (T_c) was determined from the measured values of the plenum air temperature, the injection plate temperature, and the coolant mass flow rate, using a calibration curve (shown in Appendix IV) to account for the heat transfer to the film coolant flowing through the injection plate.

II.C. Experimental Conditions

This experimental program was conducted to investigate the reduction in the local heat flux due to film cooling from a single row of spanwise angled holes on a cylindrical test surface in order to model the film cooling process on the leading edge region of a turbine vane. The experimental flow conditions used in this study are presented in Table 2. To achieve a Reynolds number of 1.7×10^5, typical of a high temperature, high pressure gas turbine engine, a freestream total pressure and total temperature of 3.9×10^5 N/m^2 (56.7 psia) and 553K (995°R), respectively, were utilized with a cylinder having D = 5.02cm. While no turbulence measurements were made, a constant turbulence level was maintained throughout the investigation by fixing the turbulence screen grid size and the screen location relative to the cylinder (see Section II.B.1.).

A nominal cylinder wall temperature of 261K (470°R) was maintained giving approximately isothermal wall conditions with the surface temperature variation $\Delta T_w/T_{w_{nom}} \leq 4\%$. The low wall temperature was chosen to simulate a gas-to-wall temperature ratio of 2.1, representative of the gas turbine environment. The injection plate temperature also was maintained at approximately the cylinder temperature, with a temperature difference $\Delta T_w/T_{w_{nom}} \leq 15\%$. A discussion of the effect of a step change in the surface temperature on the downstream heat transfer coefficient is presented in Section III.A.2. and Appendix V.

Before entering the plenum chamber, the film coolant air was precooled in a dry ice heat exchanger to a nominal value of ~228K (410°R), with the specific value of temperature varying somewhat with the coolant mass flow rate (see Table 2). The temperature of the coolant injected

Table 2 Experimental Flow Conditions	
Re_D	1.7×10^5
P_{T_∞}	3.91×10^5 N/m^2 (56.7 psia)
T_{T_∞}	553K (995°R)
Ma_{∞_o}	0.08
T_w	261K (470°R)
T_c	250K (451°R) ± 9%
ρ_c/ρ_∞	2.21 ± 9%
θ_c	1.03 ± 7%

from the holes (T_c) was determined from the measured values of the plenum air temperature, the injection plate temperature, and the coolant mass flow rate, using a calibration curve (discussed in Appendix IV)to account for the heat transfer to the film coolant flowing through the injection plate. The mean value of the coolant temperature (250K, 451°R) was used to compute nominal values of the coolant-to-freestream density ratio and the dimensionless coolant temperature, θ_c, as shown in Table 2. The percentage variations listed with the ρ_c/ρ_∞ and θ_c values correspond to the variations of T_c with mass flow rate due to the film coolant heat exchanger performance and the heat transfer from the injection plate.

The range of film coolant injection parameters studied in this program are summarized in Table 3. Three different values of the injection hole angle (β) were investigated with holes angled in the spanwise direction (α=90°). The injection plate was fabricated to ensure a length-to-diameter ratio of the coolant hole greater than 3, with the specific value varying with injection angle as shown in Table 3. The hole spacing-to-diameter ratio, s/d_o, was held constant throughout the investigation corresponding to the smallest value obtainable for β=25° within fabrication limits.

The location of the row of holes relative to stagnation, θ_i, was varied by rotating the cylinder to a new orientation on successive experiments. The important hydrodynamic parameters characteristic of the injection locations investigated, namely the acceleration parameter, K_i, the boundary layer displacement thickness-to-hole diameter ratio, δ^*/d_o, and the boundary layer momentum thickness-to-hole diameter ratio, θ_{mom}/d_o

Table 3 Film Coolant Injection Parameters

Injection Angle	β	L/d_o		
$\alpha=90°$ d_o = 0.159cm	25° 35° 45°	6.2 4.5 3.7		
s/d_o	3.3			
Injection Location	θ_i	$K_i \times 10^5$	δ^*/d_o	θ_{mom}/d_o
	20° 30° 40°	4.8 2.1 1.1	0.026 0.027 0.028	.0114 .0119 .0124
Measurement Locations	x/d_o	z/s		
	6.4 8.0 15.2	0, .33, .67 0, .33, .67 .17, .50, .83		
M	0 → 2.0 in intervals of 0.25			

are presented in Table 3.[†] It can be seen that, for the range of θ_i investigated, the change in δ^*/d_o was insignificant while the value of K_i varied fourfold.

The coolant hole diameter, d_o, was selected to simulate values of θ_{mom}/d_o typical of those expected for turbine vane leading edge applications.

The film cooling performance was determined by measuring the heat flux at the downstream distances (x/d_o) and spanwise locations (z/s) listed in Table 3.[††] The heat flux reduction was determined as a function of the blowing ratio, M, varying from M = 0 to M = 2.0 in intervals of 0.25.

II.D. Data Reduction

During each experimental test for a particular injection configuration the following measurements were recorded: (a) the freestream total temperature, total pressure, and the total-to-static pressure difference, upstream of the cylinder, (b) the cylinder surface wall temperature and wall heat flux, and (c) the injection plate temperature, the plenum air temperature and the coolant mass flow rate. These values were used to determine the film cooling performance as described below.

[†]The K_i values were calculated from potential flow for a cylinder in crossflow. The values of δ^*/d_o and θ_{mom}/d_o were calculated for a cylinder in crossflow using the integral momentum boundary layer equation [39].

[††]Of the six heat flux gages installed in the cylinder (see Table 1), two failed prior to the onset of the film cooling experiments. Film cooling data are reported for only three gage locations (see Table 3) since the effect of film cooling at x/d_o = 22.4 (the fourth operative gage) was insignificant.

The physical properties of the combustion heated air freestream flow (μ, k, γ, Mol. Wt.) were determined from Ref. 40. The physical properties of the film coolant air (μ, Pr, Mol. Wt.) were determined from Ref. 41. The freestream density was computed from the freestream static temperature and pressure assuming a perfect gas. The freestream velocity was calculated from the freestream total and static pressures and the total temperature. The Reynolds number, based on the cylinder diameter, was computed from the freestream density and velocity and the viscosity evaluated at the freestream static temperature.

For experiments without film cooling, the surface heat flux and the freestream-to-wall temperature difference were used to compute the local convective heat transfer coefficient.

$$h_o^{\dagger} = \frac{q''_{w,o}}{T_\infty - T_{w_o}} \tag{33}$$

The subscript o designates no film coolant flow (i.e. dry wall). The dry wall heat transfer coefficient, h_o, was computed directly from the heat flux, wall temperature and freestream temperature measurements recorded during each experimental run. The Nusselt number, based on the cylinder diameter, was calculated from h_o with the thermal conductivity evaluated at the mean film temperature, $(T_w + T_\infty)/2$.

For the experiments with film coolant flow, the heat flux and the freestream-to-wall temperature difference were used to compute a local convective heat transfer coefficient with film cooling.

---

† In view of the low freestream velocity (Ma=0.08), the heat transfer coefficient was defined with the freestream static temperature.

$$h_{FC} = \frac{q''_{w,FC}}{T_\infty - T_{w_{FC}}} \tag{34}$$

The subscript FC designates with film cooling.

The effect of film cooling is indicated by the ratio of the two heat transfer coefficients, h_{FC} and h_o, which is equivalent to the Stanton number ratio

$$\frac{h_{FC}}{h_o} = \frac{St_{FC}}{St_o} \tag{35}$$

where $St = \frac{h}{\rho V_\infty c_p}$

and V_∞ = local freestream velocity along the cylinder.

The film cooling data reported herein are given as a percentage reduction in the Stanton number due to film cooling which is defined as

$$1 - \frac{St_{FC}}{St_o} = \text{the Stanton Number Reduction.} \tag{36}$$

The dimensionless coolant temperature, θ_c, characteristic of the experiments reported was determined from a calculated temperature of the air leaving the coolant holes, T_c. The injection plate temperature and the plenum air temperature, recorded during each experimental test were used to correlate the temperature rise of the coolant passing through the injection plate as a function of the coolant mass flow rate (see Appendix IV), such that the film coolant temperature (T_c) could be calculated and θ_c determined.

The film coolant blowing parameters, M, V_c/V_∞, and I, were computed assuming equal flow through all of the coolant holes. The mass flux

($\rho_c V_c$) of the coolant was determined from the measured coolant flow rate, and the number and diameter of the coolant holes. The coolant velocity, V_c, was computed from the coolant mass flux ($\rho_c V_c$) and the coolant density based on T_c and P_c[†] (assuming a perfect gas). The blowing ratio, $M = \rho_c V_c / \rho_\infty V_\infty$, was determined from $\rho_c V_c$ and the local value of $\rho_\infty V_\infty$ at the point of injection on the cylinder surface. Similarly, the coolant-to-freestream velocity ratio (V_c/V_∞) and the momentum flux ratio ($\rho_c V_c^2 / \rho_\infty V_\infty^2$) were computed from the values of M and ρ_c/ρ_∞.

All of the calculations described in this section were performed using a data reduction computer program. A detailed discussion of the program and all of the geometric, thermodynamic, and hydrodynamic values calculated is presented in Appendix II.

Each experimental test was limited to a steady state run time of approximately thirty minutes due to the capacity of the air supply facility. The investigation was divided into several phases which are described in Appendix II. A detailed discussion of the results from each phase of the experimental investigation follows in Section III.

[†] P_c was assumed equal to P_∞, the local static pressure on the cylinder surface.

III. RESULTS AND DISCUSSION

The experimental investigation was divided into three separate phases:

A. Preliminary experiments to determine the freestream flow, cylinder surface, and coolant flow conditions that were maintained constant throughout the investigation.

B. Experiments without film cooling to determine the dry wall heat flux distribution around the cylinder.

C. Experiments with film cooling to determine the influence of injection geometry and coolant flow rate.

The results from each phase are described in the following sections.

III.A. Preliminary Experiments

This initial phase of the investigation was conducted to determine the freestream flow conditions, the cylinder and coolant temperatures, and the cylinder pressure distribution characteristic of the experimental apparatus.

III.A.1. Freestream Flow Conditions

The freestream flow conditions were determined by measuring the horizontal and vertical total temperature and velocity profiles upstream (6.4cm) of the test cylinder. Figures 43 and 44 present the initial vertical and horizontal velocity profiles obtained before the flow straightener had been inserted into the flow channel. A traversing probe

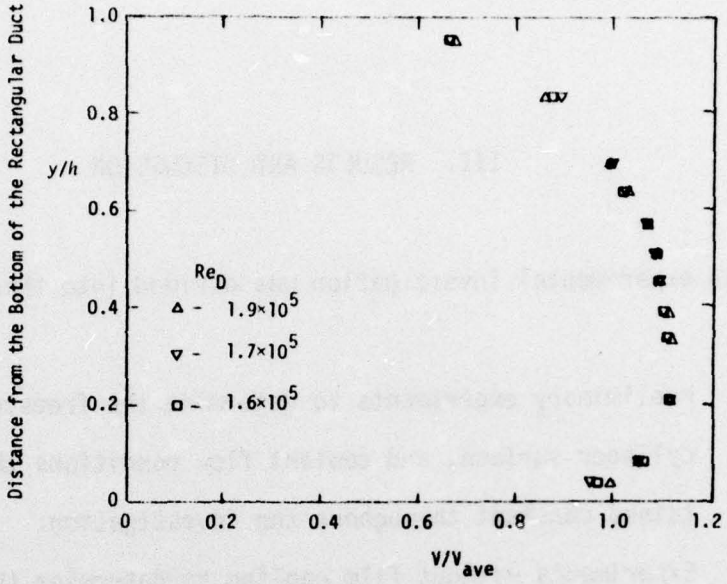

Figure 43. Vertical Velocity Profile (without the Flow Straightener)

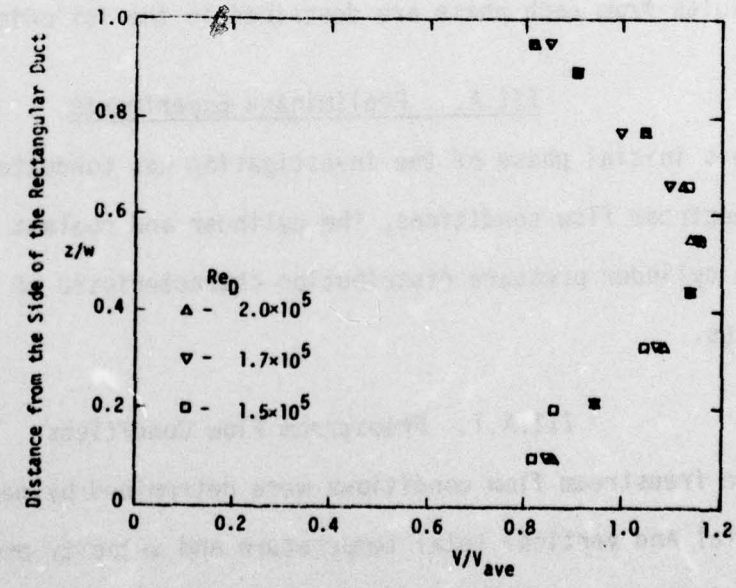

Figure 44. Horizontal Velocity Profile (without the Flow Straightener)

(discussed in Appendix II) was indexed in 1.27cm (0.5") increments to within 1cm of the test section walls. The Reynolds number used to characterize the film cooling experiments and the profiles is based on the freestream conditions at the test section centerline. As shown in Fig. 43, the profiles were examined for the nominal Reynolds number of 1.7×10^5 (used in Phases B and C) and for values above and below. The profile data, in Figs. 43 and 44, are presented in non-dimensional form. A numerical integration of the measured velocity profiles was performed to compute an average velocity, defined by Eq. (37), to non-dimensionalize the profiles.

$$\text{Vertical Profile} \quad V_{ave} = \int_0^h Vwdy/Area$$

$$\text{Horizontal Profile} \quad V_{ave} = \int_0^w Vhdz/Area \qquad (37)$$

The vertical velocity profile presented in Fig. 43 shows a non-symmetric variation of the dimensionless velocity, with a maximum value of ~1.1 occurring at the y/h location of 0.3, while a minimum value of ~0.65 occurs close to the top of the test section. Figure 44, showing the horizontal velocity profile, indicates a symmetrical distribution about the test section centerline with a dimensionless velocity varying from a maximum of ~1.15 at the centerline to a minimum of ~0.8 close to the test section walls. Since it was desired to conduct the film cooling experiments in a two-dimensional flow, a flow straightener (described in Appendix II) was inserted at the front end of the flow channel and the profile measurements were repeated.

Figures 45 and 46 illustrate the vertical and horizontal velocity profiles obtained with the flow straightener installed. The dotted lines represent the profiles (without the flow straightener installed) previously seen in Figs. 43 and 44. In Fig. 45 the cross hatched area represents the vertical region occupied by the test cylinder. The profiles presented in Figs. 45 and 46 show the velocity of the flow approaching the cylinder to be uniform in the z-direction and approximately constant in the y-direction. It is noted that the variation of the Reynolds number had a negligible effect on the velocity profiles.

Total temperature profiles upstream of the cylinder were also measured with the traversing probe and the results are presented in Figs. 47 and 48. Since no significant changes were found in the profiles before and after the flow straightener was installed in the flow channel, only the final vertical and horizontal profiles (with the flow straightener installed) are presented. The total temperature is non-dimensionalized by an average temperature, defined by Eq. (38), using a numerical integration of the measured data to compute the average temperature.

$$\text{Vertical Profile} \qquad T_{T,ave} = \int_0^h \rho V T_T dy \Big/ \int_0^h \rho V dy \tag{38}$$

$$\text{Horizontal Profile} \qquad T_{T,ave} = \int_0^w \rho V T_T dz \Big/ \int_0^w \rho V dz$$

The horizontal profile shown in Fig. 48 indicates a uniform freestream total temperature in the z-direction. The vertical profile presented in Fig. 47 exhibits some variation with the temperature decreasing as y/h increased. However, for the location of the cylinder shown by the cross hatched area, the temperature variation of the freestream directly

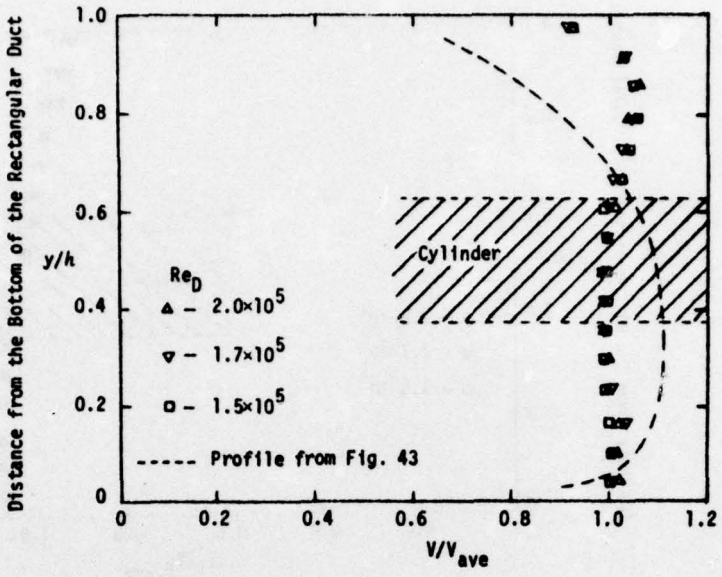

Figure 45. Vertical Velocity Profile (with the Flow Straightener)

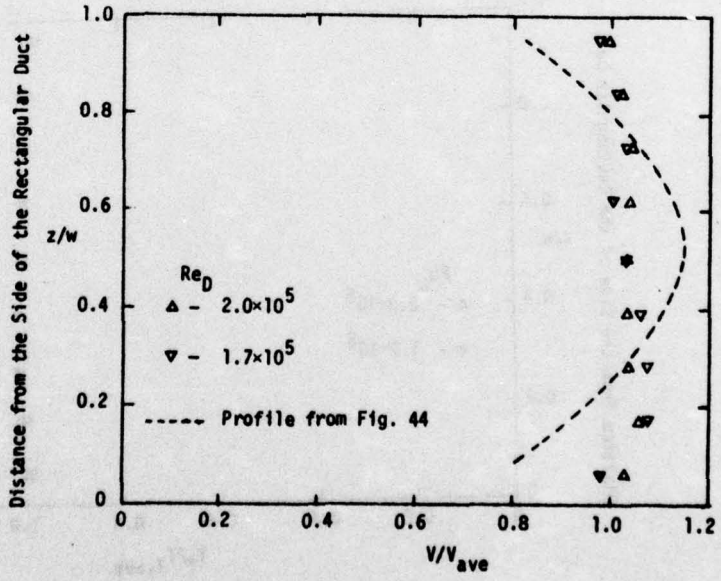

Figure 46. Horizontal Velocity Profile (with the Flow Straightener)

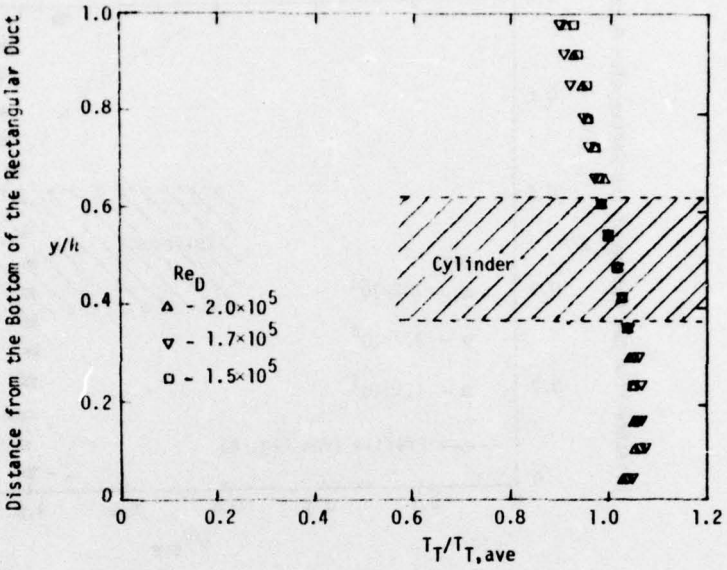

Figure 47. Vertical Total Temperature Profile (with the Flow Straightener)

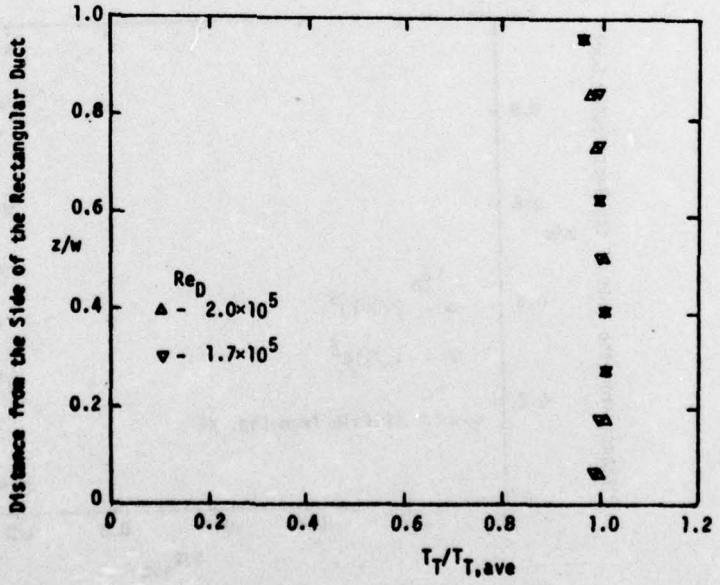

Figure 48. Horizontal Total Temperature Profile (with the Flow Straightener)

in front of the cylinder was $\leq$ 5%, which was judged acceptable. Figures 47 and 48 again reveal that the variation of the Reynolds number had a negligible effect on the total temperature profiles.

While the Reynolds number listed with the profile data was based on the test section centerline conditions, another Reynolds number, based on the $T_{T,ave}$ and V_{ave} values computed from each profile, was calculated and found to never differ from the centerline Reynolds number by more than 1%.

III.A.2. Cylinder and Coolant Conditions

The ten internal coolant channels distributed evenly around the cylinder surface and the use of copper for the cylinder material resulted in a nearly uniform temperature along the cylinder surface. Thermocouples, distributed along the surface were used to measure the cylinder temperature from an angle of 3° to 214° downstream from the injection plate-cylinder wall junction. There were no thermocouples directly upstream of the injection plate to record the cylinder temperature in this region. During each experimental run, the cylinder wall temperature distribution was measured and Fig. 49 presents data for two experimental tests representative of the wall temperature variations observed. The variation of the cylinder wall temperature never exceeded more than 4% (from the maximum temperature to the minimum).

The injection plate was equipped with a coolant tube attached to the back to maintain the plate temperature near that of the cylinder. However, with no film coolant flow through the injection holes, the plate temperature was higher than the cylinder wall temperature, but the difference never exceeded 15% of the mean cylinder wall temperature. As Fig. 49

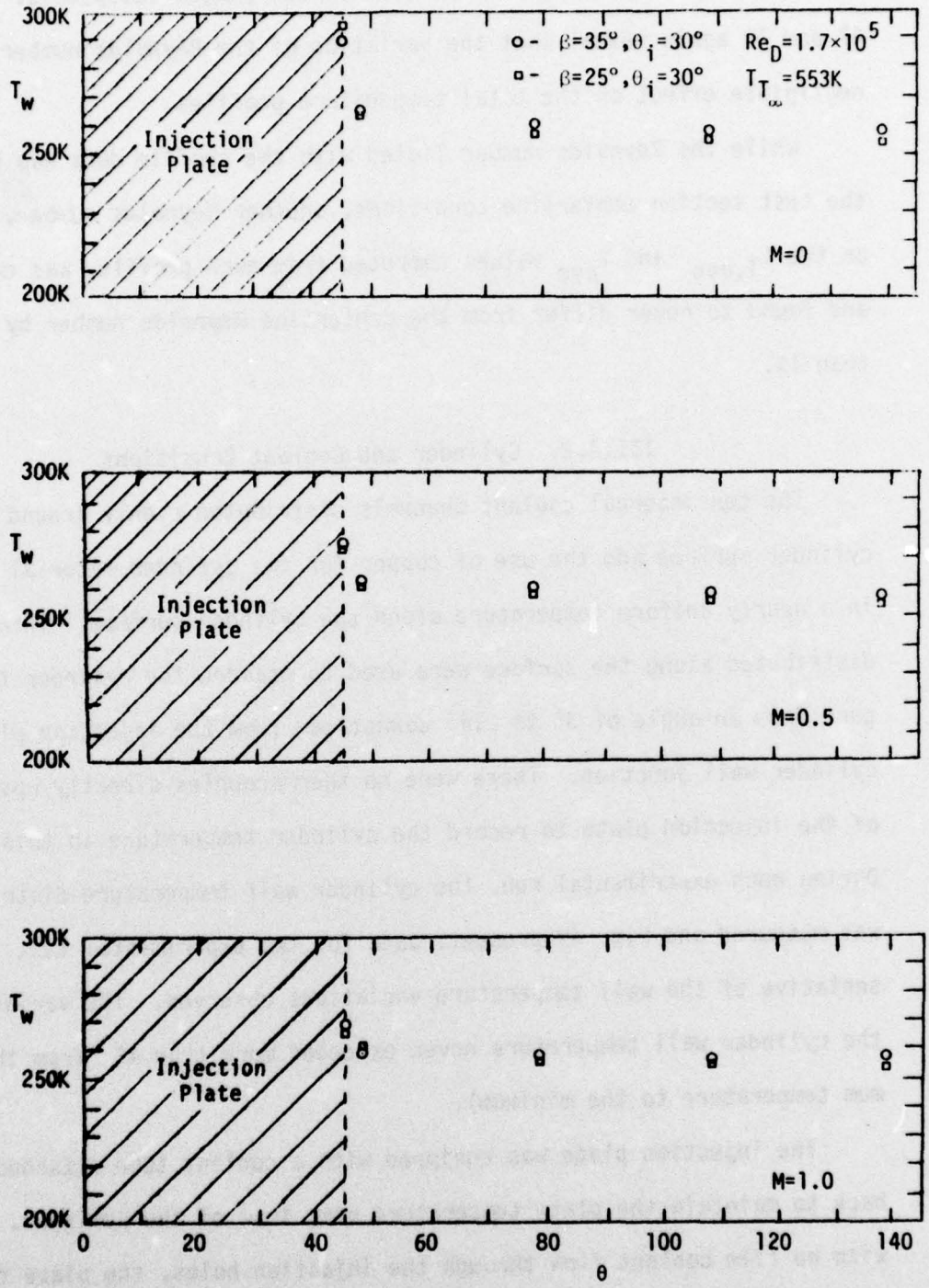

Figure 49. Wall Temperature Distribution

reveals, as the film coolant flow through the coolant holes was increased, the plate temperature decreased, approaching the cylinder wall temperature.

An analysis of the influence of this step change in the surface temperature on the heat transfer coefficient downstream of the injection plate is presented in Appendix V. The analysis was performed assuming a surface temperature equal to the injection plate temperature for the region extending from the stagnation line, with a step decrease to the cylinder temperature at the injection plate-cylinder junction. The analysis revealed that, for a step change in temperature of 39K, the heat transfer coefficient (h_o) at the heat flux gage closest to the injection plate (8° downstream of the injection plate-cylinder junction) increased ~11% over the case with an isothermal surface. Further downstream, at the heat flux gage 39° from the injection plate-cylinder junction, the increase was only ~4%. For a step change in temperature of $\leq$ 11K, which is more representative of the injection plate temperature with blowing, the corresponding value of h_o would differ from the isothermal case by $\leq$ 3% (as shown in Appendix V).

Figure 49 reveals a variation of the injection plate temperature as the coolant blowing ratio was varied. Since the important parameter influencing the film cooling performance is the temperature of the coolant leaving the hole, T_c, an experimental study was conducted to determine the temperature rise of the coolant in passing through the injection holes. A discussion of this experimental study and the results are presented in Appendix IV. From this study, a calibration curve was developed so that the coolant temperature (T_c) could be calculated by measuring the

coolant temperature in the plenum, the injection plate temperature, and the coolant mass flow rate.

The temperature of the film coolant in the plenum chamber was directly related to the coolant temperature emerging from the film coolant dry ice bath heat exchanger which varied with the coolant flow rate. Representative data from the experimental runs showed a film coolant plenum temperature of 257K (3°F) with a coolant flow rate of 5.2×10^{-4} kg/sec, and a temperature of 219K (-66°F) with a flow rate of 8.55×10^{-3} kg/sec. Thus increasing the coolant flow rate caused the plenum temperature to decrease, but the higher flow rate increased the heat addition to the coolant as it passed through the injection plate. Figure 50 presents a plot of the calculated coolant temperature leaving the injection hole as a function of the coolant mass flow rate. The length-to-diameter ratio of the coolant holes was constant for β=25°. The trend shows a gradual decrease in the coolant temperature as the mass flow rate was increased. Thus, as the flow rate was increased, the lower plenum temperature more than compensated for the increased heat addition from the injection plate to the coolant. The coolant temperature for each coolant configuration (i.e. particular values of β, θ_i, and blowing ratio) were used to compute a mean coolant temperature of 250K (-9°F). The coolant temperature (T_c) for any experimental condition varied by less than 9% from this mean value.

III.A.3. Cylinder Pressure Distribution

In order to provide the background for understanding the cylinder heat transfer characteristics in the present study, it is informative to review the results of previous cylinder drag and pressure distribution

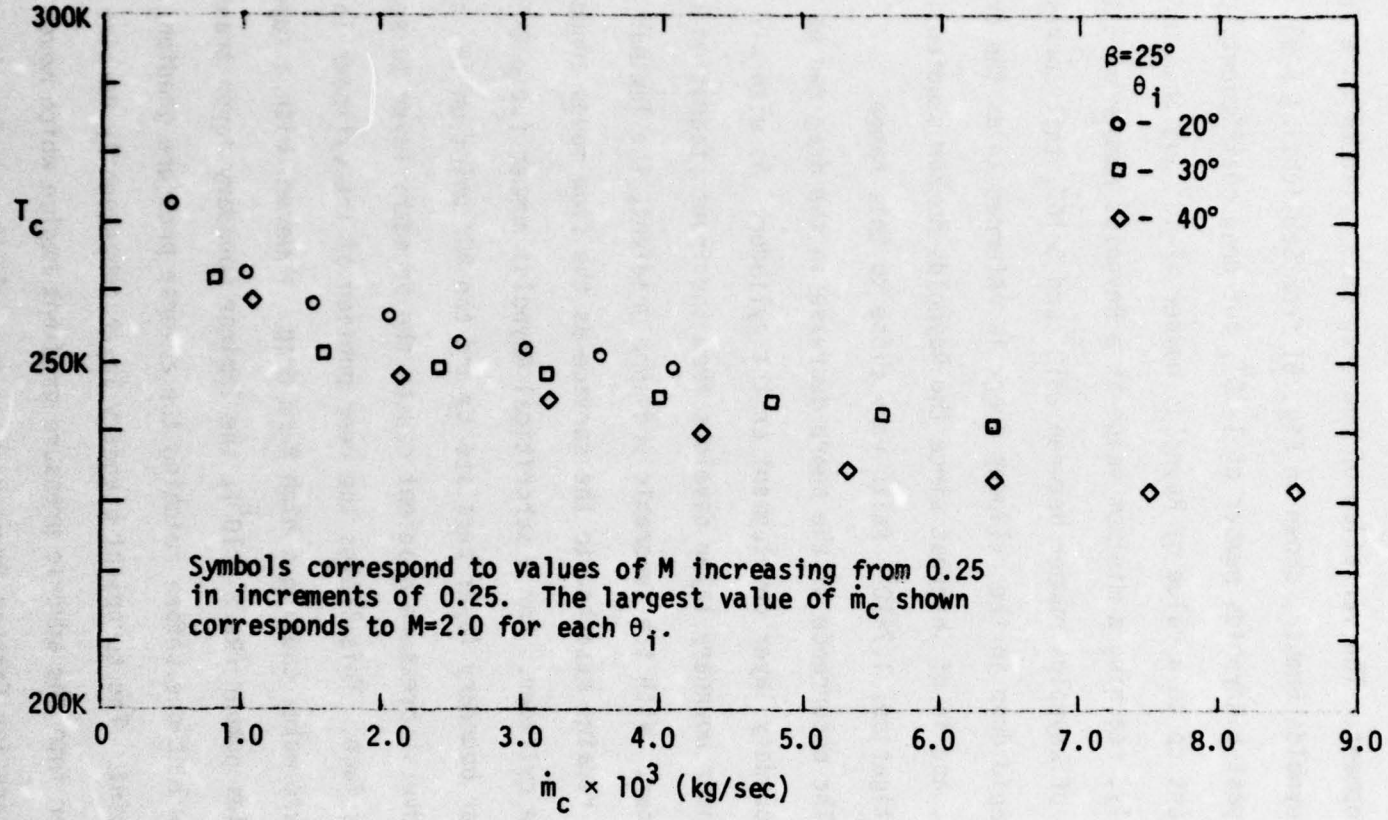

Figure 50. Variation of the Coolant Temperature with Coolant Flow Rate

studies that have defined the nature of the cylinder boundary layer development. The variation of the drag on a cylinder as a function of the Reynolds number, shown in Fig. 51 from Schlichting [39], illustrates that past a Reynolds number of 1×10^4, the drag coefficient, C_D, remains constant up to a value of Reynolds number $\approx2\times10^5$ and then drops off sharply, reaching a minimum value at a Reynolds number of 5×10^5. The range of Reynolds number between 2×10^5 and 5×10^5, that corresponds to the rapid drop in the cylinder drag, is referred to as the critical range, and is of interest since the Reynolds number studied in this investigation, 1.7×10^5, falls very close to this range.

The occurrence of the sharp decrease in the drag can be related to the boundary layer development on the cylinder. As with all blunt bodies, a laminar boundary layer develops from the front stagnation line on the cylinder. With the favorable pressure gradient, the laminar boundary layer remains attached to the surface as the flow moves around the front of the cylinder. For a subcritical Reynolds number ($Re \lesssim 2\times10^5$), the laminar boundary layer persists toward the 90° point on the cylinder where the adverse pressure gradient causes the boundary layer to separate from the surface. This leaves the rear portion of the cylinder in a low pressure wake, causing a high form drag. However, with a supercritical Reynolds number ($Re \gtrsim 2\times10^5$), the laminar boundary layer transitions to a turbulent one before reaching the adverse pressure gradient near the 90° point. The turbulent boundary layer subsequently remains attached further into the adverse pressure gradient region which moves the point of separation farther downstream on the cylinder surface (beyond the 90° point), reducing the low pressure wake behind the cylinder and resulting in a much lower drag force.

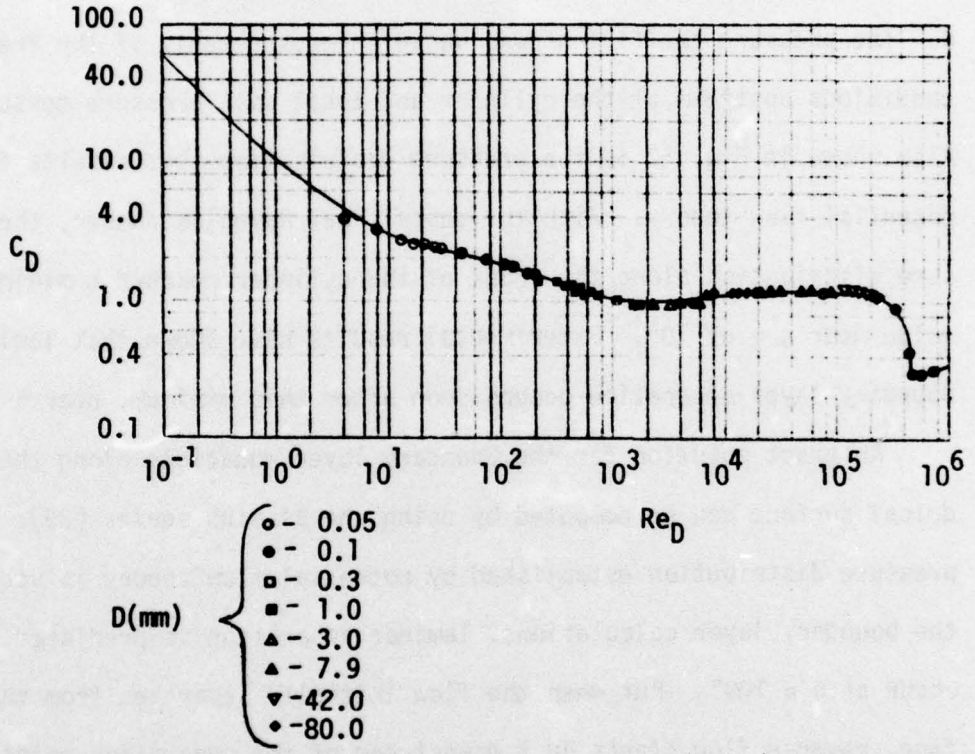

Figure 51. Variation of Cylindrical Drag with Reynolds Number (Schlicting [39])

This boundary layer development can be illustrated by reviewing the pressure distributions around a cylinder for both a subcritical and supercritical Reynolds number. Figure 52 presents the results of Flachshart [42], measured in a near turbulence free wind tunnel, with the pressure coefficient plotted as a function of the angular distance from stagnation θ. The pressure coefficient was based on measurements of the freestream conditions upstream of the cylinder and local wall pressure measurements. Also shown in Fig. 52 is the pressure distribution that results from potential flow theory. With the subcritical Reynolds number, the pressure distribution along the front of the cylinder reached a minimum value near a θ of 70°. Experimental results have shown that laminar boundary layer separation occurs soon after this minimum, near $\theta \approx 80°$.

An exact solution for the boundary layer equations along the cylindrical surface can be computed by using the Blasius series [39]. If the pressure distribution established by potential flow theory is used for the boundary layer calculations, laminar separation is predicted to occur at $\theta \approx 109°$. But when the flow initially separates from the surface, reverse flow starts just downstream of the separation point. This reverse flow starts to penetrate forward along the cylinder surface, altering the pressure distribution along the surface from that established by the potential flow theory. When the boundary layer calculations are repeated using an experimentally measured pressure distribution around the cylinder, the laminar separation point is found to be near 80°, the same location observed experimentally [39]. As Fig. 52 reveals, the pressure distribution from 80° to the rear point on the cylinder is relatively flat.

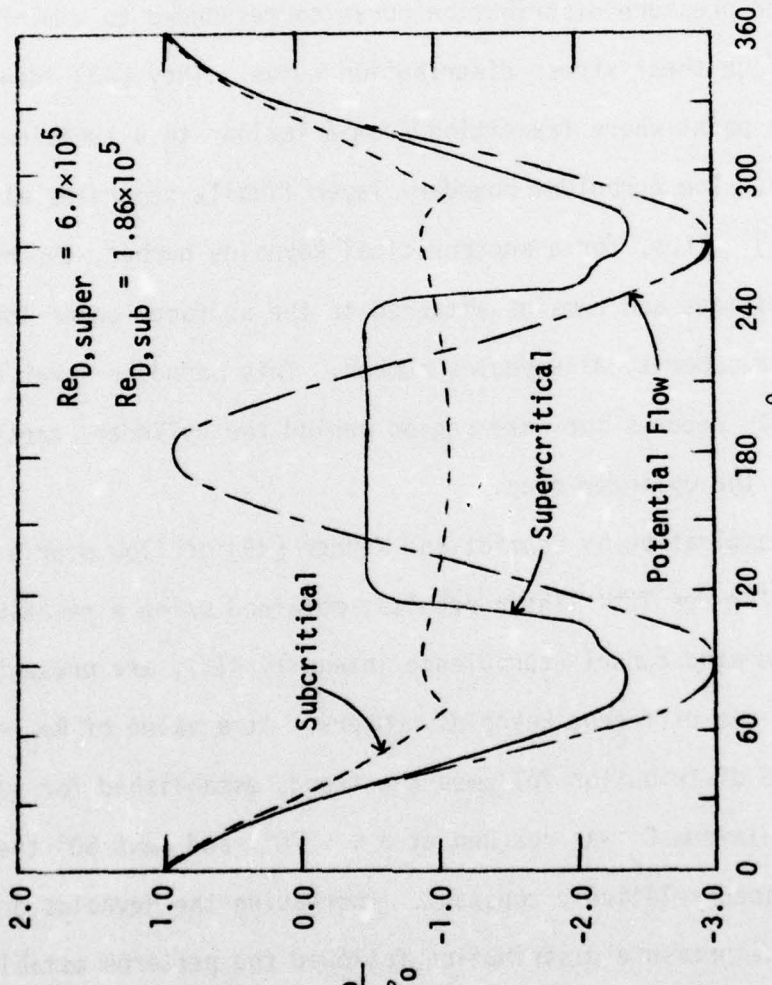

Figure 52. The Pressure Distribution for a Cylinder in Cross Flow (Flachshart [42])

When the Reynolds number becomes supercritical, Fig. 52 shows that the pressure distribution deviates much less from the potential flow than seen for the subcritical Reynolds number. The minimum value of C_p is reached at $\theta \approx 90°$ and just past the minimum, an inflection point is visible in the curve. Fage and Faulkner [43] found that this inflection point in the pressure distribution curve corresponded to a minimum point on the surface shear stress distribution curve. They [43] identified this as the point where transition from a laminar to a turbulent boundary layer began. The turbulent boundary layer finally separates at $\theta \approx 120°$ to 130° [44]. Thus, for a supercritical Reynolds number, the boundary layer transitions and remains attached to the surface longer than it would with a subcritical Reynolds number. This boundary layer attachment significantly reduces the wake region behind the cylinder, causing a large decrease in the cylinder drag.

An investigation by Schmidt and Wenner [45] of flow over a cylinder showed similar results. Their results, obtained using a relatively turbulence free wind tunnel (turbulence intensity <1%), are presented in Fig. 53 for two different Reynolds numbers. At a value of $Re_D = 1.7 \times 10^5$, the pressure distribution followed the trends established for subcritical flow. The minimum C_p was reached at a $\theta \approx 70°$, and past 80° the distribution remained relatively constant. Increasing the Reynolds number to 4.26×10^5, the pressure distribution followed the patterns established for supercritical flow. The minimum C_p was reached near a $\theta \approx 90°$, and just beyond an inflection point occurred, indicating the beginning of the transition from a laminar to a turbulent boundary layer. For a value $\gtrsim 130°$, the pressure distribution remained relatively constant indicating separation of the turbulent boundary layer.

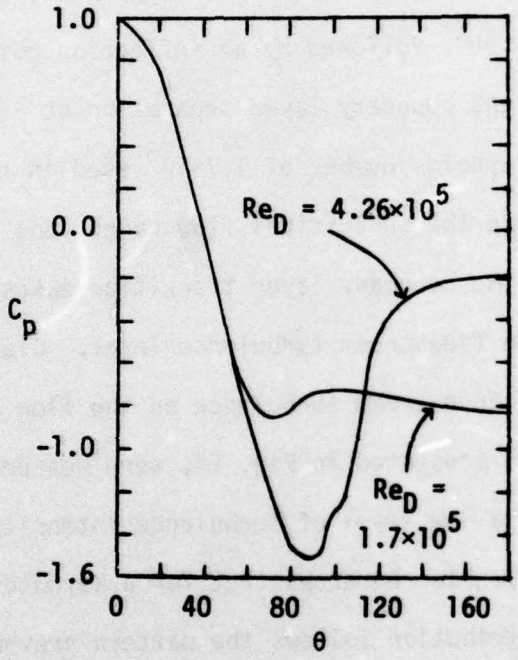

Figure 53. The Pressure Distribution for a Cylinder in Cross Flow (Schmidt and Wenner [45])

From these experimental observations it is concluded that for subcritical flow, the laminar boundary layer separates from the surface, the minimum C_p is reached near $\theta \approx 70°$, the flow separates near $\theta \approx 80°$, and thereafter the pressure distribution remains relatively constant. However, for the case of supercritical flow, when the laminar boundary layer transitions to turbulent before separation, the minimum C_p is reached near $\theta \approx 90°$, followed by an inflection point indicating transition, and turbulent boundary layer separation at $\theta \approx 120°$ to 130°.

While the Reynolds number of 1.7×10^5 used in this investigation appears to fall in the subcritical flow range, the critical Reynolds number at which the boundary layer transition takes place can be strongly influenced by the freestream turbulence level. Giedt [46] investigated the influence of freestream turbulence on the flow around a cylinder. His [46] results, presented in Fig. 54, were measured for two levels of turbulence. For a low level of turbulence intensity generated by a screen mesh (~1%), Fig. 54 shows that for a Reynolds number of 0.98×10^5, the pressure distribution follows the pattern previously described for subcritical flow. However, at the Reynolds number of 2.12×10^5, the pressure distribution followed the pattern characteristic of supercritical flow. Data for a low level of turbulence intensity at $Re_D = 1.66\times10^5$ (see Fig. 54) indicate a trend similar to subcritical flow but with the appearance of delayed separation somewhat characteristic of supercritical flow. Comparing the results in Figs. 52 and 54 it can be seen that in a relatively turbulence free wind tunnel ([42] Fig. 52), 2×10^5 would be a subcritical Reynolds number, while in a wind tunnel with a low turbulence intensity of 1% ([46] Fig. 54), the Reynolds number of 2.12×10^5 would

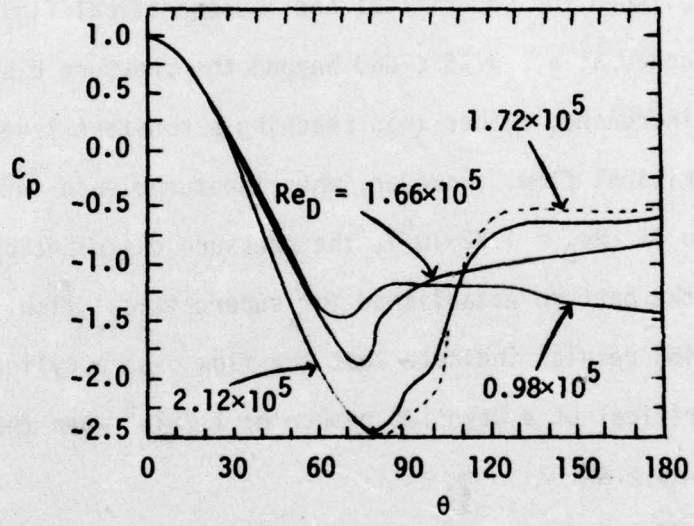

$Re_D \times 10^{-5}$	Grid	Tu
0.98	16 Mesh Screen	1%
1.66	16 Mesh Screen	1%
2.12	16 Mesh Screen	1%
1.72	Rope Net	4%

Figure 54. The Influence of Freestream Turbulence on the Pressure Distribution for a Cylinder in Cross Flow (Giedt [46])

have a pressure distribution representative of supercritical flow. Thus, the freestream turbulence can significantly decrease the Reynolds number where transition first occurs.

Giedt [46] also measured the pressure distribution at $Re_D \approx 1.7\times10^5$ for two different levels of turbulence intensity (1% and 4%) with the results shown in Fig. 54. For the lower turbulence intensity ($Re_D = 1.66\times10^5$), the pressure distribution followed a pattern somewhat between that established for subcritical and supercritical flow. The minimum C_p was reached at a $\theta \approx 75°$, and beyond the pressure distribution continually increased, rather than reaching a constant level characteristic of supercritical flow. However, when the turbulence intensity was increased to 4% ($Re_D = 1.72\times10^5$), the pressure distribution definitely followed the pattern established for supercritical flow. Therefore, Giedt's [46] results indicate that the flow over a cylinder is likely to be supercritical at a Reynolds number of 1.7×10^5 when the turbulence intensity is $\gtrsim$ 4%.

The effect of the freestream turbulence on the boundary layer development was confirmed by the results of Seban [47] who investigated the flow over a cylinder at $Re_D \approx 1.7\times10^5$ in a clear tunnel and in a tunnel with a 4 mesh screen inserted. Figure 55, showing the measured pressure distributions, indicates subcritical flow for the clear tunnel and supercritical flow for the tunnel with a 4 mesh screen. Thus, the turbulence generated by the screen was sufficient to cause supercritical flow at $Re_D \approx 1.7\times10^5$. Therefore, it is highly probable that the turbulence generated in the flow channel used in this investigation was sufficient to cause supercritical flow for $Re_D = 1.7\times10^5$.

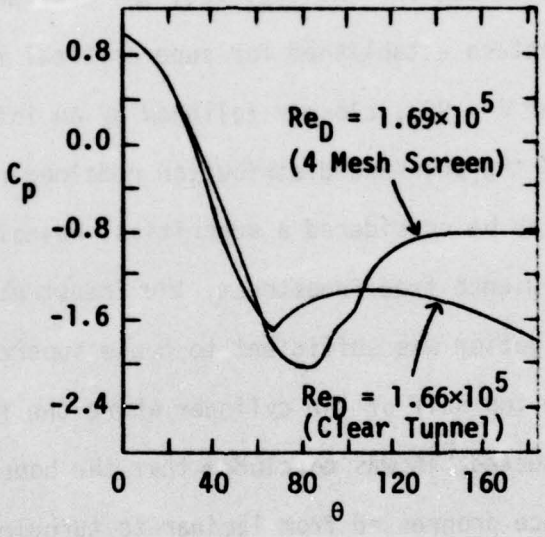

Figure 55. The Influence of Freestream Turbulence on the Pressure Distribution for a Cylinder in Cross Flow (Seban [47])

Figure 56 shows the pressure distribution measured around the test cylinder used in this investigation. The results are plotted as C_p as a function of θ, with the pressure coefficient being computed from the freestream conditions upstream of the cylinder and the local wall pressure measurements. The results are presented for a Reynolds number of 1.7×10^5 for cold flow and hot flow (combustor in use). Figure 56 shows that the temperature level and the combustor operation had no effect on the pressure distribution. As expected, the pressure distribution followed the pattern established for supercritical flow. The minimum C_p was reached near $\theta \approx 90°$, closely followed by an inflection point, and beyond $\theta \approx 130°$ the pressure distribution remained relatively constant. While 1.7×10^5 may be considered a subcritical Reynolds number for a relatively turbulence free freestream, the freestream turbulence level in this investigation was sufficient to cause supercritical flow. Therefore, along the top half of the cylinder where the film cooling experiments were conducted, it was concluded that the boundary layer development along the surface progressed from laminar to turbulent with separation occurring on the rear half of the cylinder.

III.B. Heat Transfer Without Film Cooling

The second phase of the investigation dealt with a study of the cylinder heat transfer without film cooling, hereafter referred to as the dry wall heat transfer. The dry wall heat transfer data were obtained as a function of position relative to stagnation, θ. By rotating the cylinder on successive experiments, it was possible to position each heat flux gage at selected locations in the range of $\theta = 0°$ to $90°$. The objectives of this phase of the study were:

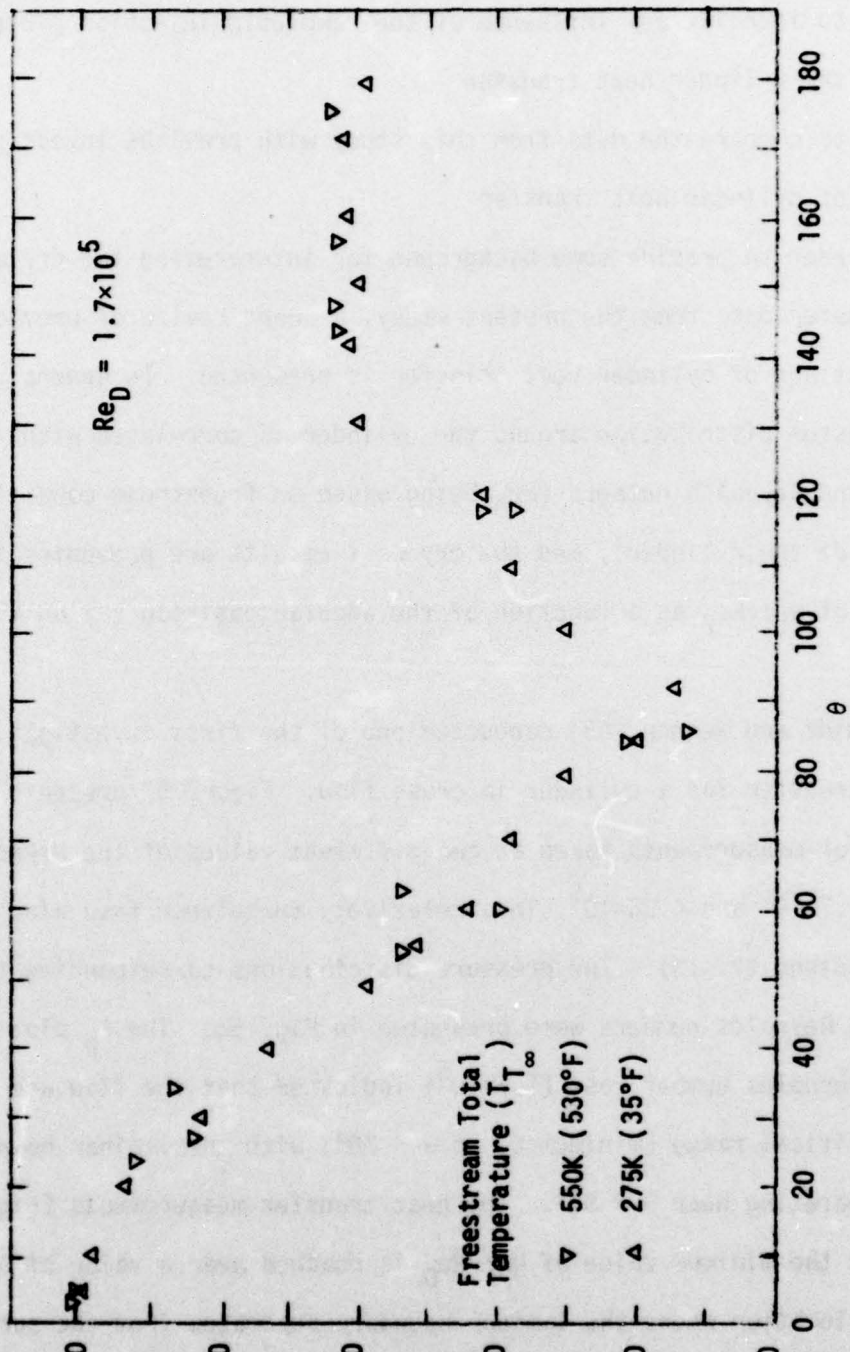

Figure 56. The Pressure Distribution for the Test Cylinder in Cross Flow

1) to check the calibration of the heat flux gages

2) to identify any influence of the removable injection plate on the cylinder heat transfer

3) to compare the data from this study with previous investigations of cylinder heat transfer

In order to provide some background for interpreting the dry wall heat transfer data from the present study, a short review of previous investigations of cylinder heat transfer is presented. In general, the heat transfer distribution around the cylinder is correlated with the Nusselt and Reynolds numbers (Re_D being based on freestream conditions upstream of the cylinder), and the dry wall results are presented in the form of $Nu/\sqrt{Re_D}$ as a function of the angular position (θ) on the cylinder.

Schmidt and Wenner [45] conducted one of the first investigations of heat transfer for a cylinder in cross-flow. Figure 57 presents their results for measurements taken at two different values of the Reynolds number, 1.7×10^5 and 4.26×10^5, in a relatively turbulence free wind tunnel (intensity <1%). The pressure distributions corresponding to these two Reynolds numbers were presented in Fig. 53. The C_p plot for the low Reynolds number case (1.7×10^5) indicated that the flow was in the subcritical range (minimum C_p at $\theta \sim 70°$) with the laminar boundary layer separating near $\theta \sim 80°$. The heat transfer measurements (Fig. 57) show that the minimum value of $Nu/\sqrt{Re_D}$ is reached near a value of $\theta = 80°$, the same location where the laminar boundary separates from the surface. For subcritical flow, the point of minimum heat transfer can be identified as the point of separation for the laminar boundary layer.

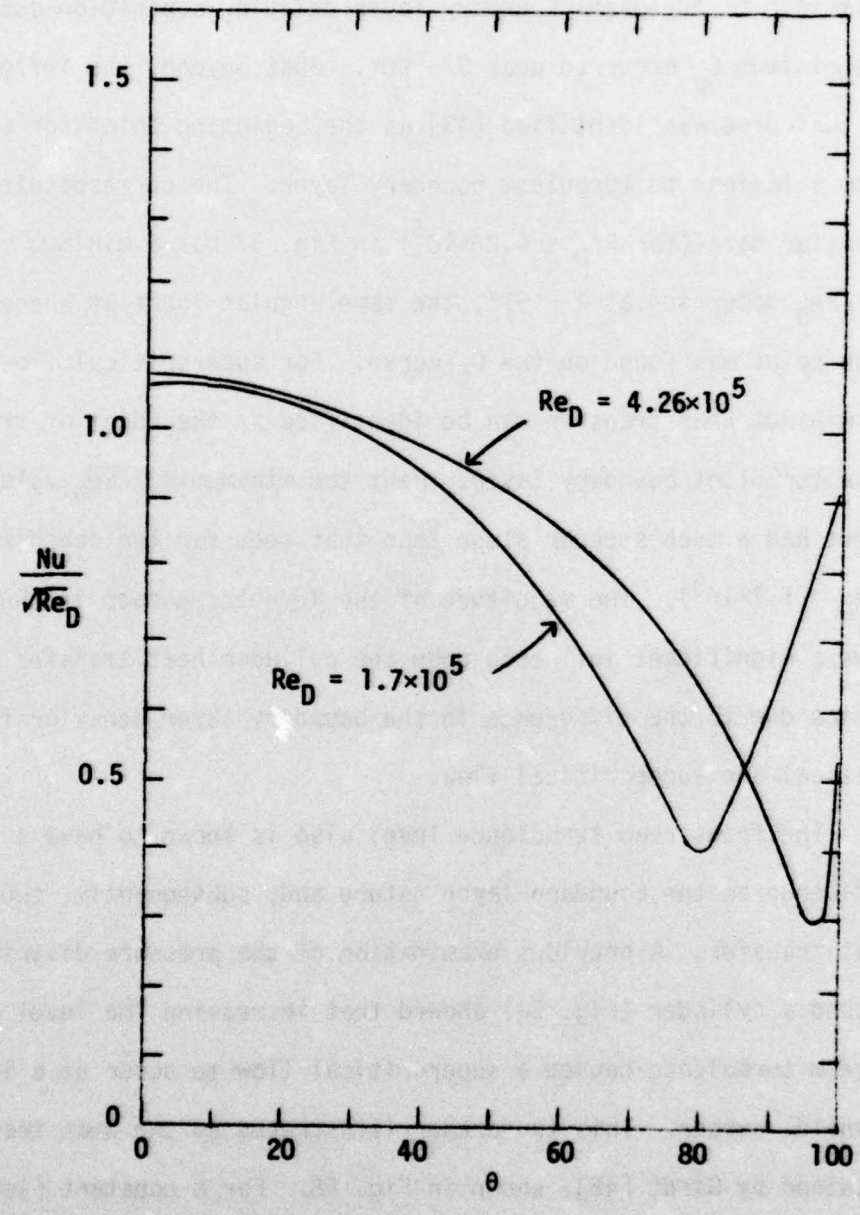

Figure 57. Heat Transfer Distribution around a Cylinder in Cross Flow (Schmidt and Wenner [45])

For the measurements taken with the higher Reynolds number (4.26×10^5), the pressure distribution (Fig. 53) exhibited the trends characteristic of flow in the supercritical range with transition from a laminar to turbulent boundary layer delaying separation such that the minimum C_p occurred near $\theta \sim 90°$. Just beyond, the inflection point in the curve was identified [43] as the beginning point for transition from a laminar to turbulent boundary layer. The corresponding heat transfer data (for $Re_D = 4.26\times10^5$) in Fig. 57 has a minimum value of $Nu/\sqrt{Re}_D$ occurring at $\theta \sim 97°$, the same angular location where the inflection point was found on the C_p curve. For supercritical flow, the point of minimum heat transfer can be identified as the point of transition to a turbulent boundary layer. Past the minimum $Nu/\sqrt{Re}_D$ value, the curve had a much steeper slope than that seen for the subcritical flow ($Re_D = 1.7\times10^5$). The magnitude of the Reynolds number is thus seen to have a significant influence upon the cylinder heat transfer characteristics due to the difference in the boundary layer behavior for subcritical and supercritical flow.

The freestream turbulence level also is known to have a substantial influence on the boundary layer nature and, subsequently, the cylinder heat transfer. A previous examination of the pressure distribution around a cylinder (Fig. 54) showed that increasing the level of freestream turbulence caused a supercritical flow to occur at a lower Reynolds number. This is further illustrated by the heat transfer data obtained by Giedt [46], shown in Fig. 58. For a constant (low) level of turbulence intensity, curves A and C exhibit the features of subcritical and supercritical flow, respectively. For curve A, the laminar

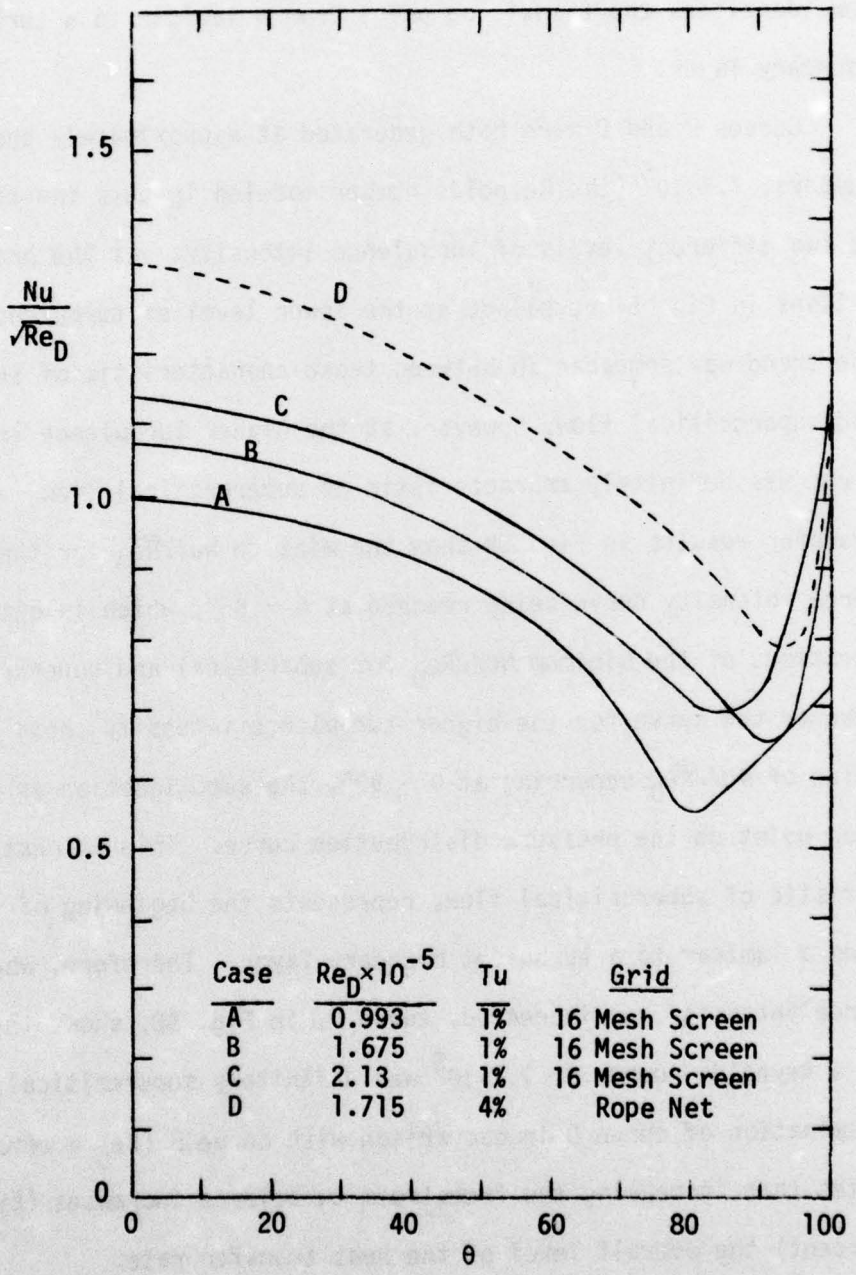

Figure 58. The Influence of Freestream Turbulence on the Heat Transfer Distribution around a Cylinder in Cross Flow (Giedt [46])

boundary layer separation is identified at the minimum heat transfer point, near 80°. For curve C, the minimum heat transfer point, near 92°, now identifies the transition point from a laminar to a turbulent boundary layer.

Curves B and D were both generated at approximately the same Reynolds numbers, 1.7×10^5 (the Reynolds number modeled in this investigation), but at two different levels of turbulence intensity. As the pressure distributions in Fig. 54 revealed, at the lower level of turbulence intensity the trend was somewhat in between those characteristic of subcritical and supercritical flow, however, at the higher turbulence level, the trend was definitely characteristic of supercritical flow. The heat transfer results in Fig. 58 show the minimum $Nu/\sqrt{Re}_D$ for the low turbulence intensity curve being reached at $\theta \sim 85°$, which is between the locations of the minimum $Nu/\sqrt{Re}_D$ for subcritical and supercritical flow. However the curve for the higher turbulence intensity shows the minimum value of $Nu/\sqrt{Re}_D$ occurring at $\theta \sim 93°$, the same location as the inflection point on the pressure distribution curve. This θ location, characteristic of supercritical flow, represents the beginning of transition from a laminar to a turbulent boundary layer. Therefore, when the turbulence intensity was increased, curve D, in Fig. 58, shows that the flow at a Reynolds number of 1.7×10^5 was definitely supercritical. Further examination of curve D in comparison with curve B ($Re_D \approx$ constant) indicates that increasing the freestream turbulence increases (by 20 to 30 percent) the overall level of the heat transfer rate.

Seban [47] has obtained similar heat transfer results as shown in Fig. 59 with the corresponding pressure distributions shown previously

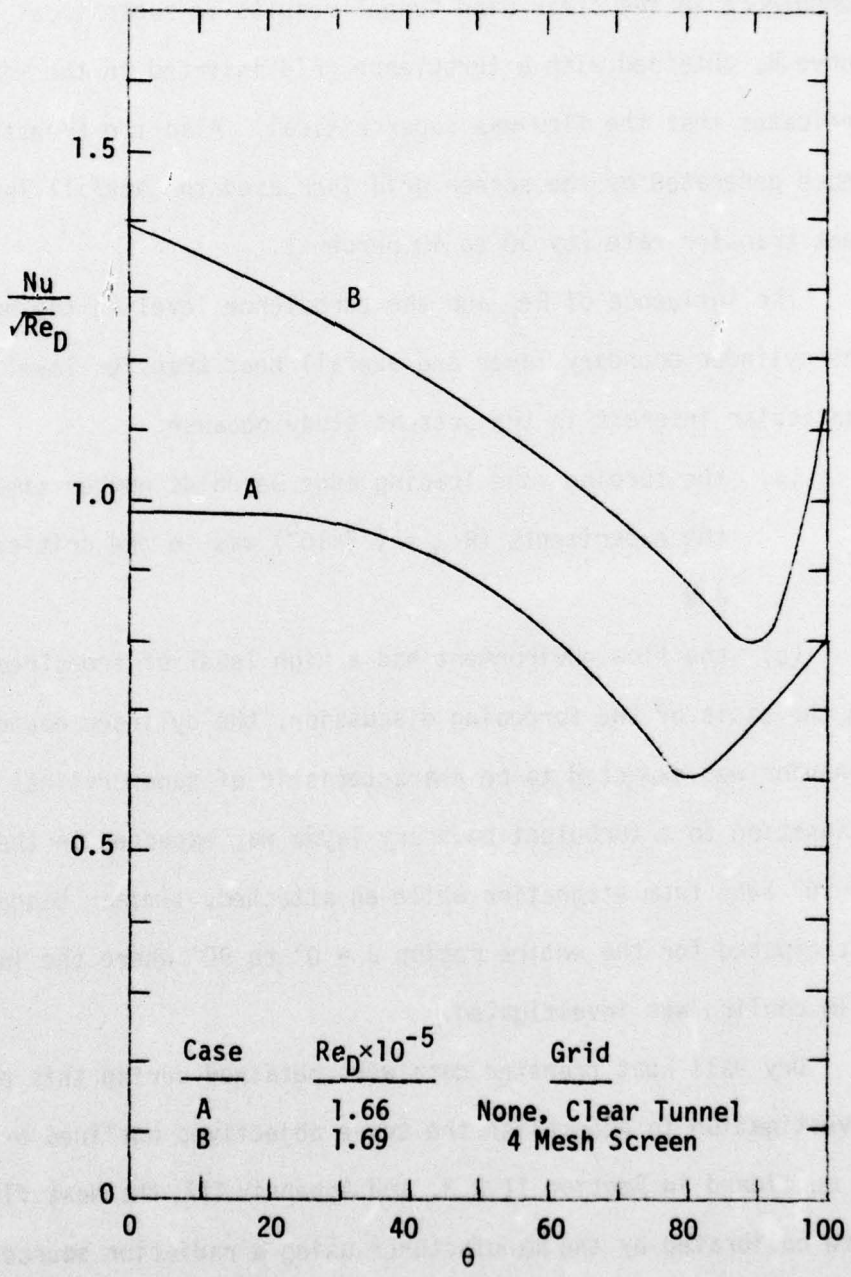

Figure 59. The Influence of Freestream Turbulence on the Heat Transfer Distribution around a Cylinder in Cross Flow (Seban [47])

in Fig. 55. For a Reynolds number that is near the critical value (1.7×10^5), curve A (Fig. 59) shows chat the low level of freestream turbulence in the clear wind tunnel results in subcritical flow, while curve B, obtained with a turbulence grid inserted in the wind tunnel, indicates that the flow was supercritical. Also the freestream turbulence generated by the screen grid increased the overall level of the heat transfer rate (by 30 to 40 percent).

The influence of Re_D and the turbulence level on the behavior of the cylinder boundary layer and overall heat transfer level was of particular interest in the present study because:

(a) the turbine vane leading edge Reynolds number simulated in the experiments ($Re_D = 1.7\times10^5$) was in the critical range, and

(b) the flow environment had a high level of freestream turbulence.

On the basis of the foregoing discussion, the cylinder boundary layer behavior was expected to be characteristic of supercritical flow. Transition to a turbulent boundary layer was expected in the neighborhood of 90° away from stagnation while an attached, laminar boundary layer was anticipated for the entire region θ = 0° to 90° where the influence of film cooling was investigated.

Dry wall heat transfer data were obtained during this phase of the investigation to accomplish the three objectives outlined previously. As mentioned in Section II.B.3. and Appendix III, the heat flux gages were calibrated by the manufacturer using a radiation source. It was desired to check the validity of the calibration curves and to establish a standard heat transfer condition to permit a periodic check of the

performance of each gage during the course of the investigation.† Figure 60 presents the dry wall heat transfer results for three heat flux gages, #0, #1, and #4. Figure 61 shows how the gage identification number corresponds to the heat flux gage location on the cylinder surface. The ability to rotate the cylinder allowed the heat flux gages to be positioned at any angular position (θ) from the stagnation point. To check the calibration of the gages, the cylinder was rotated around so that the removable injection plate was downstream of the heat flux gages, thereby eliminating any influence of the plate on the heat transfer rate measured by the gages. As Fig. 60 reveals, the data from all three gages were reproducible, confirming the calibration of the gages. A smooth curve was fared through the data to establish a standard heat transfer condition with which to check the dry wall heat transfer data generated during the course of this investigation. The data are seen to fall in a band (± 11%) about the standard curve.

The dry wall heat transfer results from Gage #2 (see Fig. 62), fell far below the standard curve shown in Fig. 60, indicating an error in the calibration curve for Gage #2. However, a shift of the standard heat transfer curve down 0.25 units ($Nu/\sqrt{Re_D}$ units) shows that the shifted curve (— - —) and standard data band provide a good representation of the data for Gage #2. It was concluded that a zero shift for Gage #2 (and/or its amplifier) caused the consistently low results. Therefore,

† This periodic check was conducted, however no change in gage sensitivity due to surface erosion or oxidation was observed in this study which is in contrast to that reported in Ref. [48].

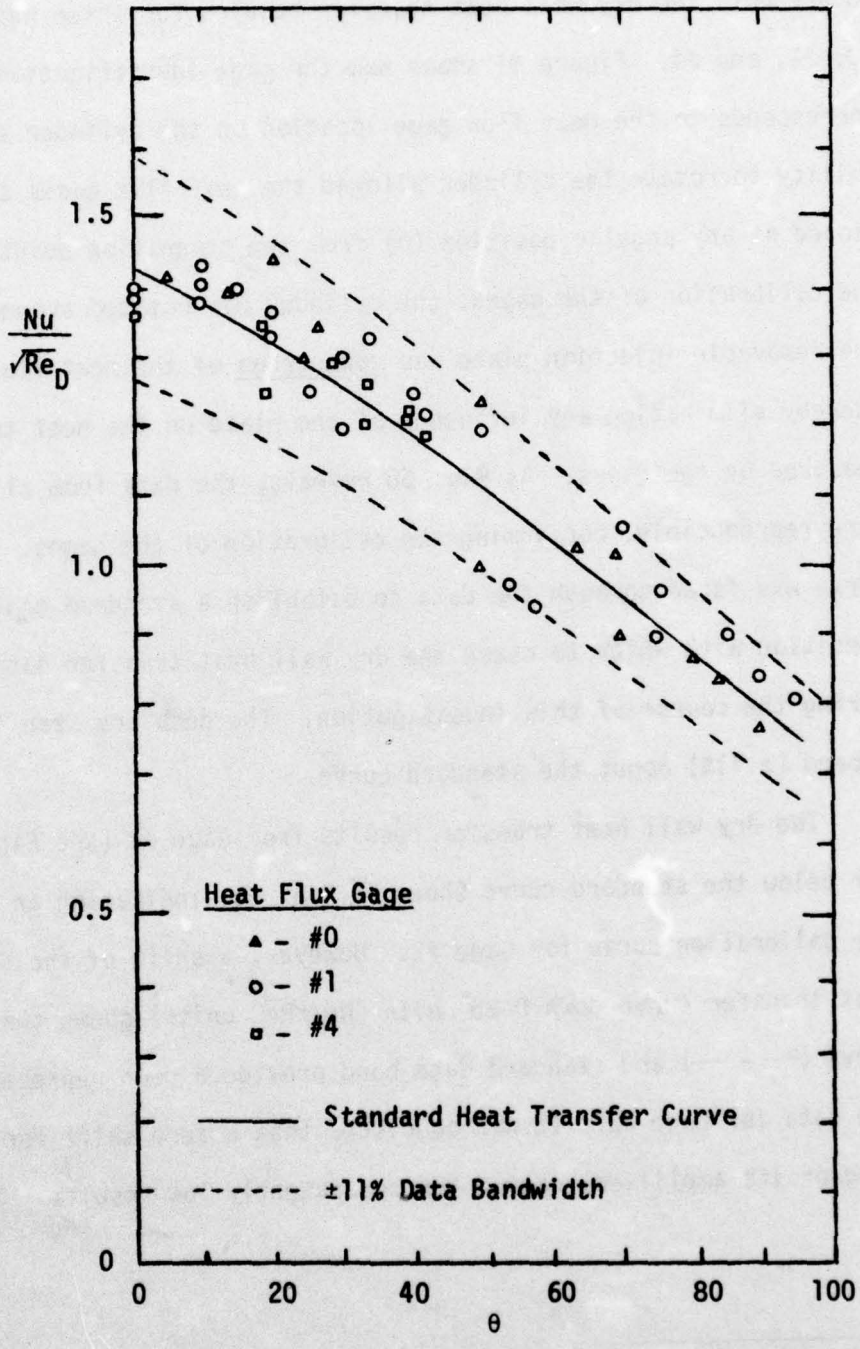

Figure 60. Dry Wall Heat Transfer Data along a Smooth Test Cylinder (Injection Plate Downstream, Gages #0, 1, 4)

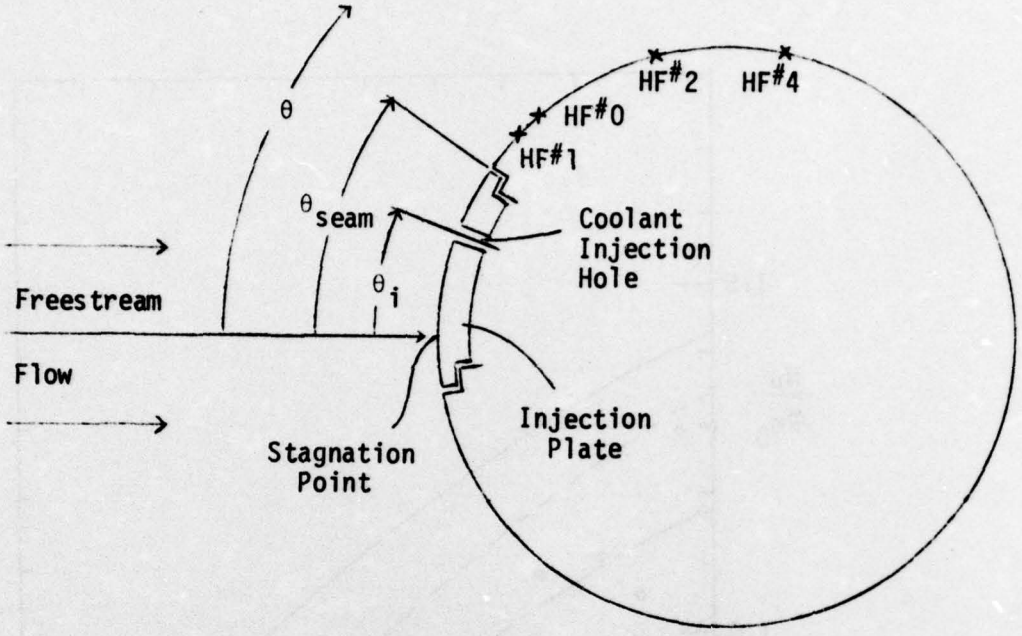

(a) Injection Plate Upstream of Heat Flux Gages

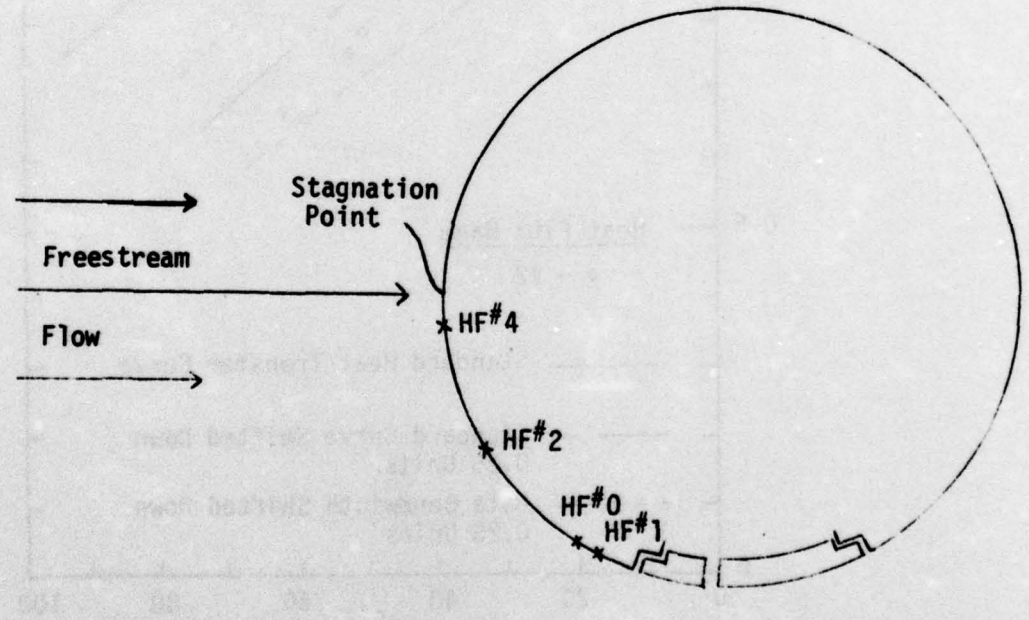

(b) Injection Plate Downstream of Heat Flux Gages

Figure 61. The Correspondence between Heat Flux Gage Identification Numbers and Angular Position on the Cylinder

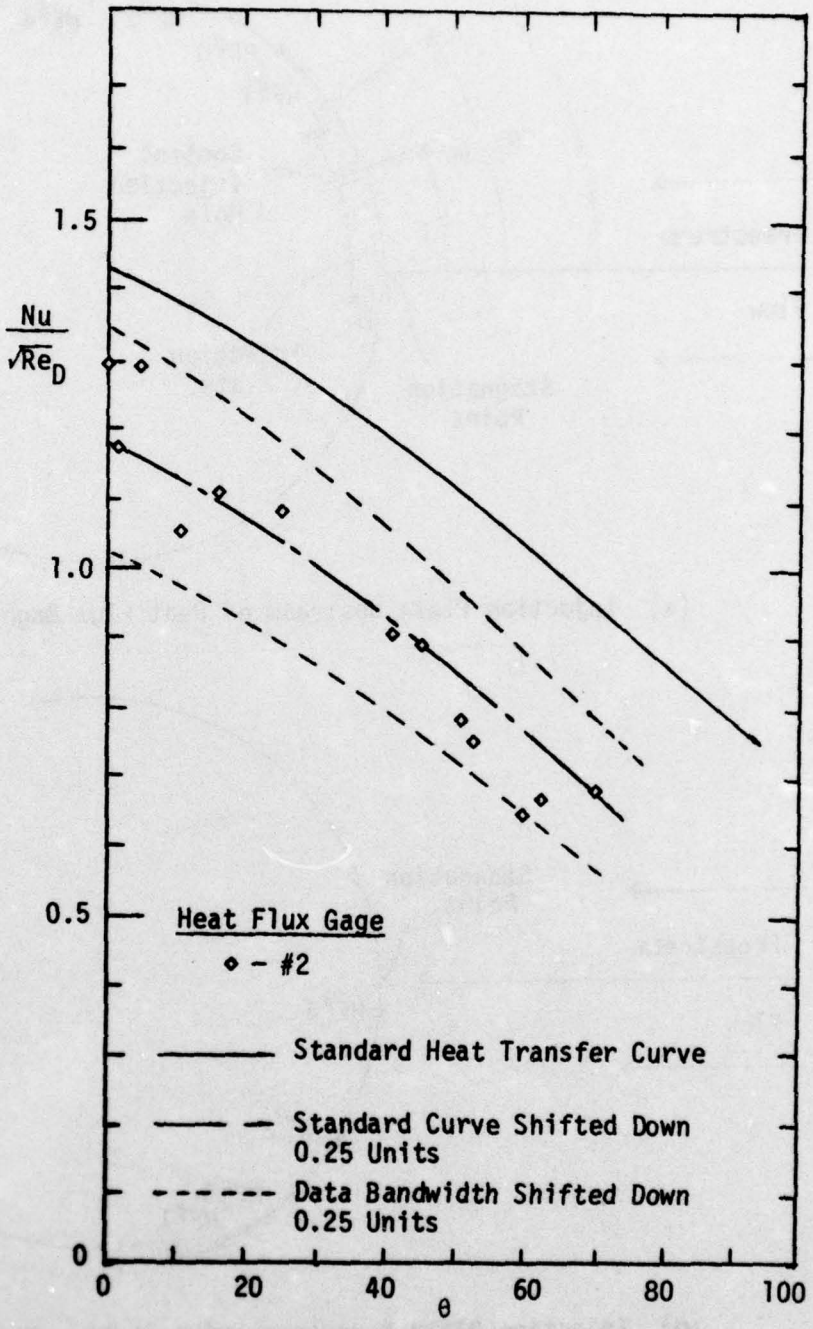

Figure 62. Dry Wall Heat Transfer Data along a Smooth Test Cylinder (Injection Plate Downstream, Gage #2)

throughout the rest of the study, the results for $Nu/\sqrt{Re_D}$ from Gage #2 have been increased by 0.25 units to compensate for the erroneous calibration curve.

It will be recalled that the test cylinder was designed with a removable film coolant injection plate (see Section II.B.2.) in order to permit investigation of a wide range of coolant injection geometry parameters. However, the necessity of a removable plate resulted in a juncture (or seam) where the injection plate was sealed to the cylinder surface, the seam being located immediately downstream from the row of film coolant holes and upstream from the heat flux gages. Although each injection plate was hand rubbed to minimize the surface roughness presented by the injection plate seam, it was of interest to determine what influence this seam had on the heat flux measured by the gages downstream.

To accomplish this, dry wall heat transfer data were collected with the injection plate positioned upstream from the heat flux gages (see Fig. 61) and then data were collected with the cylinder rotated so that the plate was downstream from the heat flux gages. In both cases, a smooth injection plate (i.e. no coolant holes) was used. A third series of experiments were conducted with coolant holes drilled in the injection plate (but no coolant flow), and with the plate positioned upstream from the heat flux gages to examine the influence of the holes. The ability to rotate the cylinder allowed the heat flux gages to be positioned at any angular location (θ) from stagnation. Therefore, as was shown in Fig. 60, data were obtained for each heat flux gage as a function of θ by rotating the cylinder to a new position before each experimental run. Figure 63 shows a schematic diagram of the cylindrical surface and the

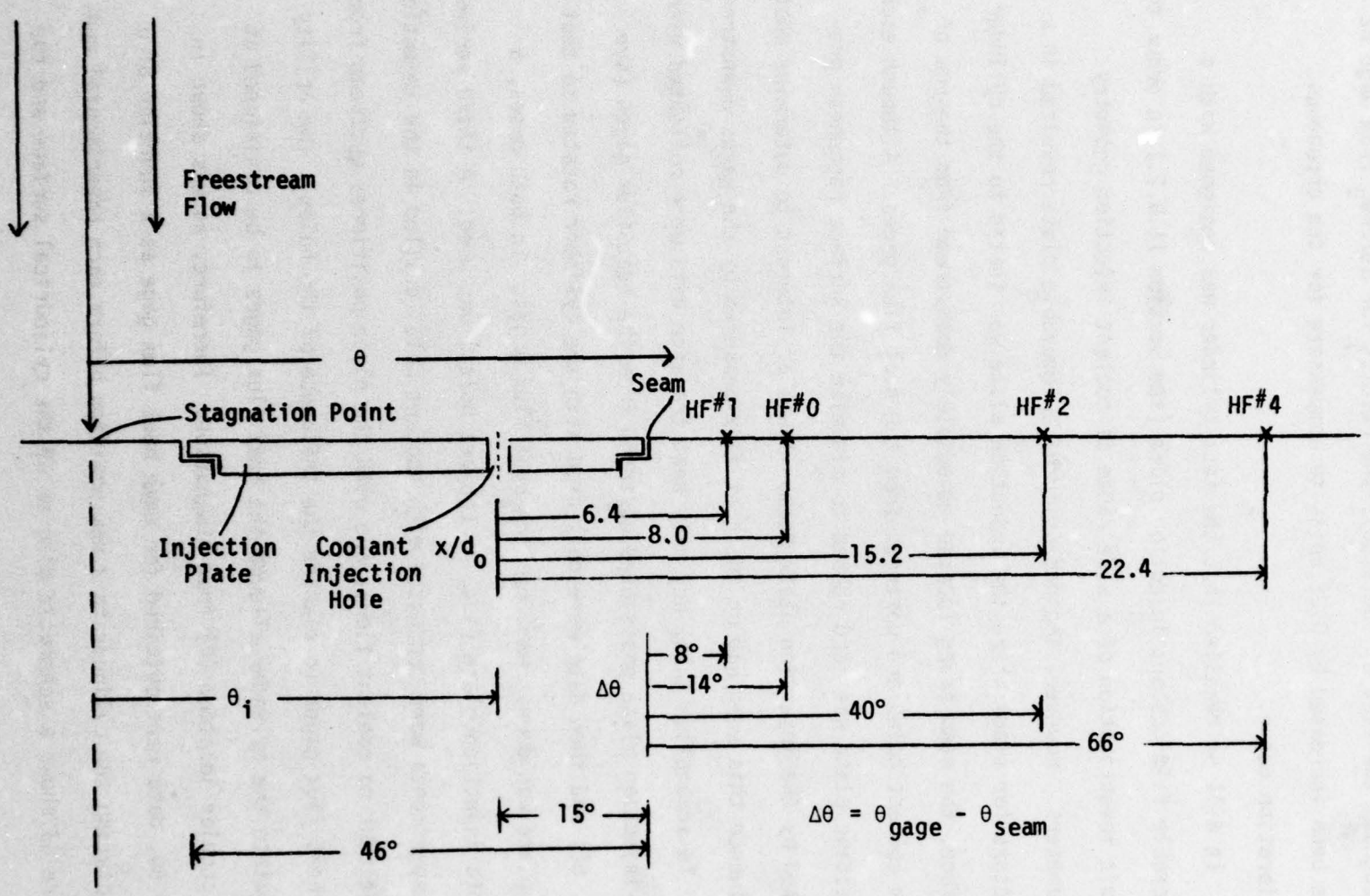

Figure 63. Angular Location of the Heat Flux Gages Relative to the Coolant Holes and the Plate-Cylinder Seam

location of each heat flux gage in relation to the stagnation point, the row of injection holes, and the injection plate-cylinder seam. Each gage was positioned a different distance downstream from the injection plate seam with the position labeled $\Delta\theta(\theta_{gage}-\theta_{seam})$. The dry wall data are presented in the form of $Nu/\sqrt{Re_D}$ versus the angular position from stagnation (θ) for each gage, since each is a different distance downstream from the seam. On the figures, the standard heat transfer curve including the data scatter band from Fig. 60 is included to show the results for a smooth cylinder with the injection plate downstream.

Figure 64 presents the results for Gage #4 ($\Delta\theta = 66°$), the gage positioned farthest from the seam. The data for all three cases investigated are accurately represented by the standard curve for θ in the range of 0° to 95°; thus indicating that there was no discernable effect of the presence of the seam when it occurred in the range of 0° to 29° (i.e. $\theta_{seam} = \theta_{gage} - \Delta\theta = 95° - 66° = 29°$). The data for Gage #4 in the range of $\theta = 95°$ to 120°, with the plate upstream, are represented by the — · — curve, which appears as a logical extension of the standard curve. The results of Giedt [46] from Fig. 58 ($Re_D = 1.715\times10^5$), shown by the — - — curve in Fig. 64, are seen to be in good agreement with the "extended standard curve" (——— + — · —). The only difference is in the value of θ where the minimum $Nu/\sqrt{Re_D}$ occurs. While Giedt [46] shows the minimum near the location of $\theta \approx 90°$, the present investigation observed the minimum near $\theta \approx 100°$. This effect is attributed to tunnel blockage due to the use of a 5.08cm (2 in.) diameter cylinder in a 20.32cm (8 in.) high wind tunnel. The increased acceleration of the freestream near $\theta \approx 90°$ could have delayed the onset of boundary

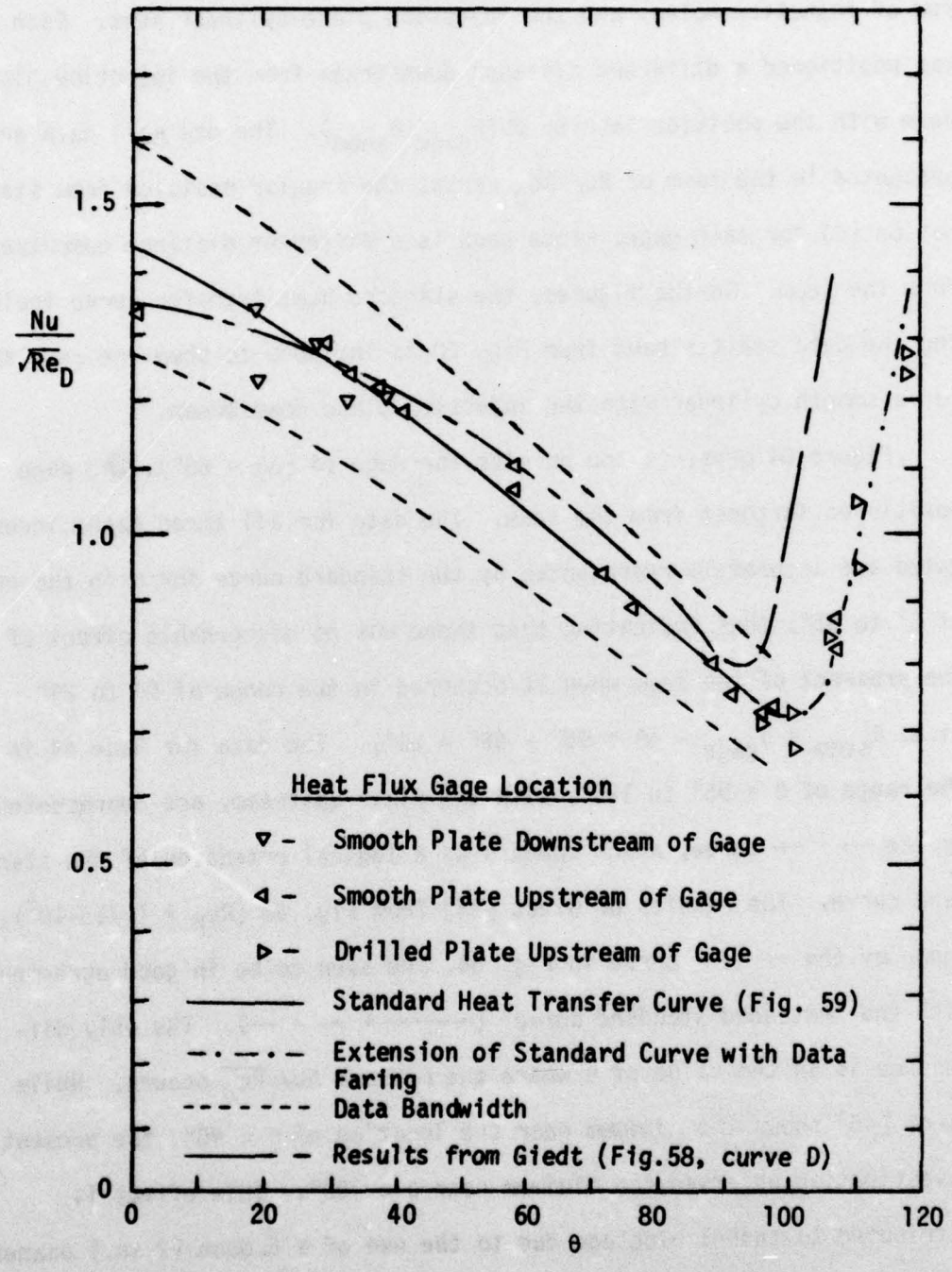

Figure 64. Dry Wall Heat Transfer Distribution around the Test Cylinder as Measured by Gage #4 ($\Delta\theta = 66°$)

layer transition until near $\theta \approx 100°$. Figure 65 shows the local freestream velocity distribution calculated from potential flow for a cylinder in an infinite freestream and a cylinder in a finite tunnel representative of the present investigation. At the location $\theta = 90°$, the local freestream velocity in the finite tunnel was 5% greater than that computed for an infinite freestream. Thus, it is concluded that the increased freestream acceleration delayed the boundary layer transition until $\theta \approx 100°$. Besides this discrepancy, the results of Giedt [46] and the present investigation for Gage #4 were in excellent agreement. Therefore, while no data were obtained for the smooth cylinder with Gage #4 in the range of 95° to 120°, it was concluded that there was no discernable effect of the presence of the upstream seam on the data for Gage #4. The "extended standard curve" is presented for comparison in the remaining dry wall heat transfer figures.

For Gage #2, which is closer to the seam ($\Delta\theta = 40°$), the results for the three cases investigated are shown in Fig. 66. The data for the smooth cylinder (i.e. plate downstream of gage), the data are in good agreement with the standard curve from Figs. 60 and 64. However, with the plate upstream of the gage, the data are higher than the standard curve for $\theta \gtrsim 85°$. Therefore, the presence of the seam appears to have affected the value of $Nu/\sqrt{Re}_D$ near the transition point.

Figure 67 presents similar results for Gage #0 which is even closer to the seam ($\Delta\theta = 14°$). Again, the data for the smooth cylinder (i.e. plate downstream of the gage) is accurately represented by the standard curve. The data for the plate upstream agree with the standard curve (within the ± 11% band) for $\theta \lesssim 45°$. Reference to Fig. 63 shows that

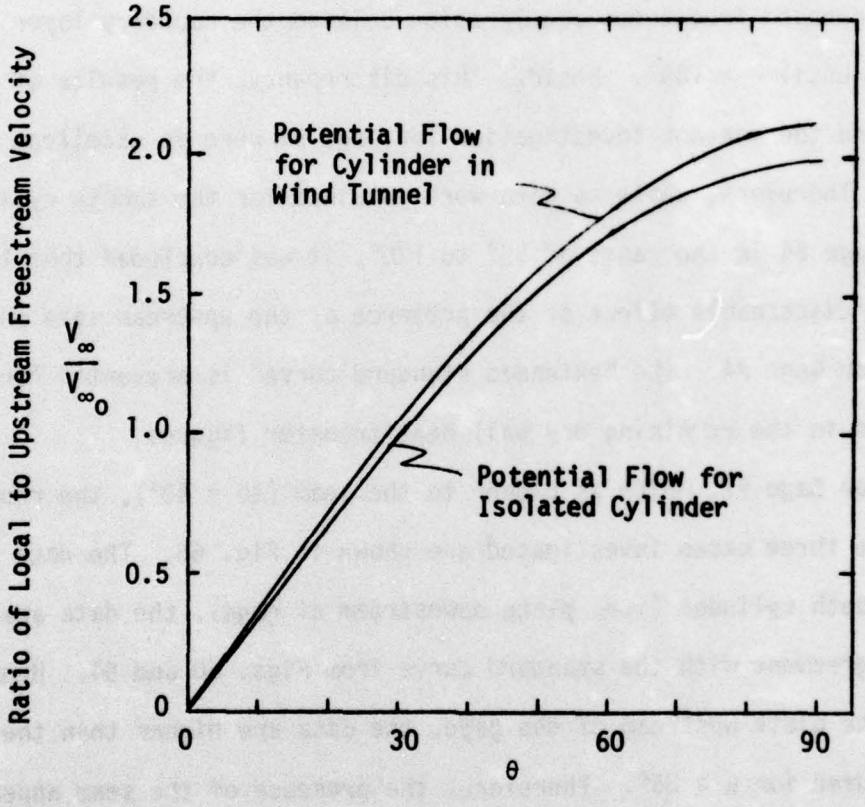

Figure 65. Local Freestream Velocity Distribution With and Without Flow Blockage

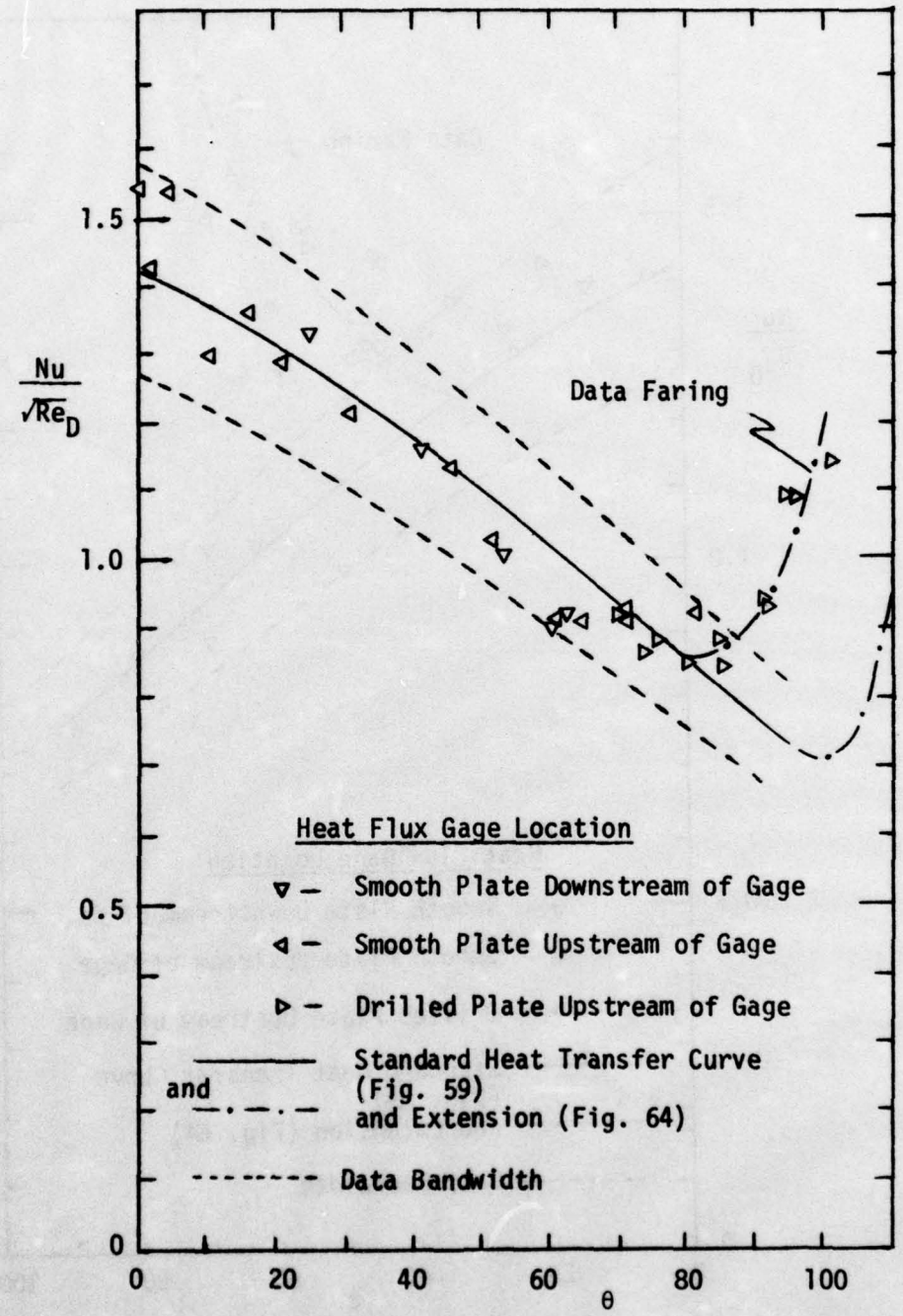

Figure 66. Dry Wall Heat Transfer Distribution around the Test Cylinder as Measured by Gage #2 ($\Delta\theta = 40°$)

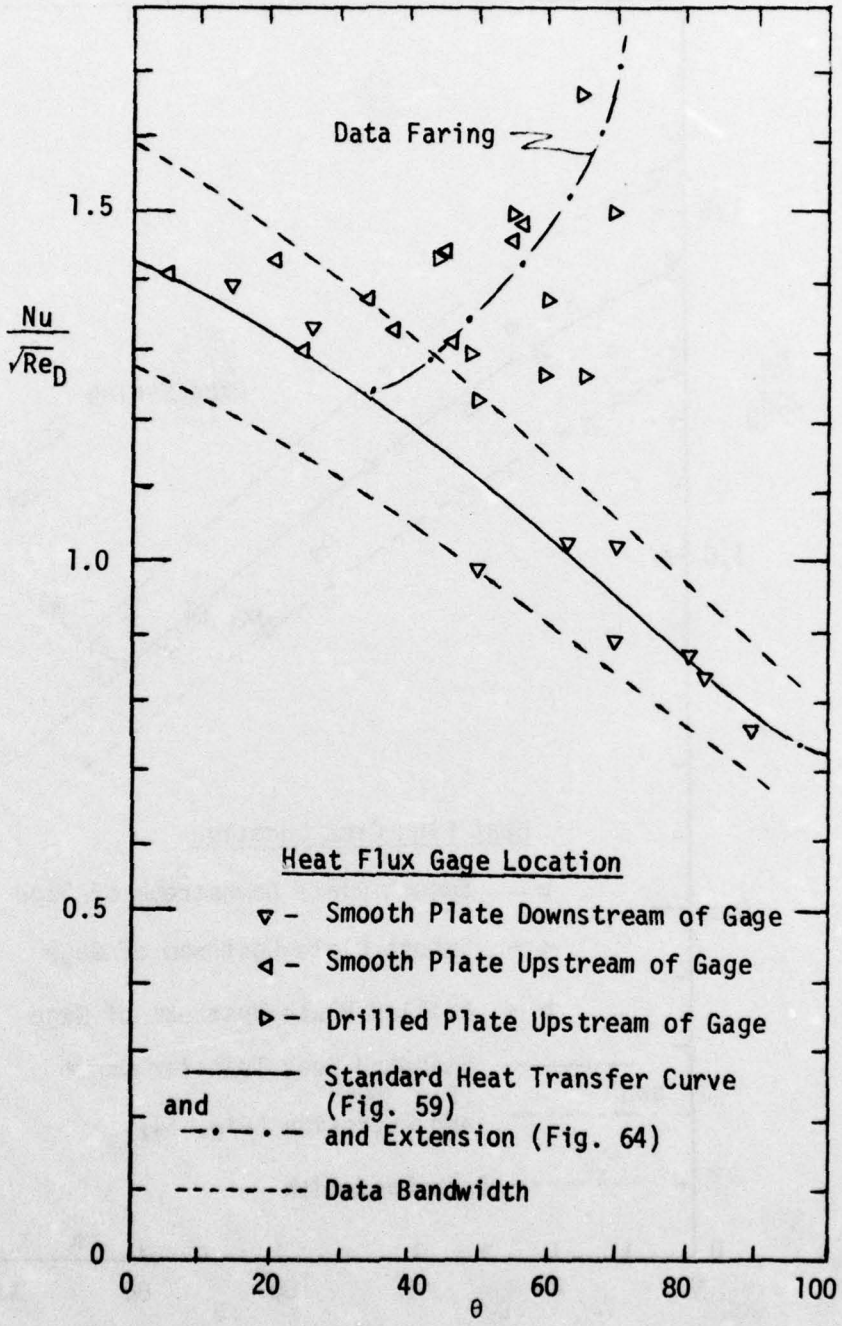

Figure 67. Dry Wall Heat Transfer Distribution around the Test Cylinder as Measured by Gage #0 ($\Delta\theta$ = 14°)

this corresponds to θ_{seam} in the range of 0 to 31°. However, for values of $\theta \gtrsim 45°$ ($\theta_{seam} \gtrsim 31°$), the data for the plate upstream of the gage (◁,▷) were substantially higher than the standard curve. Therefore, the presence of the seam caused a significant increase in the heat transfer rate measured by Gage #0 when the gage was moved past 45° or the seam location was moved past 31°. For $\theta_{seam} \lesssim 31°$, the seam does not appear to create a sufficient disturbance to cause the heat transfer to increase above the level found for a smooth cylinder. As to be expected, there is some scatter of the data (for the plate upstream) as the heat transfer rate increased with θ, since the boundary layer is very sensitive to the size of the surface disturbance.

Figure 68 presents the results for the gage closest to the seam, Gage #1 ($\Delta\theta = 8°$). The data show that up to $\theta \lesssim 40°$, all of the data fall within the data bandwidth for the standard heat transfer curve, indicating no effect of the presence of the seam upstream of the gage. For values of $\theta \gtrsim 40°$, the data for the plate upstream of the gage (◁,▷) increased sharply as θ was increased. Therefore, the influence of the seam on the heat transfer rate for Gage #1 was first observed at $\theta \approx 40°$, corresponding to a seam θ location of 32°. This is in close agreement with the seam location for Gage #0 where the heat transfer rate began to deviate from the standard curve. It is apparent that up to $\theta \approx 31°$, the seam had a negligible effect on the surface heat transfer rate, but moving the seam past $\theta = 31°$ caused a disturbance in the flow that definitely affected the downstream heat transfer.

To better isolate the dependence of this disturbance on the angular location of the seam, the dry wall data were replotted to present results

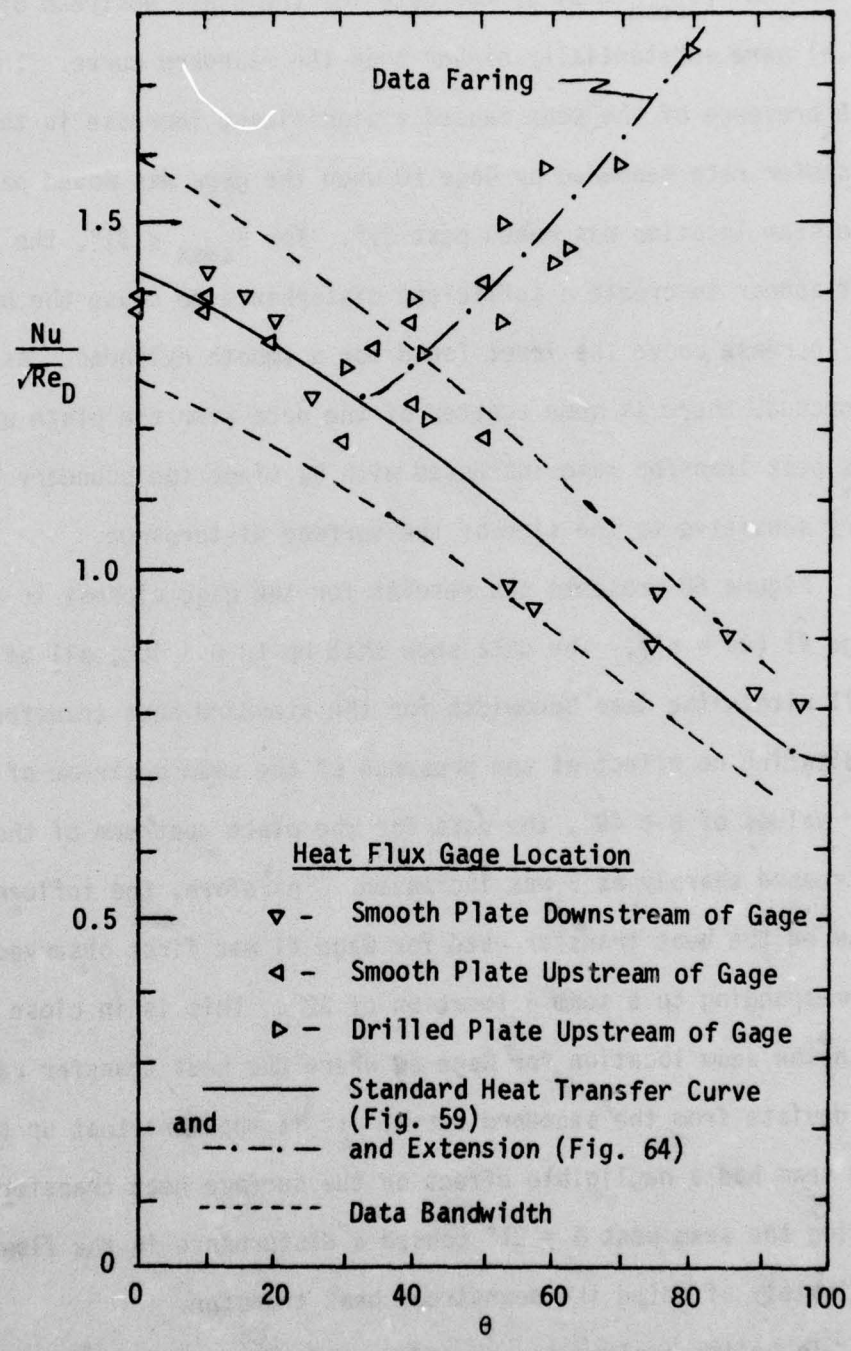

Figure 68. Dry Wall Heat Transfer Distribution around the Test Cylinder as Measured by Gage #1 ($\Delta\theta = 8°$)

for four different seam locations, θ_{seam} = 25°, 35°, 45°, and 55° (corresponding to the injection hole locations of θ_i = 10°, 20°, 30°, and 40°). The last three values of θ_i were the row locations investigated during the film cooling phase of this investigation. For each seam location, the corresponding values of $Nu/\sqrt{Re}_D$ for the four downstream gages were plotted as shown in Fig. 69(a). The values were obtained from the smooth curves fared through the data for each gage in Figs. 66 through 68. The standard heat transfer curve (obtained from Figs. 60 and 64) is also shown on each plot to provide a basis for comparison. Recalling the results from the individual heat flux gage plots of the $Nu/\sqrt{Re}_D$ distribution, the influence of the seam was not observed until the value of θ_{seam} had increased past ~31°. Figure 69(a), with the seam at θ = 25°, shows that all four heat flux gages have $Nu/\sqrt{Re}_D$ values close to the standard heat transfer curve. However, when the seam was moved to 35°, the results in Fig. 69(b) reveal that the heat transfer rate indicated by Gages #1 and 0 was significantly higher than the standard heat transfer curve while the data from Gage #2 agreed with the standard curve. The dashed line in Fig. 69(b) represents the probable heat transfer distribution defined by the points for Gages #0 and #1. Apparently the disturbance created by the seam at θ_{seam} = 35° caused the laminar boundary layer to begin a transition to a turbulent boundary layer. However, the acceleration of the freestream along the cylinder was apparently sufficient to return the boundary layer to a laminar form, with the data for Gage #2 in good agreement with the standard heat transfer curve.

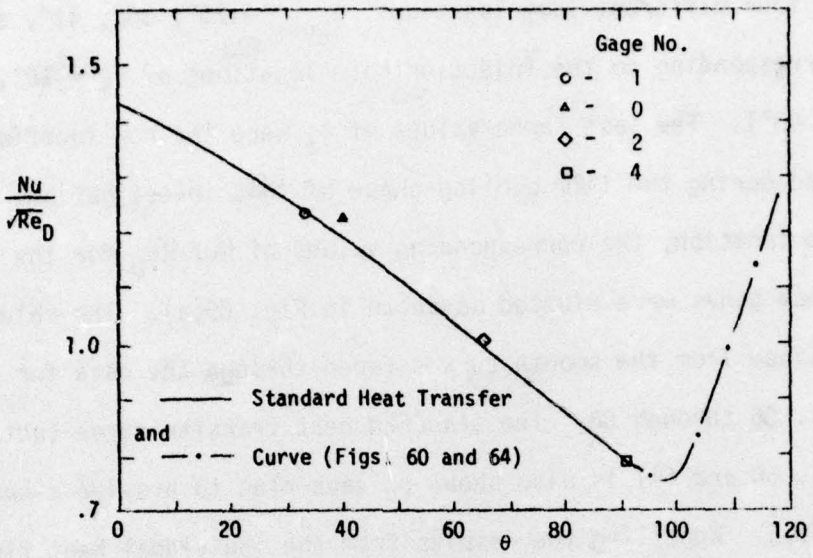

(a) Θ_i=10°, Θ_{seam}=25°

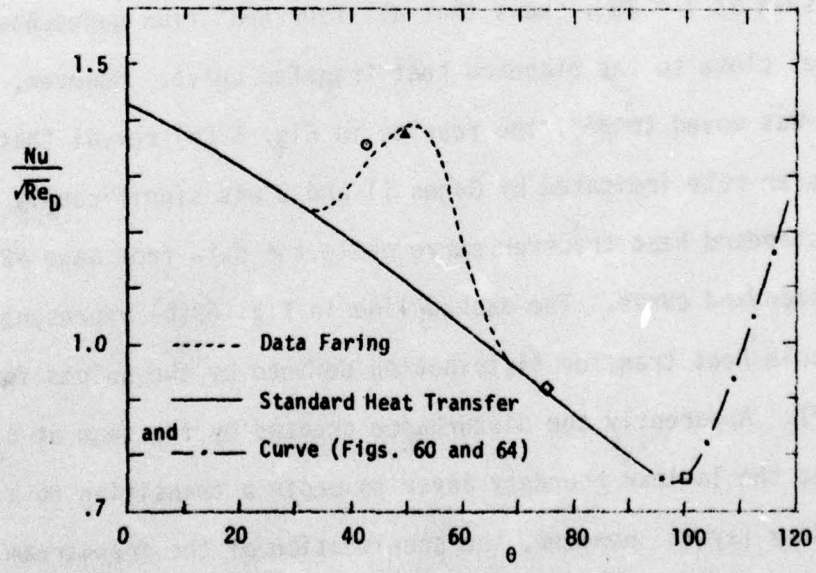

(b) Θ_i=20°, Θ_{seam}=35°

Figure 69. The Influence of the Cylinder-Injection Plate Seam on the Downstream Heat Transfer

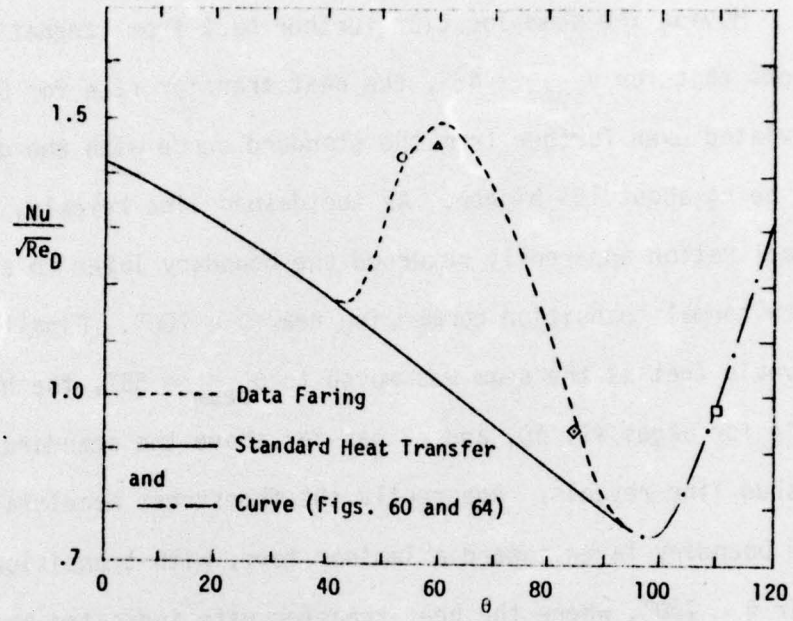

(c) $\Theta_i = 30°$, $\Theta_{seam} = 45°$

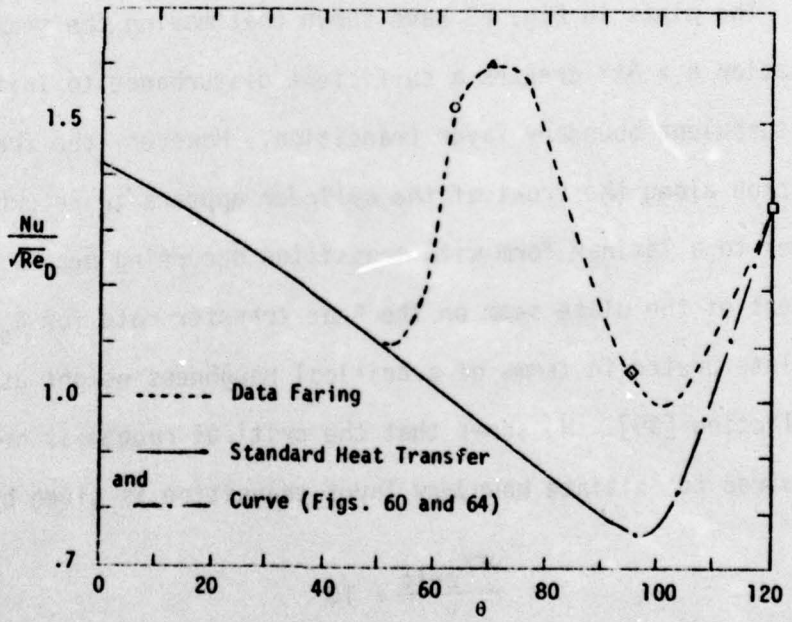

(d) $\Theta_i = 40°$, $\Theta_{seam} = 55°$

Figure 69 (cont'd). The Influence of the Cylinder-Injection Plate Seam on the Downstream Heat Transfer

Moving the seam location further back from stagnation, Fig. 69(c) shows that for $\theta_{seam} = 45°$, the heat transfer rate for Gages #0 and #1 deviated even farther from the standard curve with the data from Gage #2 being about 15% higher. As the dashed line reveals, the freestream acceleration apparently returned the boundary layer to a laminar form with normal transition commencing near $\theta \approx 100°$. Finally, Fig. 69(d) reveals that as the seam was moved to $\theta_{seam} = 55°$, the heat transfer rate for Gages #1, #0, and #2 was far above the standard curve as the dashed line reveals. Apparently the freestream acceleration returned the boundary layer toward a laminar form, with transition occurring near $\theta \approx 100°$, where the heat transfer rate indicated by Gage #2 was about 40% above the standard curve.

The plots in Fig. 69 have shown that moving the seam past the location $\theta \approx 31°$ creates a sufficient disturbance to initiate a laminar to turbulent boundary layer transition. However, the freestream acceleration along the front of the cylinder appears to return the boundary layer to a laminar form with transition occurring near $\theta \approx 100°$. The effect of the plate seam on the heat transfer rate for $\theta_{seam} \gtrsim 31°$ can be interpreted in terms of a critical roughness height as discussed by Schlicting [39]. He shows that the critical roughness height (K_{crit}) required to initiate boundary layer transition is given by

$$\frac{v^* K_{crit}}{\nu} = 15 \tag{39}$$

where

$$v^* = \frac{\tau_w}{\rho}$$

To estimate the effective roughness height of the injection plate seam, the shear stress at the wall of a cylinder for a laminar boundary layer† was used to determine τ_w vs. θ from which the value of K_{crit} was estimated. For $\theta = 30°$, a value of $K_{crit} = 0.0025$ in. would be required to initiate transition, while for $\theta = 10°$, $K_{crit} = 0.0043$ in. It can be concluded that the effective roughness of the seam was ≤ 0.0025 in.

The final objective of this phase of the investigation was to compare the data from this study with previous investigations of cylinder heat transfer. Figure 70 shows the data of Giedt [46] and Seban [47] for a high turbulence level plotted for comparison with the standard heat transfer curve for the smooth cylinder (from Figs. 60 and 64) obtained in the present study. As the figure shows, the standard curve of the present study is in good agreement with the previous investigations. The only discrepancy is in the value of θ where the minimum $Nu/\sqrt{Re_D}$ occurs. While Giedt [46] and Seban [47] show the minimum near the location of $\theta \approx 90°$, the present investigation observed the minimum near $\theta \approx 100°$. As has been discussed, this effect is attributed to the tunnel blockage due to the 5.02cm cylinder in the 20.32cm high wind tunnel. It is expected that increased acceleration of the freestream near $\theta \approx 90°$, shown previously in Fig. 65, delayed boundary layer transition until $\theta \approx 100°$, however for the range $0 \leq \theta \leq 90°$, the dry wall results from the present investigation are in excellent agreement with the results of previous investigations.

---

† presented in Figure 9.7 [39].

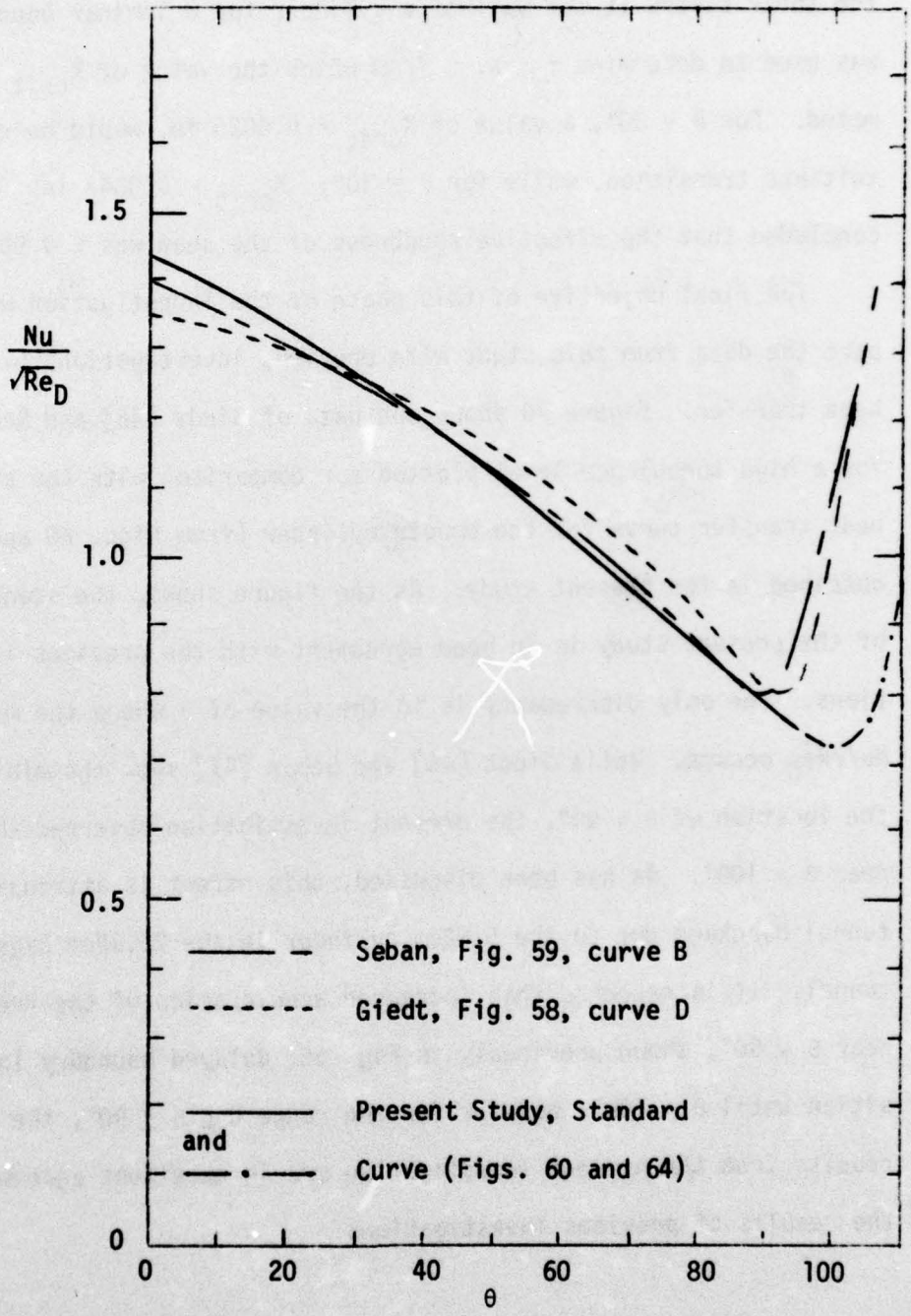

Figure 70. Comparison of Dry Wall Heat Transfer Results

III.C. Film Cooling Results

The third phase of the investigation involved a study of film cooling using a single row of spanwise angled holes. The data to be presented in this section are discussed only in a qualitative fashion with the analysis of the data being presented in the following section. As previously explained, this study was conducted to model the leading edge of a turbine vane using the stagnation region of a cylinder in cross flow. Therefore all data presented represent local heat flux measurements obtained on the test cylinder in the range of 0 to 90° from the stagnation line. The major objective of the study was to determine the influence of the injection angle, β, the row location, θ_i, and the coolant blowing ratio, M, on the film cooling performance at various downstream and spanwise locations.

Table 4 outlines the range of parameters investigated. The row location relative to stagnation, θ_i, was investigated at three different values, 20°, 30°, and 40°. Likewise three different values of injection angle, β, were investigated, 25°, 35°, and 45°. Also the film cooling performance was measured at three different downstream distances (x/d_o), and at each of the downstream distances, the performance was measured at the three different spanwise locations (z/s) as listed in Table 4.

While the coolant injection parameters were varied during the investigation, the freestream conditions were held constant. As Table 2 in Section II.C. showed, a freestream Reynolds number of 1.7×10^5 and a freestream-to-wall temperature ratio of 2.1, both representative of a gas turbine environment, were maintained throughout the investigation. The coolant blowing ratio, M, which provides an indication of the

Table 4 Summary of Film Cooling Configurations

Case No.	I			II			III			IV			V			VI			VII		
Injection Angle, β	25°			25°			25°			35°			35°			35°			45°		
Injection Angle from Stagnation, θ_i †	40°			30°			20°			40°			30°			20°			40°		
Distance Downstream, x/d_o	6.4	8.0	15.2	6.4	8.0	15.2	6.4	8.0	15.2	6.4	8.0	15.2	6.4	8.0	15.2	6.4	8.0	15.2	6.4	8.0	15.2
	Spanwise Distance, z/s																				
	0.00	0.00	0.17	0.00	0.00	0.17	0.00	0.00	0.17	0.00	0.00	0.17	0.00	0.00	0.17	0.00	0.00	0.17	0.00	0.00	0.17
	0.33	0.33	0.50	0.33	0.33	0.50	0.33	0.33	0.50	0.33	0.33	0.50	0.33	0.33	0.50	0.33	0.33	0.50	0.33	0.33	0.50
	0.67	0.67	0.83	0.67	0.67	0.83	0.67	0.67	0.83	0.67	0.67	0.83	0.67	0.67	0.83	0.67	0.67	0.83	0.67	0.67	0.83

† Data also obtained at θ_i=10° are not reported since the value of the Stanton Number Reduction did not exceed 0.05.

amount of coolant blown onto the surface, was varied throughout the investigation, and as was discussed in Section III.A.2., the variation of the coolant mass flow rate had a small influence on the temperature of the coolant emerging from the injection hole. However, Table 2 in Section II.C. shows that the coolant-to-freestream density ratio was within a ±9% bandwidth of a mean value of 2.21.

The film cooling performance data are presented in terms of the Stanton Number Reduction, which is defined as:

$$\text{Stanton Number Reduction} \equiv 1 - \frac{St_{FC}}{St_o} \tag{36}$$

As was discussed in Section II.D., the Stanton number ratio (St_{FC}/St_o) is equal to the heat transfer coefficient ratio (h_{FC}/h_o) when the wall temperature is the same with and without film cooling ($T_{w_{FC}} = T_{w_o}$).

The Stanton Number Reduction represents the fractional reduction in the Stanton number due to film cooling. Figure 71 illustrates the data typical of that obtained in the present study, showing the Stanton Number Reduction as a function of the coolant blowing ratio, M. The values of the geometric film cooling parameters (β, θ_i, x/d_o) that were held constant for these experiments are listed. Figure 71 presents the results obtained from a single heat flux gage ($x/d_o = 8.0$) for three different locations (z/s) of the gage between the holes. For each z/s location, a smooth curve was fared through the data showing the variation of the Stanton Number Reduction vs. M for the particular location on the cylinder surface.

As Fig. 71 demonstrates, the Stanton Number Reduction increased as the blowing ratio initially was increased indicating that St_{FC}

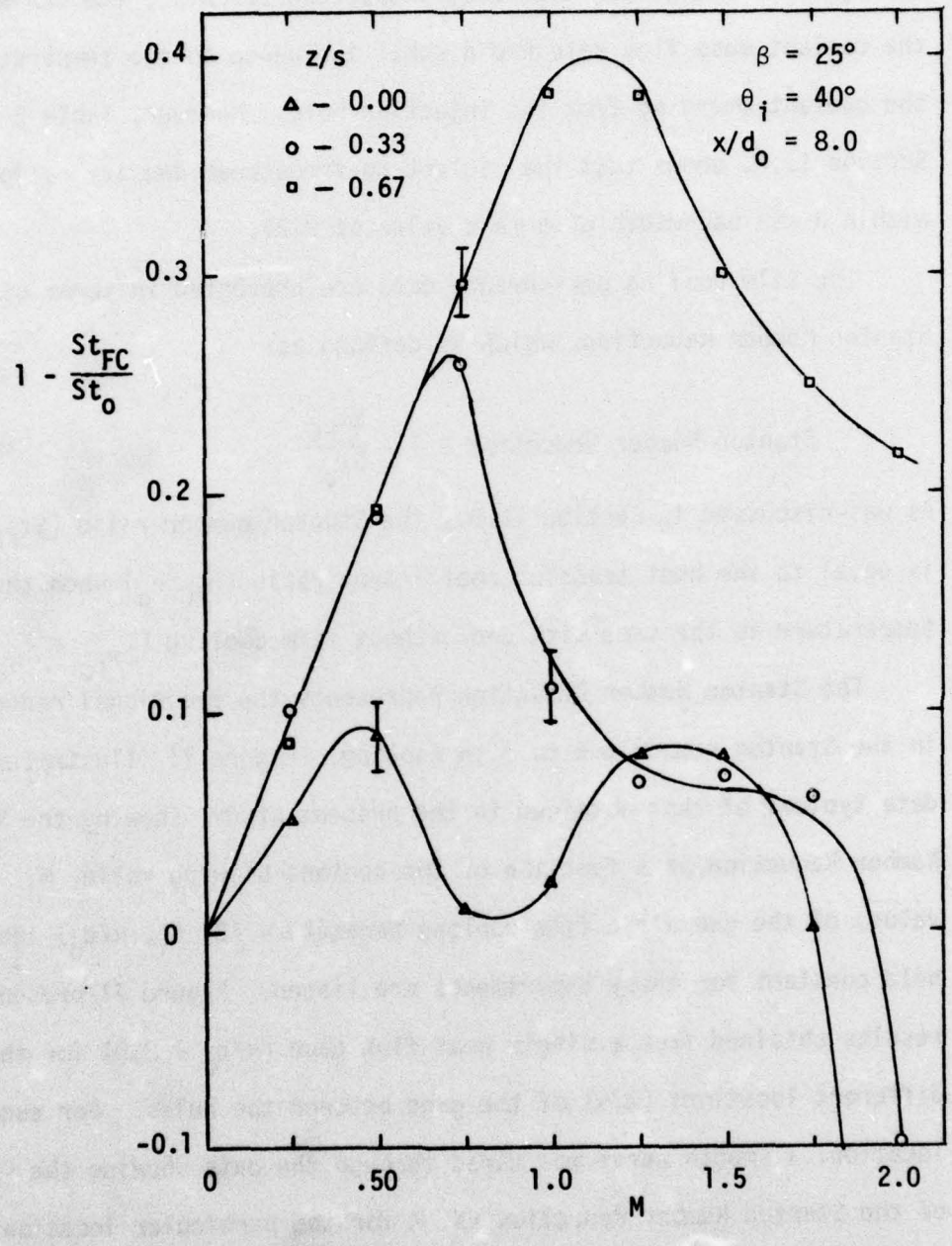

Figure 71. Variation of the Stanton Number Reduction with the Blowing Ratio, M

decreased as the film cooling process became more effective. However, above a certain level of M, further increases in M caused the Stanton Number Reduction to decrease, indicating poorer film cooling performance. Figure 71 shows that at high values of the blowing ratio the Stanton Number Reduction may become negative (i.e. $St_{FC} > St_o$), indicating that film cooling has resulted in a surface heat transfer rate higher than the dry wall heat transfer rate.

The repeatability of the data obtained from separate experiments using a fixed coolant injection configuration is shown by the uncertainty bandwidth (⊢o⊣) applied to selected data points. The uncertainty range from these experiments did not exceed ±.015 units. To avoid any effects due to changes in freestream flow conditions or wall temperature conditions during a given experiment, the dry wall heat flux (q''_o) was measured before and after the film cooling measurements. The data were discarded and retaken if the value of the dry wall Nusselt number shifted by more than 3 percent.†

The injection plate-cylinder wall seam was observed to influence the downstream dry wall heat transfer rate, as discussed in Section III.B. It was not possible to determine the influence of the seam on the heat transfer rate with film cooling. If the influence of the seam on the values of q''_o and q''_{FC} was of the same order magnitude, then the Stanton Number Reduction reported herein (cylinder with a seam) would

† The check on the value of q''_o before and after the film cooling measurements was undertaken to ensure a constant sensitivity of the heat flux gages during a given experiment. No change in gage sensitivity due to surface erosion or oxidation was observed in this study which is in contrast to that reported in Ref. [48].

apply to a perfectly smooth cylinder. If the influence of the seam on the value of q''_{FC} was substantially less than its influence on the value of q''_o, due to the aerodynamic smoothing caused by coolant injection, the Stanton Number Reduction reported herein would be greater than that expected for a smooth cylinder. Although there is some uncertainty of the "seam effect" on the magnitude of the Stanton Number Reduction, the trends with respect to the blowing ratio, M, and injection geometry established in this study are expected to be representative of those found on a smooth cylinder.

Figures 72(a), (b), (c) present the film cooling performance (corresponding to Case I in Table 4) for an injection angle of $\beta = 25°$ at the three downstream distances of $x/d_o = 6.4$, 8.0, and 15.2. The location of the row of holes was fixed at $\theta_i = 40°$ and on each figure the data are presented for three different spanwise locations (z/s). Throughout the entire investigation, the data for the downstream distance $x/d_o = 8.0$, exhibited the least data scatter and the most orderly trends. The increased scatter and/or less orderly trend of the data for $x/d_o = 6.4$ is attributed to the influence of the seam, while the data for $x/d_o = 15.2$ were generally influenced by the low level of the film cooling effect.

The level of the Stanton Number Reduction for all three values of z/s in Fig. 72(b) increased as the blowing ratio was initially increased. Then at a particular blowing ratio, each curve reached a maximum, so that increasing M farther only caused the film cooling performance to deteriorate. For z/s of 0.00 and 0.33, the Stanton Number Reduction even became negative. The highest levels of film cooling performance

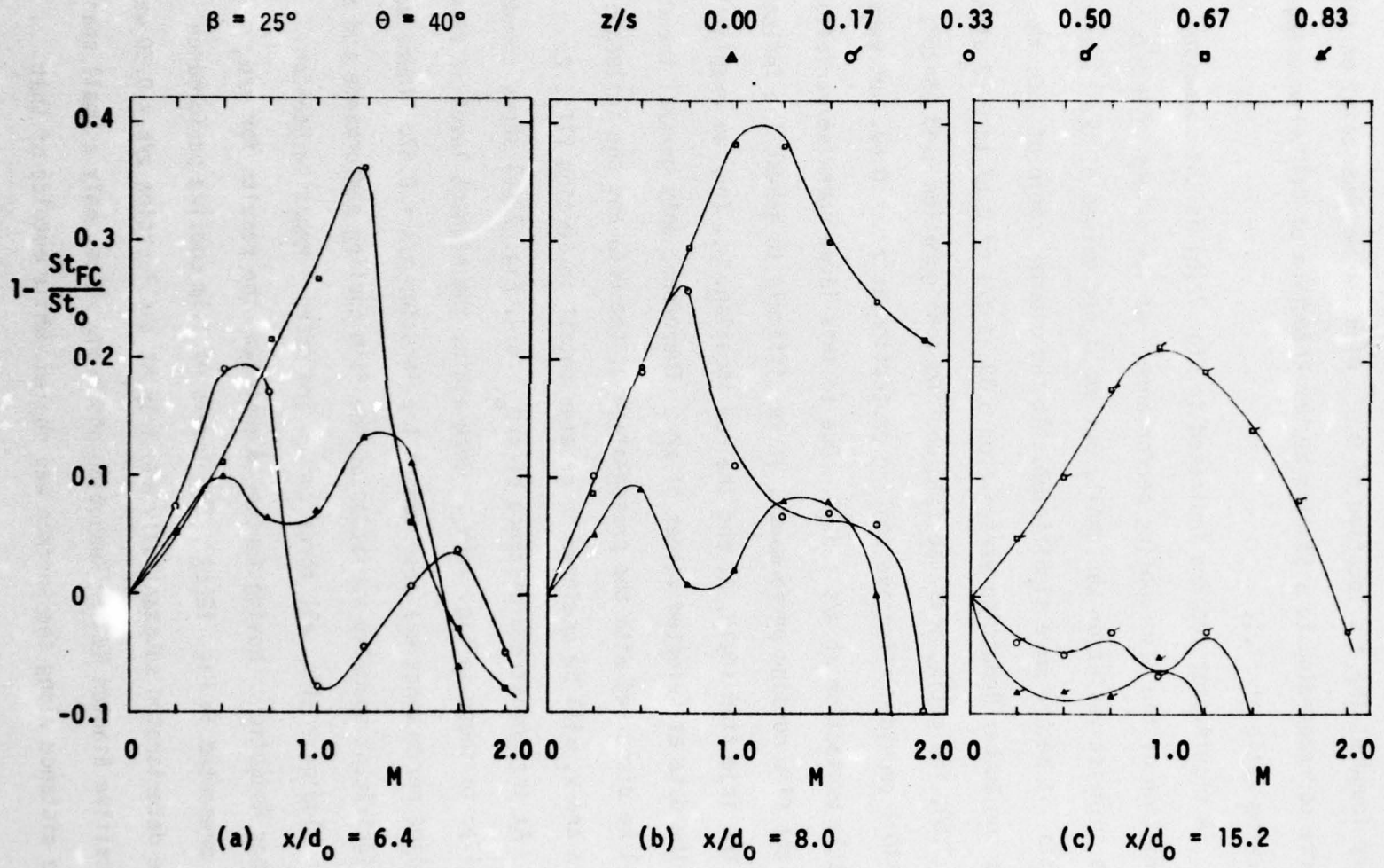

Figure 72. Variation of the Stanton Number Reduction with Blowing Ratio, Case I

were found at the z/s location of 0.67, with the maximum point on the curve corresponding to a Stanton Number Reduction of 0.40 when using a blowing ratio of ~1.1.

A significant feature indicated in Fig. 72(b) is the spanwise variation of the film cooling performance. At low values of M (~0.25), the spanwise variation was small, but at higher values of the blowing ratio, it became more significant. At the blowing ratio of 1.0, the Stanton Number Reduction varied from 0.39 at z/s of 0.67 to 0.02 at z/s of 0.00, indicating that the film cooling configuration used (β=25°, θ_i=40°) provided effective cooling protection at z/s = 0.67, but very little protection at z/s = 0.00. Due to this large spanwise variation in the film cooling performance, it is difficult to assess the influence of the injection angle, β, and the row location, θ_i, from an examination of the data at selected values of z/s. Therefore, only general trends will be discussed with the presentation of the data and the influence of β and θ_i will be analyzed in greater detail in Section III.C.2.

At the downstream distance of x/d_o = 6.4, Fig. 72(a) shows trends similar to those in Fig. 72(b). Once again, the highest level of film cooling performance was observed at the location z/s = 0.67. There was a significant spanwise variation of the film cooling performance and at high blowing ratios, all three curves indicated a negative Stanton Number Reduction. Moving farther downstream, the results for x/d_o = 15.2 are presented in Fig. 72(c). The levels of film cooling performance have deteriorated substantially and only at the location z/s = 0.50 was a positive Stanton Number Reduction observed. Thus, only a small spanwise distance along the surface was cooled, while outside of that

region the surface heat flux was greater than without film cooling.

The next set of data (Case II in Table 4), corresponding to the row of holes located at θ_i = 30°, is presented in Figs. 73(a), (b), (c). The injection angle, β, and the downstream distances, x/d_o, are the same as those in Fig. 72. Figure 73(b), for x/d_o = 8.0, shows similar trends for the Stanton Number Reduction as seen in Fig. 72(b). The highest levels of film cooling performance were found at the location z/s = 0.67 with a maximum Stanton Number Reduction of 0.21 observed at a blowing ratio of ~1.1. The spanwise variation of the film cooling performance was negligible for values of M up to 0.75, but at M ≈ 1.1, the Stanton Number Reduction varies from 0.21 at z/s = 0.67 to 0.07 at z/s = 0.00.

Figure 73(a) shows similar trends for x/d_o = 6.4. The spanwise variation was small up to M ≈ 0.50, but for greater values of M the spanwise variation was significant. Figure 73(c) presents the data for x/d_o = 15.2, showing the Stanton Number Reduction to be negative for the entire range of M investigated.

Comparing Figs. 73(b) and 72(b), the effect of moving the row of holes closer to stagnation (from θ_i = 40° to 30°) was to decrease the maximum Stanton Number Reduction from 0.40 to 0.21, while the corresponding blowing ratio remained constant at ~1.1. However, while the film cooling performance level decreased, the row location closer to stagnation (θ_i = 30°) did result in less spanwise variation of the film cooling performance. Both figures show that the highest level of Stanton Number Reduction was found at the spanwise location of z/s = 0.67.

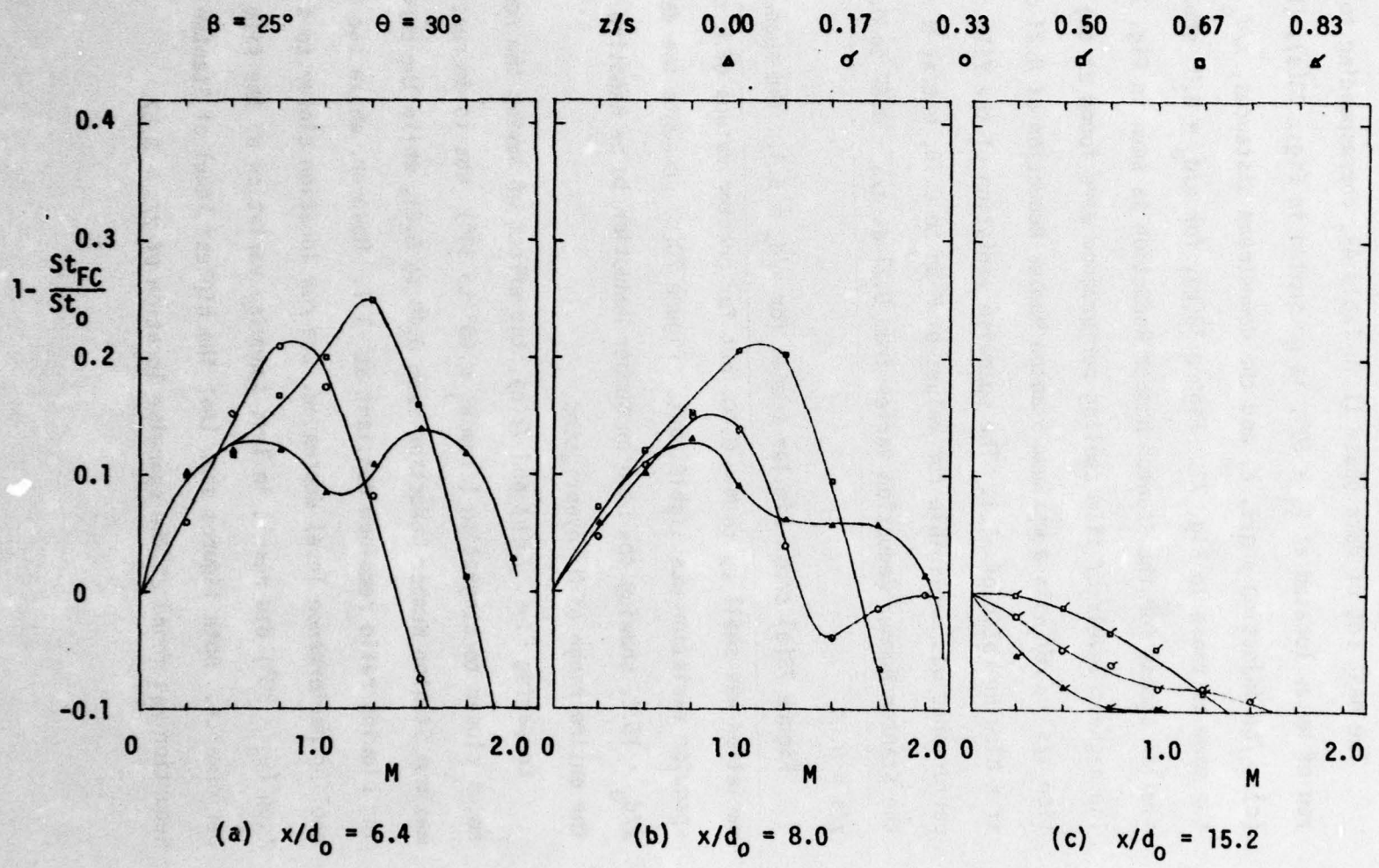

Figure 73. Variation of the Stanton Number Reduction with Blowing Ratio, Case II

The third data set (Case III in Table 4) again represents only a change in the row location to θ_i = 20°. The results in Fig. 74(a), (b), (c) are for the same injection angle, β, and downstream distances presented in Figs. 72 and 73. Figure 74(b) follows the basic trends observed for the previous two data sets. The curves for all three values of z/s reach a maximum level of Stanton Number Reduction at a particular blowing ratio, and increasing M past that value only causes the film cooling performance to deteriorate. As seen in the past two data sets, high values of M result in the Stanton Number Reduction becoming negative. The highest level of film cooling performance was found at the location z/s = 0.67 with a maximum Stanton Number Reduction of 0.14 at a blowing ratio of ~1.4.

The spanwise variation of the film cooling performance was small up to the blowing ratio of 1.0. In this range, the Stanton Number Reduction for z/s = 0.33 even exceeded that for z/s of 0.67, but for M > 1.0, the highest levels were found at z/s = 0.67. Figure 74(a) shows basically the same trends found in Fig. 74(b). The spanwise variation of the film cooling performance is larger than that in Fig. 74(b) because, while the Stanton Number Reduction for z/s of 0.33 and 0.67 was nearly the same, the Stanton Number Reduction for the curve of z/s = 0 never varied far from zero. At the downstream distance of x/d_o = 15.2, Fig. 74(c) shows that the film cooling performance was negligible. Only at z/s of 0.50 did the Stanton Number Reduction ever become positive, and even at that spanwise location it never exceeded 0.03.

A comparison of Figs. 72(b), 73(b), and 74(b), shows that moving the row of injection holes closer to stagnation (θ_i = 40° to 20°) resulted

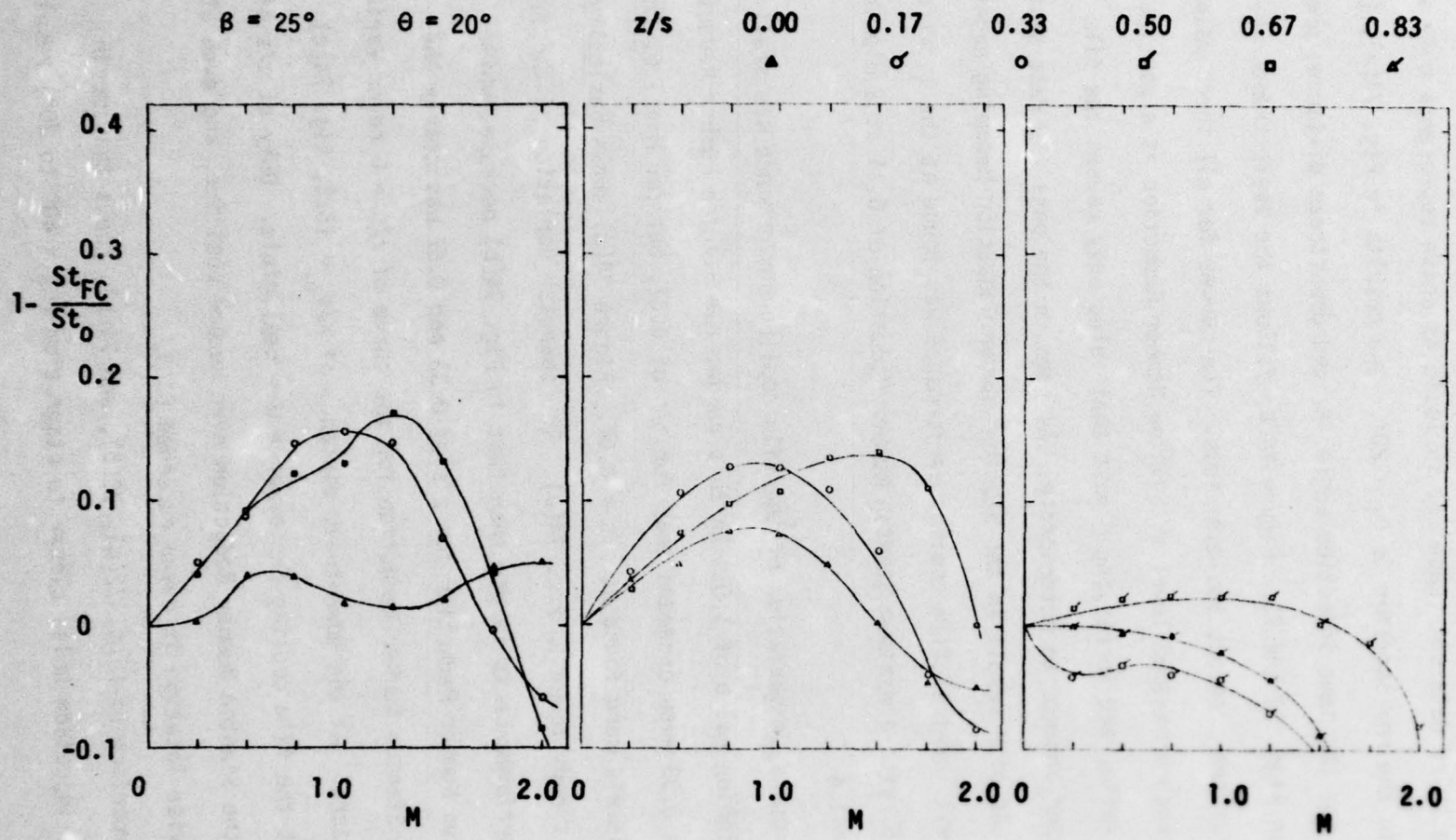

Figure 74. Variation of the Stanton Number Reduction with Blowing Ratio, Case III

in a decrease of the film cooling performance. The maximum Stanton Number Reduction varied from a value of 0.40 at θ_i = 40°, to 0.21 at θ_i = 30°, and finally to 0.14 at θ_i = 20° while the corresponding blowing ratio for maximum performance increased slightly from 1.1 (θ_i = 40°, 30°) to 1.4 (θ_i = 20°). For all three cases, the spanwise variation was small at low values of the blowing ratio, but the value of M at which the spanwise variation became significant increased as θ_i was decreased. Therefore, a more uniform spanwise film cooling performance was obtained across the surface up to a higher value of M as the row location was moved closer to stagnation.

The fourth data set (Case IV in Table 4), presented in Figs. 75(a), (b), (c), represents an injection angle, β = 35°, with the row location at θ_i = 40°. With the steeper injection angle, the general trend of the data in Fig. 75(b) is similar to that established in the first three data sets for the injection angle of 25°. The curves for all three values of z/s increase as M is initially increased reaching a maximum level at a particular value of the blowing ratio. For greater values of M, the Stanton Number Reduction continually decreased, resulting in the Stanton Number Reduction becoming negative at some locations. The highest level of film cooling performance was observed at the location z/s = 0.33, with a maximum Stanton Number Reduction of 0.28 at a blowing ratio of 0.75. The spanwise variation of the film cooling performance was small only for M $\lesssim$ 0.3,

Figure 75(a), representing the downstream distance of x/d_o = 6.4, shows basically the same trends as those described in Fig. 75(b), although the spanwise non-uniformity of the film cooling performance

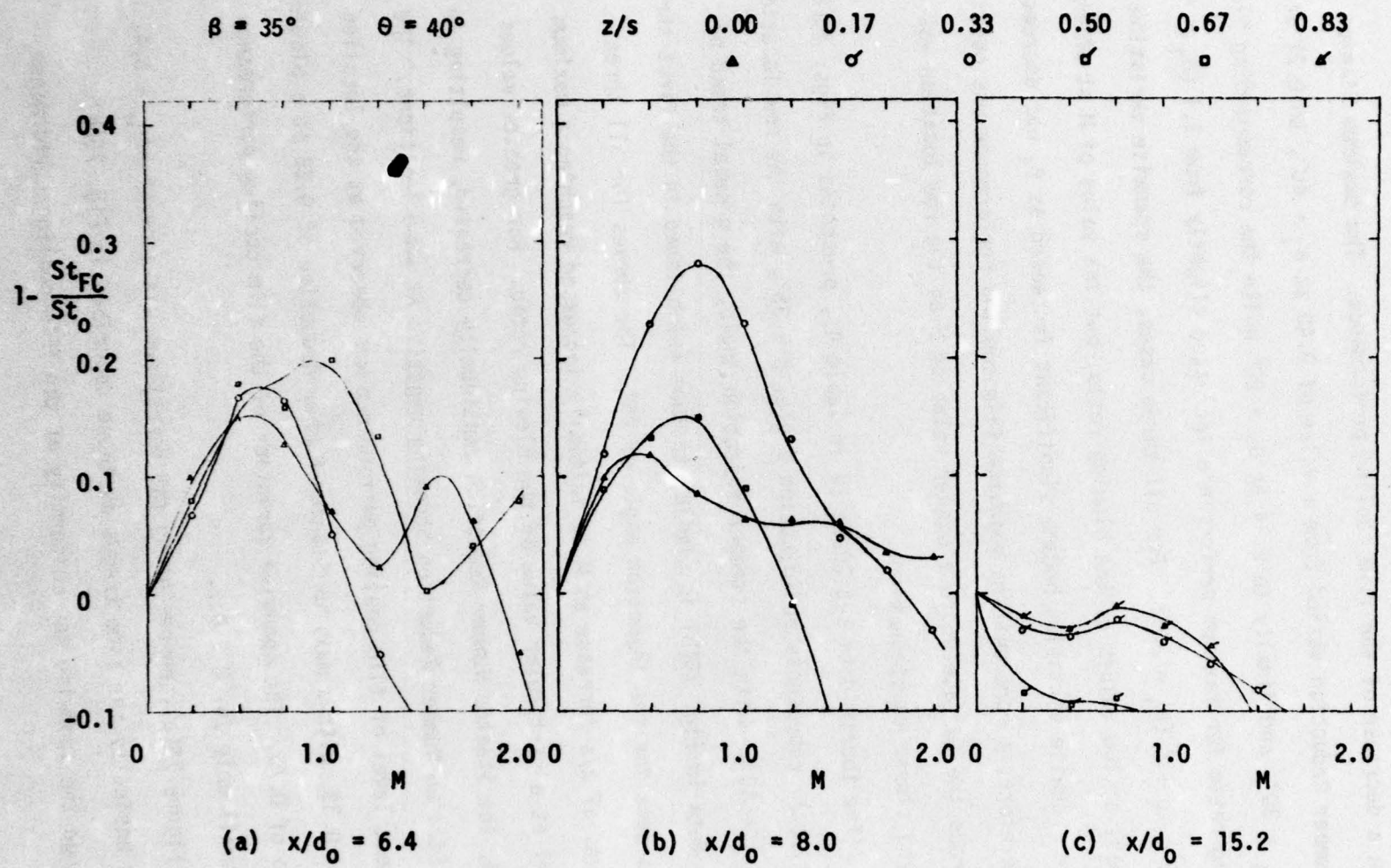

Figure 75. Variation of the Stanton Number Reduction with Blowing Ratio, Case IV

did not become significant until M exceeded 0.75. At the downstream distance of x/d_o = 15.2, Fig. 75(c) shows that film cooling causes the Stanton Number Reduction to be negative for all values of M.

The effect of the injection angle is shown by comparing Figs. 72(b) and 75(b). The maximum Stanton Number Reduction decreased from 0.40 for β = 25° to 0.28 for β = 35°, while the corresponding blowing ratio was M ~ 1.1 for β = 25° to M ~ 0.75 for β = 35°. Also, the location where the maximum Stanton Number Reduction was observed shifted from z/s = 0.67 for β = 25° to z/s = 0.33 for β = 35°.

Figures 76(a), (b), (c) present the fifth data set, corresponding to Case V in Table 4, with row location moved to θ_i = 30°. Figure 74(b) shows a maximum Stanton Number Reduction of 0.21 at a blowing ratio of 0.9 for the location z/s = 0.33. The spanwise variation of the film cooling performance was not negligible although it was not as large as that seen in previous figures. Figure 76(a) shows that, for x/d_o = 6.4, the highest level of film cooling performance was found at the location z/s = 0.67. Also, the spanwise variation is larger than that seen in Fig. 76(b). At the downstream distance of x/d_o = 15.2, Fig. 76(c) reveals that the film cooling performance had deteriorated such that the Stanton Number Reduction was generally negative.

A comparison of Figs. 75(b) and 76(b), with β = constant, and θ_i decreased from 40° to 30°, shows the maximum Stanton Number Reduction decreasing from 0.28 (θ_i = 40°) to 0.21 (θ_i = 30°) while the corresponding blowing ratio was approximately constant in the range of 0.75 to 0.9. Once again, the location of the row of holes at θ_i = 30° resulted in less spanwise variation of the film cooling performance.

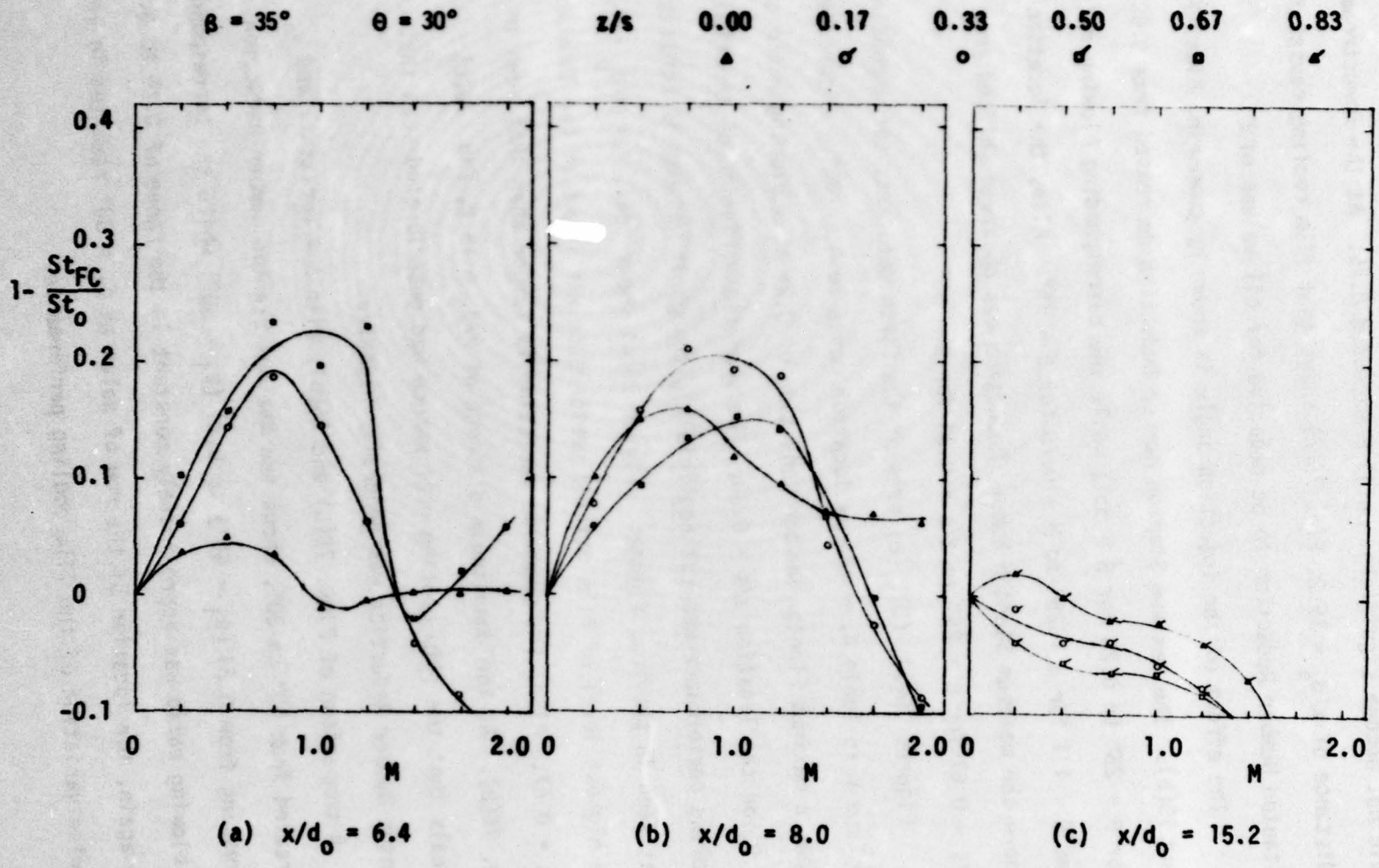

Figure 76. Variation of the Stanton Number Reduction with Blowing Ratio, Case V

The sixth data set (Case VI in Table 4), shown in Figs. 77(a), (b), (c) corresponds to injection closest to stagnation, $\theta_i = 20°$, with $\beta = 35°$. Figure 75(b) shows a maximum Stanton Number Reduction of 0.17 corresponding to a blowing ratio of ~0.9. The spanwise variation was significant for values of $M \gtrsim 0.3$ and, once again the highest level of film cooling performance was found at the location $z/s = 0.33$.

Figure 77(a) shows a maximum Stanton Number Reduction of 0.11 at the location $z/s = 0.67$. Figure 77(c) shows that for $\theta_i = 20°$, the Stanton Number Reduction at the downstream distance of $x/d_o = 15.2$ was minimal although positive for values of M up to ~1.3.

Comparing Figs. 75(b), 76(b), and 77(b), for $\beta = 35°$, shows that moving the location of the row of holes closer to stagnation resulted in a decrease in the film cooling performance as was observed previously for an injection angle of $\beta = 25°$. The maximum Stanton Number Reduction decreased from 0.28 for $\theta_i = 40°$, to 0.21 for $\theta_i = 30°$, and finally to 0.14 for $\theta_i = 20°$, while the corresponding values of the blowing ratio were approximately constant in the range of 0.75 to 0.9.

The final data set (Case VII in Table 4) presented in Figs. 78(a), (b), (c) corresponds to an injection angle of $\beta = 45°$ with the row located at $\theta_i = 40°$. Figure 78(b) shows that the maximum Stanton Number Reduction observed for $x/d_o = 8.0$ was 0.11 at the blowing ratio of 0.45. There was some spanwise variation of the film cooling performance even at this low level of Stanton Number Reduction with the highest level of film cooling performance being found at the location $z/s = 0.33$ for $M \lesssim 0.75$. Figure 78(a) shows the highest level of film cooling performance at the location $z/s = 0.33$ with the maximum Stanton Number Reduction

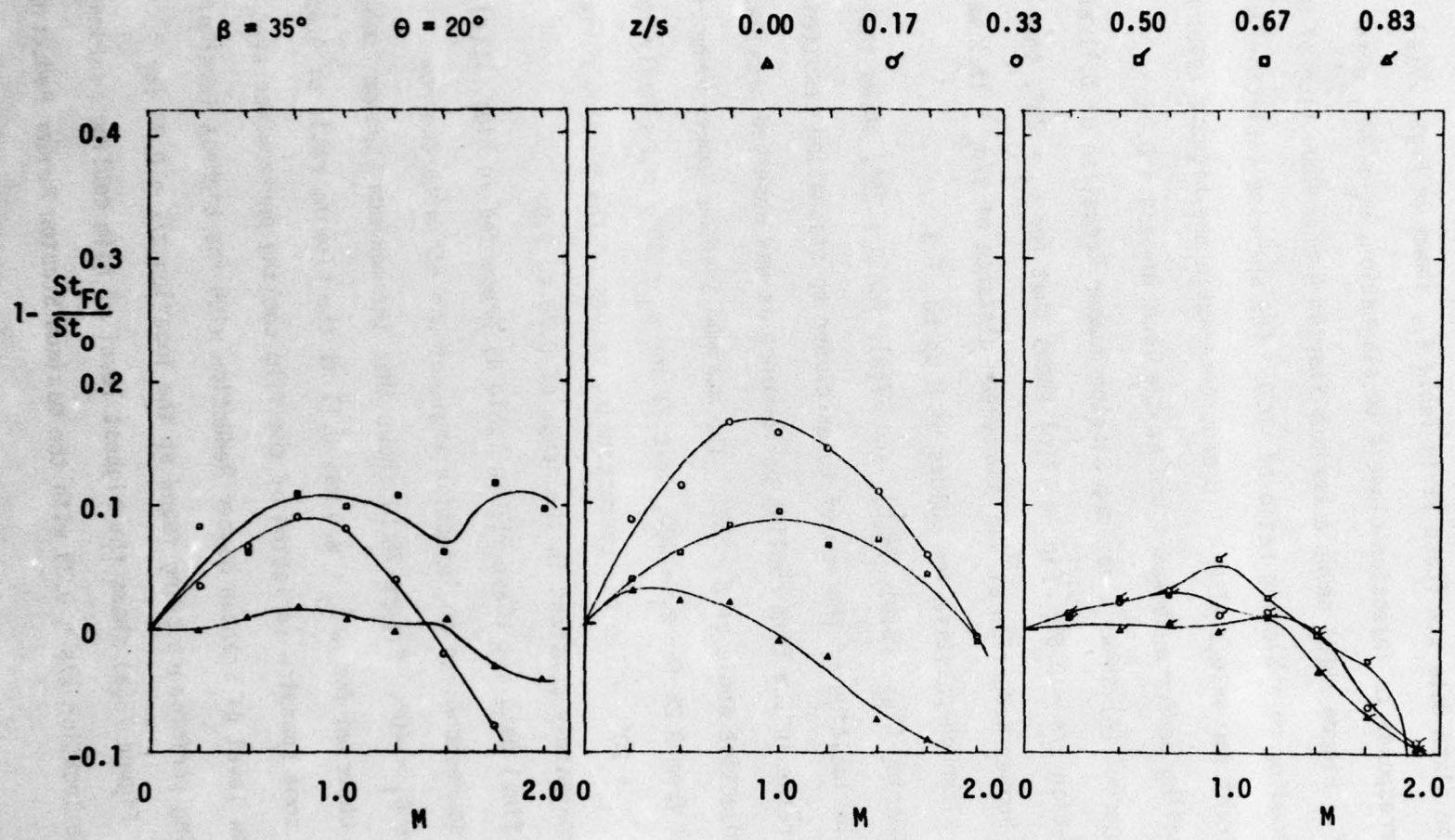

Figure 77. Variation of the Stanton Number Reduction with Blowing Ratio, Case VI

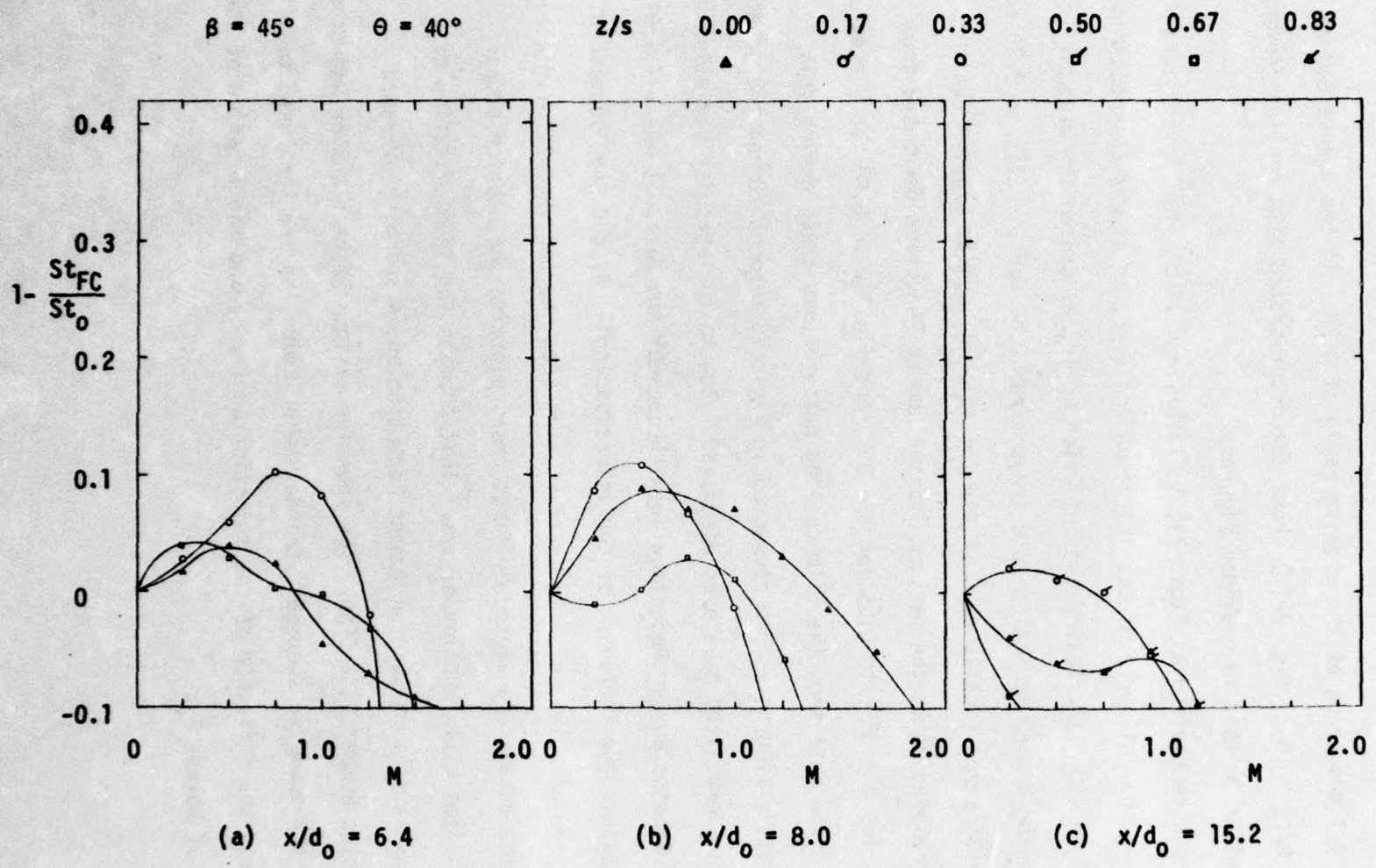

Figure 78. Variation of the Stanton Number Reduction with Blowing Ratio, Case VII

of 0.1 occurring at the blowing ratio of 0.75. At the downstream distance of x/d_o = 15.2, Fig. 78(c) shows the deteriorated film cooling performance similar to that in previous figures.

A comparison of Figs. 72(b), 75(b), and 78(b), for θ_i =constant(40°), shows the influence of the injection angle, β, as it was changed from 25° to 45°. Increasing the injection angle, β, caused the maximum Stanton Number Reduction to decrease from 0.40 for β = 25°, to 0.28 for β = 35°, and finally to 0.11 for β = 45°. Also, the blowing ratio corresponding to the maximum Stanton Number Reduction decreased from 1.1 for β = 25°, to 0.75 for β = 35°, and finally to 0.45 for β = 45°.

The data from the film cooling measurements taken during this investigation have been presented in Figs. 72 through 78 and the general trends exhibited have been discussed. Due to the spanwise variation of the Stanton Number Reduction seen throughout the data, it was difficult to assess the influence of the injection angle, β, and the location of the row of holes, θ_i. In the following section, the spanwise variation of the data are analyzed by first cross plotting the Stanton Number Reduction as a function of z/s. This permits the identification of a spanwise maximum Stanton Number Reduction and a spanwise averaged Stanton Number Reduction. The spanwise maximum Stanton Number Reduction and the spanwise averaged Stanton Number Reduction are then used to assess the influence of the injection angle, β, and the location of the row of holes, θ_i.

III.D. Analysis of Film Cooling Data

In the preceeding section, the film cooling results were presented for the seven different film cooling configurations studied, each configuration being identified by a particular case number in Table 4. Due to the spanwise variation of the Stanton Number Reduction found in the data, it was difficult to assess the influence of the injection angle, β, or the row location, θ_i, on the film cooling performance by examining the data at specific values of z/s. In order to characterize the spanwise variation of the Stanton Number Reduction, the measured data were cross plotted as a function of z/s for selected values of M. Figure 79 is a representative figure of the cross plotted data resulting from Case I. The values of the geometric parameters held constant for the case are presented on the figure. The data from Fig. 70(b) were cross plotted for selected values of the blowing ratio using the measured data points for the three values of z/s and a fourth point based on the assumption of periodicity (z/s = 0.0 equivalent to 1.0). A smooth curve was fared through the four points using the following guidelines:

1) if one measured z/s data point had a significantly higher level of Stanton Number Reduction than the other two measured points, the smooth curve was drawn so as to peak close to the z/s location with the highest magnitude of Stanton Number Reduction.
2) if two measured z/s data points had approximately the same level of Stanton Number Reduction (higher than that of the third point), a smooth curve was drawn so that the peak occurred near the middle of the two z/s locations.

AD-A035 716 PURDUE UNIV LAFAYETTE IND THERMAL SCIENCES AND PROPU--ETC F/G 21/5
STAGNATION REGION GAS FILM COOLING SPANWISE ANGLED COOLANT INJE--ETC(U)
DEC 76 D W LUCKEY, M R L'ECUYER N00014-75-C-0873
UNCLASSIFIED TSPC-TR-76-2 NL

3 OF 4
AD A035716

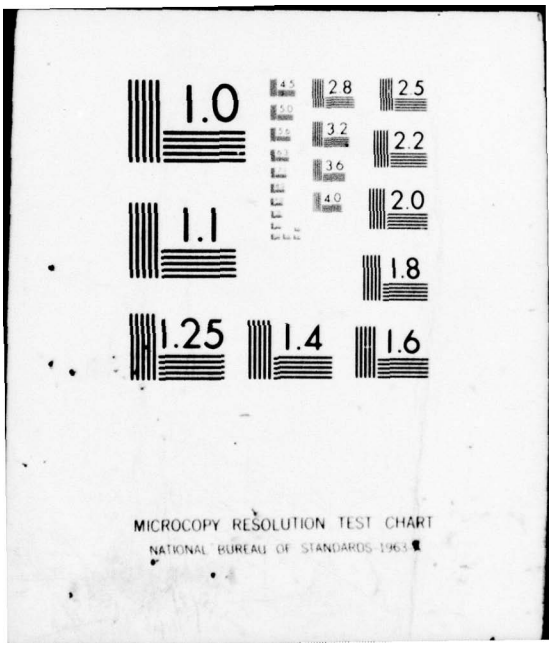
1.0
1.1
1.25
1.4
1.6
1.8
2.0
2.2
2.5
2.8
3.2
3.6
4.0
MICROCOPY RESOLUTION TEST CHART
NATIONAL BUREAU OF STANDARDS-1963-A

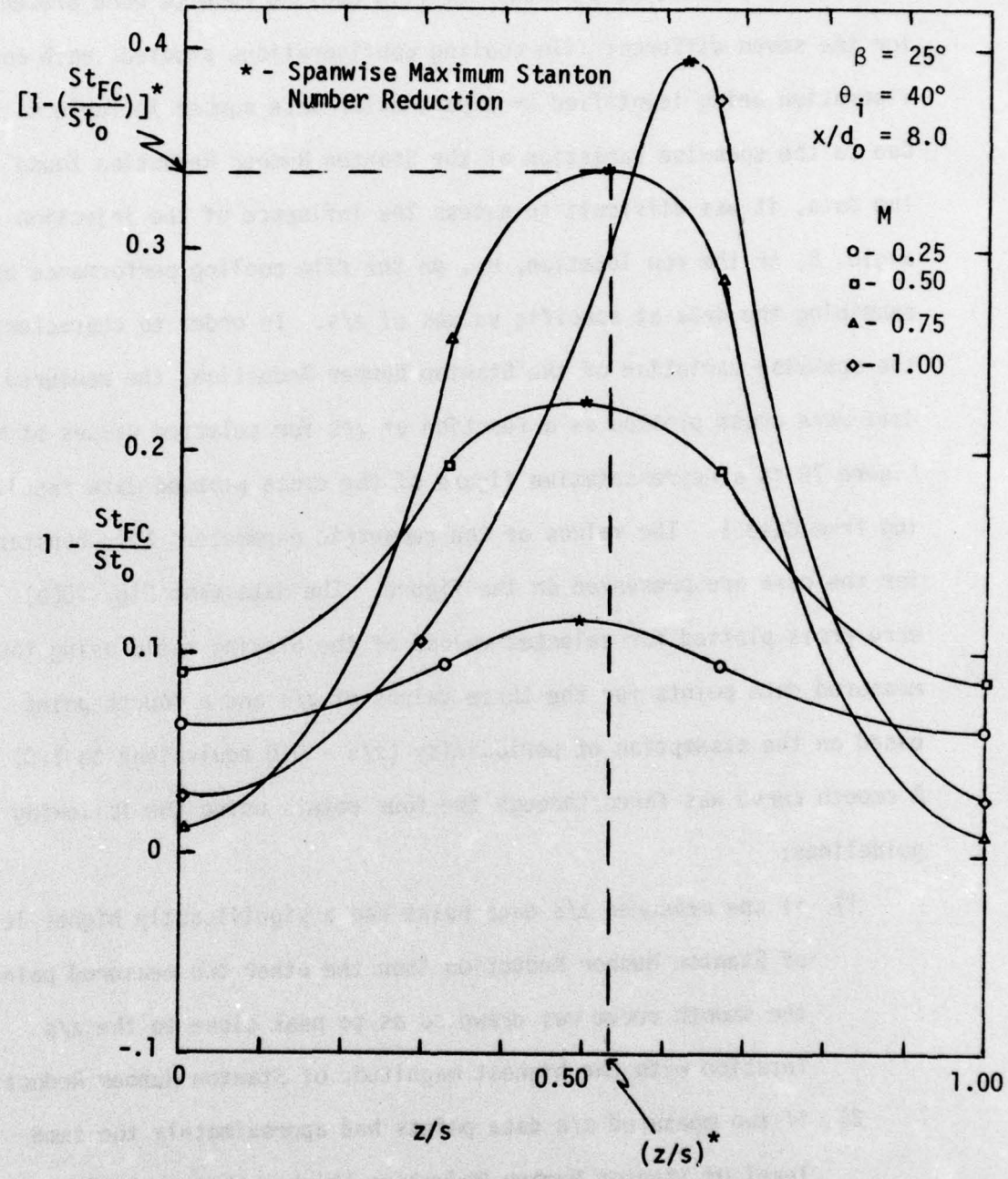

Figure 79. Spanwise Variation of the Stanton Number Reduction (β=25°, θ_i=40°, x/d_o=8.0)

3) due to periodicity, the slope of the curve at the z/s location of 0.0 was drawn to match the slope at the z/s location of 1.00.

The smooth curves shown in Fig. 79 represent the spanwise variation of the Stanton Number Reduction for an injection angle of $\beta = 25°$. From the curve for a selected value of M, one can identify a "spanwise maximum Stanton Number Reduction", $[1-(St_{FC}/St_o)]^*$, and the corresponding location $(z/s)^*$, hereafter referred by the "*" designation. The location of the *-point on each curve is shown in Fig. 79, with the values of $[1-(St_{FC}/St_o)]^*$ and $(z/s)^*$ for M = 0.75 identified along the axes for clarification. As the blowing ratio was increased from 0.25 to 1.0, the value of $[1-(St_{FC}/St_o)]^*$ increased from 0.11 to 0.42, although the non-uniformity of the film cooling performance was much more severe for the higher values of M as shown in Fig. 79. The values of $(z/s)^*$ shown in Fig. 79 were in a range between 0.50 and 0.65, with $(z/s)^*$ increasing slightly with M.

In contrast, Fig. 80 shows similar results for the same values of θ_i and x/d_o, but with an injection angle of $\beta = 35°$. The results in Fig. 80 show the level of $[1-(St_{FC}/St_o)]^*$ increasing with M up to a value of 0.30 at the blowing ratio of 0.75, and then decreasing as M was increased to 1.00. For the coolant injection angle of $\beta = 35°$, the "spanwise maximum Stanton Number Reduction" was observed to occur in the range of $(z/s)^* = 0.35$ to 0.45. Comparing Figs. 79 and 80, it is apparent that, for a given value of M, the steeper film coolant injection angle resulted in lower levels of film cooling performance with the *-point occurring at smaller values of (z/s).

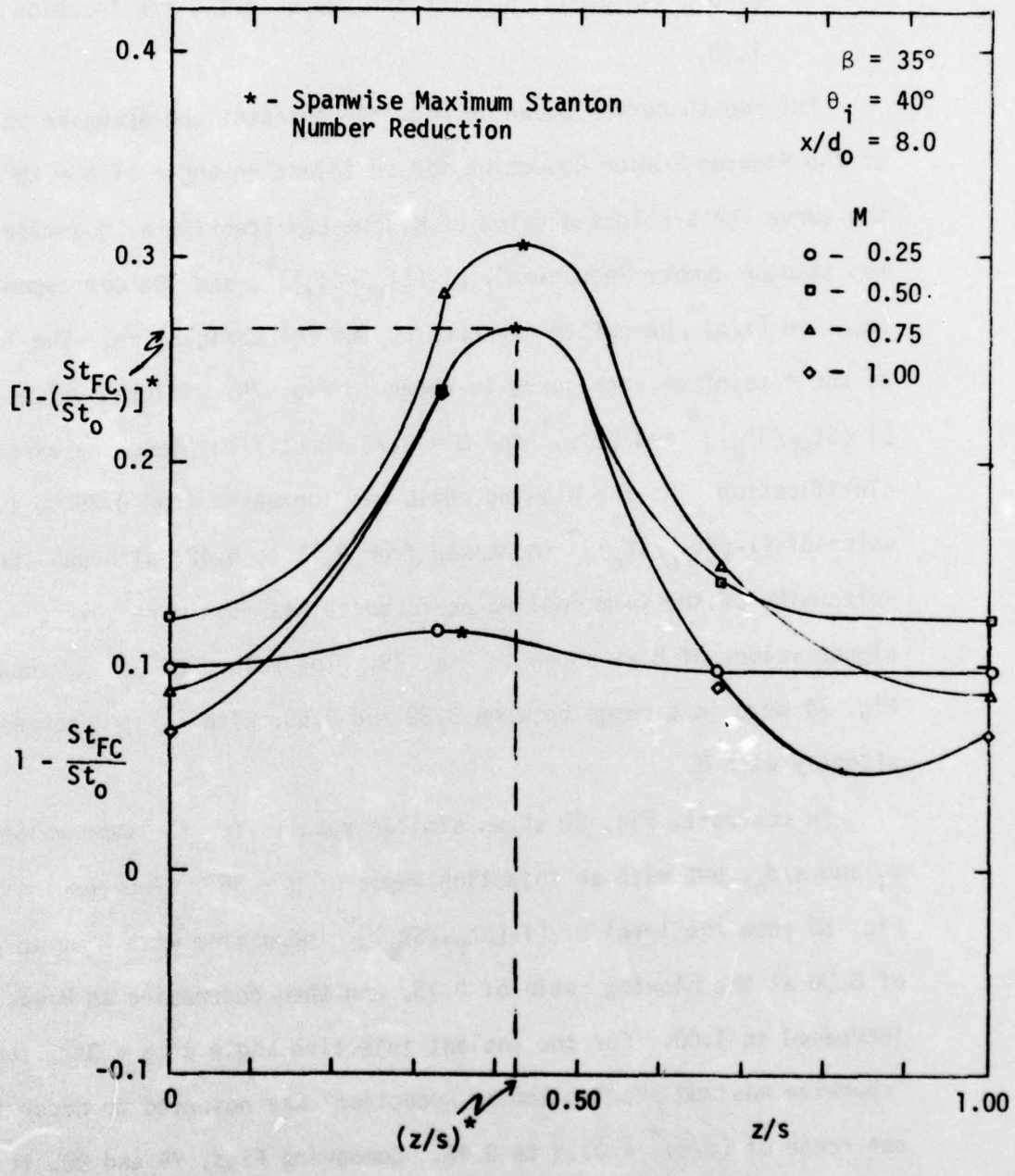

Figure 80. Spanwise Variation of the Stanton Number Reduction (β=35°, θ_i=40°, x/d_o=8.0)

All of the data presented in Figs. 72 to 78 were cross plotted in the manner illustrated in Figs. 79 and 80 and are included in Appendix VI. To assess the influence of the injection angle, β, and the row location, θ_i, on the film cooling performance, the spanwise distributions were interpreted by:

1) analyzing the variation of $[1-(St_{FC}/St_o)]^*$ and $(z/s)^*$ with respect to M, β, and θ_i (Section III.D.1.),
2) analyzing the variation of the "spanwise averaged Stanton Number Reduction", $[1-(St_{FC}/St_o)]_{AVG}$, with respect to M, β, and θ_i (Section III.D.2.).

The results from both procedures are presented and discussed in the following sections.

III.D.1. Data for Spanwise Maximum Stanton Number Reduction

From the presentation of the data (Section III.C.), the coolant injection angle, β, was seen to have a definite influence on the film cooling performance. To determine the influence of β, the values of $[1-(St_{FC}/St_o)]^*$, as defined in Section III.D., are analyzed in this section. Figures 81(a), (b), and (c) present the Stanton Number Reduction for the *-points as a function of the blowing ratio, M, for a constant value of x/d_o. The data have been plotted for the different values of the injection angle, β, investigated at each particular row location, θ_i, as shown on the figures. For each value of β, a smooth curve was fared through the data points to describe the variation with respect to M. It should be recalled that the values for the *-points were obtained from data fairings (see Figs. 79 and 80). A flag is

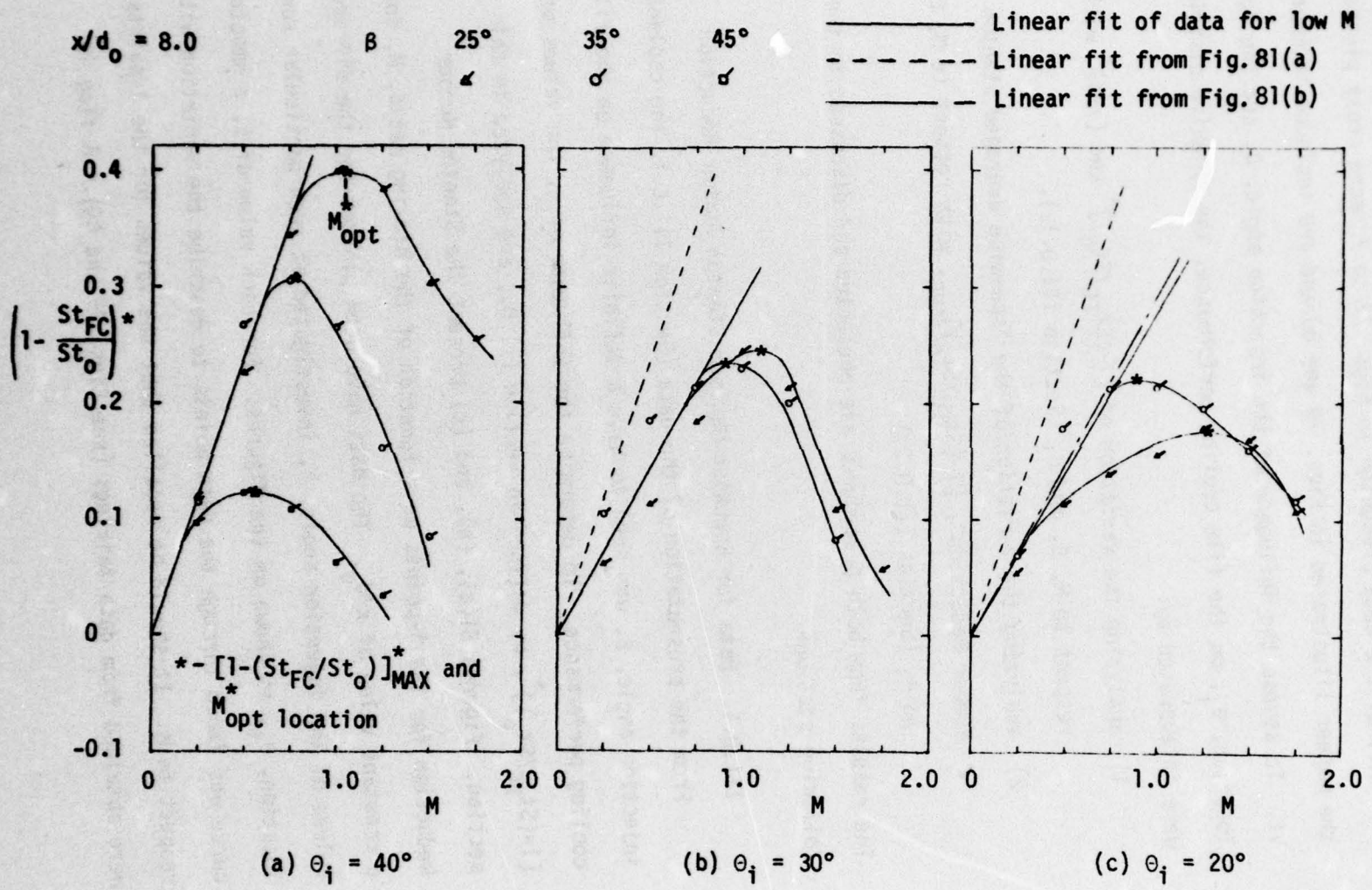

Figure 81. Variation of the Spanwise Maximum Stanton Number Reduction with the Blowing Ratio(x/d_o=8.0)

attached to all symbols (σ) designating the *-points to distinguish them from measured data points.

Figure 81(a), for the location $\theta_i = 40°$, shows that at low values of the blowing ratio, the magnitude of $[1-(St_{FC}/St_o)]^*$ increases approximately linearly with M independent of the value of β. For each value of β, as M is progressively increased, the trend of $[1-(St_{FC}/St_o)]^*$ deviates from the linear behavior, and reaches a maximum level, $[1-(St_{FC}/St_o)]^*_{MAX}$ at a particular blowing ratio, which will be identified as the optimum blowing ratio, M^*_{opt}. Increasing the blowing ratio past M^*_{opt} results in a deterioration of the film cooling performance. The curve for $\beta = 25°$ follows the linear trend up to a blowing ratio of $M \sim 0.75$. A maximum value of $[1-(St_{FC}/St_o)]^*$ of 0.40 was observed at $M^*_{opt} \approx 1.07$. As the injection angle was increased from 25° to 45°, the level of $[1-(St_{FC}/St_o)]^*_{MAX}$ decreased from 0.40 to 0.12 while at the same time, the magnitude of M^*_{opt} decreased from 1.07 to 0.60.

Figure 81(b) presents similar results for injection angles of 25° and 35°, at the row location $\theta_i = 30°$. (Data were not obtained for $\beta = 45°$, $\theta_i = 30°$.) The results show the same linear trend of the film cooling performance with M at the lower values of the blowing ratio. A close examination of the data points reveals that slightly higher values of the Stanton Number Reduction were observed for $\beta = 35°$. The maximum level of $[1-(St_{FC}/St_o)]^*$ is 0.25 for $\beta = 25°$, and 0.23 for $\beta = 35°$, with the value of M^*_{opt} decreasing from 1.10 to 0.90 as β was increased from 25° to 35°.

The dotted line in Fig. 81(b) represents the linear trend found in Fig. 81(a) at the location $\theta_i = 40°$. Comparing Figs. 81(a) and (b),

reveals that the slope of the linear trend decreased as θ_i was decreased. In Fig. 81(a), increasing β from 25° to 35° caused $[1-(St_{FC}/St_o)]^*$ to decrease ~ 22%, while in Fig. 81(b), the decrease was only ~ 8%. Both figures show a decrease in M^*_{opt} as the value of β was increased.

Figure 81(c) presents the data with the row location at θ_i = 20°. The same linear variation with M is evident at low values of the blowing ratio. Both curves reach a maximum at a particular blowing ratio, M^*_{opt}, and then decrease as M is increased past it. The maximum level of $[1-(St_{FC}/St_o)]^*$ for β = 35° reached 0.22 exceeding the value of 0.18 for β = 25°. However, the optimum blowing ratio, M^*_{opt} continued to decrease as the injection angle was increased, going from 1.25 for β = 25° to 0.90 for β = 35°.

The linear trends established in Figs. 81(a) and (b) are included in Fig. 81(c), showing that the linear trend established for low values of M was essentially the same for the locations of θ_i = 30° and 20°, with a steeper slope observed for the location θ_i = 40°. Figures 81(a), (b), and (c) reveal an optimum blowing ratio that decreased as the injection angle was increased. While the value of $[1-(St_{FC}/St_o)]^*_{MAX}$ at θ_i = 40° showed a significant decrease (~ 22%) as β was increased from 25° to 35°, the decrease at θ_i = 30° was much less (~ 8%) and, in Fig. 81(c), the change with respect to β was seen to reverse. The influence of β (at θ_i = 20°) is illustrated further by examining the spanwise distributions of the Stanton Number Reduction shown in Figs. 82(a) and (b). It can be seen that while the values of the spanwise maximum Stanton Number Reduction at β = 35° exceeded those at β = 25°, a more uniform distribution was found at the shallower angle. This results in

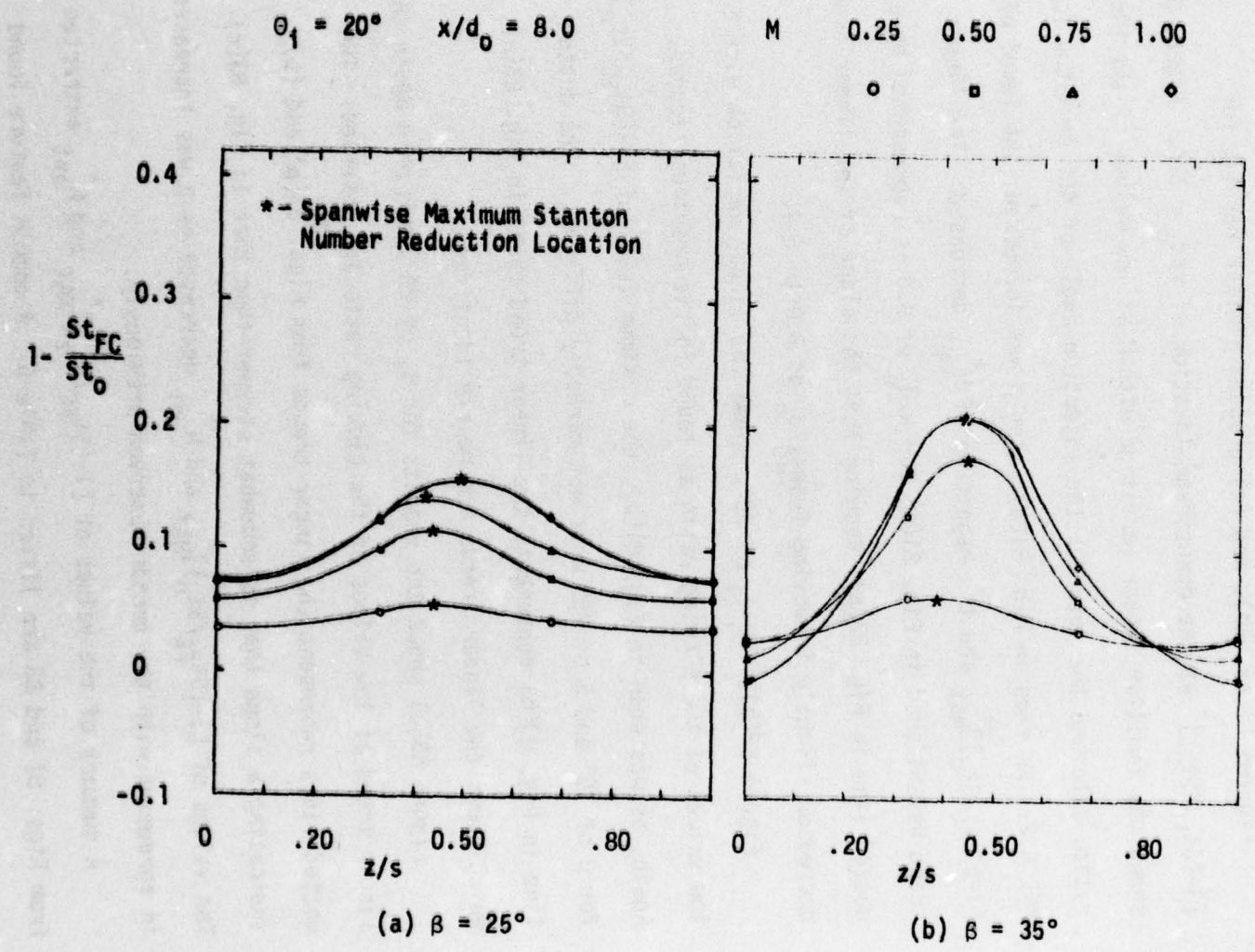

Figure 82. Spanwise Variation of the Stanton Number Reduction (Θ_i=20°, x/d_o=8.0)

a larger spanwise averaged Stanton Number Reduction for β = 25° as is shown in Section III.D.2.

Figures 83(a), (b), and (c) present similar results for $[1-(St_{FC}/St_o)]^*$ at the downstream location of x/d_o = 6.4. Figure 83(a) shows the familiar linear variation with M at low values of the blowing ratio, although the data for the injection angle of 45° deviates for $M \gtrsim 0.2$. As seen in Fig. 81(a), when β was increased, the level of $[1-(St_{FC}/St_o)]^*_{MAX}$ and the magnitude of M^*_{opt} decreased. The linear trend established in Fig. 81(a) for x/d_o of 8.0 is represented by a dotted line in Fig. 83(a), showing that the slope of the linear trend decreased slightly in moving from x/d_o of 8.0 to 6.4.

Figure 83(b), for θ_i of 30°, shows the linear variation with M at low values of the blowing ratio as found in the previous figures. Again, as was seen in Fig. 81(b), the maximum level of $[1-(St_{FC}/St_o)]^*$ for β of 35° and β of 25° were not markedly different. The dotted line in Fig. 83(b) represents the linear trend found in Fig. 83(a), which shows the linear trends are nearly identical.

Figure 83(c) shows the results for θ_i of 20°, and once again the linear trend at low values of the blowing ratio are observed. The dotted lines represent the linear trends from Figs. 83(a) and (b) indicating a slope that is somewhat steeper than that in Fig. 83(c). The values of $[1-(St_{FC}/St_o)]^*_{MAX}$ and M^*_{opt} decreased as β was increased in agreement with the trends observed previously.

A summary of the values of $[1-(St_{FC}/St_o)]^*_{MAX}$ and M^*_{opt} extracted from Figs. 81 and 83 are listed in Table 5. A common feature found throughout the data was that the value of M^*_{opt} always decreased as the

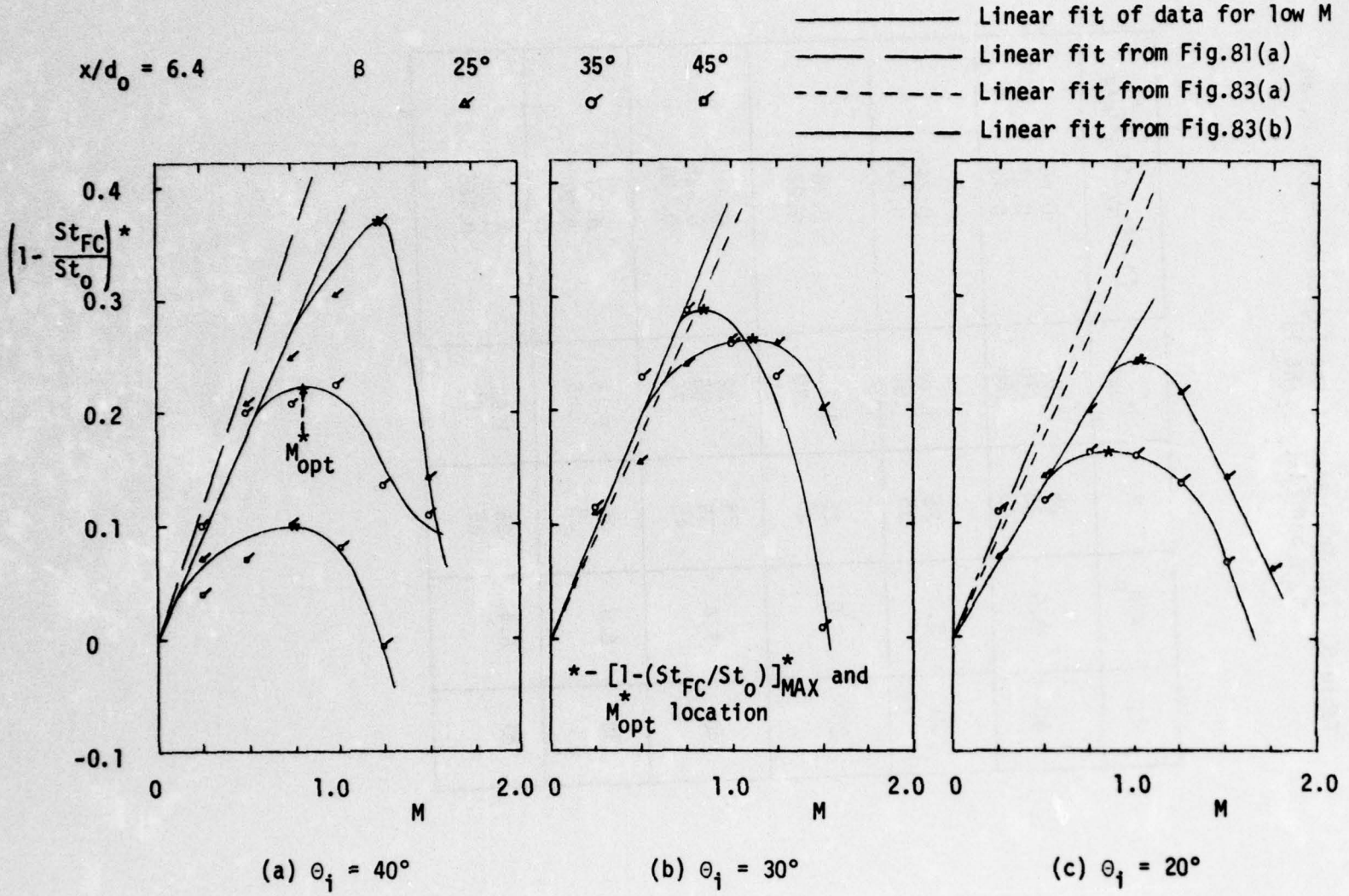

Figure 83. Variation of the Spanwise Maximum Stanton Number Reduction with the Blowing Ratio(x/d_o=6.4)

Table 5. The Influence of the Injection Angle, β, on M^*_{opt} and $[1-(St_{FC}/St_o)]^*$

θ_i	x/d_o	β	M^*_{opt}	$[1-(St_{FC}/St_o)]^*_{MAX}$
40	8.0	25 35 45	1.07 .78 .60	0.40 0.31 0.12
30	8.0	25 35	1.10 .90	0.245 0.235
20	8.0	25 35	1.25 .90	0.18 0.22
40	6.4	25 35 45	1.22 .85 .75	0.37 0.235 0.100
30	6.4	25 35	1.13 .85	0.26 0.29
20	6.4	25 35	1.00 .85	0.24 0.165

injection angle, β, was increased. At a location of $\theta_i = 40°$, the value of $[1-(St_{FC}/St_o)]^*_{MAX}$ also decreased as the injection angle was increased. However, moving closer to stagnation ($\theta_i = 30°$ or $20°$), this trend was not observed. The value of $[1-(St_{FC}/St_o)]^*_{MAX}$ for $\theta_i = 30°$ was essentially the same for β of $25°$ and $35°$. For $\theta_i = 20°$, the value of $[1-(St_{FC}/St_o)]^*_{MAX}$ at $x/d_o = 8.0$ increased somewhat as β was increased, while at $x/d_o = 6.4$ the opposite trend was observed.

The predominate trend observed throughout Figs. 81 and 83 was that, for given values of β, θ_i, and x/d_o, the value of $[1-(St_{FC}/St_o)]^*$ reached a maximum at a particular blowing ratio, M^*_{opt}. These trends are consistent with previous investigations by LeBrocq, Launder, and Pridden [49], Goldstein, Eckert, and Burggraf [23] and Launder and York [35], indicating an increase in the film cooling effectiveness with increasing M in the low M range due to an increase in the coolant thermal capacity, followed by a deterioration of the effectiveness in the high M range ($M > M^*_{opt}$) due to penetration of the coolant and enhanced mixing with the freestream. For low values of the blowing ratio, the freestream-coolant mixing is held to a minimum, and a larger coolant mass addition (larger M) leads to improved film cooling performance. This feature is clearly evident in Figs. 81 and 83 with a linear trend of $[1-(St_{FC}/St_o)]^*$ vs. M at low values of the blowing ratio, independent of the value of β. As long as the coolant jet penetration into the freestream is minimal, the injection angle β had no influence, and the film cooling performance continually increased as the blowing ratio was increased. However, for a sufficiently large value of the blowing ratio, the coolant jet penetrates into the freestream, allowing

the freestream flow to pass underneath the jet, greatly enhancing the mixing process. Thus, as the blowing ratio is increased, the increased mixing starts to degrade the effects of coolant mass addition and the film cooling effectiveness (or Stanton Number Reduction) reaches a maximum value as demonstrated in Figs. 81 and 83. Increasing M above M^*_{opt} lead to a rapid deterioration in the film cooling performance as the detrimental effects of increased mixing completely overwhelmed the beneficial effects of increased mass addition.

Since the penetration of the coolant plays such a significant role in the mixing process, the injection hole angle is important in determining the optimum blowing ratio. With a steeper injection angle, significant penetration of the coolant can be expected to occur at a smaller value of the blowing ratio. Therefore, as Figs. 81(a) and 83(a) have shown, the data for an injection angle of 45° deviated from the linear trend first, followed by the data for β = 35°, and then β = 25°.

In addition to the influence of the injection angle, β, on the value of the optimum blowing ratio, the injection angle also influenced the spanwise location along the surface where the maximum Stanton Number Reduction occurred. Previously, in Fig. 79, the location $(z/s)^*$ was defined and, for β = 25°, was observed to fall in the range of 0.50 to 0.65. Increasing the injection angle to β = 35°, as shown in Fig. 80, the location $(z/s)^*$ fell in the range of 0.35 to 0.45. A more comprehensive illustration of the variation of $(z/s)^*$ with β and M was prepared from the data in Appendix VI and is shown in Fig. 84. The solid curves represent data farings for $M \leq M^*_{opt}$. The data for

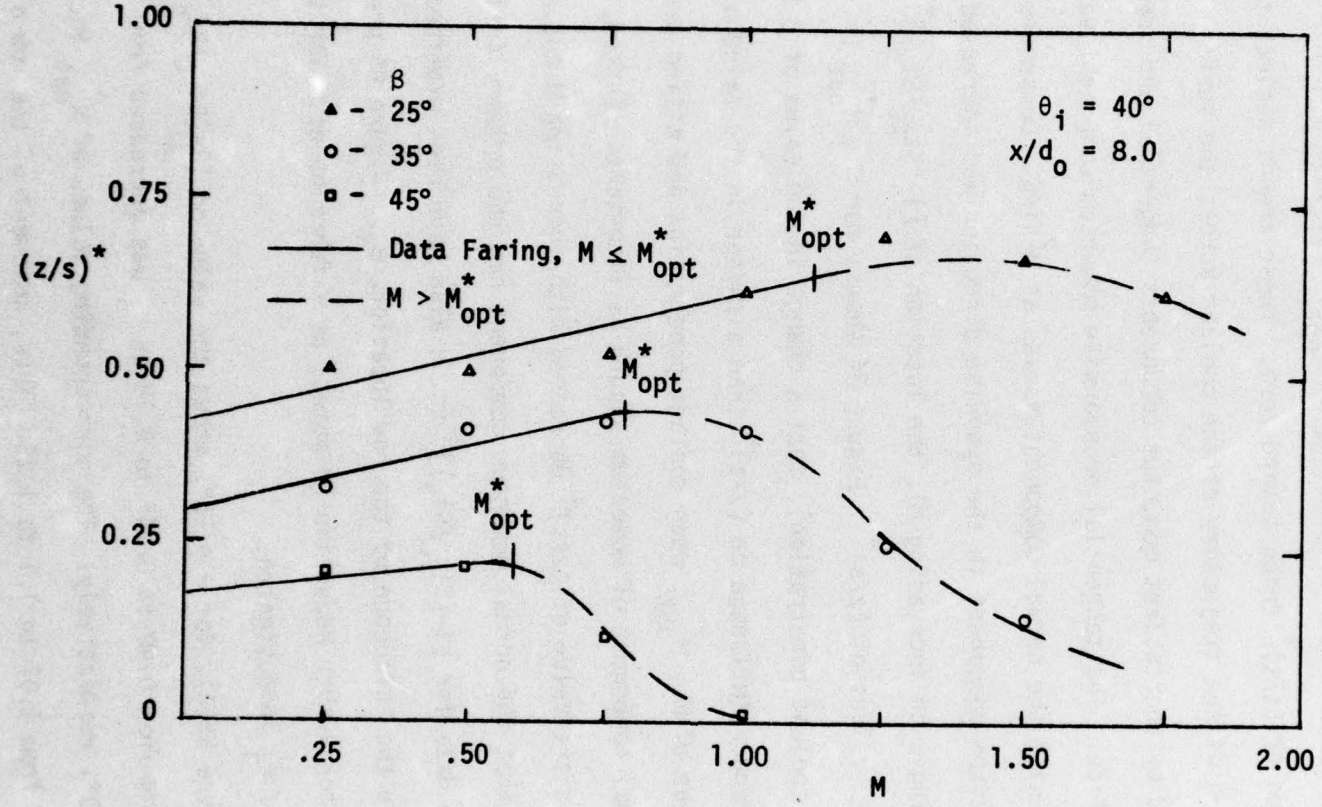

Figure 84. The Influence of the Injection Angle, β, on the Location of the Spanwise Maximum Stanton Number Reduction

$M \leq M^*_{opt}$ show a substantial increase in the level of $(z/s)^*$ as β was decreased from 45° to 25° and a more gradual increase of $(z/s)^*$ along each faring as M was increased up to M^*_{opt}. For values of $M > M^*_{opt}$, the value of $(z/s)^*$ tends toward zero. These trends reflect the variation of the trajectory of the coolant across the surface which is governed by the coolant momentum components tangential and normal to the surface. The tangential or spanwise momentum component varies as $M^2\cos\beta$ while the normal component varies as $M^2\sin\beta$. Consequently, as the momentum component in the spanwise direction was increased (by decreasing β or increasing M), the location of $[1-(St_{FC}/St_o)]^*$ shifted to larger values of $(z/s)^*$. Figure 84 shows, for $M \leq M^*_{opt}$ (i.e. minimal coolant penetration), that a change in the value of β had a much stronger influence on $(z/s)^*$ than a change in the value of M. For values of $M > M^*_{opt}$, when coolant penetration and mixing predominate, the normal component of momentum should be important. Indeed, the data show that the value of $(z/s)^*$ decreased with increasing M and β, suggesting that the normal momentum component had the primary influence.

The data for $[1-(St_{FC}/St_o)]^*$ vs. M also have been examined to determine the influence of the row location, θ_i. Figure 85 presents the Stanton Number Reduction (*-point) as a function of M for the three values of θ_i investigated.

Figure 85(a), for $\beta = 25°$, shows the value of $[1-(St_{FC}/St_o)]^*_{MAX}$ decreasing from 0.40 to 0.245 to 0.18 as θ_i was decreased from 40° to 30° to 20°, respectively. The corresponding values of M^*_{opt} increased slightly from 1.07 to 1.1 to 1.25. Thus, movement of the row of holes closer to stagnation resulted in a 50 percent decrease in

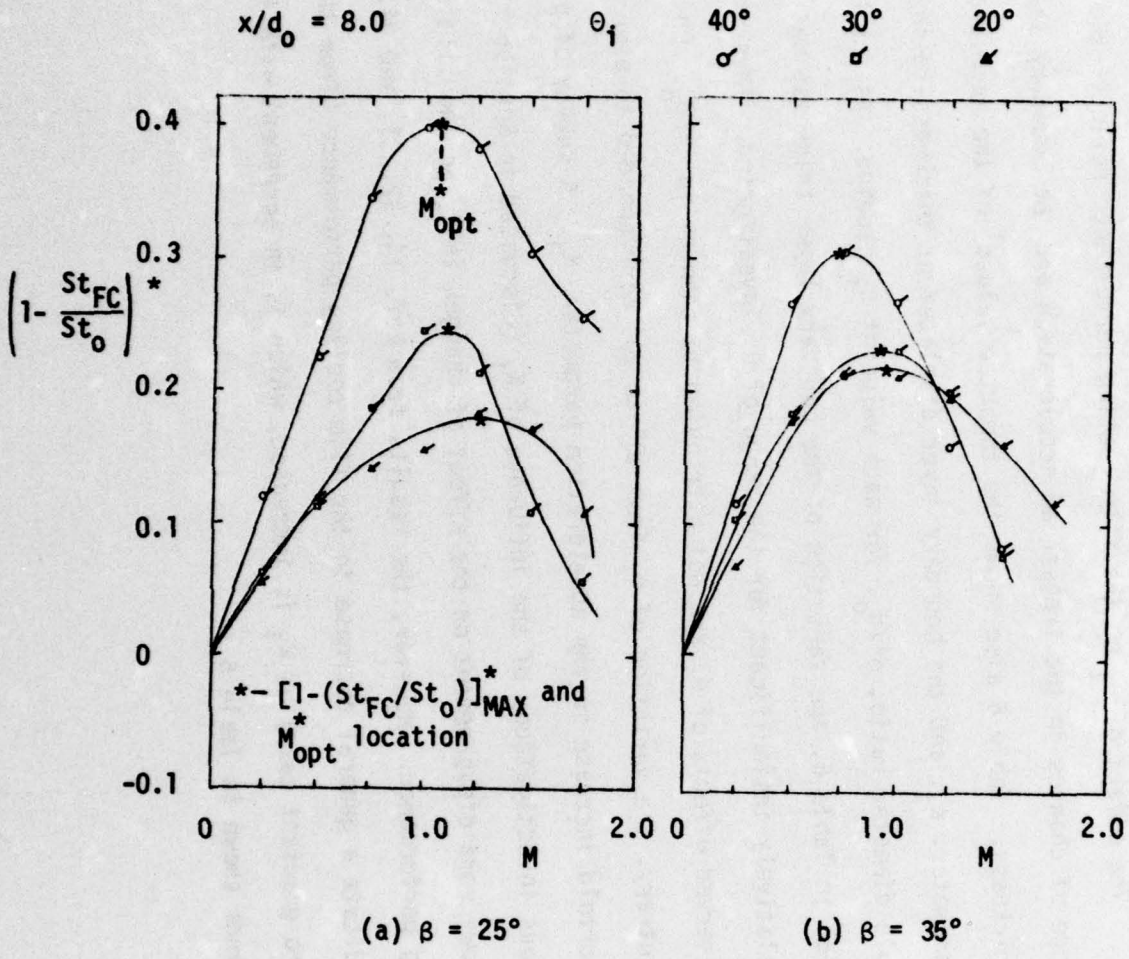

Figure 85. The Influence of the Injection Angle, Θ_i, on the Spanwise Maximum Stanton Number Reduction (x/d_o=8.0)

$[1-(St_{FC}/St_o)]^*_{MAX}$ while the value of M^*_{opt} was relatively unaffected. Figure 83(b) illustrates similar trends for the data with $\beta = 35°$ and a summary of the results indicating the influence of θ_i is presented in Table 6.

The effect of θ_i on the film cooling performance reflects the influence of changes in the freestream acceleration and the boundary layer thickness. Table 6 also shows the computed values† of the acceleration parameter, K_i, and the boundary layer displacement thickness-to-injection hole diameter ratio, δ^*/d_o, for each value of θ_i studied. As can be seen in Table 6, the variation of the boundary layer thickness was relatively insignificant for the range of θ_i investigated. Thus, the observed effects of θ_i are not attributed to changes in δ^*/d_o. On the contrary, the variation of θ_i from 40° to 20° corresponded to over a fourfold increase in the acceleration parameter, K_i. A survey of previous investigations of the influence of K_i (discussed in Section I.C.5.) shows some disagreement on the effect of changes in K_i on the film cooling performance. However, the results from Ref. 14, 32, 33, and 34, indicate a general decrease in the film cooling performance (from the zero gradient case) as K_i is increased, which is in agreement with the trends shown in Table 6.

†See Section II.C. for the method of computation.

Table 6 The Influence of Row Location, θ_i, on M^*_{opt} and $[1-(St_{FC}/St_o)]^*_{MAX}$ $(x/d_o = 8.0)$

Injection Location	β	M^*_{opt}	$[1-St_{FC}/St_o]^*_{MAX}$
$\theta_i = 40°$ $K_i = 1.1\times10^{-5}$ $\delta^*/d_o = 0.028$	25° 35° 45°	1.07 .78 .60	0.40 0.31 0.12
$\theta_i = 30°$ $K_i = 2.1\times10^{-5}$ $\delta^*/d_o = 0.027$	25° 35°	1.10 .90	0.245 0.235
$\theta_i = 20°$ $K_i = 4.8\times10^{-5}$ $\delta^*/d_o = 0.026$	25° 35°	1.25 .70	0.18 0.22

III.D.2. Data for Spanwise Averaged Stanton Number Reduction Data

The spanwise variation of $[1-(St_{FC}/St_o)]$ was used to calculate a "spanwise averaged Stanton Number Reduction" designated as $[1-(St_{FC}/St_o)]_{AVG}$. The spanwise averaged values were determined by graphical integration using data farings such as those shown in Figs. 79 and 80 and in Appendix VI. Figure 86 presents the spanwise averaged film cooling performance as a function of the blowing ratio, M, for $\beta = 25°$ and three downstream locations (x/d_o).

Figure 86(a), for $\theta_i = 40°$, shows that the spanwise averaged film cooling performance at the distances $x/d_o = 6.4$ and 8.0 was approximately the same, with a maximum value (designated as $[1-(St_{FC}/St_o)]_{AVG,MAX}$) of ~0.19 occurring at $M_{opt} \approx 1.00$. As the blowing ratio was increased above M_{opt}, the film cooling performance for both values of x/d_o decreased substantially. At the downstream distance $x/d_o = 15.2$, the film cooling performance had deteriorated to a negligible level.

The results in Fig. 86(b), for $\theta_i = 30°$, follow similar trends. Again, the film cooling performance for $x/d_o = 6.4$ and 8.0 were essentially the same while the performance at $x/d_o = 15.2$ was negative. The same observations are made for the data at $\theta_i = 20°$, shown in Fig. 86(c).

Similar results are presented in Fig. 87 for the injection angle, $\beta = 35°$. Figure 87(a), for $\theta_i = 40°$, shows again that the film cooling performance for $x/d_o = 6.4$ and 8.0 was essentially the same with a maximum value of 0.19 occurring at a blowing ratio of ~0.67. Downstream at $x/d_o = 15.2$, the film cooling performance had again deteriorated to negative levels. Comparing Figs. 86(a) and 87(a) for different values of β, the value of $[1-(St_{FC}/St_o)]_{AVG,MAX}$ was essentially the same for

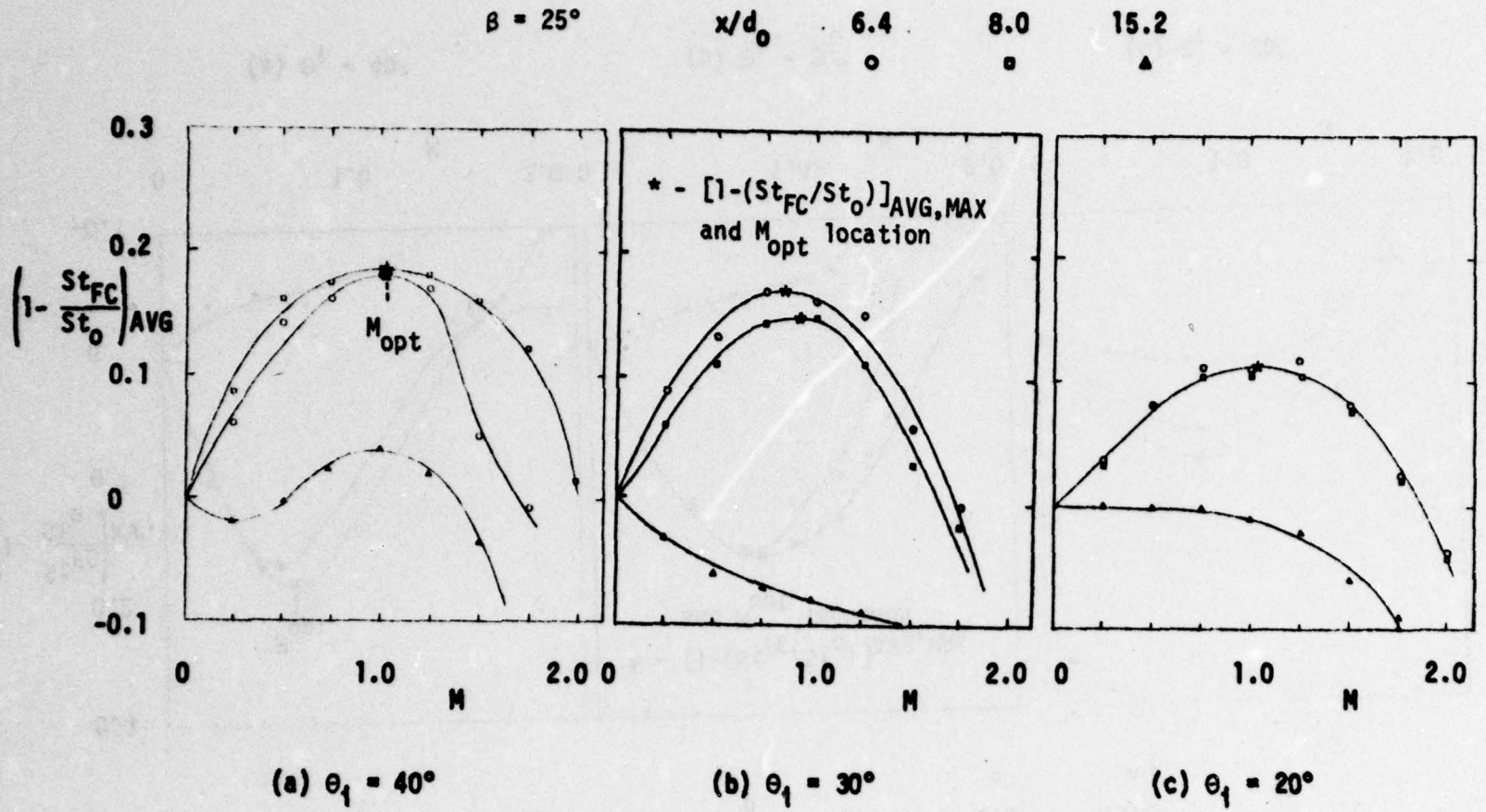

Figure 86. Variation of the Spanwise Averaged Stanton Number Reduction with the Blowing Ratio (β=25°)

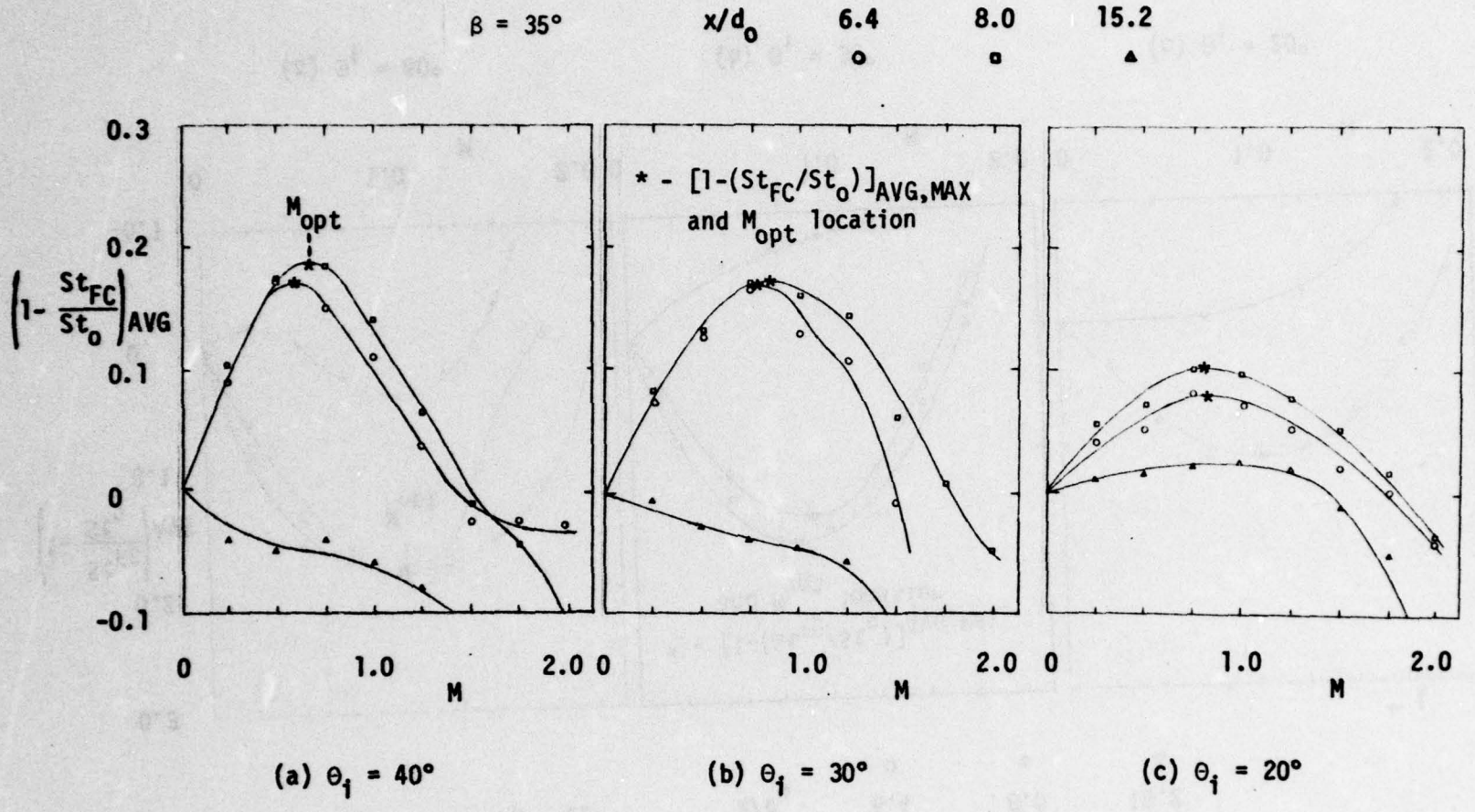

Figure 87. Variation of the Spanwise Averaged Stanton Number Reduction with the Blowing Ratio (β=35°)

β = 25° and 35°, while the value of M_{opt} decreased as the injection angle, β, was increased. The film cooling performance for θ_i = 30° in Fig. 87(b) and Fig. 87(c) for θ_i = 20° showed similar trends. The data for β = 45° at the location θ_i = 40° are shown in Fig. 88.

A comparison of Figs. 86, 87, and 88 shows that the spanwise averaged Stanton Number Reduction for x/d_o = 6.4 and 8.0 was essentially the same while the values for x/d_o = 15.2 were generally negative. Increasing the injection angle from 25° to 35° was found to have little influence on the value of $[1-(St_{FC}/St_o)]_{AVG,MAX}$. However, increasing β to 45° (at θ_i = 40° only) resulted in a large decrease in the value of $[1-(St_{FC}/St_o)]_{AVG,MAX}$. The value of M_{opt} decreased as β was increased from 25° to 45°. Table 7 summarizes the numerical values for x/d_o = 8.0. It can be seen that moving the row of holes closer to stagnation (θ_i decreasing) resulted in a decrease in the level of $[1-(St_{FC}/St_o)]_{AVG,MAX}$, but the value of M_{opt} and the influence of β on the level of $[1-(St_{FC}/St_o)]_{AVG,MAX}$ was relatively independent of θ_i.

Therefore, the trends established by the spanwise averaged results were very similar to those found from the *-data. As the location of the row of holes was brought closer to stagnation, both the spanwise averaged and the *-data showed the film cooling performance decreased substantially, while the value of M_{opt} increased slightly. Also, both types of results demonstrated that increasing the injection angle, β, led to a decrease in the optimum blowing ratio, and that increasing β from 25° to 45° resulted in a significant decrease in the Stanton Number Reduction. However, for the *-data, the spanwise maximum film cooling performance for θ_i of 40° decreased ~22% as β was increased from 25° to

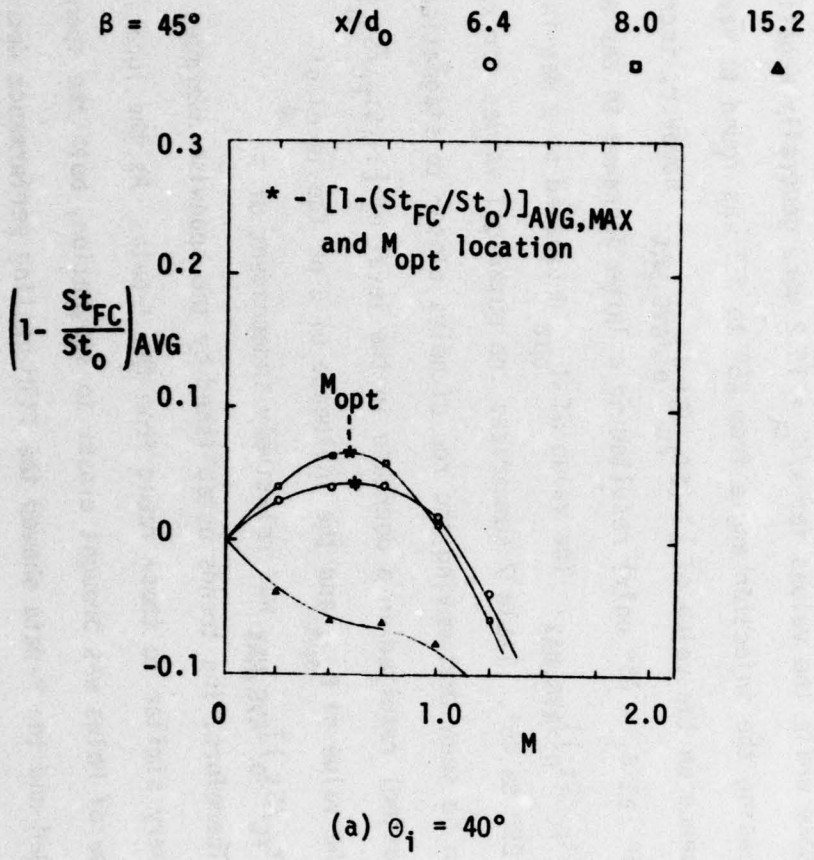

(a) $\Theta_i = 40°$

Figure 88. Variation of the Spanwise Averaged Stanton Number Reduction with Blowing Ratio (β=45°)

Table 7 The Spanwise Averaged Stanton Number Reduction Results ($x/d_o = 8.0$)

Injection Location	β	M_{opt}	$[1-St_{FC}/St_o]_{AVG,MAX}$
$\theta_i = 40°$ $K_i = 1.1\times10^{-5}$ $\delta^*/d_o = 0.028$	25° 35° 45°	1.00 0.67 0.57	0.19 0.19 0.065
$\theta_i = 30°$ $K_i = 2.1\times10^{-5}$ $\delta^*/d_o = 0.027$	25° 35°	0.90 0.83	0.15 0.17
$\theta_i = 20°$ $K_i = 4.8\times10^{-5}$ $\delta^*/d_o = 0.026$	25° 35°	1.03 0.83	0.115 0.10

35° while the spanwise averaged results showed that the value of $[1-(St_{FC}/St_o)]_{AVG,MAX}$ remained approximately the same for both angles. It is apparent that the major influence of changing the injection angle from 25° to 35° was to reduce the spanwise nonuniformity of the Stanton Number Reduction such that the spanwise averaged value was unchanged. A significant feature revealed from the averaged results is that the film cooling performance at x/d_o=6.4 and 8.0 were approximately the same while the value of $[1-(St_{FC}/St_o)]_{AVG}$ at the downstream distance x/d_o = 15.2 never exceeded 0.04 and in most cases was negative.

Both the *-data and the spanwise averaged results have shown a definite influence of β on the value of M_{opt}, and the *-data demonstrated the influence of β on the $(z/s)^*$ location. In the next section, correlations are developed to show the influence of the injection angle, β, on M^*_{opt} and $(z/s)^*$.

III.E. Correlation of the Film Cooling Data

The analysis of the data in the previous section showed the variation of the spanwise maximum Stanton Number Reduction, $[1-(St_{FC}/St_o)]^*$, and the corresponding spanwise location, $(z/s)^*$, as the coolant hole angle, β, and the blowing ratio, M, were varied over the ranges investigated. For a given value of β, it was possible to identify an optimum value of the blowing ratio, M^*_{opt}, which resulted in the maximum Stanton Number Reduction, $[1-(St_{FC}/St_o)]^*_{MAX}$. As described previously, the occurrence of an optimum blowing condition is associated with a balance between the beneficial influence of an increased coolant thermal capacity and the detrimental influence of enhanced mixing between the coolant and the

freestream. The detrimental effect of enhanced coolant-freestream mixing is expected to become significant as the coolant detaches from the surface and penetrates into the freestream. Therefore, the parameter influencing the coolant jet detachment from the surface should have a strong influence on the optimum blowing ratio.

Similarly, with the spanwise distributions of the Stanton Number Reduction, it was possible to identify a spanwise location, $(z/s)^*$, where the maximum Stanton Number Reduction was observed. As discussed in the previous section, the variation of $(z/s)^*$ with β and M is associated with the momentum components of the coolant jet tangential and normal to the surface. Apparently the momentum components, which are functions of β and M, influence the coolant trajectory as long as the coolant jet remains attached to the surface. In the following sections, the data are correlated to show the influence of both β and M on the spanwise maximum film cooling performance.

III.E.1. Linear Film Cooling Range

Figures 81 and 83 in Section III.D.1. showed the variation of $[1-(St_{FC}/St_o)]^*$ as a function of the blowing ratio, M, for each value of β investigated. All of the figures showed a linear trend of $[1-(St_{FC}/St_o)]^*$ with M at low values of the blowing ratio. As previously discussed, the linear trend was independent of the injection angle as long as the blowing ratio was below some limiting value. The linear range is associated with minimum penetration of the coolant and minimum freestream-coolant mixing. Thus, increasing the blowing ratio improved the film cooling performance due to the increased thermal capacity of the coolant. However, when the blowing ratio exceeded the limiting

value, the coolant jet penetration increased the freestream-coolant mixing, counteracting the beneficial influence of the mass addition, and the film cooling performance began to deviate from the linear behavior. The occurrence of the deviation from the linear trend, which was attributed to the increase in the coolant jet penetration, was influenced by the injection angle.

The data in the linear range ($M \leq M_{limit}$) are represented by the equation

$$[1-(St_{FC}/St_o)]^* = \text{Slope} \times M \qquad (40)$$

Table 8 summarizes the values of the slope obtained from Figs. 81 and 83 for selected values of θ_i and x/d_o. The values of the blowing ratio, M_{limit}, defining the upper limit of the linear range are also listed. Table 8 reveals a general trend that moving the row of holes closer to stagnation (θ_i decreasing) results in a decrease in the slope and a corresponding decrease in the magnitude of the film cooling performance. For values of $M < M_{limit}$, Eq. (40) can be applied to estimate $[1-(St_{FC}/St_o)]^*$ using the values indicated in Table 8. For values of $M > M_{limit}$, Figs. 81 and 83 would have to be used directly to estimate the spanwise maximum Stanton Number Reduction.

III.E.2. Correlation of M^*_{opt}

The data from Table 5 in Section III.D.1., showing the variation of M^*_{opt} with β were examined to determine what fluid dynamic parameter best characterizes the occurrence of maximum film cooling performance. Previous investigations have had some success in correlating the optimum coolant blowing condition by examining the momentum flux ratio

Table 8

The Slope of the Stanton Number Reduction for Low Blowing Ratios

θ_i	x/d_o	Slope	β	M_{limit}
40°	8.0	.470	25° 35° 45°	.78 .62 .20
30°	8.0	.290	25° 35°	.70 .78
20°	8.0	.280	25° 35°	.35 .75
40°	6.4	.360	25° 35° 45°	.75 .60 .12
30°	6.4	.370	25° 35°	.53 .72
20°	6.4	.270	25° 35°	.88 .54

($I = \rho_c V_c^2/\rho_\infty V_\infty^2$) or the velocity ratio (V_c/V_∞) as discussed in the literature review presented in Section I.C.3. Goldstein, Eckert, and Burggraf [23] were successful in correlating their maximum film cooling effectiveness data using the momentum flux ratio. Pedersen [22] found the best correlation of centerline maximum effectiveness data using the velocity ratio. Following these ideas, the data from the present study were examined in terms of both the momentum flux and velocity ratios in an attempt to correlate the variation of the optimum coolant blowing ratio, M^*_{opt}, as a function of the injection angle.

Table 9 presents the data (M^*_{opt} vs. β) previously summarized in Table 5. The pertinent values of the density ratio (ρ_c/ρ_∞) are shown and the corresponding calculated values of the velocity ratio $(V_c/V_\infty)^*$ and the momentum flux ratio $(\rho_c V_c^2/\rho_\infty V_\infty^2)^*$ are listed. It can be seen that for spanwise injection in the stagnation region, neither $(V_c/V)^*$ nor I^* correlate the variation of M^*_{opt} with β. For selected values of θ_i, x/d_o, the values of $(V_c/V_\infty)^*$ and I^* vary significantly with β.

It will be recalled from previous discussions that the occurrence of optimum film cooling performance at M^*_{opt} is associated with the balance of the beneficial influence of increased coolant thermal capacity and the detrimental influence of penetration by the coolant and enhanced mixing with the freestream. At low values of the blowing ratio the film cooling performance followed a linear trend with respect to M independent of the injection angle, indicating minimal coolant jet penetration. However, as M was increased, the film cooling performance deviated from the linear behavior apparently due to increased coolant penetration and enhanced coolant-freestream mixing. Therefore, it is expected that the

Table 9

The Influence of the Injection Angle, β, on the Optimum Blowing Ratio

θ_i	x/d_o	β	M_{opt}	ρ_c/ρ_∞	$(V_c/V_\infty)^*$	$(I)^*$	$(V_c/V_\infty \sin\beta)^*$	$(I\sin\beta)^*$
40°	8.0	25°	1.07	2.31	.463	.495	.196	.209
		35°	.78	2.26	.345	.269	.198	.154
		45°	.60	2.23	.269	.161	.190	.114
30°	8.0	25°	1.10	2.22	.495	.545	.209	.230
		35°	.90	2.23	.404	.363	.232	.208
20°	8.0	25°	1.25	2.18	.573	.716	.242	.302
		35°	.90	2.23	.404	.363	.231	.208
40°	6.4	25°	1.22	2.36	.516	.631	.218	.267
		35°	.85	2.29	.371	.316	.213	.181
		45°	.75	2.25	.333	.249	.235	.176
30°	6.4	25°	1.13	2.24	.505	.571	.213	.241
		35°	.85	2.25	.377	.320	.216	.184
20°	6.4	25°	1.00	2.15	.465	.465	.196	.196
		35°	.85	2.16	.394	.334	.226	.192

value of M^*_{opt} is governed by parameters characterizing the extent of the coolant penetration. It will be recalled that both the *-data and the spanwise averaged results showed the optimum blowing ratio decreasing as the injection angle increased. Thus, it was reasoned that perhaps the normal component of the velocity ratio or the momentum flux ratio is the dominate parameter than governs the penetration of the coolant jet and may be useful in correlating data for the M^*_{opt}.

The values of the normal components of the velocity ratio, $(V_c/V_\infty \sin\beta)^*$, and the momentum flux ratio, $(I\sin\beta)^*$, are presented in Table 9. It can be seen for the different combinations of β, θ_i, and x/d_o presented, the normal component of the momentum flux ratio varied from 0.11 to 0.30. However, the normal component of the velocity ratio remained relatively constant, falling in the range of 0.19 to 0.24. For any selected combination of θ_i, x/d_o, the normal component of the velocity ratio was constant with ±7.5% or less. Therefore, it was concluded that the normal component of the velocity ratio is the dominate factor in determining the optimum coolant blowing ratio for the range of conditions investigated.

The coolant blowing ratio for the optimum local film cooling performance can be correlated as

$$M^*_{opt} = \left(\frac{\rho_c}{\rho_\infty}\right) \frac{VR_{opt}}{\sin\beta} \tag{41}$$

where

$$VR_{opt} = \left(\frac{V_c}{V_\infty}\right) \sin\beta \approx \text{constant}$$

The values for VR_{opt} are shown in Table 9.

To further illustrate the utility of the normal component of velocity ratio to correlate the maximum film cooling performance data,

The data in Fig. 81(a) have been replotted in Fig. 89 using $(V_c/V_\infty)\sin\beta$ as the pertinent blowing parameter. As can be seen, all three curves reach a maximum peak value of $[1-(St_{FC}/St_o)]^*$ at approximately the same value of $(V_c/V_\infty)\sin\beta$.

III.E.3. Correlation of $(z/s)^*$

Figure 84 in Section III.D.1. showed the variation of $(z/s)^*$ with M and β. The coolant location $(z/s)^*$ is directly influenced by the trajectory of the coolant jet along the surface. If the coolant jet remains near the surface, the coolant trajectory is expected to be primarily governed by the coolant jet momentum as it emerges from the injection hole. The coolant jet momentum flux, represented by the momentum flux ratio, I, can be resolved into two components, one along the surface in the spanwise direction, I_z, and another normal to the surface, I_y. In the present study of spanwise angled film coolant holes, I_x was zero.

The momentum flux components, I_y and I_z, were used to correlate the influence of β and M on $(z/s)^*$. Figure 90 illustrates the coolant location $(z/s)^*$ vs. x/d_o for two different injection angles. Data for selected values of I_y and I_z are presented and the lines drawn from the coolant injection hole location ($x/d_o = 0$, $z/s = 0$) indicate the probable trajectory of the coolant along the surface. It can be seen by comparing Figs. 90(b) and 90(a), for $I_y = 0.080 =$ constant, that the coolant trajectory shifted away from the injection hole as I_z was increased from 0.080 to 0.171. Similarly, for $I_z = 0.080 =$ constant, the coolant trajectory shifted closer to the injection hole as I_y was increased from 0.037 to 0.080. Thus, both of the components, I_y and I_z, have an influence on the coolant location $(z/s)^*$.

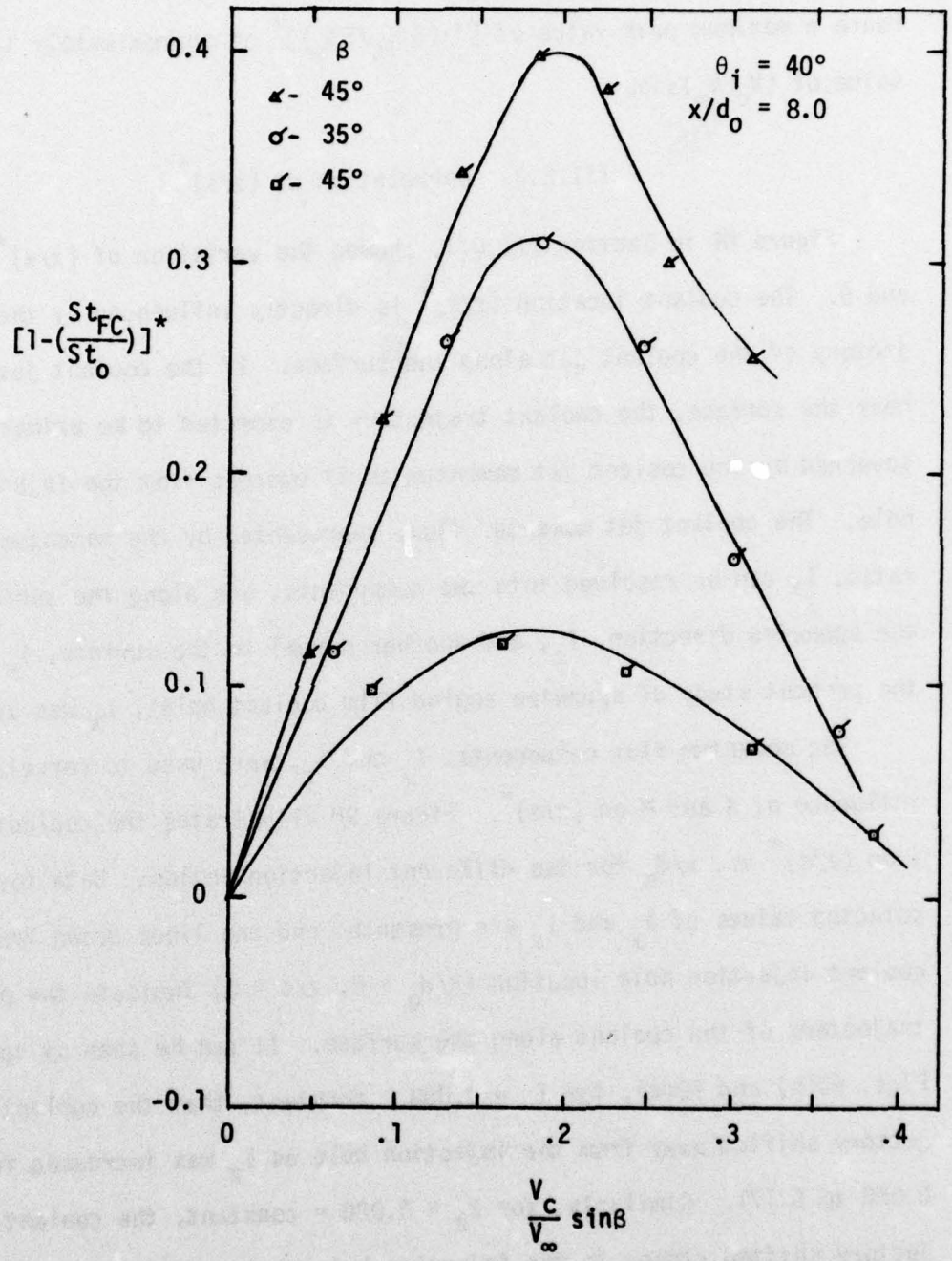

Figure 89. Variation of the Stanton Number Reduction with the Vertical Component of the Velocity Ratio

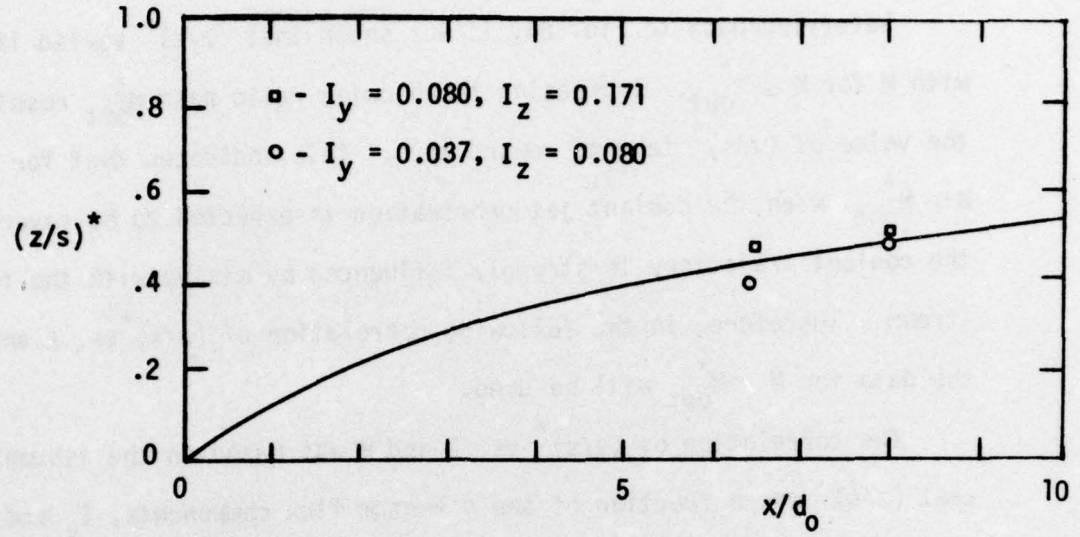

a) β = 25°

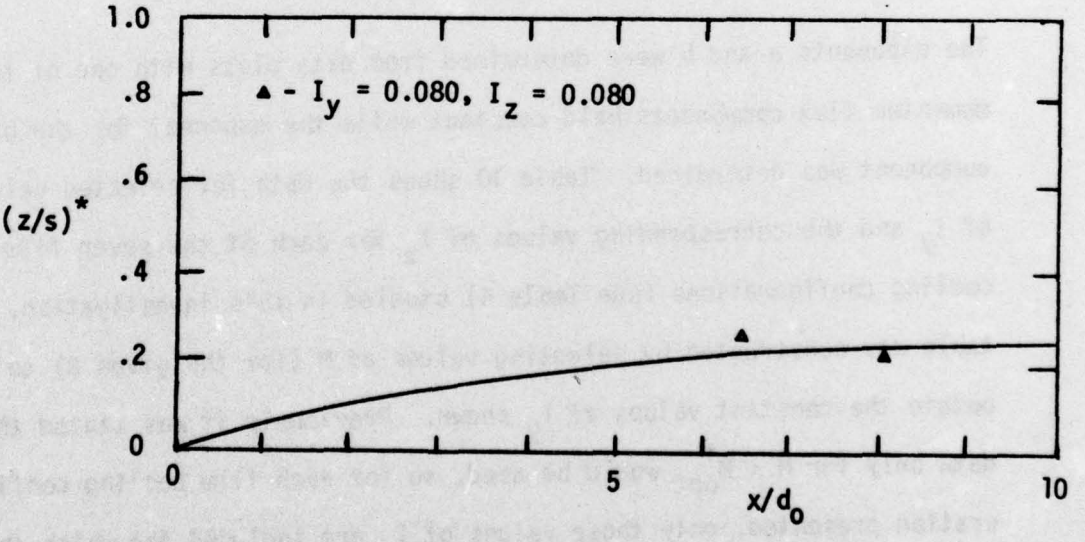

b) β = 45°

Figure 90. Test Surface Location of the Maximum Film Cooling Performance

Referring back to Fig. 84, it was shown that $(z/s)^*$ varied linearly with M for $M \leq M^*_{opt}$. Increasing the blowing ratio past M^*_{opt} resulted in the value of $(z/s)^*$ tending toward zero. This indicates that for $M > M^*_{opt}$, when the coolant jet penetration is expected to be severe, the coolant trajectory is strongly influenced by mixing with the free-stream. Therefore, in the following correlation of $(z/s)^*$ vs. β and M, the data for $M < M^*_{opt}$ will be used.

The correlation of $(z/s)^*$ vs. β and M was based on the assumption that $(z/s)^*$ was a function of the momentum flux components, I_y and I_z, represented by the following equation.

$$(z/s)^* = CI_z^a I_y^b \tag{42}$$

where C, a, b are constants

The exponents a and b were determined from data plots with one of the momentum flux components held constant while the exponent for the other component was determined. Table 10 shows the data for selected values of I_y and the corresponding values of I_z for each of the seven film cooling configurations (see Table 4) studied in this investigation. The table was constructed by selecting values of M (for the given β) to obtain the constant values of I_y shown. Previously it was stated that data only for $M < M^*_{opt}$ would be used, so for each film cooling configuration presented, only those values of I_y are included for which the corresponding blowing ratio was less than M^*_{opt}.

The I_y component is a function of the injection angle, β, and as Table 10 reveals, in order to obtain I_y = constant, the blowing ratio had to decrease as the injection angle, β, increased. Therefore many

Table 10

Blowing Ratios and $(z/s)^*$ Coolant Locations for Constant Values of the Spanwise Momentum Component, I_y, at $x/d_o = 8.0$

β	θ_i	M	I	I_y	I_z	$(z/s)^*$
25°	40°	.225	.024	.010	.022	.50
		.325	.049	.020	.044	.50
		.440	.088	.037†	.080	.50
		.515	.119	.050	.108	.50
		.650	.189	.080	.171	.50
		.810	.290	.123	.263	.56
		.930	.378	.160	.342	.58
		1.05	.477	.202	.433	.64
35°	40°	.195	.018	.010	.014	.33
		.280	.036	.020	.030	.33
		.440	.087	.050	.072	.35
		.560	.140	.080	.115	.40
		.695	.214	.123	.175	.41
		.80	.282	.161	.231	.38
45°	40°	.175	.014	.010	.010	.19
		.250	.029	.020	.020	.20
		.395	.072	.050	.050	.22
		.500	.113	.080	.080	.22
25°	30°	.220	.024	.010	.021	unif‡
		.315	.047	.020	.042	unif
		.510	.118	.050	.107	unif
		.650	.191	.080	.173	.51
		.805	.292	.123	.265	.56
		.920	.380	.160	.344	.58
		1.03	.476	.201	.431	.61
35°	30°	.190	.017	.010	.014	.16
		.280	.037	.020	.030	.18
		.440	.088	.050	.072	.18
		.560	.141	.080	.116	.19
		.690	.213	.123	.174	.19
		.790	.278	.160	.228	.22

†This value was included since the $(z/s)^*$ location was presented in Fig. 90(a).

‡The designation unif means that the spanwise distribution was too uniform to identify a $(z/s)^*$ location.

Table 10 (Cont'd)

β	θ_i	M	I	I_y	I_z	$(z/s)^*$
25°	20°	.220	.024	.010	.021	.48
		.310	.047	.020	.043	.44
		.500	.119	.050	.108	.40
		.630	.187	.080	.170	.39
		.790	.292	.123	.264	.42
		.900	.377	.160	.341	.46
		1.01	.474	.201	.430	.48
35°	20°	.190	.018	.010	.014	.40
		.270	.036	.020	.030	.39
		.425	.087	.050	.071	.41
		.545	.140	.080	.115	.42
		.675	.213	.123	.174	.42
		.775	.279	.160	.229	.42

of the values of the blowing ratio that corresponded to the selected I_y values did not match the blowing ratios for which the film cooling performance was actually measured. For these intermediate values of blowing ratio, it was necessary to use values from the smooth curve data farings in Figs. 72 through 78 (Section III.C.). Figure 91 is presented to demonstrate the procedure that was followed. For the injection angle of 25° (Fig. 91), the values of the blowing ratio corresponding to the selected values of I_y (Table 10) were used to determine the film cooling performance at the three z/s locations where the data were measured. The Stanton Number Reduction was cross plotted as a function of z/s and a smooth curve was fared through the data as in Figs. 79, 80, and Appendix VI. From these spanwise distributions, for the selected value of M and I_y, the $(z/s)^*$ locations were identified and listed in Table 10.

Using the data from six different film cooling configurations,† the log of $(z/s)^*$ was plotted as a function of the log of I_z for constant values of I_y. A linear least squares fit was applied through the data to compute the slope, a. Although the slopes from the least squares fits were not identical for all of the constant I_y values investigated, they fell within a ±15% bandwidth of the mean value of 0.9. Thus the exponent for the I_z momentum flux component was determined as, $a = 0.9$.

To find the exponent b for the I_y momentum flux component, the process was repeated with the I_z component now being held constant. Once again the slopes were not identical for each of the constant I_z

† Data from the film cooling configuration of $\beta = 35°$ and $\theta_j = 30°$ were not used in the correlation; the reason for the elimination of this data will be shown later.

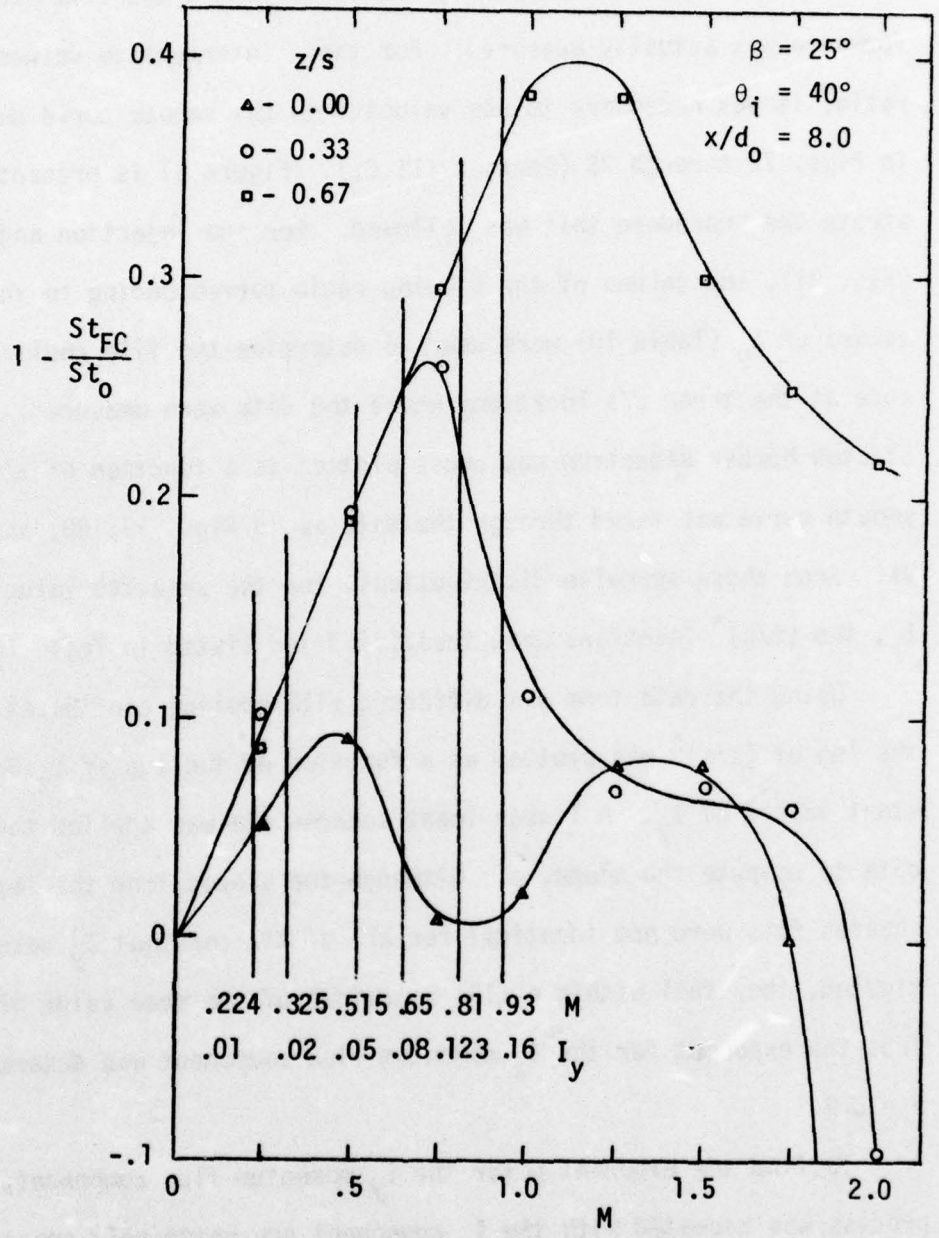

Figure 91. The Identification of the Stanton Number Reduction at Intermediate Blowing Ratios

values investigated, but they all fell within a ±10% bandwidth of the mean value of b = -0.8. Therefore the momentum parameter for correlating $(z/s)^*$ vs. β and M was determined to be $I_z^{0.9}/I_y^{0.8}$. It should be noted that the momentum parameter is strongly dependent on the injection angle, β, and weakly dependent on the blowing ratio, M.

The data for $(z/s)^*$ were plotted as a function of the momentum parameter, $I_z^{0.9}/I_y^{0.8}$, and Fig. 92 shows the resultant correlation for the data at $\theta_i = 40°$, and $x/d_0 = 8.0$. These data were chosen for the basic correlation because they represented the largest effect of film cooling on the heat flux reduction (at $\theta_i = 40°$) and the least data scatter ($x/d_0 = 8.0$). As Fig. 92 demonstrates, the variation of the coolant location $(z/s)^*$ vs. β and M was found to correlate well with the momentum parameter. A linear least squares fit was applied to the data in Fig. 92 and the coolant location $(z/s)^*$ can be represented by the following equation

$$(z/s)^* = 0.36 \left(\frac{I_z^{0.9}}{I_y^{0.8}}\right) - 0.055 \qquad (43)$$

within ±15%.

Figure 93 presents all of the data for $(z/s)^*$ at $x/d_0 = 8.0$ and Eq. (43) is represented by the solid line. As stated earlier, the data for the configuration $\beta = 35°$, $\theta_i = 30°$ were not used in the correlation process because, as Fig. 93 clearly demonstrates, this set of data fell far below the $(z/s)^*$ range established by the rest of the data. However, all of the other data for $x/d_0 = 8.0$ are correlated by Eq. (43). The additional scatter of the data for $\theta_i = 20°$ is not unreasonable since at that location the level of heat flux reduction was small, and small

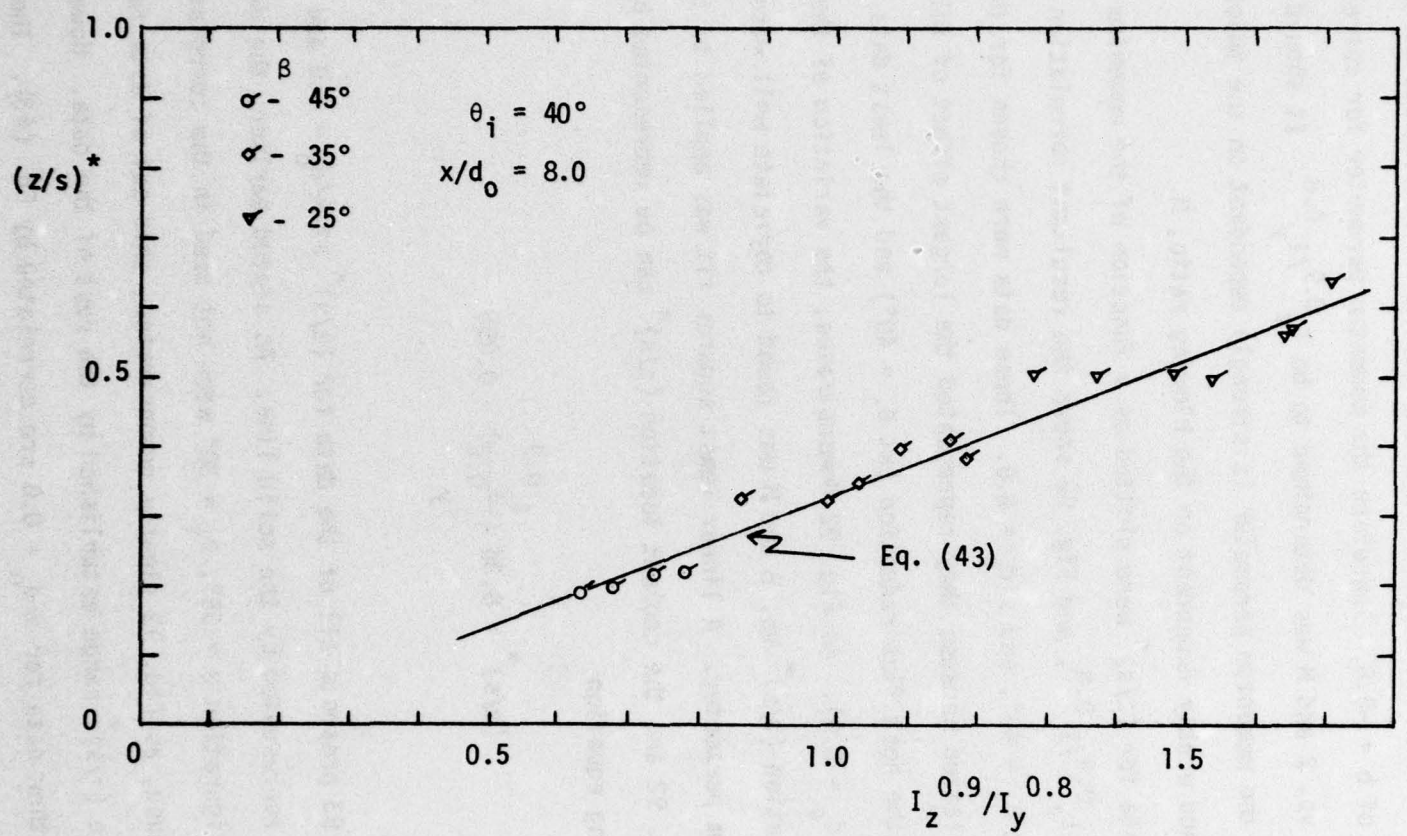

Figure 92. The Variation of $(z/s)^*$ with the Momentum Parameter, $I_z^{0.9}/I_y^{0.8}$ (θ_i=40°, x/d_o=8.0)

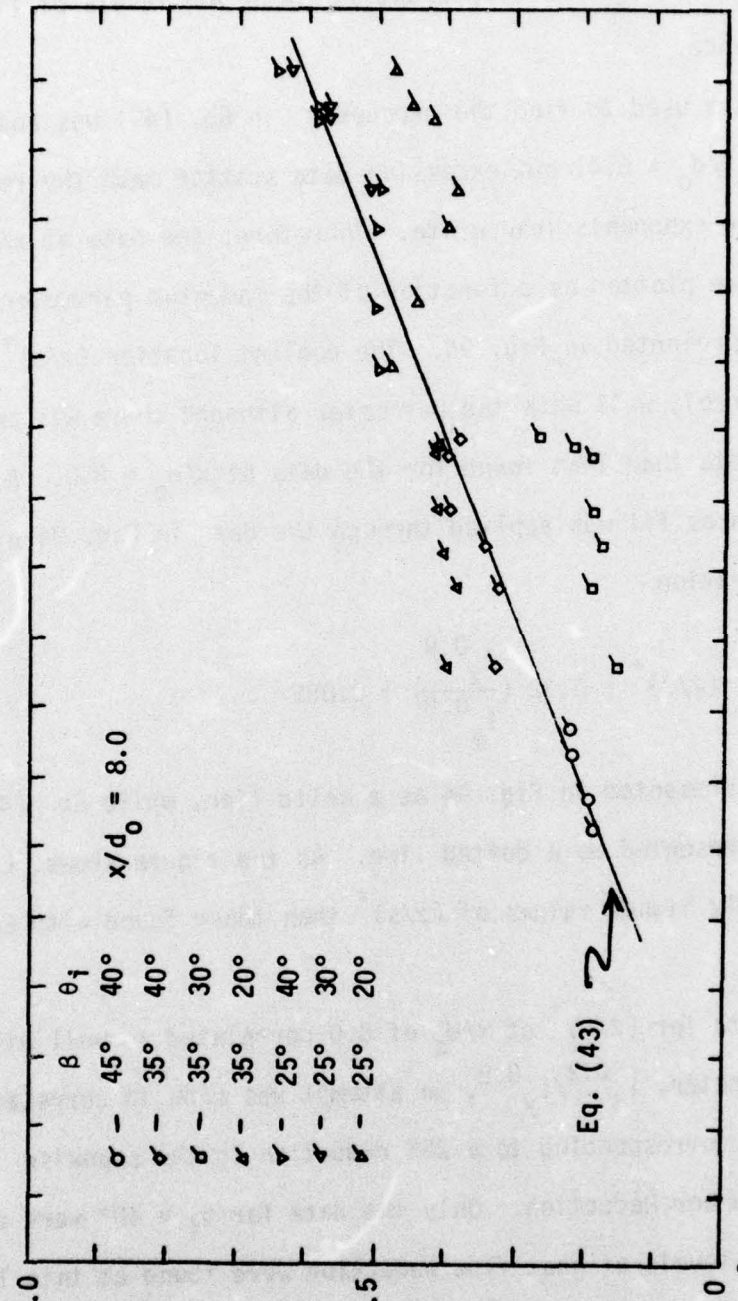

Figure 93. The Variation of $(z/s)^*$ with the Momentum Parameter, $I_z^{0.9}/I_y^{0.8}$ $(x/d_o=8.0)$

experimental errors become more apparent at these low levels of film cooling performance.

The procedure used to find the exponents in Eq. (42) was applied to the data for x/d_o = 6.4, but excessive data scatter made the re-evaluation of the exponents inaccurate. Therefore, the data at x/d_o = 6.4, θ_i = 40° were plotted as a function of the momentum parameter, $I_z^{0.9}/I_y^{0.8}$, and presented in Fig. 94. The coolant location $(z/s)^*$ correlated reasonably well with the parameter although there was more scatter in the data than that found for the data at x/d_o = 8.0. A linear least squares fit was applied through the data in Fig. 94 giving the following equation

$$(z/s)^* = 0.32 \left(\frac{I_z^{0.9}}{I_y^{0.8}}\right) + 0.085 \qquad (44)$$

This equation is presented in Fig. 94 as a solid line, while Eq. (43) from Fig. 92 is presented as a dotted line. As the figure shows, Eq. (44) gives slightly higher values of $(z/s)^*$ than those found with Eq. (43).

Since the data for $(z/s)^*$ at x/d_o of 8.0 correlated so well with the momentum parameter, $I_z^{0.9}/I_y^{0.8}$, an attempt was made to correlate the z/s positions corresponding to a 25% reduction in the spanwise maximum Stanton Number Reduction. Only the data for θ_i = 40° were used, since the highest levels of heat flux reduction were found at this location. Therefore, returning to the spanwise distributions of the Stanton Number Reduction (selected values of M, I_y) that were generated earlier in the correlation procedure, the $[1-(St_{FC}/St_o)]^*$ value was reduced 25% and the z/s locations, $(z/s)_+$, $(z/s)_-$, corresponding to this level of

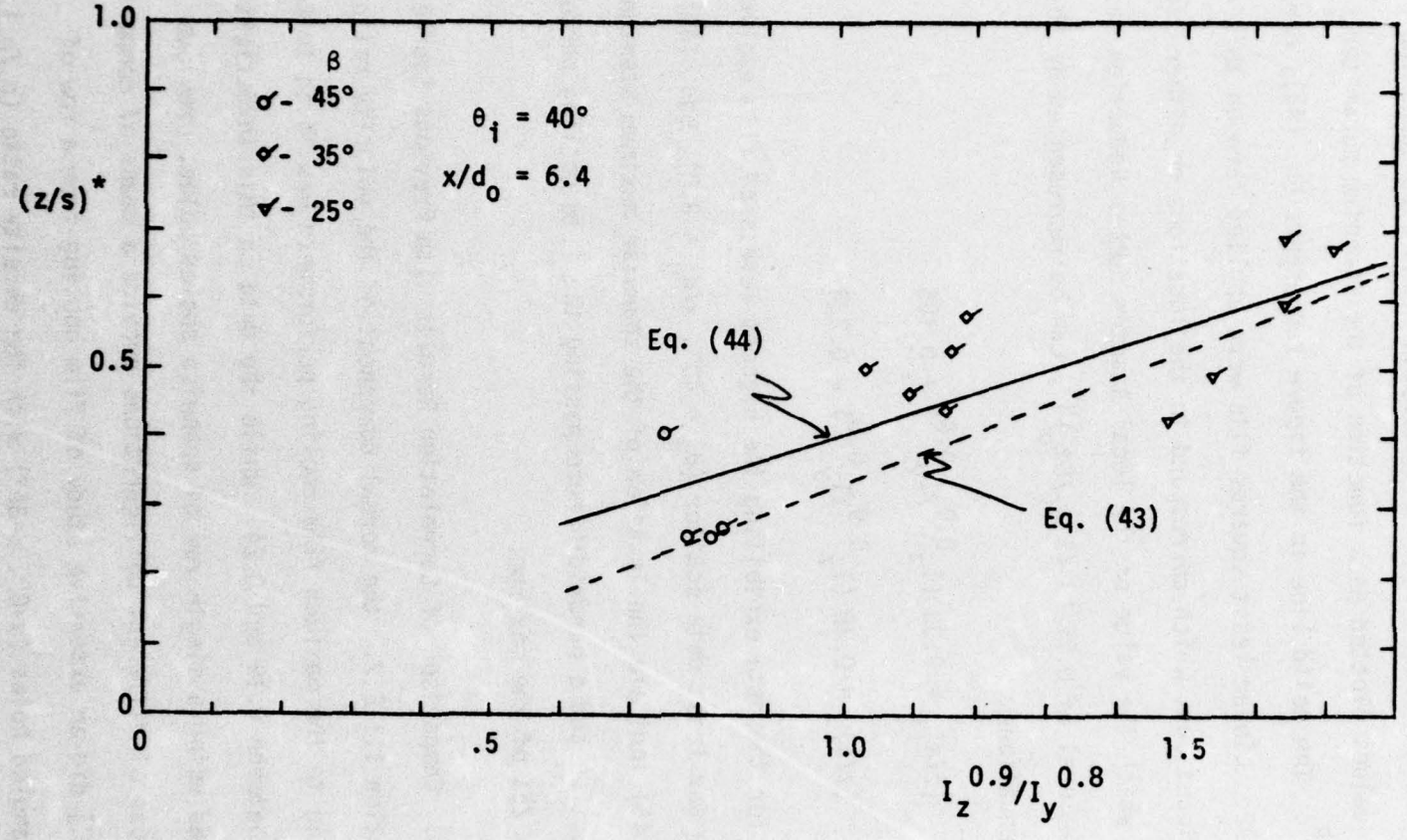

Figure 94. The Variation of $(z/s)^*$ with the Momentum Parameter, $I_z^{0.9}/I_y^{0.8}$ ($\theta_i = 40°$, $x/d_o = 6.4$)

the Stanton Number Reduction were tabulated. Figure 95 shows the $(z/s)_+$ and $(z/s)_-$ values plotted as a function of the momentum parameter, $I_z^{0.9}/I_y^{0.8}$. The solid line in the figure represents Eq. (43), derived from Fig. 92. Linear least squares fits were applied through this data. The (z/s) locations, which correspond to the locations on either side of $(z/s)^*$ for which the value of the local Stanton Number Reduction has fallen to a level of $0.75\ [1-(St_{FC}/St_o)]^*$, can be represented by the following equations.

$$(z/s)_+ = 0.38\ (I_z^{0.9}/I_y^{0.8}) + 0.125 \tag{45}$$

$$(z/s)_- = 0.38\ (I_z^{0.9}/I_y^{0.8}) - 0.238 \tag{46}$$

Therefore, for the data exhibiting the highest levels of film cooling performance and least data scatter ($\theta_i = 40°$, $x/d_o = 8.0$), Eqs. (43), (45), and (46) indicate the location of the spanwise maximum Stanton Number Reduction and a bandwidth encompassing the film cooling performance within 25% of the maximum.

III.E.4. Comparison of Correlation Results with Previous Studies

In Section III.E.2., the normal component of the velocity ratio corresponding to the maximum film cooling performance was found to fall in a range between 0.19 and 0.24. While the data in this investigation were measured using a single row of spanwise angled holes, previous investigations of different configurations provide a means of comparison. Pedersen [22] did an extensive study of film cooling from a row of streamwise angled holes ($\alpha=0°$, $\beta=35°$) with the density ratio (ρ_c/ρ_∞) ranging from 1.18 to 4.22. His results showed that for this range of

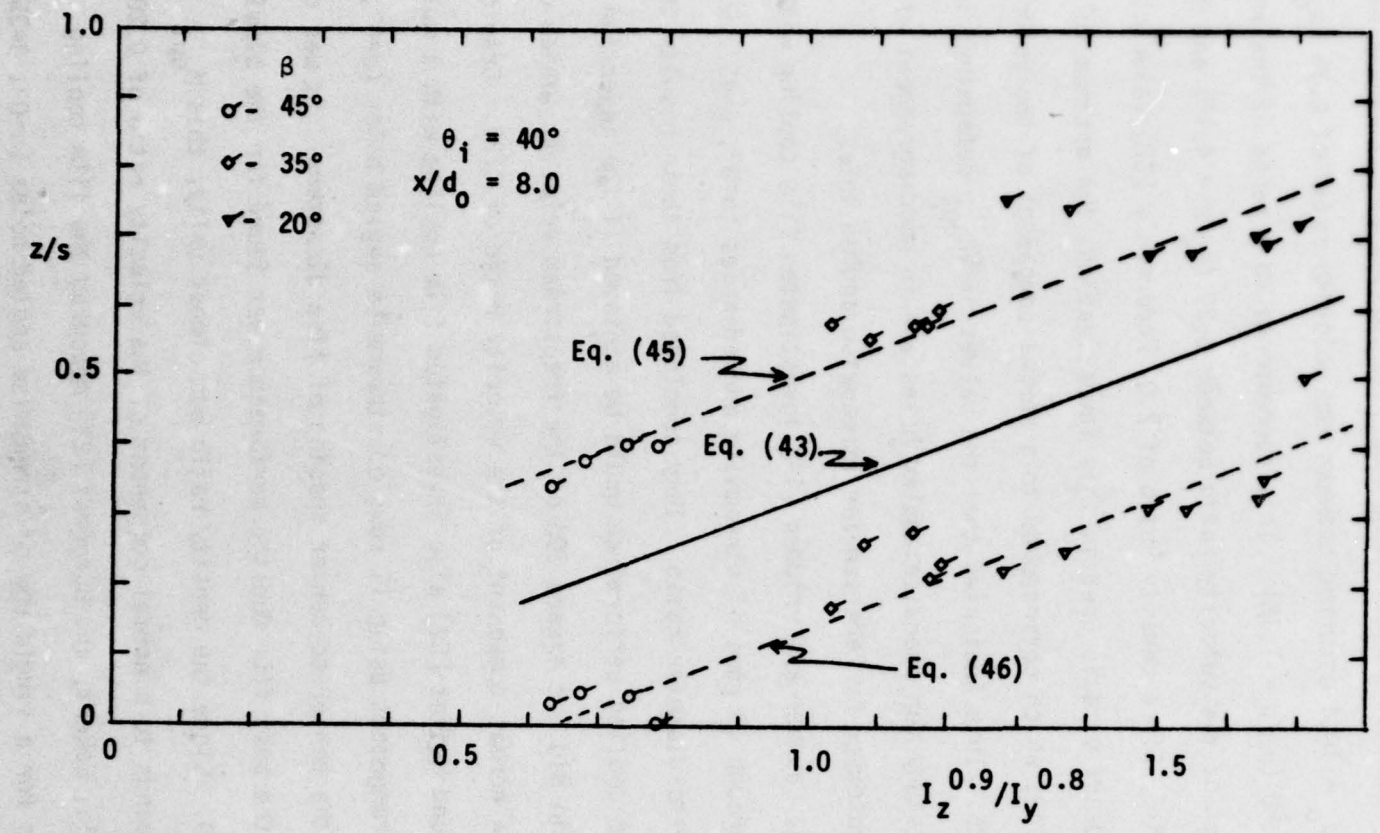

Figure 95. The Variation of the z/s Locations Representing a 25% Reduction in the Spanwise Maximum Stanton Number Reduction with the Momentum Parameter, $I_z^{0.9}/I_y^{0.8}$

density ratios, the maximum centerline film cooling effectiveness at the distance x/d_o = 10.4 occurred between the velocity ratio of 0.38 (ρ_c/ρ_∞= 4.17) and 0.50 (ρ_c/ρ_∞= 1.18). This corresponds to a range of the vertical component of the velocity ratio between 0.22 (ρ_c/ρ_∞= 4.17) and 0.29 (ρ_c/ρ_∞= 1.18). For a density ratio of 2.0, Pedersen's [22] value closest to the 2.2 density ratio used in this investigation, the optimum velocity ratio was 0.43, which corresponds to a normal component of the velocity ratio of 0.25. This indicates that the values of VR_{opt} determined in the subject study for spanwise angled holes are in good agreement with the values observed by Pedersen for streamwise angled holes.

LeBrocq, Launder and Pridden [49] investigated film cooling with injection through 19 rows of streamwise angled holes (α=0°, β=45°) with an 8/1 pitch-to-diameter ratio. They concluded from their results that the best film cooling performance would be achieved if the injection velocity ratio did not exceed 30% of the freestream velocity, which corresponds to a normal component of the velocity ratio of 0.21. Crawford, Choe, Kays, and Moffat [50] also investigated film cooling with a multiple row arrangement using 11 rows of streamwise angled holes (α=0°, β=30°) with the center-to-center spacing of five diameters. It was concluded that the best film cooling performance was found for the blowing ratio of 0.40. Since the density ratio was almost unity, this M_{opt} value corresponds to a normal component of the velocity ratio of 0.20.

Goldstein, Eckert, and Burggraf [23] measured the film cooling effectiveness for a single row of streamwise angled holes (α=0°, β=35°) at a center-to-center spacing of three diameters. With a density ratio of ~0.85, the maximum effectiveness was reached at a blowing ratio of ~0.38. This corresponds to a vertical component of the velocity ratio

of 0.26. However, their investigation of streamwise injection (α=0°, β=35°) from single holes suggests a lower value of VR_{opt} (~0.14 to 0.17). Foster and Lampard [24] investigated film cooling for injection from a single row of normal holes (β=90°) with a center-to-center spacing of three diameters. Their investigation only reported values of the velocity ratio as low as 0.25, but the results do show the film cooling effectiveness for a density ratio of 2.0 continually increasing at the downstream distance of 6.5 diameters as the velocity ratio is decreased to 0.25. Farther downstream, the results indicate that VR_{opt} may vary appreciably with x/d_o.

In view of the complex penetration and mixing phenomena governing film cooling performance, the value of VR_{opt} employed in Eq. (41) is, no doubt, restricted to some range of the hole spacing ratio (s/d_o), the downstream location (x/d_o) and the density ratio (ρ_c/ρ_∞). Nevertheless, the value of VR_{opt} found in this investigation for spanwise angled holes has been found to agree exceptionally well with the VR_{opt} values from previous investigations, and it appears that Eq. 41 may be useful as a simple criterion for estimating the coolant blowing ratio for the optimum local film cooling performance.

It was difficult to compare the results of the $(z/s)^*$ correlation with previous investigations because of the lack of film cooling data using a row of spanwise angled holes. Goldstein, Eckert, Eriksen, and Ramsey [21] did investigate the film cooling performance for a single spanwise angled hole (α=90°, β=35°) and Fig. 24 in Section I.C.3 presented the contours of constant film cooling effectiveness along the surface downstream of injection for the blowing ratios of 0.5 and 1.0.

These footprints were used to establish the spanwise location of the maximum effectiveness point at the downstream distances, x/d_o = 5 and 10. The solid line in Fig. 96 represents the data of Goldstein, et al. [21] showing the coolant trajectory with the line extrapolated back to the coolant injection hole location. Equation (43) was used to compute $(z/s)^*$ for the values of blowing ratio, injection angle, and density ratio (~0.85) corresponding to the experimental conditions of Goldstein, et al. [21]. The values computed from Eq. (43) are shown in Fig. 96 in terms of z/d_o, where $z/d_o = (z/s)^*(s/d_o)$. Figure 96(a), for M of 0.5, shows the value of $(z/d_o)^*$ predicted from Eq. (43) for a row of spanwise angled holes in good agreement with the trajectory for a single hole observed by Goldstein, et al. However, in Fig. 96(b) for M of 1.0, the predicted value of $(z/d_o)^*$ is significantly less than the trajectory for the single hole. This discrepancy could be due to the interference effects that result from a row of holes. At the low blowing ratio of 0.5 when the coolant jet penetration was minimal the coolant trajectories for a single hole or row of holes were the same. However, when the blowing ratio was increased to 1.0 and the coolant penetration became significant, the trajectory of the coolant from a row of holes differed markedly from that from a single hole.

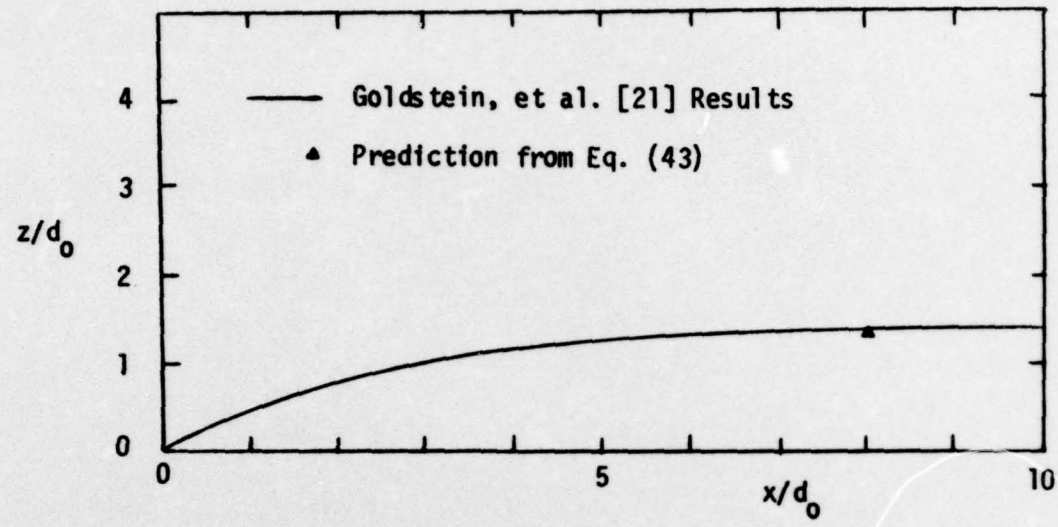

a) M = 0.5

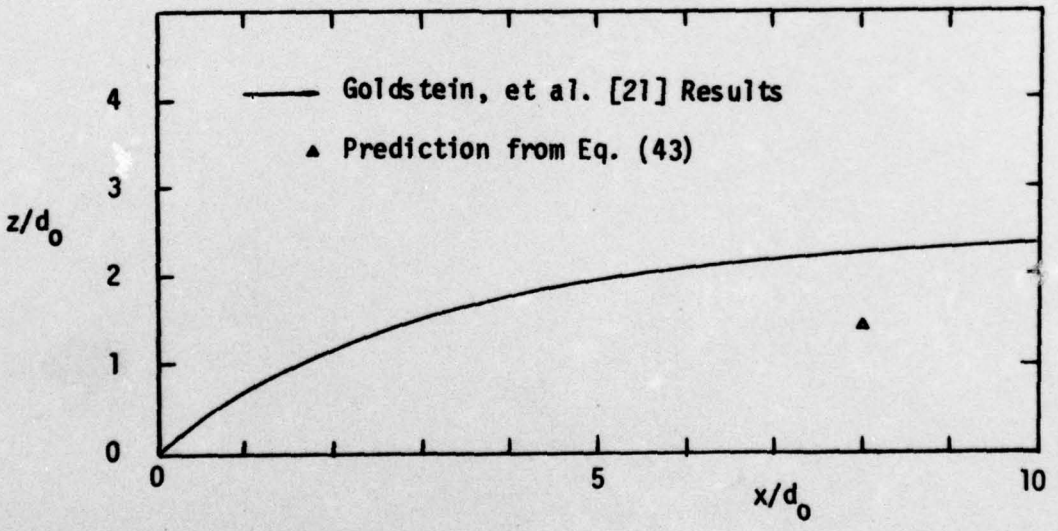

b) M = 1.0

Figure 96. Comparison of the (z/s)* Correlation (Eq. 43) with the Data of Goldstein, et al.[21]

IV. CONCLUSIONS

The subject investigation was conducted to model the film cooling performance for a turbine vane leading edge using the stagnation region of a cylinder in cross flow. Experiments were conducted with film coolant (air) injection from a single row of holes angled in the spanwise direction. A freestream-to-wall temperature ratio of T_∞/T_w of ~2.1 and a Reynolds number of $Re_D=1.7\times10^5$ were maintained throughout the investigation to simulate the gas turbine environment. A reduced film coolant temperature enabled a coolant-to-freestream density ratio of ~2.2 to be maintained.

The test cylinder was instrumented with miniature heat flux gages and thermocouples to determine the percentage reduction in the Stanton number (presented as $[1-(St_{FC}/St_o)]$) as a function of the distance downstream from injection (x/d_o) and the location between adjacent holes (z/s). The primary objectives of the study were to determine the influence of the coolant blowing ratio, M, the injection angle, β, and the injection location relative to stagnation, Θ_i, on the local heat transfer. Data were obtained over the range M= 0 to 2.0 for coolant injection angles of β= 25°, 35°, 45°, with the row of holes located at Θ_i= 20°, 30°, 40°, relative to the stagnation line.

From the analysis and correlation of the data, the following observations and conclusions were drawn concerning the effects of film cooling in the stagnation region.

1) The data revealed a substantial spanwise variation of the Stanton Number Reduction which depended both on the injection angle, β, and the blowing ratio, M. For example, for Θ_i=40°, β=25°, and x/d_o=8.0, the Stanton Number Reduction was found to vary from 0.39 at z/s=0.67 to 0.02 at z/s=0.00 for the blowing ratio of M=1.0. Cross-plots of $[1-(St_{FC}/St_o)]$ vs. (z/s) were used to identify the spanwise maximum Stanton Number Reduction, $[1-(St_{FC}/St_o)]^*$, and the corresponding location, $(z/s)^*$, between adjacent coolant holes.
2) For low values of the blowing ratio, $[1-(St_{FC}/St_o)]^*$ was found to vary linearly with M independent of the injection angle, β. However, for a sufficiently high value of M, the film cooling performance deviated from the linear trend, resulting in a maximum level of the film cooling performance, $[1-(St_{FC}/St_o)]^*_{MAX}$ at an optimum blowing ratio, M^*_{opt}.
3) The maximum level, $[1-(St_{FC}/St_o)]^*_{MAX}$, was found to decrease as the injection angle was increased, varying from 0.40 for β=25° to 0.12 for β=45° (both for Θ_i=40° and x/d_o=8.0).
4) The optimum blowing ratio, M^*_{opt}, was found to decrease as the injection angle was increased. The influence of the injection angle, β, on the optimum blowing ratio was correlated in terms of the normal component of the coolant-to-freestream velocity ratio, $(V_c/V_\infty)\sin\beta$. The value of $(V_c/V_\infty)\sin\beta$ was found to be approximately constant in the range of 0.19 to 0.24, which is in good agreement with the optimum blowing conditions from previous studies covering a wide range of coolant-to-freestream

density ratios.

5) The spanwise location, $(z/s)^*$, of the local maximum film cooling performance was found to increase as the injection angle (β) was decreased and the blowing ratio (M) was increased. The influence of β and M on the value of $(z/s)^*$ was correlated in terms of a momentum parameter, $I_z^{0.9}/I_y^{0.8}$, composed of the normal (I_y) and spanwise (I_z) components of the coolant-to-freestream momentum flux ratio.

6) The spanwise distribution, $[1-(St_{FC}/St_o)]$ vs. (z/s), was used to determine a spanwise averaged Stanton Number Reduction, $[1-(St_{FC}/St_o)]_{AVG}$. The value of $[1-(St_{FC}/St_o)]_{AVG}$ was observed to increase with M up to some optimum value of the blowing ratio. Further increase in M resulted in a deterioration of the film cooling performance. The spanwise averaged results showed that the film cooling performance at x/d_o=6.4 and 8.0 was approximately the same, while further downstream at x/d_o=15.2 the performance had deteriorated to a negligible level and in most cases was negative.

7) Moving the row of injection holes closer to stagnation (from Θ_i=40° to 20°), corresponding to an increase in the freestream acceleration parameter, K_i=1.1x10^{-5} to 4.8x10^{-5}, resulted in a 40 to 50% decrease in the film cooling performance, both the spanwise maximum Stanton Number Reduction and the spanwise averaged Stanton Number Reduction.

BIBLIOGRAPHY

1. Esgar, J.B., Colladay, R.S., and Kaufman, A., "An Analysis of the Capabilities and Limitations of Turbine Air Cooling Methods," NASA TN D-5992, September, 1970.

2. Goldstein, R.J., "Film Cooling," Advances in Heat Transfer, New York, Academic Press, 1971, Vol. 7, pp. 321-379.

3. Eckert, E.R.G., and Drake, R.M., Jr. Analysis of Heat and Mass Transfer, New York, McGraw-Hill Book Company, 1972, pp. 389-397, 417-422.

4. Hartnett, J.P., Birkebak, R.C., and Eckert, E.R.G., "Velocity Distributions, Effectiveness, and Heat Transfer in Film Cooling of a Surface with a Pressure Gradient," Proceedings of 1961 International Heat Transfer Conference, Part IV, Section A, Paper No. 81, 1961.

5. Metzger, D.E. and Fletcher, D.D., "Surface Heat Transfer with Film Cooling Near Non-Tangential Injection Slots," AIAA Paper No. 69-523, 1969.

6. Eriksen, V.L. and Goldstein, R.J., "Heat Transfer and Film Cooling Following Injection Through Inclined Circular Tubes," ASME Paper No. 74-HT-V, July, 1973.

7. Lander, R.D., Fish, R.W., and Suo, M., "The External Heat Transfer Distribution on a Film Cooled Turbine Vane," AIAA 10th Aerospace Sciences Meeting, AIAA Paper No. 72-9, 1972.

8. Eckert, E.R.G., "Mass Transfer Analogy to Study the Effect of Variable Properties on Film Cooling Effectiveness," Workshop on Film Cooling Research, University of Minnesota, May 8, 1975.

9. Metzger, D.E., "A Summary and Design Recommendations - Film Cooling," Airesearch Report No. TR-5025, Airesearch Manufacturing Company of Arizona, May, 1968.

10. Choe, H., Kays, W.M., and Moffat, R.J., "The Superposition Approach to the Film Cooling of a Uniform Temperature Wall," ASME Paper No. 74-WA/HT-27, Nov., 1974.

11. Abramovich, G.N., The Theory of Turbulent Jets, Cambridge, MIT Press, 1963.

12. Ramsey, J.W. and Goldstein, R.J., "Interaction of a Heated Jet with a Deflecting Stream," Journal of Heat Transfer, ASME Transactions, Nov., 1971, pp. 365-372.

13. Eriksen, V.L., "Film Cooling Effectiveness and Heat Transfer with Injection through Holes," University of Minnesota Heat Transfer Laboratory Paper No. 102, 1971.

14. Liess, C., "Film Cooling With Ejection From a Row of Inclined Holes-An Experimental Study for the Application to Gas Turbine Blades," von Karman Institute for Fluid Dynamics Technical Note 97, March, 1973.

15. Colladay, R.S., and Russell, L.M.,"Flow Visualization of Discrete Hole Film Cooling for Gas Turbine Applications," NASA Technical Memorandum X-71766, Lewis Research Center, Cleveland, Ohio, 1975.

16. Goldstein, R.J., Eckert, E.R.G., and Ramsey, J.W., "Film Cooling with Injection Through a Circular Hole," University of Minnesota Heat Transfer Laboratory Paper No. 82, 1968.

17. Wieghardt, K., "Hot Air Discharge for De-Icing," AAF Translation, Report No. F-TS-919-RE, 1946.

18. Seban, R.A., "Heat Transfer and Effectiveness for a Turbulent Boundary Layer With Tangential Fluid Injection," Journal of Heat Transfer, ASME Transactions, Nov., 1960, pp. 303-312.

19. Samuel, A.E. and Joubert, P.N., "Film Cooling of an Adiabatic Flat Plate in Zero Pressure Gradient in the Presence of a Hot Mainstream and Cold Tangential Secondary Injection," ASME Paper No. 64-WA/HT-48, Oct., 1965.

20. Burns, W.K. and Stollery, J.L., "The Influence of Foreign Gas Injection and Slot Geometry on Film Cooling Effectiveness," Journal of Heat Transfer, ASME Transactions, Vol. 12, 1969, pp. 935-951.

21. Goldstein, R.J., Eckert, E.R.G., Eriksen, V.L., and Ramsey, J.W. "Film Cooling Following Injection Through Inclined Circular Tubes," Israel Journal of Technology, Vol. 8, No. 1-2, 1970, pp. 145-154.

22. Pederson, D.R., "Effect of Density Ratio on Film Cooling Effectiveness for Injection Through a Row of Holes and for a Porous Slot," Ph.D. Thesis, University of Minnesota, March, 1972.

23. Goldstein, R.J., Eckert, E.R.G., and Burggraf, F., "Effects of Hole Geometry and Density on Three-Dimensional Film Cooling," International Journal of Heat and Mass Transfer, May, 1974, pp. 595-606.

24. Foster, N.W. and Lampard, D., "Effects of Density and Velocity Ratio on Discrete Hole Film Cooling," AIAA Journal, Vol. 13, No. 8, pp. 1112-1114.

25. Papell, S.S., "Effect of Gaseous Film Cooling of Coolant Injection Through Angled Slots and Normal Holes," NASA TN D-299, 1960.

26. Goldstein, R.J., Eckert, E.R.G., Eriksen, V.L., and Ramsey, J.W., "Film Cooling Following Injection Through Inclined Circular Tubes," University of Minnesota Heat Transfer Laboratory Paper No. 91, Nov., 1969.

27. Liess, C. and Carnel, J., "Application of Film Cooling to Gas Turbine Blades," AGARD Conference, Proceedings No. 73 on High Temperature Turbines, 1970.

28. Metzger, D.E., Takeuchi, D.I., and Kuenstler, P.A., "Effectiveness and Heat Transfer with Full Coverage Film Cooling," Journal of Engineering for Power, July, 1973, pp. 180-184.

29. Papell, S.S. and Trout, A.M., "Experimental Investigation of Air Film Cooling Applied to an Adiabatic Wall by Means of an Axially Discharging Slot," NASA TN D-9, 1959.

30. Carlson, L.W. and Talmor, E., "Gaseous Film Cooling at Various Degrees of Hot Gas Acceleration and Turbulence Levels," International Journal of Heat and Mass Transfer, Vol. 11, 1968, pp. 1695-1713.

31. Kays, W.M., Moffat, R.J., and Threlbahr, W.H., "Heat Transfer to the Highly Accelerated Turbulent Boundary Layer with and without Mass Addition," Journal of Heat Transfer, ASME Transactions, Vol. 92, No. 3, Aug., 1970, pp. 499-505.

32. Seban, R.W. and Back, L.H., "Effectiveness and Heat Transfer for a Turbulent Boundary Layer with Tangential Injection and Variable Freestream Velocity," Journal of Heat Transfer, ASME Transactions, Vol. 84, No. 3, Aug., 1962, pp. 235-242.

33. Pai, B.R. and Whitelaw, J.H., "The Influence of Strong Pressure Gradients on Film Cooling Effectiveness," Heat Transfer, Vol. 2, FC1.11, 1970, pp. 1-10.

34. Goldstein, R.J., "Film Cooling Downstream of Two Staggered Rows of Holes Including the Effects of Freestream Acceleration," reported by Goldstein, Workshop on Film Cooling, University of Minnesota, May 8, 1975.

35. Launder, B.E. and York, J., "Discrete Hole Cooling in the Presence of Freestream Turbulence and Strong Favorable Pressure Gradient," International Journal of Heat and Mass Transfer, Vol. 17, 1974, pp. 1403-1409.

36. Nicolas, J. and LeMeur, A., "Curvature Effects on a Turbine Blade Cooling Film," ASME Paper No. 74-GT-156, 1973.

37. Jones, W.P. and Launder, B.E., "Some Properties of Sink-Flow Turbulent Boundary Layers," Journal of Fluid Mechanics, Vol. 56, Part 2.

38. Colladay, R.S., "The Importance of Combining Convection with Film Cooling," AIAA Paper No. 72-8, Jan., 1972.

39. Schlicting, H., Boundary Layer Theory, 6th Edition, New York, McGraw-Hill Book Co., 1968, pp. 17, 154-162, 202.

40. Poferl, D., Svehla, R., and Lewandowski, K., Thermodynamic and Transport Properties of Air and the Combustion Products of Natural Gas and of ASTM-A-1 Fuel with Air, NASA TN D-5452, Lewis Research Center, Cleveland, Ohio, October, 1969, p. 14.

41. Holman, J.P., Heat Transfer, New York, McGraw-Hill Publishing Co., 1972, p. 434.

42. Flachshart, O., "Windruck auf Gasbehalter," Reports of the Aerodyn. Versuchsanstalt in Gottingen, IVth Series, 1932, pp. 134-138.

43. Fage, A. and Falkner, V.M., "Further Experiments on the Flow Around a Cylinder," R and M No. 1179, Great Britain Aeronautical Research Committee, 1928.

44. Daily, J.W. and Harleman, D.R.F., Fluid Dynamics, Reading, Mass., Addison-Wesley Publishing Co., 1966, pp. 380-382.

45. Schmidt, E. and Wenner, K., "Heat Transfer over the Circumference of Heated Cylinder in Traverse Flow," NACA Technical Memorandums No. 1050, Oct., 1943.

46. Giedt, W.H., "The Effect of Turbulence Level on Incident Air Stream on Local Heat Transfer and Skin Friction on a Cylinder," Journal of Aeronautical Sciences, Nov., 1951, pp. 725-730.

47. Seban, R.A., "The Influence of Freestream Turbulence on the Local Heat Transfer from Cylinders," Journal of Heat Transfer, ASME Transactions, Vol. 82, No. 4, Nov, 1960, pp. 305-312.

48. Hanus, G.J. and L'Ecuyer, M.R., "Turbine Vane Gas Film Cooling with Injection in the Leading Edge Region from a Single Row of Spanwise Angled Holes," Thermal Sciences & Propulsion Center, Purdue University Technical Report No. TSPC TR-76-1, May, 1976.

49. LeBrocq, P.V., Launder, B.E., and Priddin, C.H., "Discrete Hole Injection As a Means of Transpiration Cooling - An Experimental Study," Proceedings of the Institute of Mechanical Engineers, Thermodynamics and Fluid Mechanics Group, Vol. 187-17/73, 1973, pp. 149-157.

50. Crawford, M.E., Choe, H., Kays, W.M., and Moffat, R.J., "Full Coverage Film Cooling Heat Transfer Study - Summary of Data for Normal Hole Injection and 30° Slant Hole Injection," NASA CR-2648, March, 1976.

51. Tribus, M. and Klein, J., "Forced Convection from Non-Isothermal Surfaces," Heat Transfer; A Symposium, Ann Arbor, Michigan, University of Michigan Press, 1953, pp. 211-235.

52. Librizzi, J. and Cresci, R.J., "Transpiration Cooling of a Turbulent Boundary Layer in an Axisymmetric Nozzle," AIAA Journal, Vol. 2, No. 4, April, 1964, pp. 617-624.

53. Kutateladze, S.S. and Leantiev, A.I., "The Heat Curtain in the Turbulent Boundary Layer of a Gas," Thermal Physics at High Temperature, Vol. No. 2, 1963, pp. 281-293.

54. Stollery, J.L. and El-Ehwany, A.A.M., "On the Use of a Boundary Layer Model for Correlating Film Cooling Data," International Journal of Heat and Mass Transfer, Vol. 10, 1967, pp. 101-105.

55. Goldstein, R.J. and Haji-Sheikh, A., "Prediction of Film Cooling Effectiveness," Japan Society of Mechanical Engineers, 1967, Semi-International Symposium, Tokyo, Japan.

56. Seban, R.A., Chan, H.W., and Scesa, S., "Heat Transfer to a Turbulent Boundary Layer Downstream of an Injection Slot," ASME Paper No. 57-A-36, 1957.

57. Hatch, J.E. and Papell, S.S., "Use of a Theoretical Flow Model to Correlate Data for Film Cooling or Heating by Tangential Injection of Gases of Different Properties," NASA TN D-130, 1959.

58. Seban, R.W. and Back, L.H., "Velocity and Temperature Profiles in Turbulent Boundary Layer with Tangential Injection," Journal of Heat Transfer, ASME Transactions, Vol. 84, No. 1, Feb., 1962, pp. 45-54.

59. Eriksen, V.L., Eckert, E.R.G., and Goldstein, R.J., "A Model for Analysis of the Temperature Field Downstream of a Heated Jet Injected into an Isothermal Cross Flow at an Angle of 90°," University of Minnesota Heat Transfer Laboratory Paper No. 101, 1971.

60. Harnett, J.P., Birkebak, R.C. and Eckert, E.R.G., "Velocity Distributions, Temperature Distributions, Effectiveness, and Heat Transfer for Air-Injection through a Tangential Slot into a Turbulent Boundary Layer," Journal of Heat Transfer, ASME Transactions, Vol. 83, No. 3, August, 1961.

61. Samuel, A.E. and Joubert, P.N., "Film Cooling of an Adiabatic Flat Plate in Zero Pressure Gradient in the Presence of a Hot Mainstream and Cold Tangential Secondary Injection," ASME Paper No. 64-WA/HT-48, Oct., 1965.

62. Hearing, G.W., "A Proposed Correlation Scheme for Gas Film Cooling Data," AFAPL-TR-66-56 Air Force Aero Propulsion Lab, August, 1966.

63. Metzger, D.E., Carper, H.J., and Swank, L.R., "Heat Transfer with Film Cooling near Non-Tangential Injection Slots," Journal of Engineering for Power, Vol. 90, No. 2, April, 1968, pp. 157-163.

64. Kays, W.M., "Numerical Solutions for Laminar Flow Heat Transfer in Circular Tubes," Transactions of the American Society of Mechanical Engineers, Vol. 77, 1955.

APPENDIX I. MODELS AND CORRELATIONS FROM PREVIOUS INVESTIGATIONS

I.A. Analytical Models

The goal of any film cooling study is the development of a model or empirical correlation to predict the effectiveness of the coolant stream. Since a majority of the experimental investigations to date have been done on adiabatic surfaces, correlations of the data are usually presented in the form of the effectiveness parameter, η_{adw}. The heat sink model was the approach initially used by many investigators to describe coolant injection onto the surface.

Tribus and Klein [51] attempted to correlate the adiabatic effectiveness for a two-dimensional slot by using a line heat source to represent the coolant injection. The main restriction they placed on their model was that the boundary layer velocity profile was unaltered by the mass addition of the injected coolant. With this assumption, they derived the following effectiveness relation:

$$\eta_{adw} = 5.79\ Pr^{2/3} Re_c^{0.2} \left(\frac{\mu_c}{\mu_\infty}\right)^{0.2} \left(\frac{c_{p_c}}{c_{p_\infty}}\right)\left(\frac{x}{Ms_o}\right)^{-0.8} \qquad \text{(A-1)}$$

For air injected into air, with negligible property differences, the relation became:

$$\eta_{adw} = 4.62\ Re_c^{0.2}\left(\frac{x}{Ms_o}\right)^{-0.8} \qquad \text{(A-2)}$$

The development of models by Librizzi and Cresci [52] and Kutateladze and Leont'ev [53] did allow for finite mass addition into the boundary layer at injection, but they assumed complete mixing of the injected gas with the mainstream at injection and a uniform temperature within the boundary layer. Librizzi and Cresci [52], assuming that the boundary layer growth began at the point of injection, derived the following effectiveness relation:

$$\eta_{adw} = \frac{1}{1 + 0.329 \left(\frac{c_{p_\infty}}{c_{p_c}}\right)\xi^{0.8}} \qquad \text{(A-3)}$$

where $\xi = \left[\left(\frac{\mu_c}{\mu_\infty}\right)Re_c\right]^{-0.25} \left(\frac{x}{Ms_o}\right)$

Kutateladze and Leont'ev [53], assuming that the boundary layer started upstream of injection, equated the net mass flow in the boundary layer with the coolant mass flow rate. Using this assumption, they developed the following relationship:

$$\eta_{adw} = \frac{1}{1 + \left(\frac{c_{p_\infty}}{c_{p_c}}\right)[0.329(4.01+\xi)^{0.8} - 1]} \qquad \text{(A-4)}$$

The problem with these models is that while the assumption of neglecting mass addition is too liberal, the assumption of an average temperature in the boundary layer is too conservative. The fact that these assumptions counterbalance each other was shown in a model derived by Stollery and El-Ehwany [54]. Neglecting the effect of mass addition, and assuming an uniform average temperature in the boundary

layer, the effectiveness relation they derived

$$\eta_{adw} = 3.03\ Re_c^{0.2} \left(\frac{\mu_c}{\mu_\infty}\right)^{0.2} \left(\frac{x}{Ms_o}\right)^{-0.8} \qquad \text{(A-5)}$$

showed excellent agreement with experimental results. Goldstein and Haji-Sheikh [55] developed a model that did account for both the temperature variation in the boundary layer as well as the effects of mass addition on the boundary layer. The relation they derived also accounted for non-tangential injection in the streamwise direction. It was

$$\eta_{adw} = \frac{1.9\ Pr^{2/3}}{1 + 0.329 \left(\frac{c_{p_\infty}}{c_{p_c}}\right) \xi^{0.8} \gamma} \qquad \text{(A-6)}$$

where $\gamma = 1 + (1.5\times10^{-4}) Re_c \left(\frac{-\mu_c}{\mu_\infty M}\right) \sin\beta$

β = streamwise angle of injection (α=0°)

This model also showed excellent agreement with experimental results. Figure A1 shows a plot of some of the effectiveness equations described above and demonstrates how they compared with the experimental film cooling data (tangential slot) of Seban, Chin and Scesca [56].

Hatch and Papell [57] developed a model for tangential injection where the coolant existed as an unmixed, separate layer along the adiabatic wall. The injected coolant was assumed to travel a distance downstream before the wall began to feel the heating effects from the mainstream. The effectiveness relation derived was

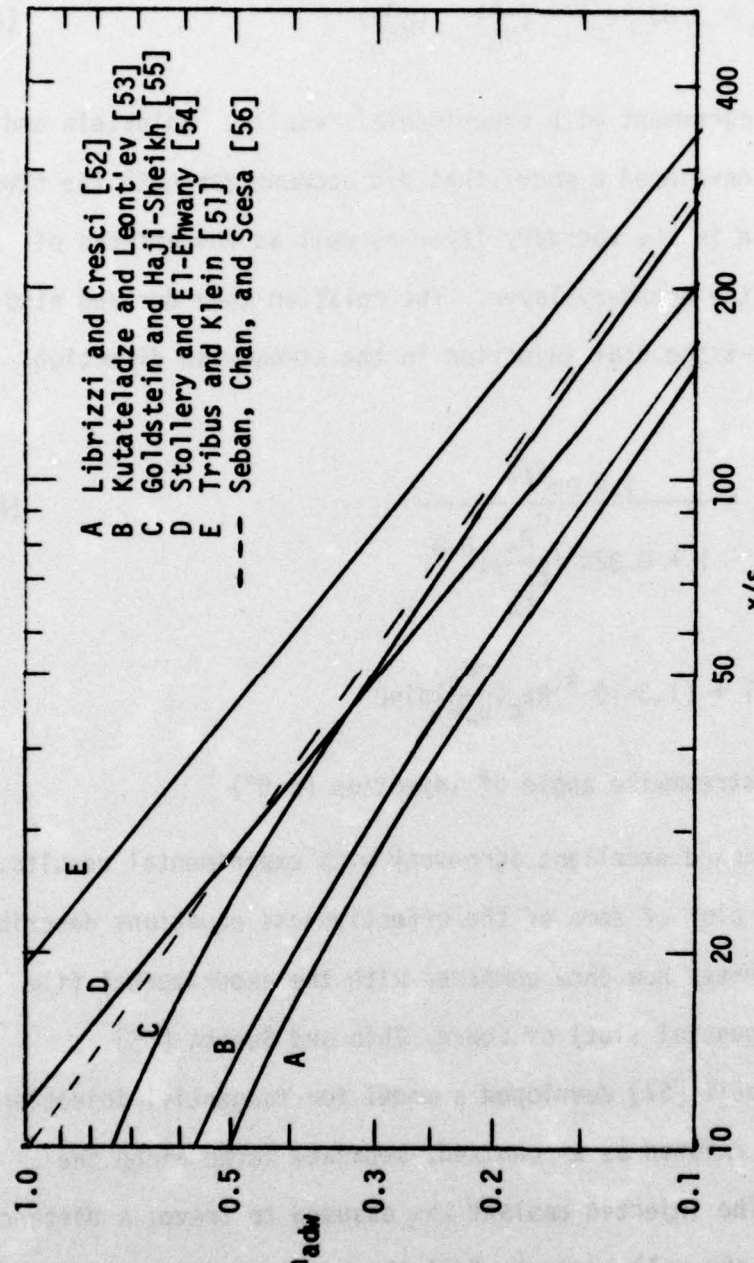

Figure A1. Comparison of Film Cooling Models

$$\ln\eta_{adw} = -\left[\frac{hLx}{(\dot{m}c_p)_c} - 0.04\right]\left[\frac{sV_\infty}{\alpha_c}\right]^{0.125} f\left(\frac{V_\infty}{V_c}\right) \qquad \text{(A-7)}$$

$$\text{for } \frac{hLx}{(\dot{m}c_p)_c} \geq 0.04$$

and $\eta = 1$

$$\text{for } \frac{hLx}{(\dot{m}c_p)_c} < 0.04$$

where $f\left(\frac{V_\infty}{V_c}\right) = 1 + 0.4 \tan^{-1}\left(\frac{V_\infty}{V_c} - 1\right)$

$$\text{at } \frac{V_\infty}{V_c} \geq 1.0$$

and $f\left(\frac{V_\infty}{V_c}\right) = \left(\frac{V_c}{V_\infty}\right)^{1.5(V_c/V_\infty - 1)}$

$$\text{at } \frac{V_\infty}{V_c} < 1.0$$

where h = external heat transfer coefficient

L = length of coolant slot

$\dot{m}_c$ = mass flow rate of coolant

α_c = thermal diffusivity of coolant

The model developed by Seban and Back [58] for tangential injection had an initial mixing region near the slot where the velocity profiles were similar to those found in a free jet boundary flow. The mixing coefficient in this region and the downstream deflection of the mixing zone toward the wall were found to be related to the velocity ratio. The amount of mixing and the deflection of the mixing zone toward the

wall by the mainstream determined when the mixing region transformed into a complex boundary layer. Far downstream ($x/s_o > 40$), the boundary layer resembled the typical turbulent power law profile. The effectiveness relation they derived was

$$\eta_{adw}^2 = 1 + \pi[25.3\times10^{-4}]M^2(Re_{s_o})^{-0.3}[(\frac{B}{s_o})^{1.7} - (\frac{B_1}{s_o})^{1.7}] \qquad (A-8)$$

where $B = x + x_o$, the distance downstream of the effective origin of the boundary layer with x_o being the distance between the slot and the effective origin of the boundary layer.

$B_1 = x + x_1$, where x_1 is the distance from the slot to where effectiveness was unity.

Eriksen, Eckert and Goldstein [59] developed a model to predict the film coolant effectiveness from discrete holes. They simulated hole injection by using a moving source in a semi-infinite medium. The relation for η_{adw} they developed was

$$\eta(x,z) = \frac{MV_\infty d_o}{8\varepsilon_p x/d_o} e^{-\{\frac{V_\infty d_o}{4\varepsilon_p x/d_o}[(\frac{Y_o}{d_o})^2 + (\frac{z}{d_o})^2]\}} \qquad (A-9)$$

where ε_p = point source thermal diffusivity

and Y_o = horizontal virtual origin of source above x-z plane

The thermal diffusivity and Y_o used in this model were found empirically. At low blowing rates ($M \leq 0.5$), the model was found to show good agreement with experimental data. However, when the blowing ratio was greater than 0.5, the heat sink analysis broke down, probably due to the separation of the coolant jet from the surface. Assuming negligible

jet interaction, the superposition principle could easily be applied to this model for the study of a row of holes or even multiple rows of holes.

I.B. Experimental Correlations

Most film cooling correlations for slot injection can be represented by the following format

$$\eta_{adw} = A\left(\frac{x}{Ms_o}\right)^B (Re_c)^F \qquad \text{(A-10)}$$

where A, B. and F are constants.

Correlations that used this form have assumed that the coolant mixed to some extent with the mainstream boundary layer, but that the boundary layer developed as usual with no further effects of injection. Differences among the various correlations are greatest at large distances, and fortunately this is not an important area of study. Most of the interest centers around the knee of the curve (η vs. x/Ms_o), the point where the effectiveness first departs from unity. For blowing rates of $M > 1.0$, this knee occurs very early, but for $M < 1.0$, Hartnett et al. [60] showed that it did not occur until $x/Ms_o = 5$. Variation in the location of this knee among the different correlations reflects the degree of initial mixing assumed.

Wieghardt [17], working on aircraft de-icing, developed the following adiabatic effectiveness relation.

$$\eta_{adw} = 5.44\left(\frac{x}{Ms_o}\right)^{-0.8} Re_c^{0.2} \qquad \text{(A-11)}$$

Hartnett et al. [60] were also able to correlate their data in a similar form.

$$\eta_{adw} = 3.59 \left(\frac{x}{Ms_o}\right)^{-0.8} Re_c^{0.2} \qquad \text{(A-12)}$$

for $\frac{x}{Ms_o} \geq 60$

Recalling the analytical model of Tribus and Klein [51], the effectiveness relation was

$$\eta_{adw} = 4.62 \left(\frac{x}{Ms_o}\right)^{-0.8} Re_c^{0.2} \qquad \text{(A-2)}$$

An important consideration when using the form of the adiabatic effectiveness correlation showed in Eq. (A-10), is that property variation across the boundary layer is assumed to be negligible.

Seban, Chan, and Scesa [56] found slightly different exponents when they correlated their data for tangential slot flow. The effectiveness relation they found was

$$\eta_{adw} = 0.83 \left(Re_c\right)^{1/3} \left(\frac{x}{Ms_o}\right)^{-0.7} \qquad \text{(A-13)}$$

for $\frac{x}{Ms_o} > 40$

and $\eta_{adw} = 0.16 \left(Re_c\right)^{1/3} \left(\frac{x}{Ms_o}\right)^{-0.25}$

for $\frac{x}{Ms_o} < 40$

Samuel and Joubert [61] correlated their data in a slightly different format and the relations they developed were valid only for $M < 1$ and tangential slot injection.

$$\eta_{adw} = 1 \qquad \text{(A-14)}$$

for $\left(\frac{x}{s_o}\right)\left(M^{-1.75}\right) < 40$

and $\eta = 10.8\left[\left(\frac{x}{s_o}\right)\left(M^{-1.75}\right)\right]^{-0.65}$

for $40 < \left(\frac{x}{s_o}\right)\left(M^{-1.75}\right) < 400$

Several investigators have attempted to show in their correlations the effect of large temperature differences between the coolant gas and the mainstream gas on the cooling effectiveness. Papell and Trout [29] used mainstream temperatures in the range of 289K (520°R) to 1111K (2000°R) and coolant temperatures of 300K (540°R) to 483K (870°R). The tangential slot height varied, but it was always kept less than 1.27cm (0.5 in.) and the correlation they developed was

with $x > 8.89$cm (3.5 in.) from the slot

$$\eta_{adw} = 12.6\ (M)\left(\frac{s_o}{x}\right)^{0.72}\left(\frac{T_c}{T_\infty}\right)^{0.5} \qquad \text{(A-15)}$$

for $M < 2.0$

An important consideration when using this correlation is that the coolant temperature, T_c, was measured in the plenum and not at the slot exit.

Hearing [62] also developed a correlation to account for temperature differences, and the fact that it differs from the relation developed by Papell and Trout [29] is probably due to the use of the plenum temperature as the coolant temperature by Papell and Trout. Hearing's relation was

$$\eta_{adw} = 1/\{1 + 3.6[(St_\infty/M)(x/s_o)(T_\infty/T_c)^{2/3} f(v)]\} \qquad \text{(A-16)}$$

where $f(v) = 1 + 0.4 \arctan (V_\infty/V_c - 1)$

Using heat transfer measurements instead of adiabatic wall measurements, Metzger, Carper, and Swank [63] investigated angled slots. They developed the following relations using the parameters, $\Phi(q''_{FC}/q''_o)$ and θ_c. The Φ values in these correlations were averaged values obtained over the entire length of the test surface.

$$\Phi = 1.09 - 7.9\theta_c M^{0.6}(s_o/\ell)^{0.5} \qquad \text{for } \beta = 20°,\ \alpha = 0° \qquad \text{(A-17)}$$

$$\Phi = 1.18 - 7.5\theta_c M^{0.6}(s_o/\ell)^{0.5} \qquad \text{for } \beta = 40°,\ \alpha = 0°$$

$$\Phi = 1.24 - 6.8\theta_c M^{0.6}(s_o/\ell)^{0.5} \qquad \text{for } \beta = 60°,\ \alpha = 0°$$

for $35 \leq \ell/s_o \leq 70$

and $0.25 \leq M \leq 0.75$

Metzger and Fletcher [5] investigated angled slots by making similar heat transfer measurements. As shown in Section I.C.1., when $\Phi = 0$, $\theta_c = \theta_{c,adw} = 1/\eta_{adw}$. Therefore, the results they correlated for angled slots were presented in the following form.

$$\theta_{c,adw} = 1.0 + 0.00619M^{-1.35}(\ell/s_o) \qquad \text{(A-18)}$$

for $0.25 \leq M \leq 0.75$, $0 \leq \ell/s_o \leq 70$, $\beta = 20°$, $\alpha = 0°$

$$\theta_{c,adw} = 1.0 + 0.01155M^{-0.75}(\ell/s_o)$$

for $0.25 \leq M \leq 0.75$, $0 \leq \ell/s_o \leq 70$, $\beta = 60°$, $\alpha = 0°$

APPENDIX II. DESCRIPTION OF THE EXPERIMENTAL INVESTIGATION

II.A. Experimental Apparatus

The investigation of stagnation region film cooling typical of a turbine vane leading edge was conducted using a cylindrical test surface exposed to a crossflow of heated air from a gas turbine combustor. The description of the experimental apparatus is presented in three sections, the flow system, the test cylinder, and the measurements and instrumentations.

II.A.1. Flow System

Gas Generator. Ambient air, pressurized (to a maximum of 2250 psi) and stored outside in tanks, provided an air flow rate of $\sim$ 4 lbm/sec for a typical run time of $\sim$ 30 minutes. As shown in the schematic drawing of the flow system, Figure A2, the air passed through a open/close isolation value, a filter (Fluid Dynamics, 20 micron), and a dome regulator. A Daniels Orifice Meter (a 40L Daniel SC-40 assembly incorporating a 2.35" dia. orifice plate) was used to measure the air mass flow rate. The flow rate through the wind tunnel was regulated by two pneumaticaly controlled valves (Minneapolis Honeywell Model No. 300-29, a 2" valve and a 1" valve). The air entered a J-47 gas turbine combustor, where methyl alcohol was burned to provide the nominal free-stream conditions of T_{T_∞} ~900°R and P_{T_∞} ~56.7 psia. The combustor

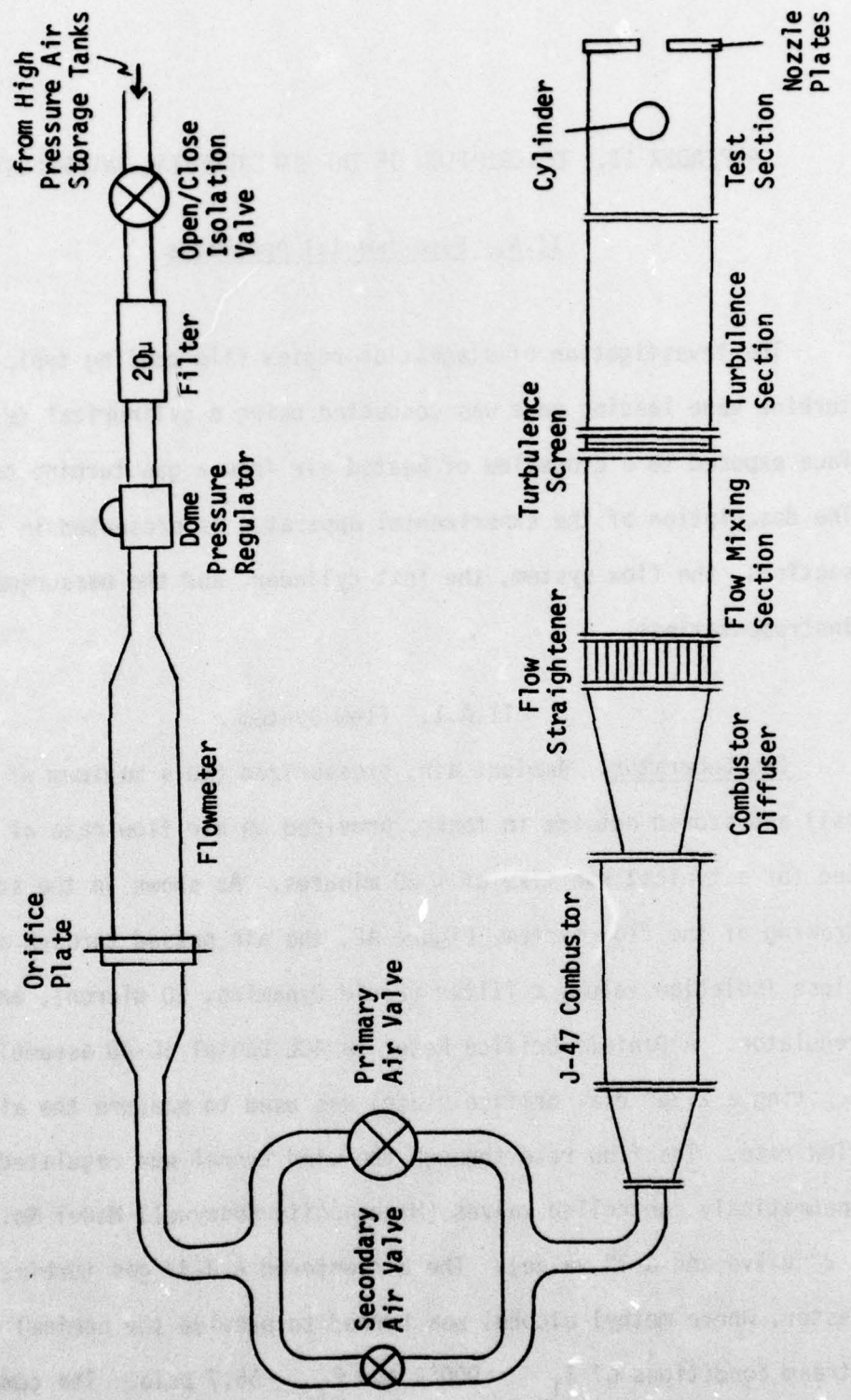

Figure A2. Schematic of the Flow System

had a standard fuel nozzle, with a primary and secondary port. Because of the low fuel flow rate needed to produce the freestream conditions, fuel was injected only through the secondary port, while air was injected through the primary port to aid in the atomization of the methyl alcohol. The combustor was equipped with a spark plug (Champion No. AA865) that was activated by an ignitor coil connected to a 24V DC supply.

Fuel System. Methyl alcohol, used as fuel for the combustor, was stored outside in large tanks. During an experimental run, these tanks were pressurized ~700 psi to achieve the desired fuel flow rate. A flat plate orifice was used to measure the flow rate while a pneumatically controlled valve was used to regulate the flow. Before reaching the combustor fuel nozzle, hand valves enabled the fuel flow to be bypassed around the combustor, thus allowing the fuel flow rate necessary for ignition to be set before any fuel entered the combustor.

Test Flow Channel. Figure A3 shows a photograph of the flow channel. Following the description of the flow channel, the important dimensions of each individual section will be listed. Downstream of the combustor, the flow passed through a diffuser into a rectangular flow channel. A flow straightener (consisting of three drilled plates and a rectangular flow mixing section) was installed to minimize the non-uniformity of the freestream flow. The turbulence section consisted of a combination of interchangeable ducts and square mesh screens. This enabled the turbulence level of the freestream at the cylinder to be varied by changing either the screen grid size or the screen location relative to the cylinder. For this investigation, the

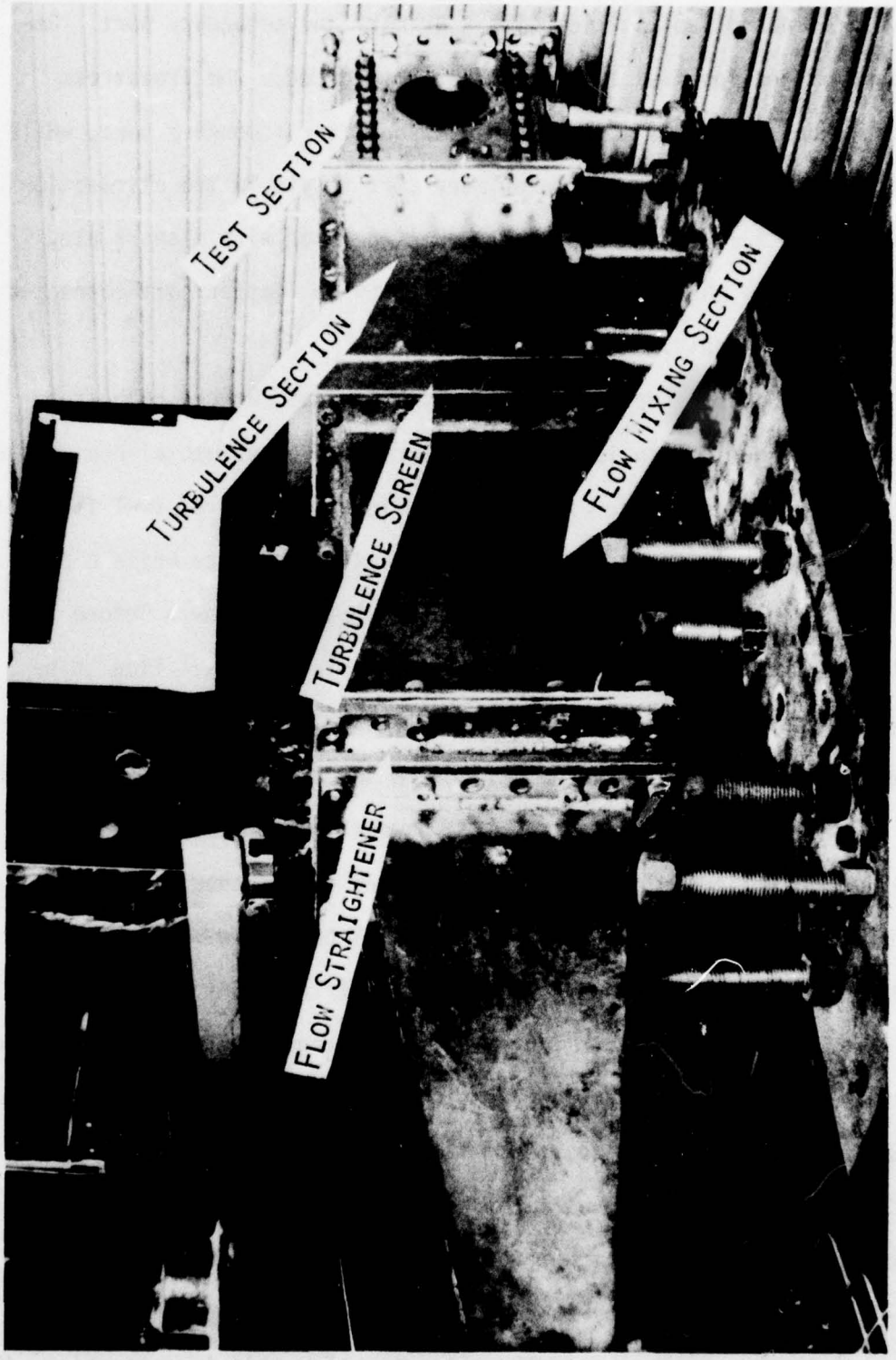

Figure A3. Photograph of the Flow Channel

turbulence level was held constant by leaving the screen location (.49m) and grid size (1.59mm wire dia. and 6.36mm center-to-center wire spacing) fixed.

Figure A4 shows a photograph of the test section with the test cylinder installed. The test cylinder was held in place by circular flanges and sealed with O'rings. Loosening of the flanges permitted rotation of the cylinder. After flowing over the test cylinder, the combustion gas left the flow channel through a flat plate nozzle attached to the end of the test section. Due to the choked flow at the exit, the flow area between the nozzle plates controlled the free-stream Mach number upstream of the test cylinder. In order to size the exit area, several flow conditions had to be considered. Since the Reynolds number (1.7×10^5) and the freestream temperature (~990°R) had already been specified by modeling conditions, the mass flux, $(\rho V)_\infty$, was fixed. Therefore the only undetermined variable was the freestream pressure or Mach number (once one was chosen, the other was fixed). Since the optimum combustor efficiency was found when the freestream pressure was between 40 and 60 psig, a nominal value of the Mach number of 0.08, corresponding to a freestream pressure of 42 psig, was chosen. This Mach number was then used to size the nozzle plate exit area. Upstream of the test cylinder (~6.45cm), ports in the top and side walls of the test section enabled probes to be inserted into the flow field. The dimensions of the test flow channel are summarized below.

Diffuser	Entrance	Width 2.6 in	Height 4.4 in
	Exit	Width 4.5 in	Height 8.0 in
		Length 20.0 in	

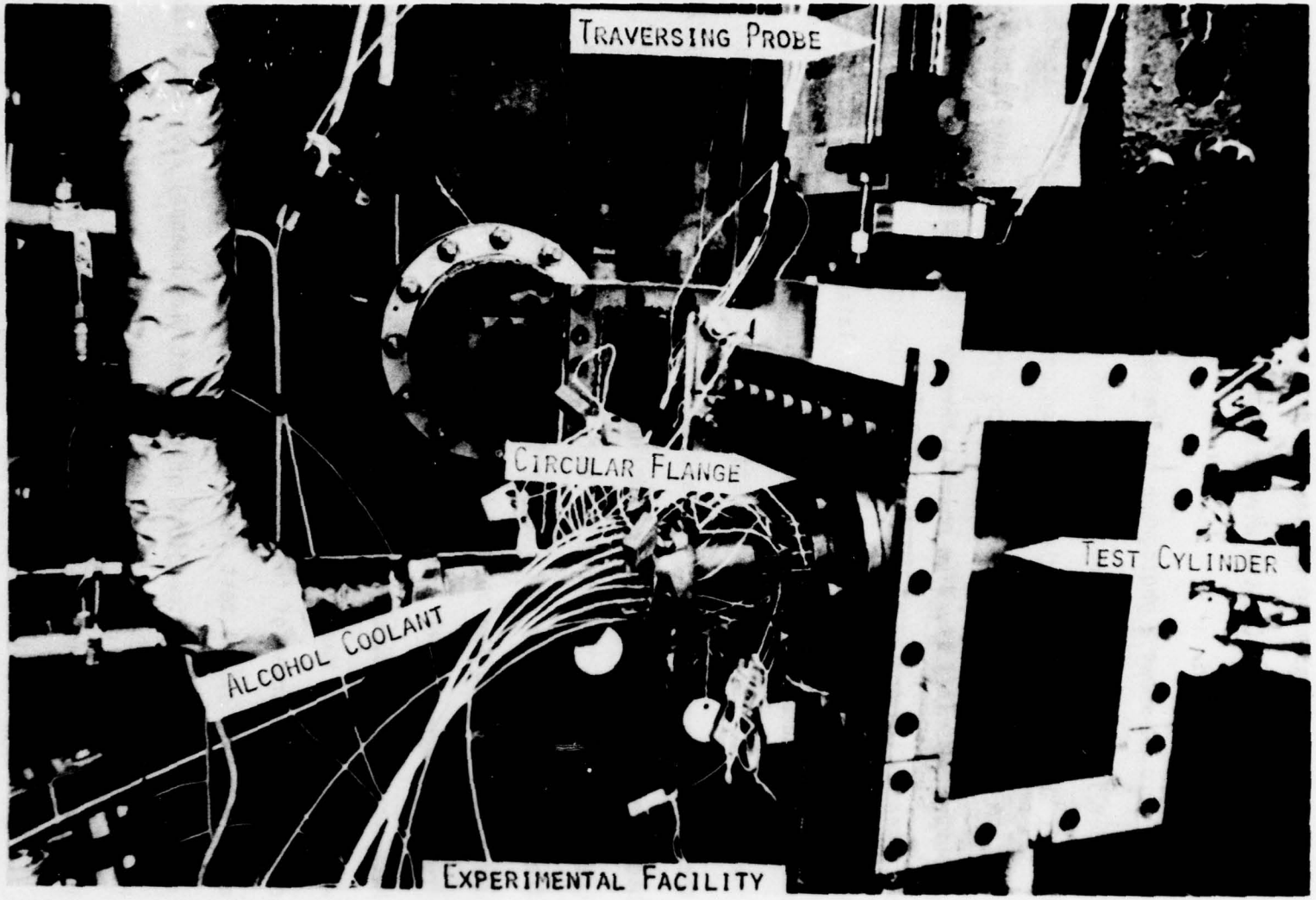

Figure A4. Photograph of the Test Cylinder in the Flow Channel

The flow channel width and height remained constant at 11.43cm and 20.32cm.

Straightener-Mixing Section

	Straightener	Length 3.0 in
	Mixing Section	Length 16.0 in
Turbulence Section		
	Screen Section	Length 2.0 in
	Turbulence Section	Length 13.8 in
Test Section		Length 12.0 in
Nozzle Exit	Width 4.5 in	Height 1.1 in

II.A.2. Test Cylinder

Cylinder. Figure A5 shows a photograph of the test cylinder prior to installation of the instrumentation. The test cylinder was fabricated from two concentric, 7 in. long copper cylinders. The outer, 2 in. O.D. cylinder was machined to a wall thickness of 1/16 in. The inner cylinder was machined to a O.D. of 1 7/8 in. and a I.D. of 1 1/4 in. Along the outside of the inner cylinder, 10 channels were milled, leaving a 8° (arc width) rib between consecutive channels to form coolant channels for internal cooling of test cylinder. The 8° rib was used for installation of instrumentation in the test cylinder surface. Holes were drilled into each end of the cylinder to provide inlet and exit ports for each coolant channel. The outer cylinder was slipped over and then oven brazed to the inner cylinder.

As shown in Figure A5, the test cylinder was equipped with a film coolant plenum chamber, soldered in place, and a removable injection plate. Two 1/2 in. dia. tubes were used to supply air film coolant

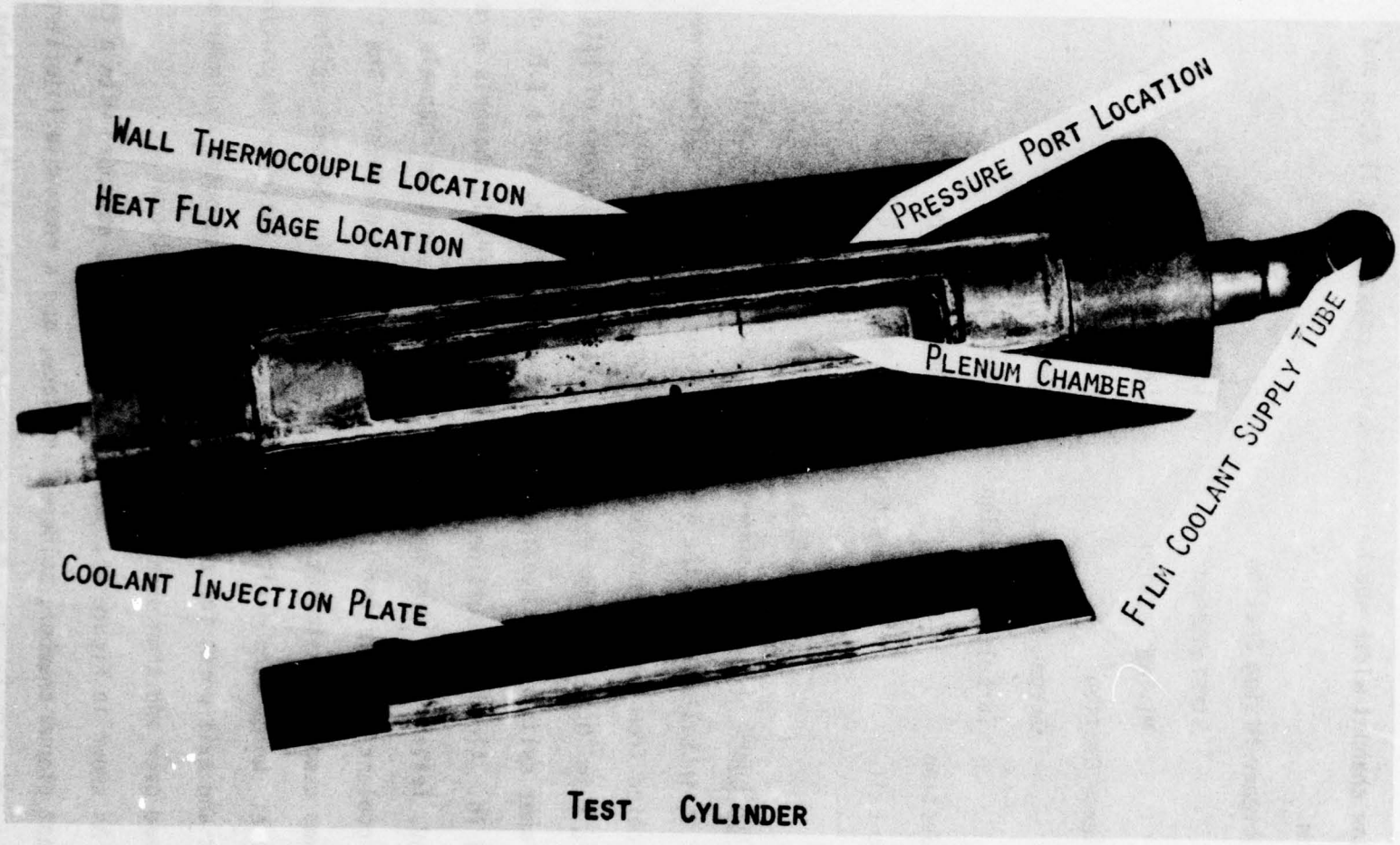

Figure A5. Photograph of the Test Cylinder without the Injection Plate over the Plenum Chamber

to the plenum chamber. The injection plate consisted of two individually fabricated plates. A 1/16 in. thick plate, that sat flush with the cylinder surface, and a smaller, thicker plate (1/8 in) bonded to the back. When placed over the plenum, the thicker plate sat down inside the plenum chamber, but the additional thickness of the injection plate was necessary to obtain a length-to-diameter ratio for the coolant hole greater than 2. This L/d_o value insured that the coolant jet maintained its identity as it left the hole. A 3/16" tube was bonded to the back side of the injection plate (see Fig. 40 back in the main body, Section II.B.2) to provide a coolant channel for cooling the injection plate. The injection plate was sealed to the cylinder with a silicone rubber (GE RTV 106). The day after the RTV sealant had been applied, the plenum chamber was pressurized and a leak detection liquid was placed on the plate-cylinder junction to test for pressure leaks. Once the pressure seal was confirmed, the cylinder was ready for experimentation. If leaks were found, the plate was removed and resealed.

Alcohol Coolant Loops. As shown in Figure A6, the cylinder was chilled by two alcohol coolant loops. The primary loop pumped cold methyl alcohol through the 10 coolant channels milled in the cylinder. Alcohol, drawn from a reservoir inside an insulated tank, was pumped through a closed methanol-dry ice bath heat exchanger. As Figures A4 and A6 show, the alcohol reached the cylinder manifold through a 1" insulated pipe. The flow from the manifold passed through 10 individual coolant channels in the cylinder, and returned to the reservoir through individual tubes, each regulated by a throttling valve.

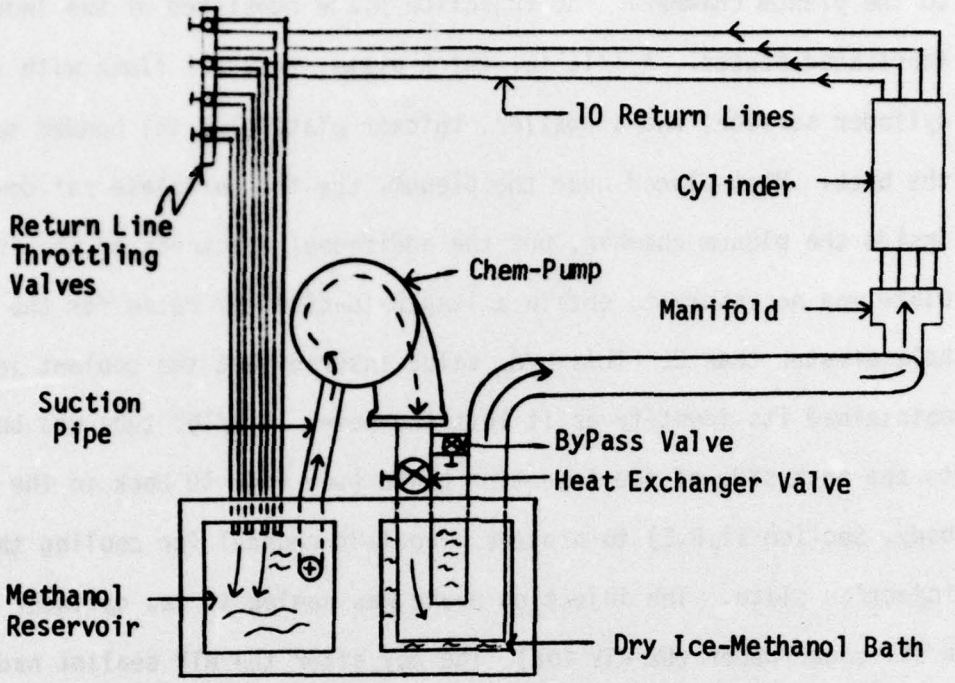

a) Primary Coolant Loop

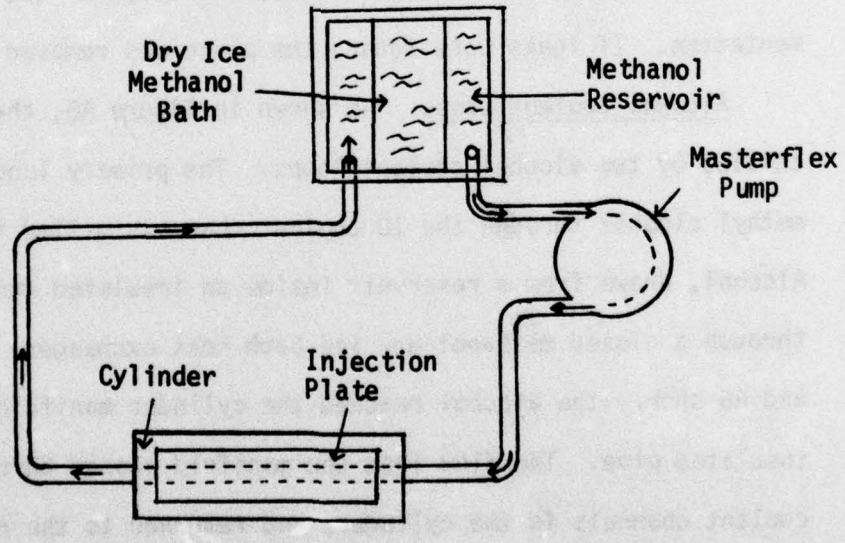

b) Secondary Coolant Loop

Figure A6. Schematics of the Alcohol Coolant Loops

The secondary loop pumped cold methyl alcohol through the coolant tube bonded to the back of the injection plate. Tygon tubing was attached to each end of the coolant tube and run through the two film coolant supply tubes. This created a concentric annular flow channel, with chilled methyl alcohol inside the Tygon tubing, and film coolant air in the annulus. The chilled alcohol was held in a small insulated reservoir-heat exchanger, and pumped to the injection plate by a variable speed tubing pump (positive displacement pump).

Film Coolant Supply. The film coolant air supply system is shown in the schematic drawing in Figure A7. The film coolant air was initially stored in a surge tank at 1500 psig. The air flow was filtered and regulated to maintain a constant flowmeter inlet pressure. The flow rate was controlled by three valves. Two hot wire mass flowmeters (Thermo System, Inc., Model No. 1352) were used to provide an accurate measurement of the film coolant flow rate in both the low flow rate (0-5 SCFM) and the high flow rate (0-20 SCFM) range. Just upstream of the film coolant plenum chamber, the film coolant air was chilled in a closed methanol-dry ice bath heat exchanger. A pressure test of the entire system was periodically conducted, to check for leaks in the film coolant system by using blank injection plate (no coolant holes) sealed to the cylinder surface. The entire system was pressurized and then isolated from the flow regulating system by a solenoid valve. The pressure inside the film coolant plenum was monitored to verify that no pressure leaks were present.

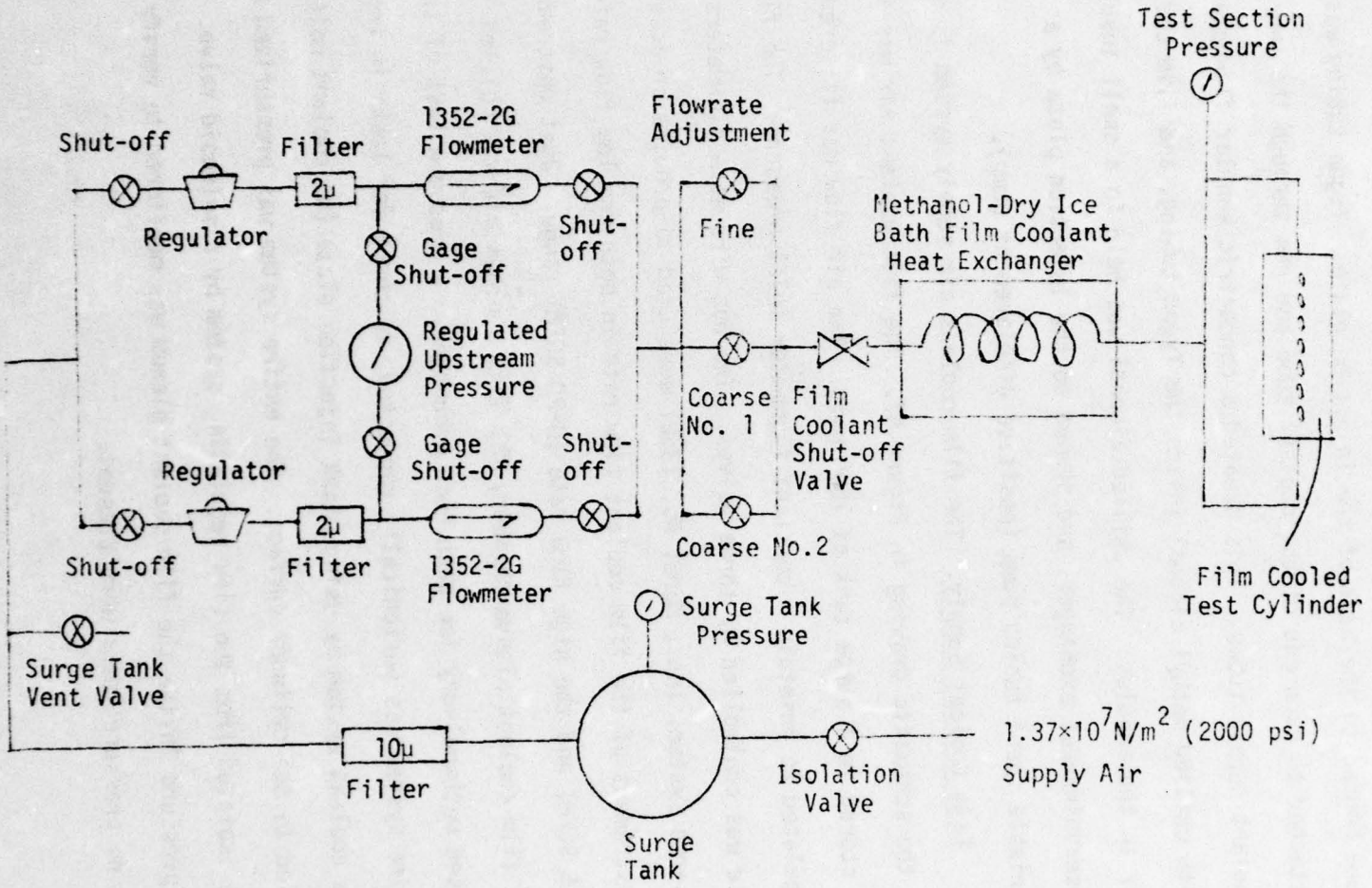

Figure A7. Schematic of the Film Coolant Flow System

II.A.3. Measurements and Instrumentation

Gas Generator Parameters. Both the main air flow and the combustor fuel flow were monitored continuously by flat plate orifice flowmeters to insure to proper freestream flow conditions in the flow channel. For the air flowmeter, the static pressure and temperature were measured upstream of the orifice plate in order to correct the manufacturer's calibration curve which was supplied for a specific upstream pressure and temperature. Upstream of the test cylinder, the freestream conditions (total pressure, $P_{T_{\infty_0}}$ static pressure, P_{∞_0} and total temperature, T_{T_∞}) were measured with a United Sensor wedge probe (Type WT). A traversing mechanism allowed both the vertical and horizontal profiles to be measured by the probe. The probe was indexed to the center of the flow channel to measure the freestream conditions at the beginning of each experimental run and then was retracted close to the top wall of the test section (~1 in) so as not to disturb the flow passing over the cylinder.

Cylinder Instrumentation. During the fabrication of the cylinder, an 8° rib was left between the coolant channel for the installation of pressure taps and thermocouples (to measure the cylinder wall static pressure, P_w, and temperature, T_w). The pressure ports were constructed with 1/32" O.D. hyperdermic tubing epoxied flush with the surface. The thermocouples, consisting of a thermocouple bead surrounded by solder and sanded into a cylindrical shape, were also epoxied flush with the surface. The hyperdermic tubing and thermocouple wires were passed through the hollow center of the cylinder. Figure A8 presents a planar view of the cylindrical test surface with the injection plate-cylinder

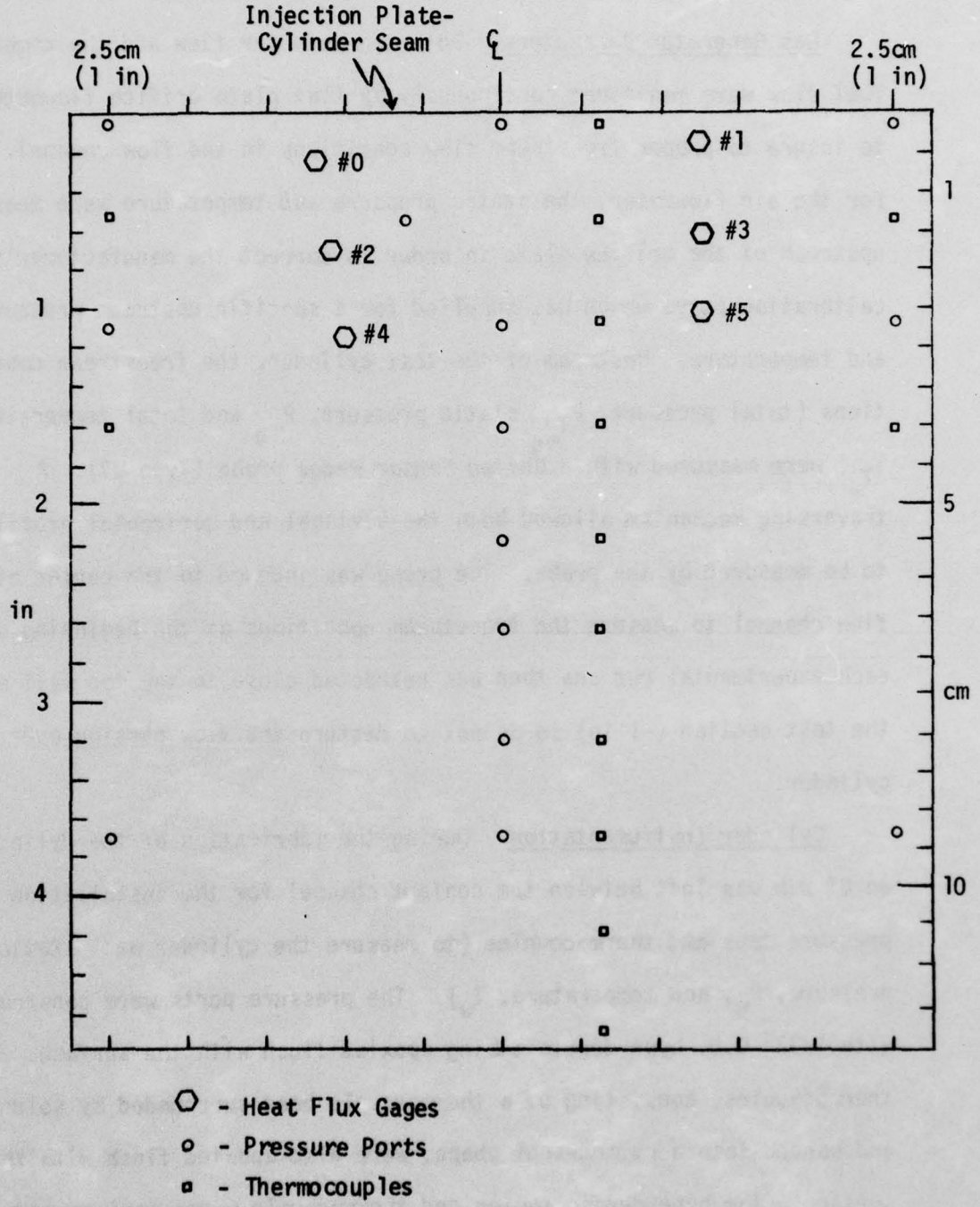

Figure A8. Planar View of the Instrumented Test Cylinder Surface Downstream of the Row of Injection Holes

seam located at the top of the figure showing the location of instrumentation downstream of the row of injection holes. The location of heat flux gages installed on the test surface are also shown in Figure A8. At each heat flux gage location, a hole was drilled through the cylinder surface, and a copper plug (3/16" O.D.) was press fitted in, to prevent any leakage from a coolant channel. A hole was drilled through the center of the plug and the heat flux gage was press fitted into it. The calibration and theory of operation of the heat flux gage are presented in Appendix III. A pressure probe and thermocouple were inserted into the plenum chamber to measure the plenum film coolant conditions. Two holes (1/16" deep), drilled into each injection plate, had thermocouples epoxied into them.

Pressure Measurements. All pressures were measured using differential variable reluctance pressure transducers (Validyne, Model DP15). The freestream total pressure (directly upstream of the cylinder), the fuel orifice plate pressure difference, the main air orifice plate pressure difference and the static pressure in the air flowmeter were all measured on individual pressure transducers. The freestream total ($P_{T_{\infty_0}}$) and static (P_{∞_0}) pressures along with the cylinder wall pressure (P_w) were fed into a pressure sampling device. This allowed the differential pressure ($P_w - P_{\infty_0}$) at discrete locations along the cylinder to be cycled through and measured while using only one transducer. This sampling device also permitted the freestream total-static pressure difference ($P_{T_{\infty_0}} - P_{\infty_0}$) to be measured. Actual measurement of the individual pressures was not done in order to avoid large errors that could have occurred by subtracting two large values of pressure with only

a small difference. Listed below are the pressure measurements made, and the pressure range of the transducer used for each measurement.

Pressure Sampling Device ($P_w - P_{\infty_o}$ and $P_{T_{\infty_o}} - P_{\infty_o}$)	-1 psi to +1 psi
Air Orifice Plate Differential Pressure	-10 psi to +10 psi
Fuel Orifice Plate Differential Pressure	-10 psi to +10 psi
Total Freestream Pressure	-100 psi to +100 psi
Air Flowmeter Static Pressure	-1000 psi to +1000 psi

Temperature Measurements. All temperature measurements of the cylinder surface, the plenum chamber air, and the injection plate were made by copper-constantan thermocouples using an ice bath reference. The freestream total temperature (T_{T_∞}) was measured with a chromel-alumel thermocouple.

Heat Flux Measurements. Due to the small size of the thin foil, Gardon heat flux sensors (Thermogage, Inc., Model 2000, 0.44cm 0.11) used in this investigation, the signal produced was in the microvolt range. Therefore each sensor was matched with an operational amplifier (gain ~ 1000) to provide a millivolt level signal. To eliminate any additional EMF sources between the sensors and the amplifiers, all solder connections were made with low noise, cadium-tin solder. The electronic circuit for the heat flux gage is shown in Fig. A9. The output from the amplifier was fed through a voltage divider-filter circuit designed to filter out any noise from other electronic equipment. This circuit also provided the external resistance to the oscillograph

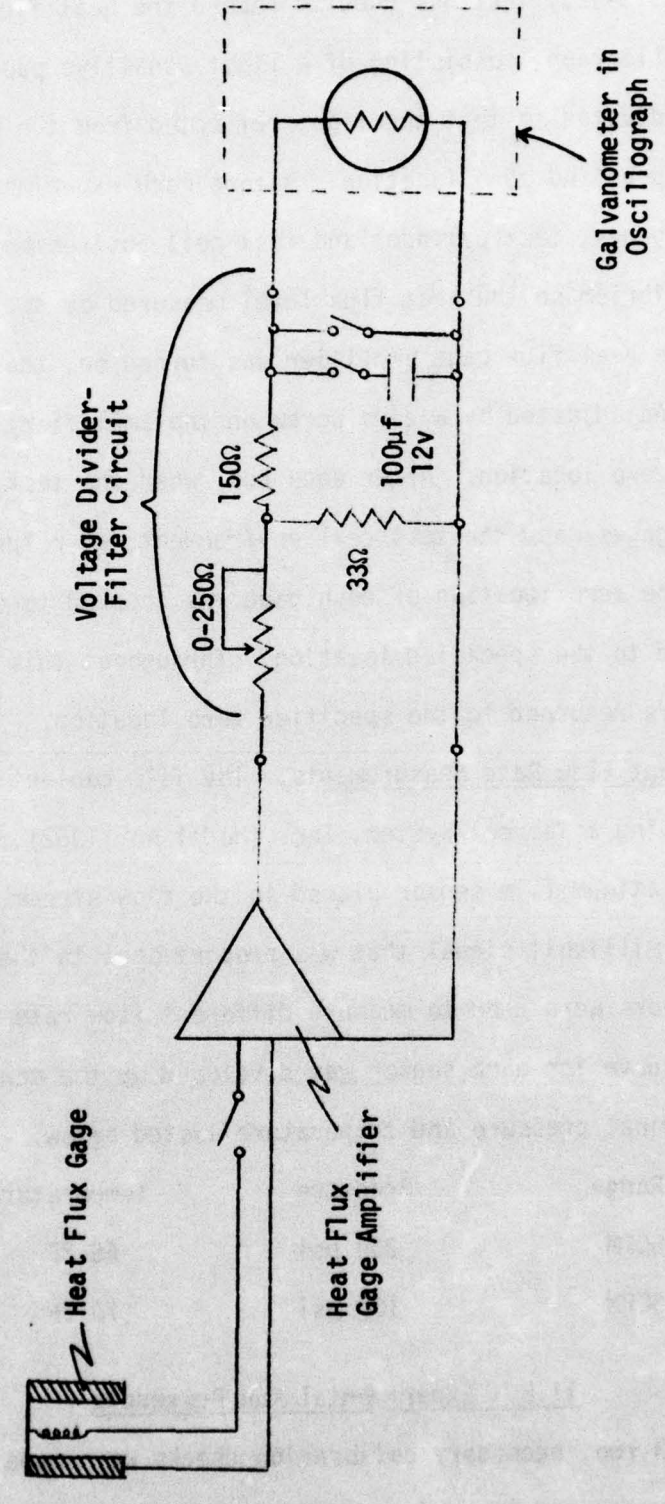

Figure A9. Schematic of the Heat Flux Gage Circuit

(CEC, Model No. 5-123) that was used to record the heat flux gage output. The oscillograph, consisting of a light sensitive paper and galvanometer, was adjusted so that the light reflected from the galvanometer was set at a specified zero location. Before each experimental run, the heat flux gages, test cylinder and test cell environment were in thermal equilibrium so the heat flux level measured by the gages was zero. When the heat flux gage amplifier was turned on, the gage output was checked (and adjusted by a zero screw on the amplifier) to verify the specified zero location. After each run, when the test cylinder, the heat flux gages, and the test cell environment had returned to thermal equilibrium, the zero location of each gage was checked to confirm if it had returned to the specified location. Throughout this investigation, the gages always returned to the specified zero location.

Film Coolant Flow Rate Measurements. The film coolant flow rate was measured using a Thermal-System, Inc. (Model No. 1352) mass flowmeter with a platinum film sensor placed in the flow stream. The sensor produced a millivolt signal that was proportional to the mass flux (ρV). Two sensors were used to measure different flow rate ranges and a calibration curve for each sensor was developed by the manufacturer, TSI, at the nominal pressure and temperature listed below.

Flow Range	Pressure	Temperature
0-5 SCFM	250 psi	65 °F
0-20 SCFM	100 psi	70 °F

II.B. Experimental Run Procedure

Before each run, necessary calibration checks were made of the pressure transducers and recording devices. Calculations were made of

the freestream pressure and temperature necessary to achieve the desired Reynolds number and freestream-to-wall temperature ratio. Since it was desirable to set the main air flow rate before the combustor was ignited, the mass flow rate computed from the hot conditions, was used to compute the cold flow freestream presssure for the cold flow freestream temperature. Once these basic pre-run procedures had been completed, the experimental run began.

The pumps in the primary and secondary coolant loops were started. Dry ice was added to the heat exchanger in the primary loop until the cylinder wall temperature reached ~460°R. The air flow rate was then increased until the calculated cold flow pressure was reached. The fuel valve was then opened, allowing fuel to flow to the secondary port of the fuel nozzle. A hand regulator was opened, allowing air to flow to the primary port of the fuel nozzle. The spark plug exciter was switched on and as soon as the methanol had been ignited, the exciter was turned off. The fuel and air flow rates were gradually adjusted until the calculated freestream pressure and temperature were achieved. Due to the hot flow over the cylinder, the wall temperature jumped about 20°F upon ignition. Dry ice was added to the methanol heat exchanger in the primary loop to bring the wall temperature down to 470°R. Additional dry ice was added during the course of the experimental run to maintain the wall temperature at this level. Once the cylinder temperature and freestream total pressure and total temperature had been set, the air orifice plate pressure difference, the air flowmeter static pressure and temperature, the freestream total-static pressure difference and the fuel orifice plate pressure difference were

recorded and then continuously monitored throughout the run to insure that the freestream flow conditions did not change. With these freestream conditions set, the investigation of the parameters of interest began.

As stated in Secion III.A.1, preliminary experiments were concluded to determine the freestream flow conditions upstream of the test cylinder. This involved the mapping of the freestream profiles in front of the cylinder. The probe, measuring freestream total temperature, total pressure, and static pressure, was attached to a traversing mechanism that moved in 1/90 in. steps. For a vertical traverse of the flow field, the probe was lifted from the center of the flow channel (placed there to set the freestream conditons) to within 0.4 in. of the top of the channel. The probe measurements were recorded at 1/2 in. intervals as the probe was inserted through the flow field to within 0.4 in. of the bottom of the channel. The probe was then moved back through the field until it was within 0.4 in. of the top of the channel. To conduct a horizontal traverse, the probe and traversing mechanism were moved to the port on the side of the flow channel, and the mapping procedure was repeated. To investigate the influence of the Reynolds number on the freestream profiles, the probe was returned to the center of the rectangular duct. The freestream total pressure and temperature corresponding to the new Reynolds number were set and the new traverses were taken.

The next phase of the preliminary experiments, discussed in Sections III.A.2. and III.A.3.,involved the measurement of the cylinder temperature and pressure distributions. With the freestream conditions

set (for the desired Reynolds number), the traversing probe was moved from the center of the channel to within 1 in. of the top of the channel (in order to not disturb the flow passing over the cylinder). The wall pressure sampling device allowed the differential pressure (P_w-P_{∞_o}) at discrete locations along the cylinder to be cycled through and recorded, while the thermocouples located around the cylinder allowed the temperature distribution to be recorded. The pressure distributions, as discussed in Section III.A.3., were measured with both heated flow (T_{T_∞} ~ 530°R) and unheated flow (T_{T_∞} ~ 35°F), at the same Reynolds number.

The second phase of this investigation, discussed in Section III.B., measurement of the test cylinder heat transfer rates without film cooling. As with all cylinder measurements, once the freestream conditions had been set, the traversing probe was lifted from the center of the channel to within 1 in. of the top of the channel. The oscillograph recorded the heat flux level from all of the gages simultaneously, while the thermocouples distributed around the cylinder allowed the wall temperature to be recorded. To investigate the effect of the injection plate-cylinder seam on the heat transfer rate, the heat flux was measured with the injection plate located at a variety of positions relative to stagnation. The plate-cylinder seam was positioned both upstream and downstream of the heat flux gages by rotating the cylinder on successive experiments.

The final phase of the investigation, as discussed in Section III.C., involved the investigation of film cooling parameters. Once the freestream conditions had been set, and the probe lifted from in front of

the cylinder, the dry wall heat flux and wall temperatures were recorded. Then the film coolant regulating valves were opened until the desired blowing ratio was achieved. With the film coolant flow rate set, the heat flux, wall temperatures, injection plate temperature, and plenum temperature were recorded. When these measurements had been completed, a new value of the blowing ratio was set and the same measurements were retaken. This process continued until each blowing ratio of interest had been investigated. The film coolant flow was shut-off and the dry wall heat flux was checked at the end of the experiment.

II.C. Data Reduction

During each experimental run, a group of basic measurements were recorded. To measure the freestream conditions upstream of the test cylinder, the total temperature, the total pressure and the total-static pressure difference were recorded. Along the cylinder surface, measurements of the wall temperature and wall heat flux were taken. In the film coolant system, the injection plate temperature, the plenum air temperature, and the coolant mass flow rate were all recorded. These values were then reduced to familiar heat transfer and flow parameters.

All properties necessary to compute the freestream flow and heat transfer parameters were determined from data found in Ref. 40. Since the data was only presented at 100°K intervals. the data for the ratio of specific heats, the viscosity and the thermal conductivity were curve fitted by the least squares method. All three properties demonstrated the best fit of the data with third order polynomials, conse-

quently the coefficients computed for the third order polynomial were used to determine the freestream properties. For the film coolant, air properties were determined from data taken from Ref. 41. With data provided only at 50°F intervals, the data for viscosity and Prandtl number were curve fitted the same way the freestream properties were, and once again a third order polynomial provided the best fit of the data. Therefore the coefficients computed for the third order polynomial were used to determine the film coolant properties.

Having measured the total and static pressure, the following equation was used to compute the Mach number.

$$\frac{P_T}{P} = \left(1 + \frac{\gamma-1}{2} Ma^2\right)^{\gamma/\gamma-1}$$

The specific heat ratio, γ, was based on the freestream total temperature, since a Mach number of ~0.08 made the difference between the total and static freestream temperatures less than 0.1%. The static temperature was computed using the following equation.

$$\frac{T_T}{T} = 1 + \frac{\gamma-1}{2} Ma^2$$

The perfect gas law was then used to calculate the freestream density.

The freestream velocity upstream of the cylinder, computed from the Mach number and static temperature, was combined with the freestream density and freestream viscosity to form a Reynolds number based on the cylinder diameter.

$$Re_D = \frac{\rho_\infty V_{\infty_0} D}{\mu_\infty} \qquad \text{(A-19)}$$

Although the freestream velocity upstream of the cylinder was computed, the local velocity along the cylinder surface differed significantly from the upstream velocity. Initially the local velocity was calculated from potential flow theory for a cylinder in an infinite flow.

$$V_\infty = 2V_{\infty_0} \sin\theta \tag{A-20}$$

A subsequent refinement in the local velocity calculation was achieved by computing the potential flow for a cylinder in the existing, finite flow channel. A comparison of both methods revealed that for θ in the range of 20° to 40° (the range of θ_i investigated in this study) the difference between the two velocities was less than 5%. All values of local V_∞ reported herein were determined from Eq.(A-22).

It is conventional to use the surface heat flux and the freestream-wall temperature difference to define a local convective heat transfer coefficient. Therefore

$$h_o = \frac{q''_{w,o}}{T_\infty - T_{w_o}} \tag{33}$$

where the subscript o designates no film cooling (dry wall). The dry wall heat transfer coefficient was computed directly from the heat flux and wall temperature measurements made during each experimental run. Since the wall temperatures at the gage locations were not measured, the temperature at each gage location was determined by interpolating between the measured temperatures surrounding the gages (see Fig. A8). Using a mean film temperature, $(T_\infty+T_w)/2$, a thermal conductivity was determined and combined with the heat transfer coefficient to compute a Nusselt number based on the cylinder diameter.

Similarly, the heat flux with film cooling can be combined with the freestream-wall temperature difference to define a local convective heat transfer coefficient with film cooling. Therefore

$$h_{FC} = \frac{q''_{w,FC}}{T_\infty - T_{w_{FC}}} \tag{34}$$

where the subscript FC designates with film cooling. The ratio of these two heat transfer coefficients can also be written as a Stanton number ratio (since the local freestream conditions are the same for both)

$$\frac{h_{FC}}{h_o} = \frac{St_{FC}}{St_o} \tag{35}$$

In order to present a percentage reduction in the Stanton number due to film cooling, the film cooling performance was defined as

$$1 - \frac{St_{FC}}{St_o} \tag{36}$$

and called the Stanton Number Reduction.

To determine the dimensionless coolant temperature, Θ_c, the temperature of the air leaving the coolant holes (T_c) needed to be determined. Since the injection plate and plenum air temperatures were recorded during each experimental run, an investigation was conducted to correlate the temperature rise of the coolant passing through the injection plate (with the coolant mass flow rates). The study and its results are discussed in detail in Appendix IV, but the temperature rise was found to be correlated with the parameters, $\overline{Nu}$ (mean Nusselt number) and x^+ (or $L/d_o/RePr$). With $\overline{Nu}$ plotted as a function of x^+, the experimental data were curve fitted with a third order polynomial (which gave the

best least squares fit of the data). To compute x^+, film coolant plenum temperature was used to determine the coolant viscosity and Prandtl number. Having measured the film coolant flow rate, and knowing the number of holes and the diameter of each holes, the mass flux $(\rho V)_c$ of the coolant through each injection hole was calculated. Then combining the mass flux with the hole diameter and coolant viscosity, the coolant Reynolds number was calculated. Although the injection plate thickness remained constant, the angle of the coolant hole affected the length-to-diameter ratio of the hole, therefore this ratio was computed for the injection angle investigated. The x^+ value was thus computed by $x^+ = (L/d_o)/(RePr)_c$. Inserting the x^+ value into the least square fit equation of the experimental data generated the $\overline{Nu}$ value. The two values, $\overline{Nu}$ and x^+, were used in the following equation

$$\frac{T_c - T_{PL}}{T_w - T_{PL}} = 1 - e^{-4\overline{Nu}x^+} \qquad \text{(A-52)}$$

to determine the temperature of the coolant as it left the injection hole (T_c). Combining T_c with the freestream static and cylinder wall temperature, Θ_c was computed.

To compute the film coolant hydrodynamic parameters, the assumption of uniform flow through all of the coolant holes was made. Knowing the number of holes and the hole area, the mass flux $(\rho_c V_c)$ of the coolant was determined. Having previously found the coolant temperature, T_c, the coolant density was computed and used with the coolant mass flux $(\rho_c V_c)$ to calculate the coolant velocity (V_c). Using the potential

flow calculations to compute the local freestream velocity, the coolant-freestream velocity and density ratios were calculated. Once the two ratios were known, the mass flux (M) and momentum flux (I) ratios were computed. The x, y, and z components of the hydrodynamic parameters were computed with the α and β injection angles.

All of the calculations discussed were done by a data reduction computer program. Besides the parameters mentioned, the program calculated several film coolant geometric parameters, including the x/d_o and z/s downstream locations of each gage from injection, and the angular location of each gage relative to stagnation. The next pages present the data reduction program followed by a listing of the program variable names and a sample output page for a typical experimental run.

AD-A035 716 PURDUE UNIV LAFAYETTE IND THERMAL SCIENCES AND PROPU--ETC F/G 21/5
STAGNATION REGION GAS FILM COOLING SPANWISE ANGLED COOLANT INJE--ETC(U)
DEC 76 D W LUCKEY, M R L'ECUYER N00014-75-C-0873
UNCLASSIFIED TSPC-TR-76-2 NL

4 OF 4
AD A035716

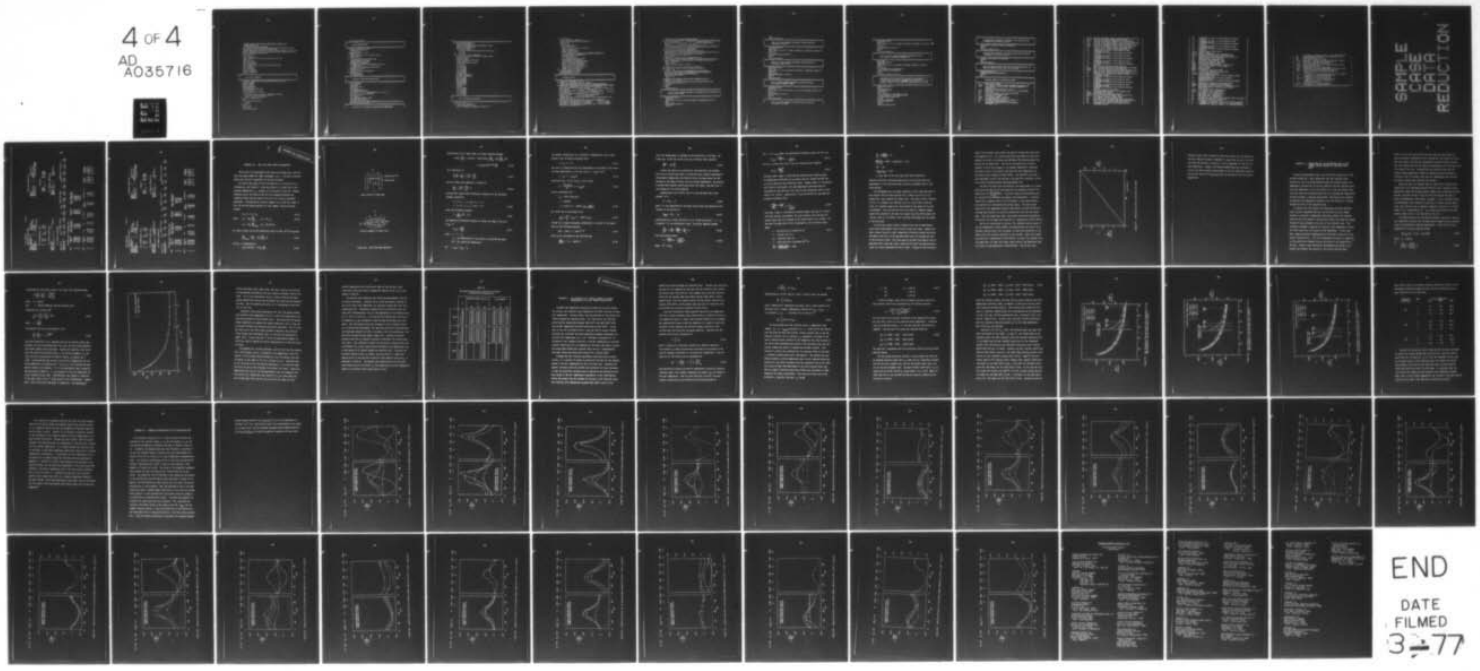

END
DATE FILMED
3-77

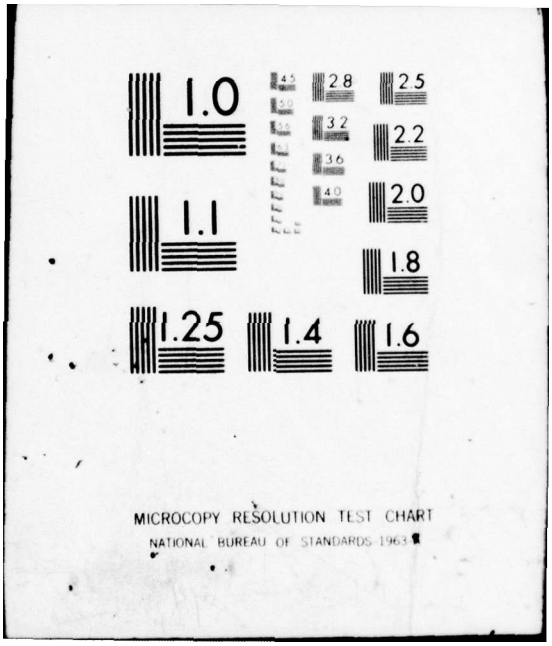
1.0
1.1
1.25
1.4
1.6
1.8
2.0
2.2
2.5
2.8
3.2
3.6
4.0
4.5
5.0
MICROCOPY RESOLUTION TEST CHART
NATIONAL BUREAU OF STANDARDS-1963-A

```
      PROGRAM DATARE(INPUT,OUTPUT,TAPE5=INPUT,TAPE6=OUTPUT)
      COMMON/ONE/VEL,A,W
      INTEGER DATE,MESSAG(10),ROUTE
      REAL MWT,MFC,K,MACH,MASFLO,MU,NUSULT(6),LD,M1,M2,MX1,MY1,MZ1,
     1MX2,MY2,MZ2,I1,I2,IX1,IY1,IZ1,IX2,IY2,IZ2
      DIMENSION XDOWN(6),XDO(6),ZS(6),HF(6),TWL(6),REDCR(6),TW(6),TM(6),
     1COND(6),HFCOF(6),HFLOC(6),ST1(6),ST2(6),STO(6),CORL(6),CORLCR(6),
     2PHI(6),STANRE(6),CRHF(6),DT(6)
      DATA GC/32.174/
      DATA NO/15/
      DATA DO/0.0625/
      DATA (XDOWN(I),I=1,6)/.24,.14,.69,.59,1.14,.96/
      DATA Z/0./
      DATA S/0.207/
      DATA DIST/0.259/
      DATA MWT/28.554/
      DATA (CRHF(I),I=1,6)/1.05,1.05,1.05,1.05,1.05/
      DATA THETA/30./
      DATA ALPHA/0./
      DATA BETA/90./
      DATA A/0.0833333/
      DATA D/0.1666667/
      DATA W/0.6719/
CCCCCCCCCCCCCCCCCCCCCCCCCCCCCCCCCCCCCCCCCCCCCCCCCCCCCCCCCCCCCCCCCCCCCC
C                                                                    C
C         INITIALIZE GEOMETRY                                        C
C                                                                    C
CCCCCCCCCCCCCCCCCCCCCCCCCCCCCCCCCCCCCCCCCCCCCCCCCCCCCCCCCCCCCCCCCCCCCC
      NAMELIST /CHANGE/MWT,THETA,ALPHA,BETA,NO,DIST,Z,S,DO
    1 READ(5,CHANGE)
      IF(EOF,5)32,2
    2 RPSI=10.73/MWT
      RBTU=1.986/MWT
      RFTLB=1545./MWT
      THETA=THETA*3.14159/180.
      XI=THETA*.99
      THETA=THETA*180./3.14159
      DO 3 I=1,6
        HFLOC(I)=(XDOWN(I)+DIST+XI)/.99*(180./3.14159)
        IF(HFLOC(I).EQ.0.0)HFLOC(I)=1.E-9
    3   XDO(I)=(XDOWN(I)+DIST)/DO
      ZS(6)=ZS(4)=ZS(2)=Z/S
      Z1=S
    4 IF(Z1.GE.(Z+.9))GO TO 5
        Z1=Z1+S
        GO TO 4
    5 Z1=Z1-S
      Z1=Z+.9-Z1
      ZS(5)=Z1/S
      ZS(3)=(Z1+.033)/S
```

```
      ZS(1)=(Z1+.067)/S
CCCCCCCCCCCCCCCCCCCCCCCCCCCCCCCCCCCCCCCCCCCCCCCCCCCCCCCCCCCCCCCCCCCCCCCC
C                                                                      C
C        READ MEASURED DATA                                            C
C                                                                      C
CCCCCCCCCCCCCCCCCCCCCCCCCCCCCCCCCCCCCCCCCCCCCCCCCCCCCCCCCCCCCCCCCCCCCCCC
    6 READ(5,7)ROUTE,MFC,TPLEN
    7 FORMAT(I1,F9.0,F9.0)
      IF(EOF,5)1,8
    8 READ(5,9)(HF(I),I=1,6)
    9 FORMAT(6F5.2)
      READ(5,10)(TWL(I),I=1,6),TPLT1,TPLT2
   10 FORMAT(8F5.2)
      DO 11 J=1,6
   11   HFLOC(J)=HFLOC(J)*3.14159/180.
      THETA=THETA*3.14159/180.
      ALPHA=ALPHA*3.14159/180.
      BETA=BETA*3.14159/180.
      IF(ROUTE.GT.1)READ(5,12)(MESSAG(I),I=1,8)
   12   FORMAT(8A10)
      IF(ROUTE.EQ.0.OR.ROUTE.EQ.2)GO TO 16
      READ(5,13)TT,PT,DP
   13  FORMAT(3F5.2)
      READ(5,14)TFMTR,PFMTR,DPFMTR
   14 FORMAT(3F5.2)
      XV=A*COS(THETA)
      YV=-A*SIN(THETA)
CCCCCCCCCCCCCCCCCCCCCCCCCCCCCCCCCCCCCCCCCCCCCCCCCCCCCCCCCCCCCCCCCCCCCCCC
C                                                                      C
C        CALCULATE FREESTREAM CONDITIONS                               C
C                                                                      C
CCCCCCCCCCCCCCCCCCCCCCCCCCCCCCCCCCCCCCCCCCCCCCCCCCCCCCCCCCCCCCCCCCCCCCCC
      TTR=TT+459.67
      PTA=PT+14.697
      PA=PTA-DP
      VISC=FVISC(TTR)
      K=FK(TTR)
      CP=(RBTU*K)/(K-1.)
      C=SQRT(K*GC*RFTLB*TTR)
      MACH=SQRT(2./(K-1.)*((PTA/PA)**((K-1.)/K)-1.))
      TR=TTR/(1.+(K-1.)/2.*MACH**2)
      DENS=PA/(RFSI*TR)
      VEL=MACH*C
      CALL VELOCS(XV,YV,U,V,100)
      VCR=SQRT(U**2+V**2)
      IF(THETA.EQ.0.0)VCR=VEL
      MASFLO=0.70711*SQRT(18.840*DPFMTR*(PFMTR+14.697)/(TFMTR+459.67))
      RED=(DENS*VEL)/(6.*VISC)
CCCCCCCCCCCCCCCCCCCCCCCCCCCCCCCCCCCCCCCCCCCCCCCCCCCCCCCCCCCCCCCCCCCCCCCC
C                                                                      C
C        CALCULATE FILM COOLANT CONDITIONS AND PARAMETERS              C
```

```
C                                                                      C
CCCCCCCCCCCCCCCCCCCCCCCCCCCCCCCCCCCCCCCCCCCCCCCCCCCCCCCCCCCCCCCCCCCCCCCC
   16 MU=FFMU(TPLEN+459.67)
      PR=FPR(TPLEN+459.67)
      REDO=4.*MFC/(FLOAT(NO)*3.14159*(DO/12.)*MU)
      LD=.1625/(SIN(BETA)*DO)
      XPLUS=LD/(REDO*PR)
      IF(MFC.EQ.0.0)GO TO 17
        T2=TPLEN-TCR(XPLUS)*(TPLEN-(TPLT1+TPLT2)/2.)
        GO TO 18
   17   T2=TPLEN
   18   DENFC=PA/(.370*(T2+459.67))
      ROVFC=4.*MFC/(FLOAT(NO)*(DO/12.)**2*3.14159)
      VFC=ROVFC/DENFC
      ROR=DENFC/DENS
      XCUMP=COS(BETA)*COS(ALPHA)
      YCOMP=SIN(BETA)
      ZCOMP=COS(BETA)*SIN(ALPHA)
      F1=VFC/VCR
      F2=VFC/VEL
      FX1=F1*XCOMP
      FY1=F1*YCOMP
      FZ1=F1*ZCOMP
      FX2=F2*XCOMP
      FY2=F2*YCOMP
      FZ2=F2*ZCOMP
      M1=ROVFC/(DENS*VCR)
      M2=ROVFC/(DENS*VEL)
      MX1=M1*XCOMP
      MY1=M1*YCOMP
      MZ1=M1*ZCOMP
      MX2=M2*XCOMP
      MY2=M2*YCOMP
      MZ2=M2*ZCOMP
      I1=M1*F1
      I2=M2*F2
      IX1=I1*XCOMP
      IY1=I1*YCOMP
      IZ1=I1*ZCOMP
      IX2=I2*XCOMP
      IY2=I2*YCOMP
      IZ2=I2*ZCOMP
CCCCCCCCCCCCCCCCCCCCCCCCCCCCCCCCCCCCCCCCCCCCCCCCCCCCCCCCCCCCCCCCCCCCCCCC
C                                                                      C
C         HEAT TRANSFER CALCULATIONS                                   C
C                                                                      C
CCCCCCCCCCCCCCCCCCCCCCCCCCCCCCCCCCCCCCCCCCCCCCCCCCCCCCCCCCCCCCCCCCCCCCCC
      DO 19 I=1,6
   19   HF(I)=HF(I)*CRHF(I)
      TW(1)=(TWL(1)+TWL(2))/2.
      TW(2)=((.75*TWL(3)+.25*TWL(4))+TWL(1))/2.
```

```
      TW(3)=TW(1)
      TW(4)=.25*TWL(4)+.75*TWL(3)
      TW(5)=(((TWL(2)+TWL(6))/2.)+TWL(5))/2.
      TW(6)=TW(5)
      DO 20 I=1,6
        TW(I)=TW(I)+459.67
        DT(I)=TR-TW(I)
        PHI(I)=(TR-(T2+459.67))/(TR-TW(I))
        TM(I)=(TR+TW(I))/2.
        COND(I)=FCOND(TM(I))
        HFCOF(I)=HF(I)/DT(I)
        IF(I.EQ.3)HFCOF(I)=HFCOF(I)+0.25*RED**0.5*COND(I)/D
        ST2(I)=HFCOF(I)/(DENS*CP*VEL)
        XL=A*COS(HFLOC(I))
        YL=-A*SIN(HFLOC(I))
        CALL VELOCS(XL,YL,UL,VL,100)
        VLOCAL=SQRT(UL**2+VL**2)
        ST1(I)=HFCOF(I)/(DENS*CP*VLOCAL)
        IF(MFC.EQ.0.0)STO(I)=ST1(I)
        NUSULT(I)=(HFCOF(I)*D)/COND(I)
        CORL(I)=NUSULT(I)/RED**0.5
        IF(HF(I).EQ.0.0)STO(I)=1.E-99
        STANRE(I)=1.-ST1(I)/STO(I)
   20   HFCOF(I)=HFCOF(I)*3600.
      THETA=THETA*180./3.14159
      ALPHA=ALPHA*180./3.14159
      BETA=BETA*180./3.14159
CCCCCCCCCCCCCCCCCCCCCCCCCCCCCCCCCCCCCCCCCCCCCCCCCCCCCCCCCCCCCCCC
C                                                              C
C        GENERATE OUTPUT                                       C
C                                                              C
CCCCCCCCCCCCCCCCCCCCCCCCCCCCCCCCCCCCCCCCCCCCCCCCCCCCCCCCCCCCCCCC
      WRITE(6,21)(MESSAG(I),I=1,8)
   21 FORMAT(1H1,21X,≠DATA TAKEN ON ≠,8A10/)
      WRITE(6,22)TTR,DENS,PTA,K,VEL,C,MACH,VISC,RED,CP,MASFLO
   22 FORMAT(21X,≠FREESTREAM CONDITIONS≠,43X,≠FREESTREAM PROPERTIES≠,//
     115X,≠TOTAL TEMPERATURE = ≠,F10.2,≠ R≠,33X,≠DENSITY             = ≠,
     2F10.3,≠ LBM/FT3≠/15X,≠TOTAL PRESSURE    = ≠,F10.2,≠ PSIA≠,
     330X,≠GAMMA              = ≠,F10.3/15X,≠VELOCITY            = ≠,F10.2,
     4≠ FT/SEC≠,28X,≠SONIC VELOCITY    = ≠,F10.2,≠ FT/SEC≠/
     515X,≠MACH NO.           = ≠,F10.3,35X,≠VISCOSITY           = ≠,E10.3,
     6≠ LBM/(FT*SEC)≠/15X,≠REYNOLDS NO.       = ≠,E10.3,35X,
     7≠SPECIFIC HEAT     = ≠,F10.3,≠ BTU/(LBM*R)≠/15X,
     8≠MASS FLOW         = ≠,F10.2,≠ LBM/SEC≠//)
      WRITE(6,23)TWL(1),TWL(5),ALPHA,TWL(2),TWL(6),BETA,TWL(3),TPLT1,
     1THETA,TWL(4),TPLT2
   23 FORMAT(21X,≠WALL TEMPERATURES, DEG F≠,48X,≠GEOMETRY≠//
     121X,≠1≠,F7.1,5X,≠5≠,3X,F7.1,41X,≠ALPHA      = ≠,F7.1,≠ DEG≠/
     221X,≠2≠,F7.1,5X,≠6≠,3X,F7.1,41X,≠BETA       = ≠,F7.1,≠ DEG≠/
     321X,≠3≠,F7.1,5X,≠PLT1≠,F7.1,41X,≠THETA INJ  = ≠,F7.1,≠ DEG≠/
     421X,≠4≠,F7.1,5X,≠PLT2≠,F7.1//)
```

```
      WRITE(6,24)TPLEN,T2,MFC,DENFC,REDO,ROR
   24 FORMAT(21X,≠FILM COOLANT CONDITIONS≠,41X,≠FILM COOLANT PROPERTIES≠
     1//15X,≠PLENUM TEMP       = ≠,F10.1,≠ F≠,35X,≠OUTLET TEMP    = ≠,
     2F10.1,≠ F≠/15X,≠MASS FLOW          = ≠,E10.3,≠ LBM/SEC≠,29X,
     3≠DENSITY          = ≠,F10.3,≠ LBM/FT3≠/
     415X,≠HOLE REYNOLDS NO. = ≠,E10.3,37X,≠DENSITY RATIO  = ≠,F10.3//)
      WRITE(6,25)F1,FX1,FY1,FZ1,M1,MX1,MY1,MZ1,I1,IX1,IY1,IZ1,F2,FX2,
     1FY2,FZ2,M2,MX2,MY2,MZ2,I2,IX2,IY2,IZ2
   25 FORMAT(21X,≠FILM COOLANT PARAMETERS≠//
     139X,≠VELOCITY RATIO≠,19X,≠MASS FLUX RATIO≠,14X,
     2≠MOMENTUM FLUX RATIO≠/15X,≠RELATIVE TO≠,6X,3(1X,≠TOTAL≠,5X,≠X≠,7X,
     3≠Y≠,7X,≠Z≠,4X)//15X,≠LOCAL VELOCITY≠,1X,12F8.3/
     415X,≠UPSTREAM VEL≠,3X,12F8.3//)
      WRITE(6,26)
   26 FORMAT(21X,≠MEASURED HEAT TRANSFERED DATA≠//
     115X,≠GAGE≠,5X,≠LOCATION≠,5X,≠LOCAL HEAT FLUX≠,5X,≠TEMP DIFF≠,5X,
     2≠HEAT TRANS COEF≠/26X,≠DEG≠,9X,≠BTU/(FT2*SEC)≠,9X,≠DEG≠,8X,
     5≠BTU/(FT2*HR*R)≠/)
      DO 27 I=1,6
      HFLOC(I)=HFLOC(I)*180./3.14159
      L=I-1
   27 WRITE(6,28) L,HFLOC(I),HF(I),DT(I),HFCOF(I)
   28 FORMAT(17X,I1,6X,F7.3,9X,F7.3,12X,F5.1,9X,F8.3)
      WRITE(6,29)
   29 FORMAT(//15X,≠GAGE≠,5X,≠LOCATION≠,5X,≠X/D≠,5X,≠Z/S≠,
     15X,≠1-ST/STO≠,7X,≠PHI≠,7X,≠NUD/RED**.5≠,7X,≠STANTON≠,5X,
     2≠STANTON≠,/26X,≠DEG≠,38X,≠COOLANT≠,23X,
     3≠LOCAL≠,6X,≠UPSTREAM≠/)
      DO 30 I=1,6
      L=I-1
   30 WRITE(6,31)L,HFLOC(I),XDO(I),ZS(I),STANRE(I),PHI(I),
     1CORL(I),ST1(I),ST2(I)
   31 FORMAT(17X,I1,6X,F7.3,5X,F5.2,3X,F5.2,3X,F8.3,8X,F5.3,6X,
     1F6.3,9X,E10.2,2X,E10.3)
      GO TO 6
   32 STOP
      END
      FUNCTION FK(T)
CCCCCCCCCCCCCCCCCCCCCCCCCCCCCCCCCCCCCCCCCCCCCCCCCCCCCCCCCCCCCCCCCCCCCCCCCC
C                                                                       C
C       FK IS A LFAST SQUARES POLYNOMIAL FUNCTION FOR THE FREESTREAM    C
C       SPECIFIC HEAT RATIO                                             C
C                                                                       C
CCCCCCCCCCCCCCCCCCCCCCCCCCCCCCCCCCCCCCCCCCCCCCCCCCCCCCCCCCCCCCCCCCCCCCCCCC
      DIMENSION COEF(4)
      DATA N/4/
      DATA (COEF(I),I=1,4)/1.3971,2.1695E-5,-7.2324E-8,2.0438E-11/
      FK=0.
      DO 1 I=1,N
    1 FK=FK+COEF(I)*T**(I-1)
      RETURN
```

```
      END
      FUNCTION FVISC(T)
CCCCCCCCCCCCCCCCCCCCCCCCCCCCCCCCCCCCCCCCCCCCCCCCCCCCCCCCCCCCCCCCCCCCCCCCCCCCCCC
C                                                                              C
C        FVISC IS A LEAST SQUARES POLYNOMIAL FUNCTION FOR THE                  C
C        FREESTREAM VISCOSITY                                                  C
C                                                                              C
CCCCCCCCCCCCCCCCCCCCCCCCCCCCCCCCCCCCCCCCCCCCCCCCCCCCCCCCCCCCCCCCCCCCCCCCCCCCCCC
      DIMENSION COEF(4)
      DATA N/4/
      DATA (COEF(I),I=1,4)/7.1190E-7,2.3902E-8,-7.0076E-12,1.1648E-15/
      FVISC=0.
      DO 1 I=1,N
    1 FVISC=FVISC+COEF(I)*T**(I-1)
      RETURN
      END
      FUNCTION FCOND(T)
CCCCCCCCCCCCCCCCCCCCCCCCCCCCCCCCCCCCCCCCCCCCCCCCCCCCCCCCCCCCCCCCCCCCCCCCCCCCCCC
C                                                                              C
C        FCOND IS A LEAST SQUARES POLYNOMIAL FUNCTION FOR THE                  C
C        FREESTREAM CONDUCTIVITY                                               C
C                                                                              C
CCCCCCCCCCCCCCCCCCCCCCCCCCCCCCCCCCCCCCCCCCCCCCCCCCCCCCCCCCCCCCCCCCCCCCCCCCCCCCC
      DIMENSION COEF(4)
      DATA N/4/
      DATA (COEF(I),I=1,4)/2.9393E-7,7.3917E-9,-1.0358E-12,1.7623E-16/
      FCOND=0.
      DO 1 I=1,N
    1 FCOND=FCOND+COEF(I)*T**(I-1)
      RETURN
      END
      FUNCTION FPR(T)
CCCCCCCCCCCCCCCCCCCCCCCCCCCCCCCCCCCCCCCCCCCCCCCCCCCCCCCCCCCCCCCCCCCCCCCCCCCCCCC
C                                                                              C
C        FPR IS A LEAST SQUARES POLYNOMIAL FUNCTION FOR THE                    C
C        FILM COOLANT PRANDTL NUMBER                                           C
C                                                                              C
CCCCCCCCCCCCCCCCCCCCCCCCCCCCCCCCCCCCCCCCCCCCCCCCCCCCCCCCCCCCCCCCCCCCCCCCCCCCCCC
      DIMENSION COEF(4)
      DATA N/4/
      DATA (COEF(I),I=1,4)/8.1161E-1,-9.0181E-5,-5.4857E-7,6.6667E-10/
      FPR=0.
      DO 1 I=1,N
    1 FPR=FPR+COEF(I)*T**(I-1)
      RETURN
      END
      FUNCTION FFMU(T)
CCCCCCCCCCCCCCCCCCCCCCCCCCCCCCCCCCCCCCCCCCCCCCCCCCCCCCCCCCCCCCCCCCCCCCCCCCCCCCC
C                                                                              C
C        FFMU IS A LEAST SQUARES POLYNOMIAL FUNCTION FOR THE                   C
C        FILM COOLANT VISCOSITY                                                C
```

```
C                                                                       C
CCCCCCCCCCCCCCCCCCCCCCCCCCCCCCCCCCCCCCCCCCCCCCCCCCCCCCCCCCCCCCCCCCCCCCCCCCC
      DIMENSION COEF(4)
      DATA N/4/
      DATA (COEF(I),I=1,4)/-4.3248E-6,5.5331E-8,-6.5640E-11,3.800E-14/
      FFMU=0.
      DO 1 I=1,N
    1 FFMU=FFMU+COEF(I)*T**(I-1)
      RETURN
      END
      FUNCTION TCR(XPLUS)
CCCCCCCCCCCCCCCCCCCCCCCCCCCCCCCCCCCCCCCCCCCCCCCCCCCCCCCCCCCCCCCCCCCCCCCCCCC
C                                                                       C
C        TCR IS A LEAST SQUARES POLYNOMIAL FUNCTION FOR THE             C
C        FILM COOLANT TEMPERATURE CORRECTION                            C
C                                                                       C
CCCCCCCCCCCCCCCCCCCCCCCCCCCCCCCCCCCCCCCCCCCCCCCCCCCCCCCCCCCCCCCCCCCCCCCCCCC
      REAL NUDO
      DIMENSION COEF(4)
      DATA N/4/
      DATA (COEF(I),I=1,4)/4.2354E2,-3.8872E5,1.3864E8,-1.5722E10/
      NUDO=0.
      DO 1 I=1,N
    1   NUDO=NUDO+COEF(I)*XPLUS**(I-1)
      TCR=1.0-EXP(-4.0*NUDO*XPLUS)
      RETURN
      END
      SUBROUTINE VELOCS(X,Y,U,V,K)
CCCCCCCCCCCCCCCCCCCCCCCCCCCCCCCCCCCCCCCCCCCCCCCCCCCCCCCCCCCCCCCCCCCCCCCCCCC
C                                                                       C
C        SUBROUTINE VELOCS CALCULATES THE VELOCITY AT POSITION (X,Y)    C
C        FOR POTENTIAL FLOW PAST A CYLINDER IN A WIND TUNNEL,           C
C        U, AND V, ARE THE X AND Y COMPONENTS OF VELOCITY, K IS THE     C
C        NUMBER OF TERMS IN THE SERIES THAT CALCULATES THE VELOCITY     C
C                                                                       C
CCCCCCCCCCCCCCCCCCCCCCCCCCCCCCCCCCCCCCCCCCCCCCCCCCCCCCCCCCCCCCCCCCCCCCCCCCC
      COMMON/ONE/VEL,A,W
      YO=W
      USUM=UPOT(X,Y,0.)
      VSUM=VPOT(X,Y,0.)
      SMU=SMUM(0.)
      DO 1 J=1,K
      USUM=USUM+UPOT(X,Y,YO)+UPOT(X,Y,-YO)
      VSUM=VSUM+VPOT(X,Y,YO)+VPOT(X,Y,-YO)
      SMU=SMU+SMUM(YO)+SMUM(-YO)
    1 YO=YO+W
      U=VEL*(1.-USUM/SMU)
      V=-2.*VEL*VSUM/SMU
      RETURN
      END
      FUNCTION UPOT(X,Y,YO)
```

```
CCCCCCCCCCCCCCCCCCCCCCCCCCCCCCCCCCCCCCCCCCCCCCCCCCCCCCCCCCCCCCCCCCCCCCCCCCCCCCC
C                                                                              C
C        FUNCTION UPOT CALCULATES THE TERMS IN THE SERIES FOR THE              C
C        X COMPONENT OF POTENTIAL VELOCITY                                     C
C                                                                              C
CCCCCCCCCCCCCCCCCCCCCCCCCCCCCCCCCCCCCCCCCCCCCCCCCCCCCCCCCCCCCCCCCCCCCCCCCCCCCCC
      UPOT=(X**2-(Y-YO)**2)/(X**2+(Y-YO)**2)**2
      RETURN
      END
      FUNCTION VPOT(X,Y,YO)
CCCCCCCCCCCCCCCCCCCCCCCCCCCCCCCCCCCCCCCCCCCCCCCCCCCCCCCCCCCCCCCCCCCCCCCCCCCCCCC
C                                                                              C
C        FUNCTION VPOT CALCULATES THE TERMS FOR THE SERIES FOR THE             C
C        Y COMPONENT OF POTENTIAL VELOCITY                                     C
C                                                                              C
CCCCCCCCCCCCCCCCCCCCCCCCCCCCCCCCCCCCCCCCCCCCCCCCCCCCCCCCCCCCCCCCCCCCCCCCCCCCCCC
      VPOT=X*(Y-YO)/(X**2+(Y-YO)**2)**2
      RETURN
      END
      FUNCTION SMUM(Z)
CCCCCCCCCCCCCCCCCCCCCCCCCCCCCCCCCCCCCCCCCCCCCCCCCCCCCCCCCCCCCCCCCCCCCCCCCCCCCCC
C                                                                              C
C        FUNCTION SMUM CALCULATES THE TERMS FOR THE STRENGTH OF THE            C
C        POTENTIAL DOUBLETS WHICH FORM THE CYLINDERS                           C
C                                                                              C
CCCCCCCCCCCCCCCCCCCCCCCCCCCCCCCCCCCCCCCCCCCCCCCCCCCCCCCCCCCCCCCCCCCCCCCCCCCCCCC
      COMMON/ONE/VEL,A,W
      SMUM=(A**2-Z**2)/(A**2+Z**2)**2
      RETURN
      END
CCCCCCCCCCCCCCCCCCCCCCCCCCCCCCCCCCCCCCCCCCCCCCCCCCCCCCCCCCCCCCCCCCCCCCCCCCCCCCC
C                                                                              C
C            VARIABLE NAMES IN ALPHABETICAL ORDER                              C
C                                                                              C
CCCCCCCCCCCCCCCCCCCCCCCCCCCCCCCCCCCCCCCCCCCCCCCCCCCCCCCCCCCCCCCCCCCCCCCCCCCCCCC
C    A         RADIUS OF CYLINDER                                              C
C    ALPHA     FILM COOLANT INJECTION ANGLE MEASURED ON SURFACE, DEG           C
C    BETA      FILM COOLANT INJECTION ANGLE MEASURED UPWARD FROM               C
C              SURFACE, DEG                                                    C
C    C         FREESTREAM SONIC VELOCITY, FT/SEC                               C
C    COND      CONDUCTIVITY BASED ON MEAN FLUID TEMP., BTU/HR*SEC*R            C
C    CORL      NU/RE **.5                                                      C
C    CP        FREESTREAM SPECIFIC HEAT RATIO BTU/LBM*R                        C
C    CRHF      HEAT FLUX CORRECTION FACTOR                                     C
C    D         DIAMETER OF CYLINDER                                            C
C    DENFC     FILM COOLANT DENSITY, LBM/FT3                                   C
C    DENS      FREESTREAM DENSITY, LBM/FT3                                     C
C    DIST      DISTANCE FROM EDGE OF PLATE TO HOLES, IN                        C
C    DO        FILM COOLANT HOLE DIAMETER, IN                                  C
C    DP        FREESTREAM (STAGNATION-STATIC) PRESSURE                         C
C              DIFFERENCE, PSI                                                 C
```

```
C   DPFMTR  PRESSURE DIFFERENCE ACROSS FLOWMETER ORIFICE PLATE, PSI      C
C   DT      WALL-TO-FREESTREAM TEMPERATURE DIFFERENCE, F                 C
C   FCOND   FUNCTION TO DETERMINE CONDUCTIVITY OF FREESTREAM             C
C   FK      FUNCTION TO DETERMINE SPECIFIC HEAT RATIO OF FREESTREAM      C
C   FFMU    FUNCTION TO DETERMINE VISCOSITY FOR FILM COOLANT             C
C   FPR     FUNCTION TO DETERMINE PRANDTL NUMBER FOR FILM COOLANT        C
C   FVISC   FUNCTION TO DETERMINE VISCOSITY OF FREESTREAM                C
C   F1      VELOCITY RATIO, BASED ON LOCAL FREESTREAM VELOCITY           C
C   F2      VELOCITY RATIO, BASED ON FREESTREAM VELOCITY                 C
C   FX1     X-COMPONENT OF VELOCITY RATIO BASED ON LOCAL                 C
C           FREESTREAM VELOCITY                                          C
C   FX2     X-COMPONENT OF VELOCITY RATIO BASED ON UPSTREAM              C
C           VELOCITY                                                     C
C   FY1     Y-COMPONENT OF VELOCITY RATIO BASED ON LOCAL                 C
C           FREESTREAM VELOCITY                                          C
C   FY2     Y-COMPONENT OF VELOCITY RATIO BASED ON UPSTREAM              C
C           VELOCITY                                                     C
C   FZ1     Z-COMPONENT OF VELOCITY RATIO BASED ON LOCAL                 C
C           FREESTREAM VELOCITY                                          C
C   FZ2     Z-COMPONENT OF VELOCITY RATIO BASED ON UPSTREAM              C
C           VELOCITY                                                     C
C   GC      GRAVITATIONAL CONSTANT, LBM-FT/LBF-SEC2                      C
C   HF      HEAT FLUX MEASURED DURING EXPERIMENAL RUN BTU/FT2*SEC        C
C   HFCOF   HEAT TRANSFER COEFFICIENT, BTU/FT2*SEC*R                     C
C   HFLDC   HEAT FLUX GAGE ANGULAR LOCATION FROM STAGNATION, DEG         C
C   I1      MOMENTUM RATIO, BASED ON THE UPSTREAM VELOCITY               C
C   I2      MOMENTUM RATIO, BASED ON THE LOCAL FREESTREAM VELOCITY       C
C   IX1     X-COMPONENT OF MOMENTUM RATIO BASED ON LOCAL                 C
C           FREESTREAM VELOCITY                                          C
C   IX2     X-COMPONENT OF MOMENTUM RATIO BASED ON UPSTREAM              C
C           VELOCITY                                                     C
C   IY1     Y-COMPONENT OF MOMENTUM RATIO BASED ON LOCAL                 C
C           FREESTREAM VELOCITY                                          C
C   IY2     Y-COMPONENT OF MOMENTUM RATIO BASED ON UPSTREAM              C
C           VELOCITY                                                     C
C   IZ1     Z-COMPONENT OF MOMENTUM RATIO BASED ON LOCAL                 C
C           FREESTREAM VELOCITY                                          C
C   IZ2     Z-COMPONENT OF MOMENTUM RATIO BASED ON UPSTREAM              C
C           VELOCITY                                                     C
C   K       FREESTREAM SPECIFIC HEAT RATIO                               C
C   LD      LENGTH-TO-DIAMETER RATIO OF FILM COOLANT HOLE                C
C   MACH    FREESTREAM MACH NUMBER                                       C
C   MASFLO  FREESTREAM MASS FLOW RATE, LBM/SEC                           C
C   MESSAG  MESSAGE TO BE PRINTED ACROSS TOP OF OUTPUT PAGE              C
C   MFC     FILM COOLANT MASS FLOW RATE, LBM/SEC                         C
C   MU      FILM COOLANT VISCOSITY, LBM/FT-SEC                           C
C   MWT     MOLECULAR WEIGHT OF COMBUSTION GASES, LBM/LBMOLE             C
C   M1      MASS FLUX RATIO, BASED ON LOCAL FREESTREAM VELOCITY          C
C   M2      MASS FLUX RATIO, BASED ON UPSTREAM VELOCITY                  C
C   MX1     X-COMPONENT OF MASS FLUX RATIO BASED ON LOCAL                C
C           FREESTREAM VELOCITY                                          C
```

```
C     MX2       X-COMPONENT OF MASS FLUX RATIO BASED ON UPSTREAM                C
C               VELOCITY                                                       C
C     MY1       Y-COMPONENT OF MASS FLUX RATIO BASED ON LOCAL                  C
C               FREESTREAM VELOCITY                                            C
C     MY2       Y-COMPONENT OF MASS FLUX RATIO BASED ON UPSTREAM               C
C               VELOCITY                                                       C
C     MZ1       Z-COMPONENT OF MASS FLUX RATIO BASED ON LOCAL                  C
C               FREESTREAM VELOCITY                                            C
C     MZ2       Z-COMPONENT OF MASS FLUX RATIO BASED ON UPSTREAM               C
C               VELOCITY                                                       C
C     NO        NUMBER OF FILM COOLANT HOLES                                   C
C     NUSULT    NUSSELT NUMBER                                                 C
C     PA        ABSOLUTE FREESTREAM STATIC PRESSURE, PSIA                      C
C     PFMTR     PRESSURE IN ORIFICE PLATE FLOW METER, PSIG                     C
C     PHI       DIMENSIONLESS TEMPERATURE RATIO,(TR-T2)/(TR-TW)                C
C     PR        PRANDTL NUMBER OF FILM COOLANT                                 C
C     PTA       FREESTREAM TOTAL PRESSURE, PSIA                                C
C     PT        FREESTREAM TOTAL PRESSURE, PSIG                                C
C     RBTU      SPECIFIC GAS CONSTANT, BTU/LBM*R                               C
C     RED       FREESTREAM REYNOLDS NUMBER                                     C
C     REDO      FILM COOLANT REYNOLDS NUMBER, BASED ON DO                      C
C     RFTLB     SPECIFIC GAS CONSTANT, FT-LBF/LBM*R                            C
C     ROR       DENSITY RATIO,                                                 C
C     ROUTE     READING ROUTER                                                 C
C     ROVFC     FILM COOLANT FLUX, LBM/FT2*SEC                                 C
C     RPSI      SPECIFIC GAS CONSTANT, PSI*FT3/LBM*R                           C
C     S         FILM COOLANT HOLE SPACING, IN                                  C
C     STANRE    STANTON NUMBER REDUCTION                                       C
C     STO       STANTON NUMBER WITHOUT FILM COOLING BASED ON LOCAL             C
C               FREESTREAM VELOCITY                                            C
C     ST1       STANTON NUMBER WITH FILM COOLING BASED ON                      C
C               FREESTREAM VELOCITY                                            C
C     ST2       STANTON NUMBER WITH FILM COOLING BASED ON UPSTREAM             C
C               VELOCITY                                                       C
C     TCR       FILM COOLANT TEMPERATURE CORRECTION RATIO                      C
C     TFMTR     TEMPERATURE OF ORIFICE PLATE FLOWMETER, F                      C
C     THETA     LOCATION OF INJECTION RELATIVE TO STAGNATION, DEG              C
C     TM        MEAN TEMPERATURE OF FREESTREAM GAS AND WALL                    C
C               TEMPERATURE, R                                                 C
C     TPLEN     FILM COOLANT PLENUM TEMPERATURE, F                             C
C     TPLT1     FILM COOLANT PLATE TEMPERATURE, F                              C
C     TPLT2     FILM COOLANT PLATE TEMPERATURE, F                              C
C     TR        FREESTREAM STATIC TEMPERATURE, R                               C
C     TT        FREESTREAM TOTAL TEMPERATURE, F                                C
C     TTR       FREESTREAM TOTAL TEMPERATURE, R                                C
C     TW        CYLINDER WALL TEMPERATURE FOR A SPECIFIC HEAT FLUX GAGE, R     C
C     TWL       MEASURED CYLINDER WALL TEMPERATURE, F                          C
C     T2        FILM COOLANT EXIT TEMPERATURE, F                               C
C     U         X COMPONENT OF POTENTIAL VELOCITY AT INJECTION LOCATION        C
C     UL        X COMPONENT OF POTENTAIL VELOCITY AT HF GAGE LOCATION          C
C     V         Y COMPONENT OF POTENTIAL VELOCITY AT INJECTION LOCATION        C
```

```
C   VL       Y COMPONENT OF POTENTIAL VELOCITY AT HF GAGE LOCATION      C
C   VCR      LOCAL FREESTREAM VELOCITY AT FC INJECTION, FT/SEC          C
C   VEL      UPSTREAM VELOCITY, FT/SEC                                 C
C   VFC      FILM COOLANT VELOCITY, FT/SEC                             C
C   VELOCS   SUBROUTINE  USED TO CALCULATE THE POTENTIAL VELOCITY      C
C            FIELD FOR A CYLINDER IN A WINDTUNNEL                      C
C   VISC     FREESTREAM VISCOSITY, LBM/FT-SEC                          C
C   VLOCAL   LOCAL FREESTREAM VELOCITY AT GAGE LOCATION, FT/SEC        C
C   W        HEIGHT OF WINDTUNNEL                                      C
C   XCOMP    X-COMPONENT, OF FC INJECTION ANGLE                        C
C   XDO      DIMENSIONLESS DISTANCE DOWNSTREAM OF INJECTION, X/DO      C
C   XDOWN    DISTANCE FROM EDGE OF PLATE TO HF GAGE, IN                C
C   XI       ANGULAR LOCATION OF INJECTION RELATIVE TO                 C
C            STAGNATION, IN                                            C
C   XPLUS    FILM COOLANT HEAT TRANSFER PARAMETER, (L/DO)/(REDO*PR)    C
C   XL       X COORDINATE OF HEAT FLUX GAGE LOCATION                   C
C   XV       X COORDINATE OF INJECTION LOCATION                        C
C   YCOMP    Y-COMPONENT OF FC INJECTION ANGLE                         C
C   YL       Y COORDINATE OF HEAT FLUX GAGE LOCATION                   C
C   YV       Y COORDINATE OF INJECTION LOCATION                        C
C   Z        SPANWISE DISTANCE, IN                                     C
C   ZCOMP    Z-COMPONENT OF FC INJECTION ANGLE                         C
C   ZS       DIMENSIONLESS SPANWISE DISTANCE, Z/S                      C
CCCCCCCCCCCCCCCCCCCCCCCCCCCCCCCCCCCCCCCCCCCCCCCCCCCCCCCCCCCCCCCCCCCCCCC
```

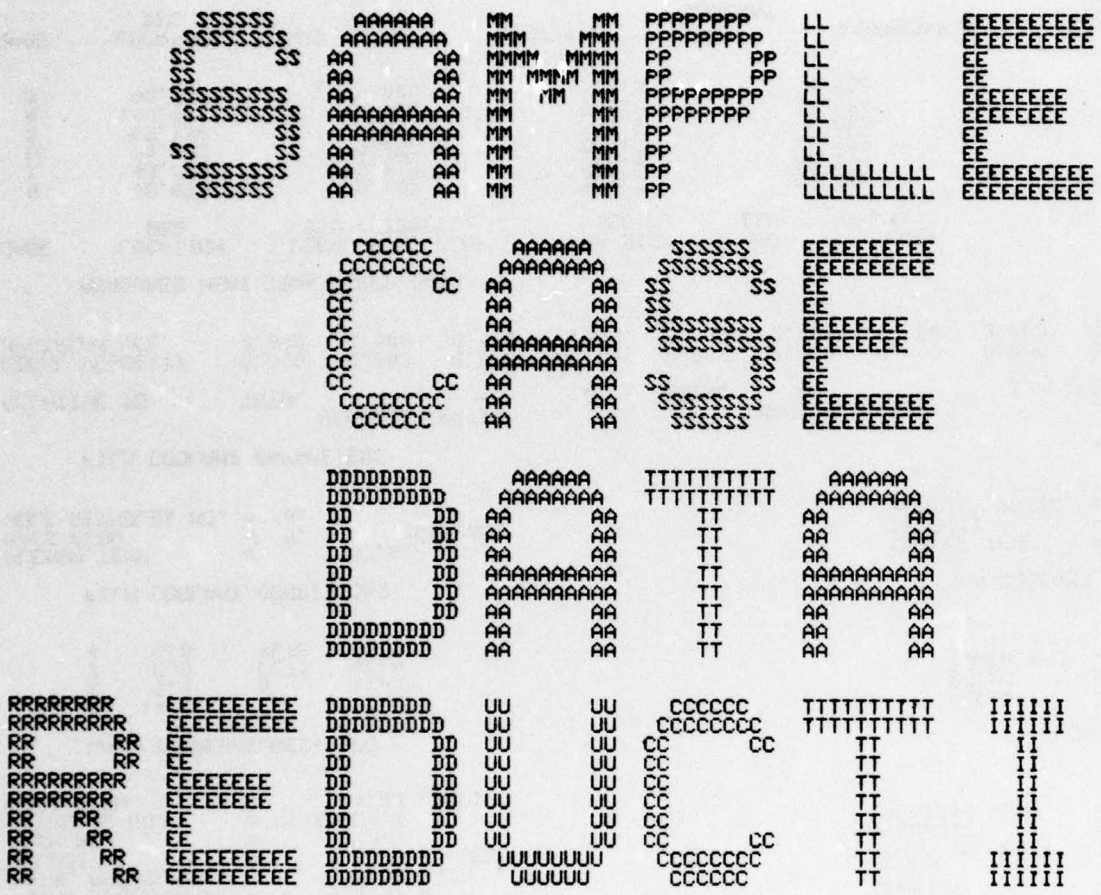
SSSSSS AAAAAA MM MM PPPPPPPP LL EEEEEEEEEE
SSSSSSSS AAAAAAAA MMMM MMMM PPPPPPPPP LL EEEEEEEEEE
SS SS AA AA MMMMM MMMM PP PP LL EE
SS AA AA MM MMM M MM PP PP LL EE
SSSSSSSSS AA AA MM MM MM PPPPPPPPP LL EEEEEEEE
SSSSSSSSS AAAAAAAAAA MM MM PPPPPPPP LL EEEEEEEE
SS AAAAAAAAAA MM MM PP LL EE
SS SS AA AA MM MM PP LL EE
SSSSSSSS AA AA MM MM PP LLLLLLLLLL EEEEEEEEEE
SSSSSS AA AA MM MM PP LLLLLLLLLL EEEEEEEEEE
CCCCCC AAAAAA SSSSSS EEEEEEEEEE
CCCCCCCC AAAAAAAA SSSSSSSS EEEEEEEEEE
CC CC AA AA SS SS EE
CC AA AA SS EE
CC AA AA SSSSSSSSS EEEEEEEE
CC AAAAAAAAAA SSSSSSSSS EEEEEEEE
CC AAAAAAAAAA SS EE
CC CC AA AA SS SS EE
CCCCCCCC AA AA SSSSSSSS EEEEEEEEEE
CCCCCC AA AA SSSSSS EEEEEEEEEE
DDDDDDDD AAAAAA TTTTTTTTTT AAAAAA
DDDDDDDDD AAAAAAAA TTTTTTTTTT AAAAAAAA
DD DD AA AA TT AA AA
DD DD AA AA TT AA AA
DD DD AA AA TT AA AA
DD DD AAAAAAAAAA TT AAAAAAAAAA
DD DD AAAAAAAAAA TT AAAAAAAAAA
DD DD AA AA TT AA AA
DDDDDDDDD AA AA TT AA AA
DDDDDDDD AA AA TT AA AA
RRRRRRRR EEEEEEEEEE DDDDDDDD UU UU CCCCCC TTTTTTTTTT IIIIII OOOOOO NN NN
RRRRRRRRR EEEEEEEEEE DDDDDDDDD UU UU CCCCCCCC TTTTTTTTTT IIIIII OOOOOOOO NNN NN
RR RR EE DD DD UU UU CC CC TT II OO OO NNNN NN
RR RR EE DD DD UU UU CC TT II OO OO NN NN NN
RRRRRRRRR EEEEEEEE DD DD UU UU CC TT II OO OO NN NN NN
RRRRRRRR EEEEEEEE DD DD UU UU CC TT II OO OO NN NN NN
RR RR EE DD DD UU UU CC TT II OO OO NN NNNN
RR RR EE DD DD UU UU CC CC TT II OO OO NN NNN
RR RR EEEEEEEEEE DDDDDDDDD UUUUUUUU CCCCCCCC TT IIIIII OOOOOOOO NN NN
RR RR EEEEEEEEEE DDDDDDDD UUUUUU CCCCCC TT IIIIII OOOOOO NN NN

DATA TAKEN ON 9/26/75

FREESTREAM CONDITIONS

TOTAL TEMPERATURE	= 994.67	R
TOTAL PRESSURE	= 56.40	PSIA
VELOCITY	= 126.79	FT/SEC
MACH NO.	= .082	
REYNOLDS NO.	= 1.699E+05	
MASS FLOW	= 4.28	LBM/SEC

FREESTREAM PROPERTIES

DENSITY	= .150	LBM/FT3
GAMMA	= 1.367	
SONIC VELOCITY	= 1538.67	FT/SEC
VISCOSITY	= 1.870E-05	LBM/(FT*SEC)
SPECIFIC HEAT	= .259	BTU/(LBM*R)

WALL TEMPERATURES, DEG F

1	14.0	5	-1.0
2	5.0	6	11.0
3	2.0	PLT1	67.0
4	2.0	PLT2	71.0

GEOMETRY

ALPHA	= 90.0	DEG
BETA	= 35.0	DEG
THETA INJ	= 20.0	DEG

FILM COOLANT CONDITIONS

PLENUM TEMP	= 57.0	F	
MASS FLOW	= 0.		LBM/SEC
HOLE REYNOLDS NO.	= 0.		

FILM COOLANT PROPERTIES

OUTLET TEMP	= 57.0	F
DENSITY	= .294	LBM/FT3
DENSITY RATIO	= 1.953	

FILM COOLANT PARAMETERS

RELATIVE TO	VELOCITY RATIO TOTAL	X	Y	Z	MASS FLUX RATIO TOTAL	X	Y	Z	MOMENTUM FLUX RATIO TOTAL	X	Y	Z
LOCAL VELOCITY	0.000	0.000	0.000	0.000	0.000	0.000	0.000	0.000	0.000	0.000	0.000	0.000
UPSTREAM VEL	0.000	0.000	0.000	0.000	0.000	0.000	0.000	0.000	0.000	0.000	0.000	0.000

MEASURED HEAT TRANSFERED DATA

GAGE	LOCATION DEG	LOCAL HEAT FLUX BTU/(FT2*SEC)	TEMP DIFF DEG	HEAT TRANS COEF BTU/(FT2*HR*R)
0	48.879	9.187	524.3	63.089
1	43.092	9.712	525.8	66.504
2	74.923	4.357	524.3	41.529
3	69.136	0.000	531.8	0.000
4	100.967	5.092	530.3	34.574
5	90.549	0.000	530.3	0.000

GAGE	LOCATION DEG	X/D	Z/S	1-ST/STO	PHI COOLANT	NUD/RED**.5	STANTON LOCAL	STANTON UPSTREAM
0	48.879	7.98	.34	0.000	.909	1.359	2.24E-03	3.550E-03
1	43.092	6.38	.67	0.000	.907	1.434	2.61E-03	3.742E-03
2	74.923	15.18	.17	0.000	.909	.894	1.15E-03	2.337E-03
3	69.136	13.58	.67	1.000	.897	0.000	0.	0.
4	100.967	22.38	.01	0.000	.899	.747	9.41E-04	1.945E-03
5	90.549	19.50	.67	1.000	.899	0.000	0.	0.

DATA TAKEN ON 9/26/75

FREESTREAM CONDITIONS

TOTAL TEMPERATURE	= 994.67	R
TOTAL PRESSURE	= 56.40	PSIA
VELOCITY	= 126.79	FT/SEC
MACH NO.	= .082	
REYNOLDS NO.	= 1.699E+05	
MASS FLOW	= 4.28	LBM/SEC

FREESTREAM PROPERTIES

DENSITY	= .150	LBM/FT3
GAMMA	= 1.367	
SONIC VELOCITY	= 1538.67	FT/SEC
VISCOSITY	= 1.870E-05	LBM/(FT*SEC)
SPECIFIC HEAT	= .259	BTU/(LBM*R)

WALL TEMPERATURES, DEG F

1	11.0	5	-1.0
2	5.0	6	8.0
3	2.0	PLT1	38.0
4	2.0	PLT2	16.0

GEOMETRY

ALPHA	= 90.0	DEG
BETA	= 35.0	DEG
THETA INJ	= 20.0	DEG

FILM COOLANT CONDITIONS

PLENUM TEMP	= -15.0	F
MASS FLOW	= 2.200E-03	LBM/SEC
HOLE REYNOLDS NO.	= 3.369E+03	

FILM COOLANT PROPERTIES

OUTLET TEMP	= 3.7	F
DENSITY	= .327	LBM/FT3
DENSITY RATIO	= 2.178	

FILM COOLANT PARAMETERS

RELATIVE TO	VELOCITY RATIO TOTAL	X	Y	Z	MASS FLUX RATIO TOTAL	X	Y	Z	MOMENTUM FLUX RATIO TOTAL	X	Y	Z
LOCAL VELOCITY	.231	.000	.132	.189	.503	.000	.288	.412	.116	.000	.067	.095
UPSTREAM VEL	.166	.000	.095	.136	.361	.000	.207	.296	.060	.000	.034	.049

MEASURED HEAT TRANSFERED DATA

GAGE	LOCATION DEG	LOCAL HEAT FLUX BTU/(FT2*SEC)	TEMP DIFF DEG	HEAT TRANS COEF BTU/(FT2*HR*R)
0	48.879	8.137	525.8	55.719
1	43.092	9.135	527.3	62.371
2	74.923	4.252	525.8	40.715
3	69.136	0.000	531.8	0.000
4	100.967	5.617	531.0	38.084
5	90.549	0.000	531.0	0.000

GAGE	LOCATION DEG	X/D	Z/S	1-ST/STO	PHI COOLANT	NUD/RED**.5	STANTON LOCAL	STANTON UPSTREAM
0	48.879	7.98	.34	.117	1.008	1.201	1.98E-03	3.135E-03
1	43.092	6.38	.67	.062	1.005	1.346	2.44E-03	3.509E-03
2	74.923	15.18	.17	.020	1.008	.878	1.13E-03	2.291E-03
3	69.136	13.58	.67	1.000	.997	0.000	0.	0.
4	100.967	22.38	.01	-.102	.998	.824	1.04E-03	2.143E-03
5	90.549	19.50	.67	1.000	.998	0.000	0.	0.

APPENDIX III. HEAT FLUX GAGE THEORY AND OPERATION

Direct heat flux measurements were made using Gardon-type, thin-foil heat flux gages (Model No. 2000, Thermogage, Inc.). The basic principle behind the thin-foil transducer will now be explained.

The sensor body shown in Fig. A10 consists of a circular foil of thickness, S_o, and radius, R. Along the radius R is a heat sink at the constant temperature, T_o. Because of the thinness of the foil, thermal gradients across the width of the foil are assumed negligible and radiation losses from the faces of the foil will also be considered negligible. Considering the circular segment, dr, of the foil shown in Fig. A10 and the energy equation for this segment, the heat balance becomes

$$Q_1 + q = Q_s + Q_2 \tag{A-21}$$

where
$$Q_1 = -kA_1 \left.\frac{\partial T}{\partial r}\right)_r \qquad A_1 = 2\pi r\, S_o \tag{A-22}$$

$$Q_2 = -kA_2 \left.\frac{\partial T}{\partial r}\right)_{r+dr} \qquad A_2 = 2\pi(r+dr)S_o$$

By using a Taylor series and neglecting terms of order $(dr)^2$ and greater

$$\left.\frac{\partial T}{\partial r}\right)_{r+dr} = \left.\frac{\partial T}{\partial r}\right)_r + \frac{\partial}{\partial r}\left(\left.\frac{\partial T}{\partial r}\right)_r\right) dr \tag{A-24}$$

Also Q_s is represented by

$$\rho c[\pi(r+dr)^2 S_o - \pi r^2 S_o]\frac{\partial T}{\partial t} \tag{A-25}$$

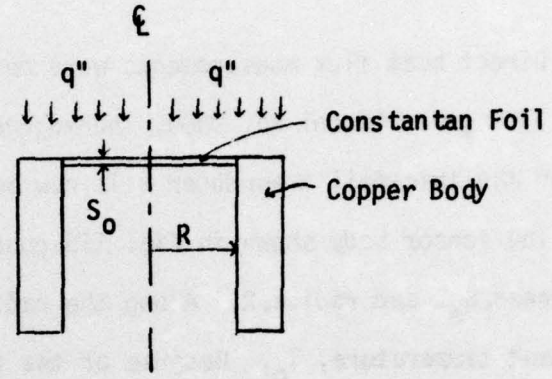

Cross Section of Gage Body

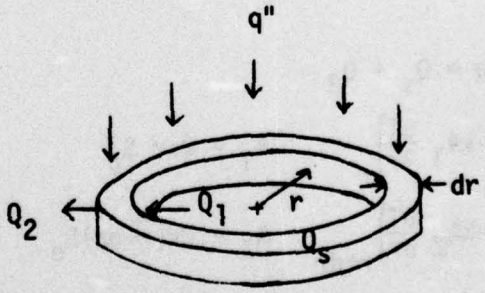

Circular Segment of Sensor Foil

Figure A10. Heat Flux Gage Operation

Substituting in all these terms, the energy equation becomes

$$-k2\pi rS_o \left(\frac{\partial T}{\partial r}\right)_r + q''2\pi r dr = -k2\pi(r+dr)S_o \left[\left(\frac{\partial T}{\partial r}\right)_r + \frac{\partial}{\partial r}\left(\frac{\partial T}{\partial r}\right)_r dr\right]$$

$$+ \rho c\pi S_o[(r+dr)^2 - r^2] \frac{\partial T}{\partial t} \qquad \text{(A-26)}$$

This simplifies to

$$\frac{\rho c}{k}\frac{\partial T}{\partial t} = \frac{q''}{S_o k} + \frac{1}{r}\frac{\partial T}{\partial r} + \frac{\partial^2 T}{\partial r^2} \qquad \text{(A-27)}$$

and for steady state behavior it reduces to

$$\frac{q''}{S_o k} + \frac{1}{r}\frac{\partial T}{\partial r} + \frac{\partial^2 T}{\partial r^2} = 0 \qquad \text{(A-28)}$$

Solving this second order differential equation for the following boundary conditions

$$T = 0 \text{ at } \tau = 0 \text{ and } 0 < r < R$$

$$T = 0 \text{ at } 0 < \tau < \infty \text{ and } r = R \qquad \text{(A-29)}$$

gives the following solution.

$$T = \frac{q''}{4S_o k}(R^2 - r^2) \qquad \text{(A-30)}$$

The temperature difference between the center and edge of the foil, Φ'_{CTR}, is

$$\Phi'_{CTR} = \frac{q''R^2}{4S_o k} \qquad \text{(A-31)}$$

where $\Phi' = T - T_o$

T_o = the temperature on the surface (surrounding the gage)

CTR = the centerline temperature

and $\Phi'_{CTR} = T_{CTR} - T_o$

The thermal conductivity, as a function of temperature, can be represented in the following functional form

$$k = k_o (1 + \varepsilon T) \tag{A-32}$$

The value of temperature will be represented as an average of the center and edge temperatures, so for this case, $T = T_{CTR}/2$, and

$$k = k_o (1 + \varepsilon T_{CTR}/2) \tag{A-33}$$

Substituting Eq. (A-33) into Eq. (A-31) gives

$$q'' = \frac{4S_o k_o T_{CTR}}{R^2} (1 + \varepsilon T_{CTR}/2) \tag{A-34}$$

and for constantan foil

$$k_o = .02174 \text{ kJ/m•sec•K}$$

$$\varepsilon = .00745/K$$

$$k = 0.02174 (1 + .00745 T_{CTR}) \frac{kJ}{m•sec•K} \tag{A-35}$$

Eq. (A-34) can be rearranged to be

$$\frac{1}{4k_o} q'' \frac{R^2}{S_o} = T_{CTR} (1 + .00373 T_{CTR}) \tag{A-36}$$

The EMF for a copper-constantan thermocouple is related to the temperature by the following equation

$$EMF = .0378 T + 1.44 \times 10^{-4} T^2 \tag{A-37}$$

which can be rearranged in the following way

$$\frac{EMF}{.0378} = T (1 + .00378 T) \tag{A-38}$$

Since the thermocouple is attached at the centerline of the gage, combining Eqs. (A-36) and (A-38) gives the following linear equation

$$\frac{EMF}{q''} = .435 \frac{R^2}{S_o} \tag{A-39}$$

Usually the gages are calibrated by radiative heat flux methods, and are not directly applicable to convective heat transfer measurements. The parabolic temperature distribution across the gage causes the temperature on the gage to differ from the surface temperature. By assuming a uniform heat transfer coefficient across the sensor, the heat flux is not uniform as it is with radiation.

Looking back at Eq. (A-27), the q" is not the heat flux to the surface, it is

$$q'' = h(T_\infty - T) \tag{A-40}$$

where T is the temperature on the gage surface while the convective heat transfer to the surface is

$$q''_{CONV} = h(T_\infty - T_o) \tag{A-41}$$

Substituting Eqs. (A-40) and (A-41) in Eq. (A-28) and using $\Phi' = T - T_o$ instead of T in the differential terms, the energy equation becomes

$$\frac{d^2\Phi'}{dr^2} + \frac{1}{r}\frac{d\Phi}{dr} + \frac{q''_{CONV}}{kS_o} - \frac{h\Phi'}{kS_o} = 0 \tag{A-42}$$

with the solution being

$$\Phi' = \frac{q''_{CONV}}{h}\left[1 - \frac{I_o(mr)}{I_o(mR)}\right] \tag{A-43}$$

where $m^2 = h/kS_o$

For $r = 0$, Φ'_{CTR} equals the temperature difference across the foil and

$$\Phi'_{CTR} = \frac{q''_{CONV}}{h}\left[1 - \frac{1}{I_o(mR)}\right] \tag{A-44}$$

But for a uniform heat flux, like with radiation heat transfer,

$$\Phi'_{CTR} = \frac{q''_{RAD}R^2}{4S_o k} \tag{A-45}$$

Therefore when a gage is calibrated by radiative heat transfer means, the temperature difference set up across the foil creates the EMF that is used to generate the calibration curve. However, when in a convective heat transfer environment, the same temperature difference may not correspond to the same heat flux level on the calibration curve as that found in Eq. (A-44). Equating Eqs. (A-44) and (A-45) for the same temperature difference gives

$$\frac{q''_{CONV}}{q''_{RAD}} = \frac{(mR)^2}{4}\,\frac{1}{1 - \frac{1}{I_o(mR)}} \tag{A-46}$$

Thus when a gage is calibrated by radiative means and used in a convective heat transfer environment, the heat transfer rate from the calibration chart must be increased by the factor shown in Eq. (A-46). For the heat flux gage used in this investigation, the following values apply

$$k \sim 80 \text{ kJ/hr-m-K } (13 \text{ Btu/hr}\cdot\text{ft}\cdot{}^\circ\text{F}) \tag{A-47}$$

$$R = .254 \text{ mm } (.01 \text{ in.})$$

$$S_o = .0254 \text{ mm } (.001 \text{ in.})$$

$$h \sim 1022 \text{ kJ/hr}\cdot\text{m}^2\cdot\text{K } (50 \text{ Btu/hr}\cdot\text{ft}^2\cdot{}^\circ\text{F})$$

$$\frac{hR}{k} = \frac{(1022)(.254)}{(80)(1000)} = .0032$$

$$\frac{R}{S_o} = \frac{(.254)}{(.0254)} = 10$$

$$\left(\frac{hR}{k}\right)\left(\frac{R}{S_o}\right) = m^2R^2 = (.0032)(10) = .032$$

$$mR = .179$$

$$q_{CONV}/q_{RAD} = 1.007$$

or less than 1% for this gage under these conditions

Therefore radiative calibrated gages would give accurate heat flux measurements in the convective heat transfer environment used in this investigation.

The Thermogage heat flux gages employed in this study consisted of heat sensors that had been pressed into a .4445 cm (0.175 in.) O.D. oxygen-free, high conductivity copper plug. The sensor itself, 0.508 mm (.02 in.) in diameter and .0254 mm (.001 in.) thick, had a 0.051 mm (.002 in.) diameter copper wire laser-welded to the center of the foil from beneath. This wire and the 0.127 mm (.005 in.) diameter copper, ground wire attached to the heat sink copper body were both coated with .051 mm (.002 in.) of teflon, fully shielded and brought out the bottom of the plug body.

To avoid any surface contour irregularities and to approximate a point source measurement, these miniature gages were used. However the small sensors had only a small temperature difference between the center and edge of the foil, so the maximum output level of the gage was only in the microvolt range. Thus each gage was matched individually with an amplifier with a gain near 1000, converting the heat flux gage microvolt signal to a more convenient millivolt signal. Because of this microvolt

signal from the gage, every effort was made to isolate the system from environmental noise. All solder convections were made with low-noise, cadmium-tin solder to eliminate any additional EMF sources between the sensors and the amplifiers. The zero of the amplifiers did have a tendency to drift with changes in the ambient temperature, therefore they were placed in the control room where the room temperature was maintained fairly constant at 294K (70°F). Each amplifier also had a zero adjustment screw on the outside of the amplifier container, so the zero could be adjusted before each experimental run.

The heat flux gages were calibrated by the manufacturer in a black-body cavity and the gain of each amplifier was adjusted to obtain the sensitivity of $\frac{115.7 \text{ joule}}{m^2\text{-sec}}$/mv. Figure All shows the calibration curve for the heat flux transducer provided by the manufacturer. A typical sensor has a response time of 2.4 millisecond. A few qualifications were required for interpreting the sensor output. The sensor body should be in the temperature range of 283K (510°R) to 505K (910°R) and the gage must operate in a field of uniform heat flux over the sensor body. Since the gages were small, the second restriction presented no difficulty, but the gages were operated at a temperature of 261K (470°R).

Due to the uncertainty in the heat flux readings from the gages at the low temperature of 261K (470°R), the manufacturer was able to use a portable radiative heat flux calibrator to check the calibration of the gages after they had been installed in the cylinder. When the cylinder was cooled to a temperature of 261K (470°R), the heat flux readings from the gages were ~5% lower than those values given by the gages when they were kept at room temperature (~294K [530°R]). The dry wall heat

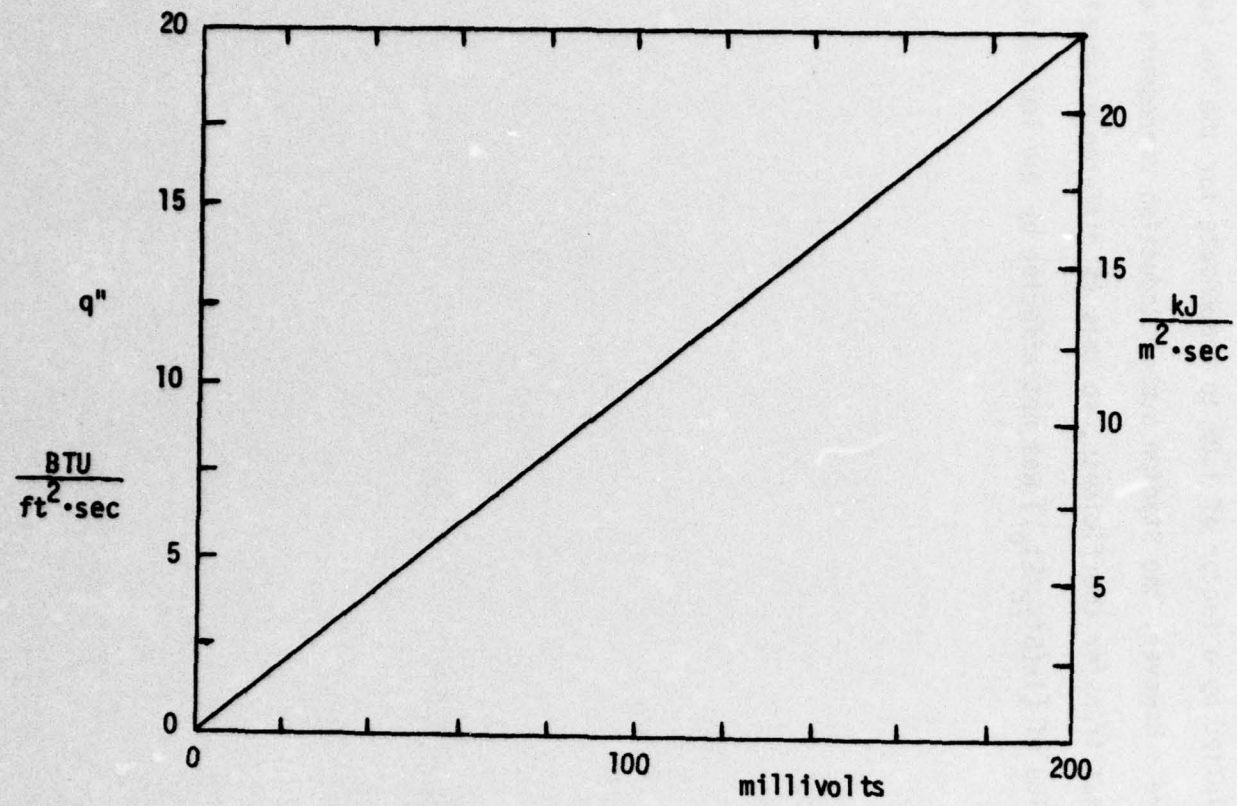

Figure A11. Calibration Curve for the Heat Flux Gages

transfer results were corrected to take into account this 5% difference. The data reduction program in Appendix II shows that the heat flux readings were multiplied by a factor of 1.05 to compensate for the low surface temperature. However, the Stanton Number Reduction represents a ratio of the heat transfer coefficients, so this 5% difference cancelled out and the value of $[1-(St_{FC}/St_o)]$ was not affected by the low surface temperature.

APPENDIX IV. CORRELATION FOR THE TEMPERATURE RISE OF FILM COOLANT FLOWING THROUGH THE INJECTION PLATE HOLES

During the experimental runs, the chilled film coolant air in the cylinder plenum had a lower temperature than the injection plate. Therefore as the film coolant passed through the injection holes, its temperature increased due to the heat addition from the injection plate. Since the temperature of the film coolant as it left the coolant injection hole could not be measured when the hot freestream was flowing over the test cylinder, a separate experimental investigation was conducted to determine the temperature increase of the film coolant as it passed through the holes in the injection plate.

To measure the film coolant exit temperature from the injection plate, the hot freestream flow over the cylinder had to be ceased. Therefore to maintain a temperature difference between the injection plate and the film coolant in the cylinder plenum, warm water was pumped through the tube attached to the back of the injection plate. This procedure succeeded in keeping the injection plate temperature at least 33K (60°F) above the film coolant plenum temperature. A fine, open bead, copper-constantan thermocouple was positioned at the exit of the coolant injection hole. This exit thermocouple was small in comparison to the coolant hole diameter and was positioned at the centerline of the hole. Another copper-constantan thermocouple was placed in the plenum, just beneath the entrance to the coolant injection hole.

Finally a small hole was drilled into the injection plate enabling a copper-constantan thermocouple to be situated near the coolant hole wall. Thus the coolant inlet and exit temperatures and the coolant injection hole wall temperature were all measured simultaneously for each particular film coolant flow rate. Although both the injection plate and film coolant plenum temperatures tended to decrease with each incremental increase in the film coolant flow rate, all temperatures were recorded only when a steady state condition was reached.

Analytical work for internal flows in tubes (with a thermal entry length and a fully developed velocity profile) with a constant surface temperature found that the mean Nusselt number had an eigenvalue solution and was a function of the x^+ value for the flow through the tube (x^+ being a nondimensional tube length, $L/d_o/RePr$). With a combined thermal and hydrodynamic entry length in a tube with a constant surface temperature, Kays [64] was able to compute a numerical solution for a Prandtl number of 0.7 (representing air). His results are plotted as the mean Nusselt number versus x^+ and are shown in Fig. A12.

The energy equation for flow passing through a tube with a constant wall temperature revealed that the mean Nusselt number could be computed from the experimentally measured temperatures. Using the bulk fluid temperature, the energy equation became

$$\dot{m}_{CL} c_{p_{CL}} dT_{CL} = h_x (T_w - T_{CL}) \pi d_o dx \qquad \text{(A-48)}$$

where CL = coolant

or

$$\frac{dT_{CL}}{T_w - T_{CL}} = \frac{h_x \pi d_o}{\dot{m}_{CL} c_{p_{CL}}} dx \qquad \text{(A-49)}$$

Integrating for the entire length of the tube, this equation became

$$\ell n \left(\frac{T_w - T_c}{T_w - T_{PL}} \right) = \frac{-\bar{h} \pi d_o L}{m_{CL} c_{p_{CL}}} \tag{A-50}$$

where PL = plenum

and c = coolant emerging from the injection hole

Simplifying Eq. (A-50) gives

$$\frac{-1}{4x^+} \ell n \left(\frac{T_w - T_c}{T_w - T_{PL}} \right) = \overline{Nu} \tag{A-51}$$

where $x^+ = \frac{L/d_o}{RePr}$

The equation can also be rearranged to read

$$\frac{T_c - T_{PL}}{T_w - T_{PL}} = 1 - e^{-4\overline{Nu}x^+} \tag{A-52}$$

Using the properties of air, computed with the film coolant plenum temperature, and the film coolant mass flow rate, the film coolant Reynolds and Prandtl numbers were calculated. Knowing the injection plate thickness, the angle of the coolant hole, β, and the hole diameter, d_o, the L/d_o ratio was calculated and divided by $(RePr)_{CL}$ to compute the x^+ value. Having measured the coolant inlet and exit temperatures and the plate temperature, and knowing the x^+ value, Eq. (A-51) enabled the mean Nusselt number to be computed. All of the experimental data, plotted as the mean Nusselt number vs. x^+, are presented in Fig. A12 along with the values computed by Kays [64]. Unfortunately, Kays lowest x^+ value fell in the upper range of the x^+ values used for this investigation. However Kays' values did provide some means of comparison. The experimental

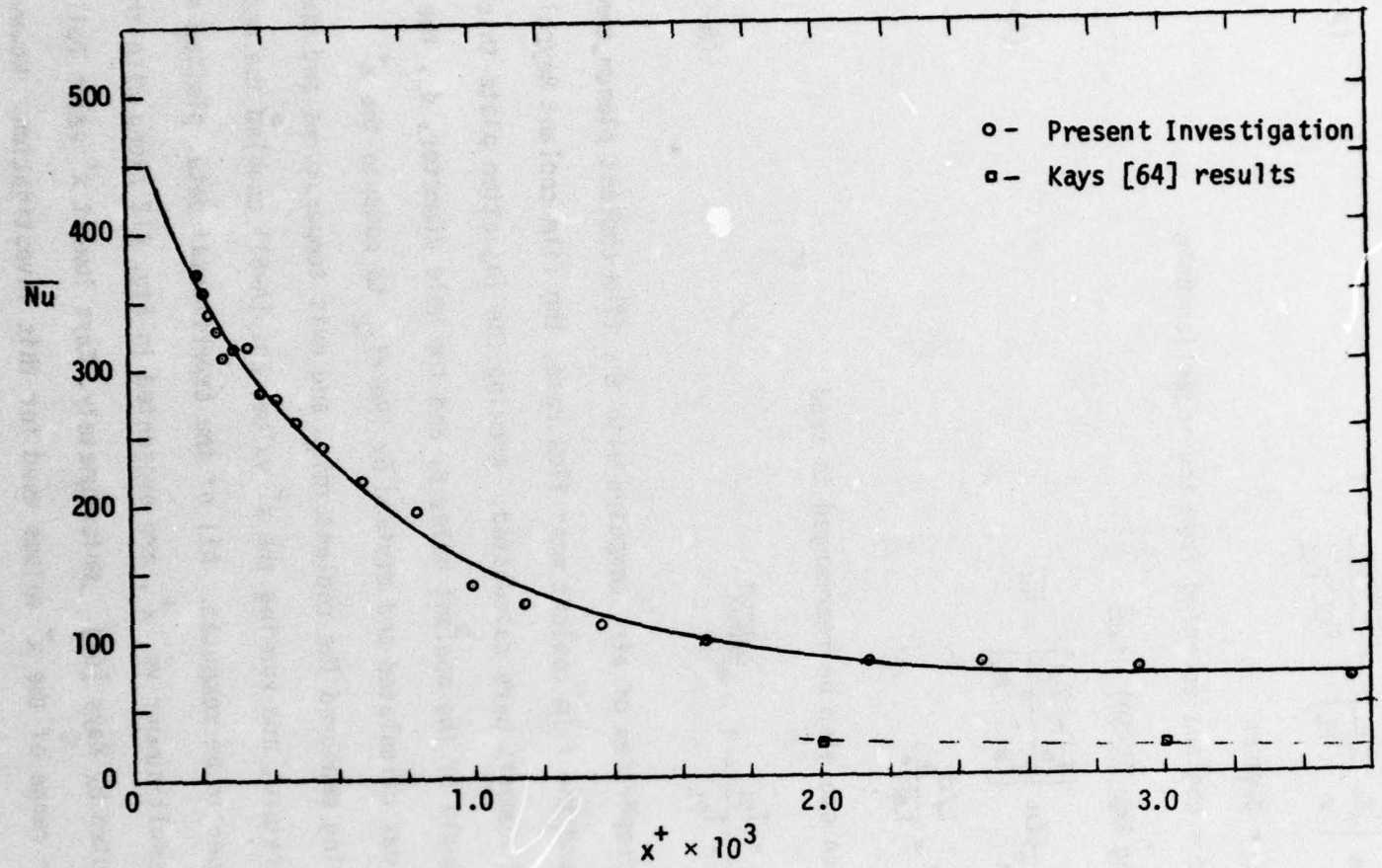

Figure A12. Heat Addition to the Film Coolant as it Passes Through the Holes in the Injection Plate

values were about three times larger than Kays' results, but this was not unreasonable considering the short length-to-diameter ratio of the holes. All of the experimental data was curved fitted by the least squares method and a third order polynomial was found to best represent the data. The line showing the curve fit is represented by the solid line in Fig. A12.

Therefore, during each experimental run, the film coolant plenum and injection plate temperatures as well as the film coolant mass flow rate were measured for each blowing ratio. Then using the film coolant plenum temperature to compute the coolant properties, the x^+ value was calculated following the procedure previously described. This x^+ value was then used in the third order polynomial equation, that had been fitted through the experimental data, to calculate the mean Nusselt number value. Having found the x^+ value and mean Nusselt number, Eq. (A-52) was used to compute the coolant temperature as it left the injection hole.

The methanol-dry ice heat exchanger, used to chill the film coolant, had a fixed length, and as a consequence, the temperature of the film coolant in the cylinder plenum decreased as the film coolant flow rate increased, as was shown in Fig. 50 in Section III.A.2. Therefore some of the variation in the film coolant temperature as it left the injection hole was due to the different film coolant flow rates. Taking the temperature data from all of the experimental runs, and comparing the film coolant exit temperature upon ejection (T_c) for cases where the film coolant mass flow rate and L/d_o ratio were the same, the film

coolant temperature never varied more than 2% from the mean value. These mean values were used to compute the density ratios (ρ_c/ρ_∞) presented in Table A1.

The density ratio tended to vary during the experimental runs due to several conditions. Changing the θ_i value (the angular location of the row of holes from stagnation) for injection altered the local freestream mass flux. Therefore a blowing ratio of 0.25 did not have the same local freestream mass flux (in the denominator of the blowing ratio) at $\theta_i = 40°$ as it did at $\theta_i = 20°$ and the film coolant mass flux had to be changed as θ_i was increased in order to keep the blowing ratio constant. Also the blowing ratio was increased in 0.25 increments from 0 to 2.0 during each experimental run, and since the local freestream mass flux remained constant at fixed θ_i locations, the film coolant mass flux had to be increased to get higher values of M. Therefore different blowing ratios and θ_i locations resulted in different film coolant mass flow rates. Also different β angles for the coolant injection holes led to different L/d_o ratios, which had an influence on the temperature rise of the coolant as it passed through the injection hole. Therefore the different blowing ratios, θ_i angles, and L/d_o ratios all caused the density ratio to vary and this variation of the density ratio and θ_c is presented in Table A1. The density ratio demonstrated a 9% variation from a mean value of 2.21 while θ_c, the dimensionless coolant temperature showed a 7% variation from a mean value of 1.035.

Table A1

The Density Ratio and θ_c Value for Different Film Cooling Configurations

	M	Density Ratio (ρ_c/ρ_∞) θ_i			θ_c Parameter θ_i		
		20°	30°	40°	20°	30°	40°
β=25°	.25	2.02	2.11	2.13	.96	1.00	1.01
	.50	2.10	2.20	2.23	1.00	1.04	1.05
	.75	2.14	2.22	2.25	1.01	1.04	1.06
	1.00	2.15	2.23	2.30	1.02	1.05	1.08
	1.25	2.18	2.25	2.36	1.03	1.06	1.10
	1.50	2.19	2.26	2.37	1.03	1.06	1.10
	1.75	2.20	2.27	2.38	1.04	1.07	1.10
	2.00	2.22	2.27	2.38	1.04	1.07	1.10
β=35°	.25	2.01	2.13	2.17	.96	1.01	1.03
	.50	2.11	2.21	2.23	1.00	1.04	1.05
	.75	2.15	2.24	2.26	1.02	1.05	1.06
	1.00	2.17	2.27	2.32	1.03	1.07	1.08
	1.25	2.20	2.33	2.36	1.04	1.09	1.10
	1.50	2.21	2.33	2.38	1.04	1.09	1.10
	1.75	2.22	2.33	2.41	1.05	1.09	1.11
	2.00	2.23	2.33	2.40	1.05	1.09	1.11
β=45°	.25			2.05			.98
	.50			2.12			1.01
	.75			2.16			1.02
	1.00			2.19			1.03
	1.25			2.20			1.04
	1.50			2.24			1.05
	1.75			2.29			1.07
	2.00			2.27			1.06

APPENDIX V. THE INFLUENCE OF A STEPWISE CHANGE IN THE WALL TEMPERATURE ON THE HEAT TRANSFER COEFFICIENT

Although the temperature distribution around the cylinder surface was uniform, the injection plate temperature did differ from the cylinder wall temperature. The most severe case occurred when no film coolant was flowing through the injection holes. This resulted in the injection plate reaching temperatures between 289K (60°F) and 300K (80°F) while the cylinder temperature was being maintained at 261K (10°F). As was seen in Fig. 49 in Section III.A.2., once the flow of coolant through the holes was initiated, the plate temperature dropped, approaching the cylinder wall temperature, $\Delta T_w \lesssim 11K$. Therefore a discussion of the influence of this stepwise variation in the wall temperature on the heat transfer coefficient will be conducted for the worst case when no coolant was being blown through the injection holes and for a representative case when coolant was being blown through the injection holes.

Although the heat transfer measurements were made along a curved surface, it is possible to obtain an analytical solution for the stepwise change in the wall temperature for the flat plate case. Therefore the angular locations along the cylinder were converted to linear distances, so that the analytical solution could be applied to the particular stepwise change in the wall temperature encountered in this investigation. Before the coolant tube was attached to the back of the injection plate, the injection plate temperature exceeded 366K (200°F) when no film

coolant was flowing through the injection holes. Therefore the analytical solution will be computed for the case with the injection plate without the coolant tube (372K [210°F], first example case), with the injection plate with the coolant tube and without blowing (300K [80°F], second example case), with the injection plate with the coolant tube and with blowing (272K [30°F], third example case), and with the injection plate and cylinder wall being held constant at 261K (10°F).

Since the differential energy equation describing the temperature field for a laminar boundary layer (found along a cylindrical surface in its stagnation region) is linear (when constant properties are assumed), the superposition theory allows the summation of a number of particular solutions to this equation for specific boundary conditions into a solution that also satisfies the energy equation. Therefore the temperature field can be represented as

$$t = \sum_{1}^{n} C_i t_i \tag{A-53}$$

where i stands for a particular solution to a specific condition
The constant C_i allows the particular solutions to be adjusted to the specific boundary conditions of a variable wall temperature. Then the heat flux at the surface can be represented by

$$q''_w = - K \left(\frac{\partial t}{\partial y}\right)_w = - K \sum_{1}^{n} C_i \left(\frac{\partial t_i}{\partial y}\right)_w \tag{A-54}$$

Each particular solution can then be represented as having an unheated starting length, then suddenly changing by an amount Δt_w, the change in the wall temperature. Then for each particular solution, the heat transfer coefficient can be defined by the following equation

$$-K \left(\frac{\partial t_i}{\partial y}\right)_w = h_i \, \Delta t_{w,i} \tag{A-55}$$

Substituting Eq. (A-55) into Eq. (A-54), the wall heat flux becomes

$$q''_w = \sum_1^n C_i h_i \Delta t_{w,i} \tag{A-56}$$

With a stepwise wall temperature variation, the C_i values become unity. Therefore with a stepwise temperature variation of $\Delta t_{w,1}$, $\Delta t_{w,2}$, ..., at locations ξ_1, ξ_2, ..., the heat flux at the wall is

$$q''_w = \sum_1^n h(x,\xi_i) \, \Delta t_{w,i} \tag{A-57}$$

For the cylinder with the injection plate, a temperature step change, $t_w = t_\infty - t_{plate}$ occurred at $\xi_1 = 0$. With the hot gas flowing over the plate and onto the cylinder surface, another step in the temperature occurred, and its location, ξ_2, depended on the angle of the row of injection holes relative to the stagnation line (the location of the row of holes determined the length of the injection plate that the hot gas flowed over before it reached the cylinder surface). This analytical solution was conducted for the injection plate at the three θ_i locations studied during this investigation. The analysis was performed assuming a surface temperature equal to the injection plate temperature for the region extending from the stagnation line to the injection plate-cylinder seam downstream of the row of coolant holes (ξ_2). These ξ_2 angular locations along the cylinder were converted to linear dimensions for these calculations. With the row of holes set at the different θ_i injection locations, ξ_2, became

$$\theta_i = 20° \qquad \xi_2 = 1.536 \text{ cm} \qquad \text{(A-58)}$$
$$30° \qquad 1.975 \text{ cm}$$
$$40° \qquad 2.414 \text{ cm}$$

A laminar boundary layer with an unheated starting length has a heat transfer coefficient represented by the following equation

$$h_x = \frac{0.332 \text{ K } (Pr)^{1/3}(Re_x)^{1/2}}{x[1 - (\xi/x)^{3/4}]^{1/3}} \qquad \text{(A-59)}$$

The first particular solution, according to the superposition theory, has the entire surface at the injection plate temperature. Therefore, using Eq.(A-59)and setting $\xi = 0$, the heat transfer coefficient was computed. Then the heat flux along the injection plate was

$$q''_w = h_1 \text{ (550K - 372K)} \quad \text{(372K plate)} \qquad \text{(A-60)}$$
$$q''_w = h_1 \text{ (550K - 300K)} \quad \text{(300K plate)}$$
$$q''_w = h_1 \text{ (550K - 272K)} \quad \text{(272K plate)}$$

The subscript 1 represents the first particular solution from the superposition theory.

For the second particular solution, it was assumed that there was an unheated starting length until ξ_2, when the wall temperature dropped 111K for the first example case, 39K for the second sample case, and 11K for the third example case. The heat transfer coefficient, h_2, was found using Eq.(A-59) and the ξ_2 values shown in Eq. (A-58). Then the total heat flux at the cylinder surface was found by summing the two particular solutions.

$$q''_w = h_1 (550K - 372K) + h_2 (372K - 261K) \quad (372K \text{ plate}) \qquad (A\text{-}61)$$

$$q''_w = h_1 (550K - 300K) + h_2 (300K - 261K) \quad (300K \text{ plate})$$

$$q''_w = h_1 (550K - 272K) + h_2 (272K - 261K) \quad (272K \text{ plate})$$

Along the cylinder surface, the heat flux was then divided by the total temperature difference, 289K, to compute a single heat transfer coefficient along the cylinder surface. These results were plotted for the three θ_i locations studied during this investigation and are presented in Figs. A13, A14, and A15 (representing the θ_i locations of 40°, 30°, and 20°, respectively). On each curve, the heat transfer coefficient with the injection plate and cylinder wall at the same temperature, 261K (10°F) was also plotted.

Looking at Fig. A13 (θ_i = 40°), the different heat flux gage locations were marked on the figure. At Gage #1, the closest gage to the injection plate, the 300K injection plate heat transfer coefficient was ~11.5% higher than the heat transfer coefficient for the isothermal surface (261K [10°F]),while the 272K (30°F) plate had a heat transfer coefficient that was ~3% higher. However, the heat transfer coefficient with the 372K (210°F) plate was ~37% higher than the heat transfer coefficient for the isothermal surface (261K [10°F]). Gage #0, the next closest gage to the injection plate, showed a heat transfer coefficient ~8% higher for the 300K (80°F) plate, ~2.4% higher for the 272K (30°F) plate and ~26% higher for the 373K (210°F) plate. By the time the flow had reached the location for Gage #2, the heat transfer coefficient was ~4% higher for the 300K (80°F) plate, ~1.4% higher for the 272K (30°F) plate, and ~13% higher for the 372K (210°F) plate. Figures A14 and A15

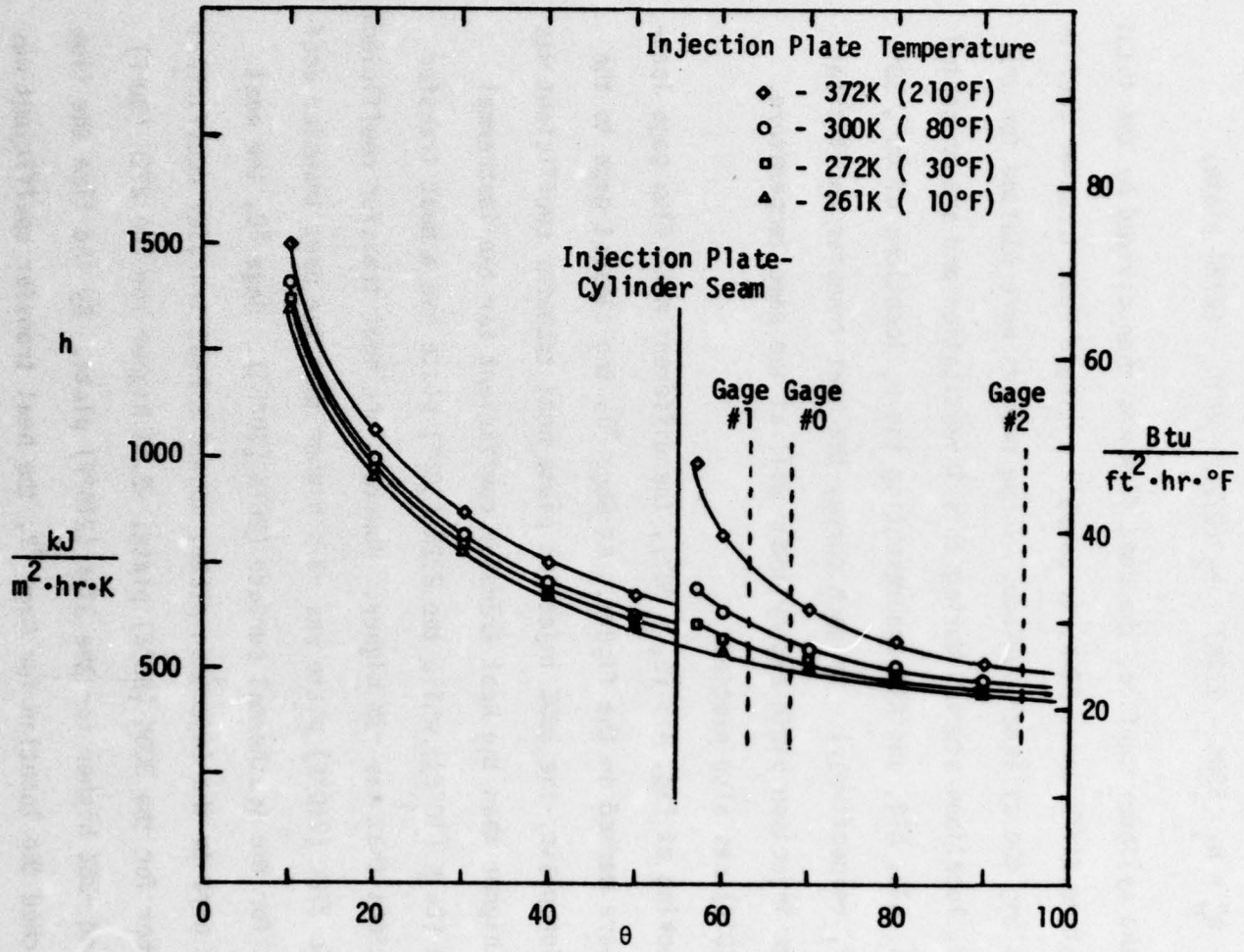

Figure A13. The Influence of the Injection Plate Temperature on the Downstream Heat Transfer Coefficient (Θ_i=40°)

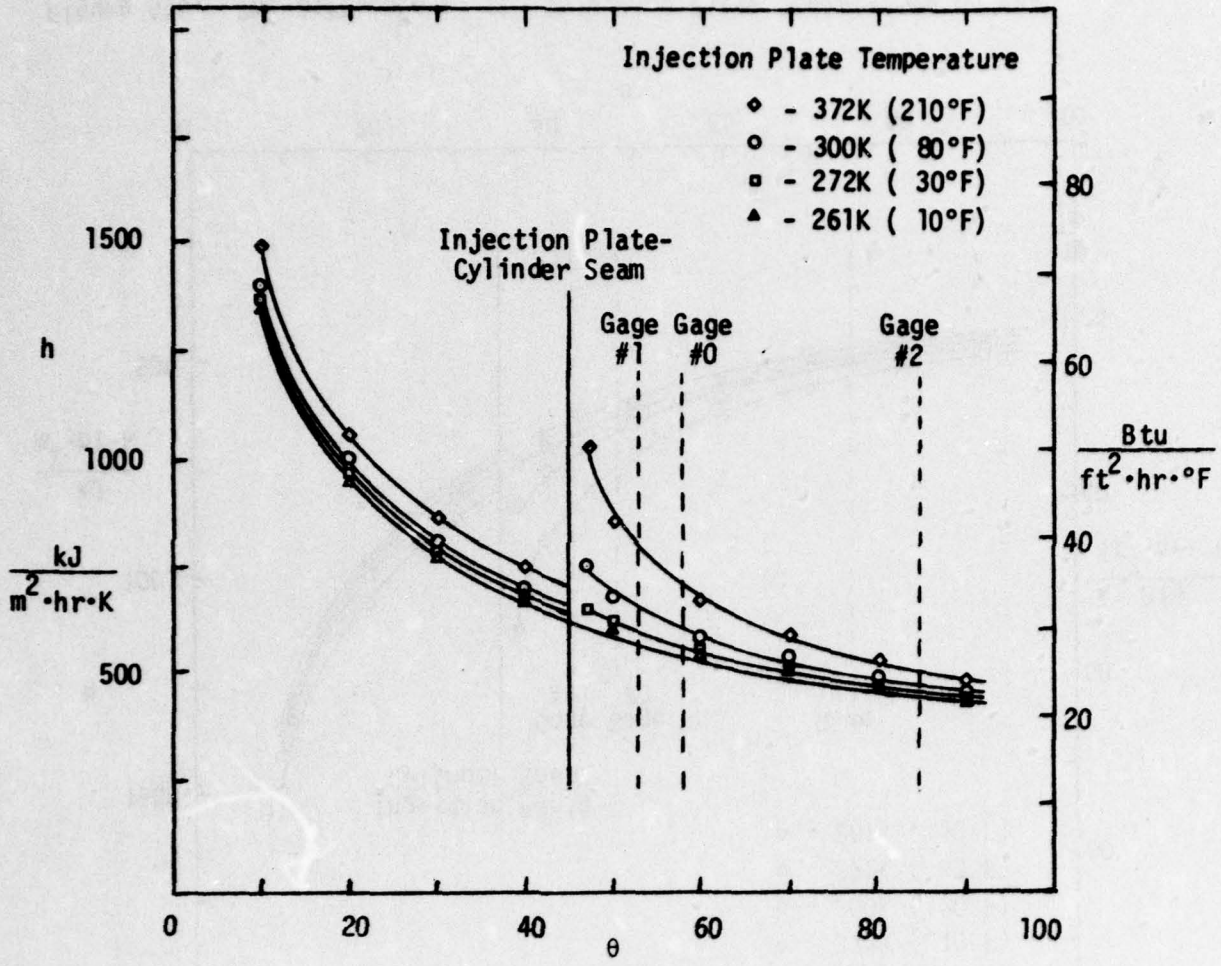

Figure A14. The Influence of the Injection Plate Temperature on the Downstream Heat Transfer Coefficient (Θ_i=30°)

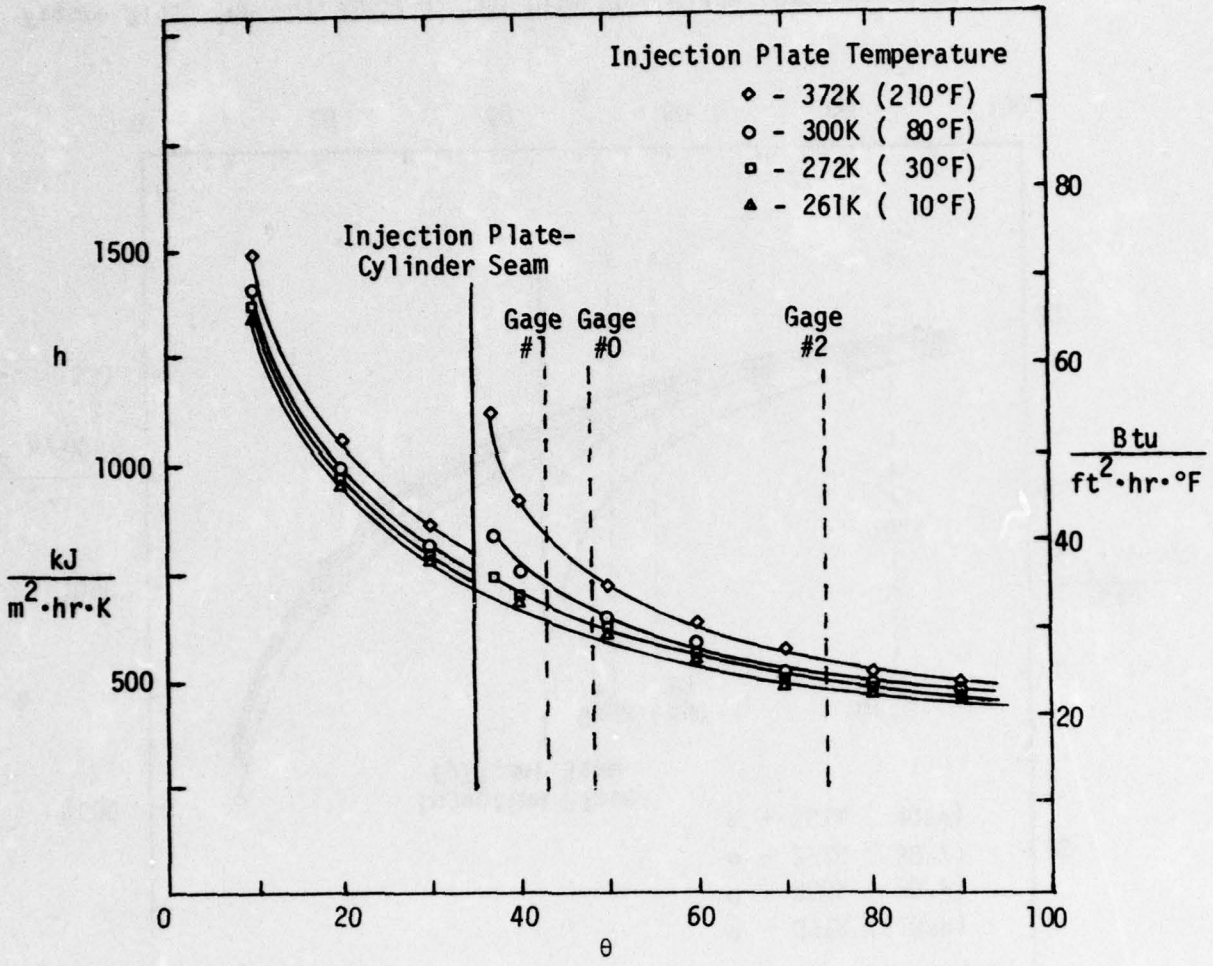

Figure A15. The Influence of the Injection Plate Temperature on the Downstream Heat Transfer Coefficient (θ_i=20°)

show similar results for the heat transfer coefficient, and all of the percentage differences between the heat transfer coefficients at the gage locations will be listed below.

Injection Location(θ_i)	Gage	Plate Temperature 272K	300K	372K
	1	3.1	11.5	35.8
40°	0	2.4	8.0	31.6
	2	1.4	3.8	24.1
	1	2.8	9.8	32.5
30°	0	2.2	7.4	23.7
	2	0.9	3.1	11.5
	1	2.4	8.5	28.1
20°	0	1.7	6.1	19.9
	2	0.8	2.9	9.6

Therefore the analytical results show that for the worst case when no coolant was flowing through the injection holes, the heat transfer coefficient was increased by 9 to 11% over the isothermal surface case for the gage closest to the injection plate, but without the coolant tube attached to the back of the injection plate, the heat transfer coefficient would have been 30 to 35% larger. As expected, when the film coolant was blowing and the injection plate temperature dropped down closer to the cylinder temperature, the increase in the heat transfer coefficient was lower (~3%) than when no coolant was blowing.

This analysis was conducted realizing that the flat plate boundary layer did not exactly model the boundary layer on the cylinder surface in its stagnation region and that the assumption of constant properties was not highly accurate. However it did provide an analytical analysis of the influence of this stepwise change in the wall temperature on the heat transfer coefficient. Besides the heat transfer coefficient downstream of the injection plate, the temperature of the plate also effected the film coolant temperature. As it passed through the injection holes in the plate, a high plate temperature would have raised the film coolant temperatures significantly. A correlation for this temperature rise of the coolant as it passed through the injection holes was developed in Appendix IV. Without the coolant tube attached to the backside of the injection plate, the resulting high temperatures of the plate would have produced a significant temperature rise in the film coolant, dropping the θ_c value far below 1.0. Therefore the cooling of the injection plate not only reduced the effect of a stepwise temperature change on the heat transfer coefficient downstream of the plate, but also prevented the film coolant from being heated significantly above the cylinder wall temperature.

APPENDIX VI. SPANWISE DISTRIBUTIONS OF THE FILM COOLING DATA

As discussed in Section III.D., it was difficult to assess the influence of the injection angle, β, or the row location, θ_i, on the film cooling performance by examining the data at specific values of z/s. Therefore, the measured data was cross plotted as a function of z/s for the different values of blowing ratio (M) investigated, and Figures 79 and 80 (in Section III.D.) were presented as representative cases. The spanwise distributions for all of the film cooling configurations investigated (as listed in Table 4) are presented in this appendix in Figures A16 to A36. The values of the geometric parameters held constant for each distribution are listed at the top of each figure. The guidelines for the plotting of the figures and the drawing of the distributions are the same as those described in Section III.B. However, the distribution at every blowing ratio for each film cooling configuration is not presented. When the magnitude of one of the data points fell below a Stanton Number Reduction of -0.12, the film coolant being injected at that configuration and blowing ratio was judged to be ineffective in protecting the surface. Therefore the spanwise distribution for these cases were not presented. This occurrence was limited to the higher values of the blowing ratio ($M > M_{opt}$) and the steeper injection angles, β, when the penetration of the coolant into the freestream led to a rapid deterioration in the film cooling performance. From the spanwise distributions presented, the spanwise maximum

Stanton Number Reduction ($[1-(St_{FC}/St_o)]^*$) and its corresponding z/s location (z/s^*) were identified on each curve (represented by the symbol (*) on each curve), and the spanwise averaged Stanton Number Reduction ($[1-(St_{FC}/St_o)]_{AVG}$) was found by graphical integration of each curve.

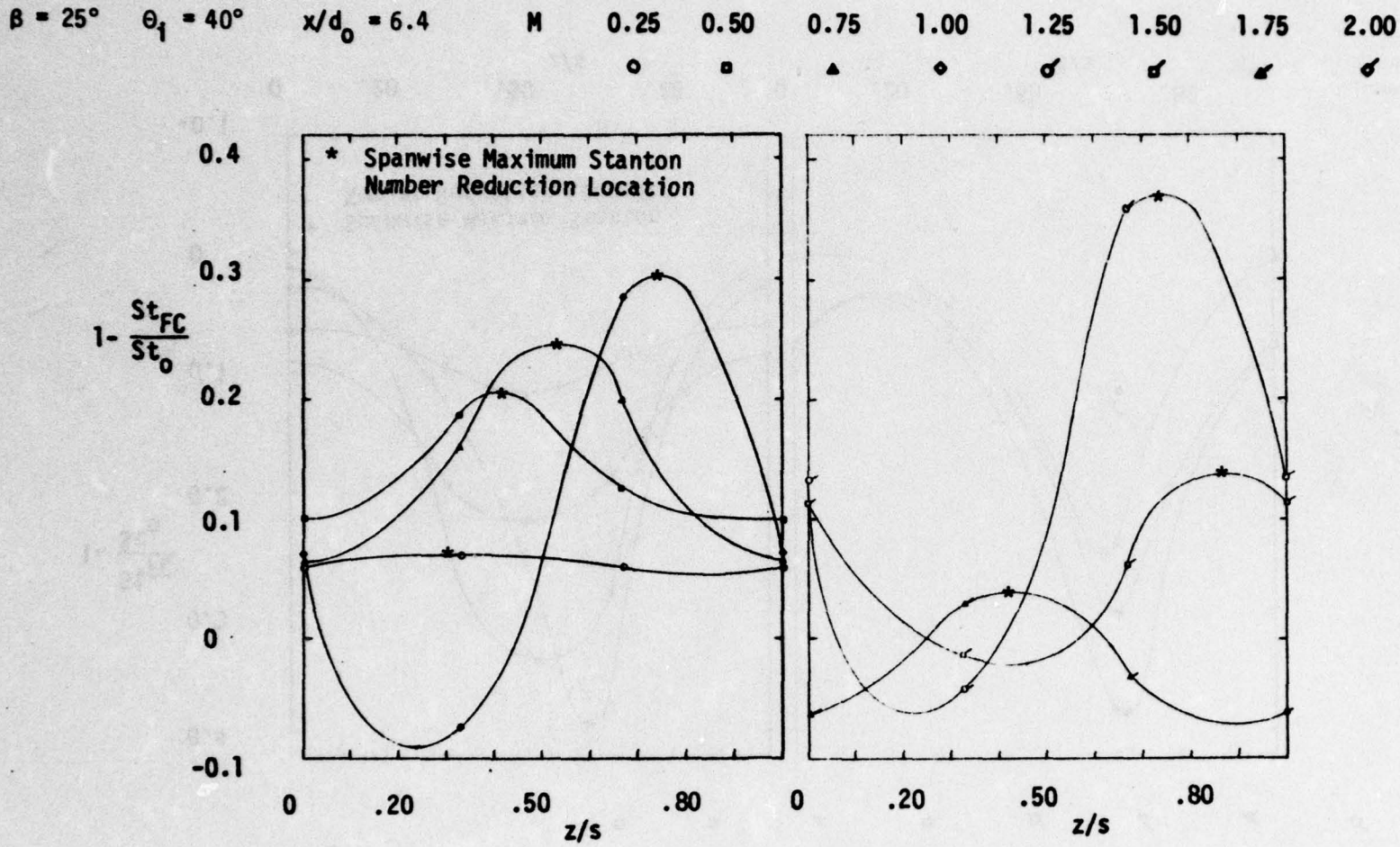

Figure A16. Spanwise Variation of the Stanton Number Reduction (β=25°, Θ_i=40°, x/d_o=6.4)

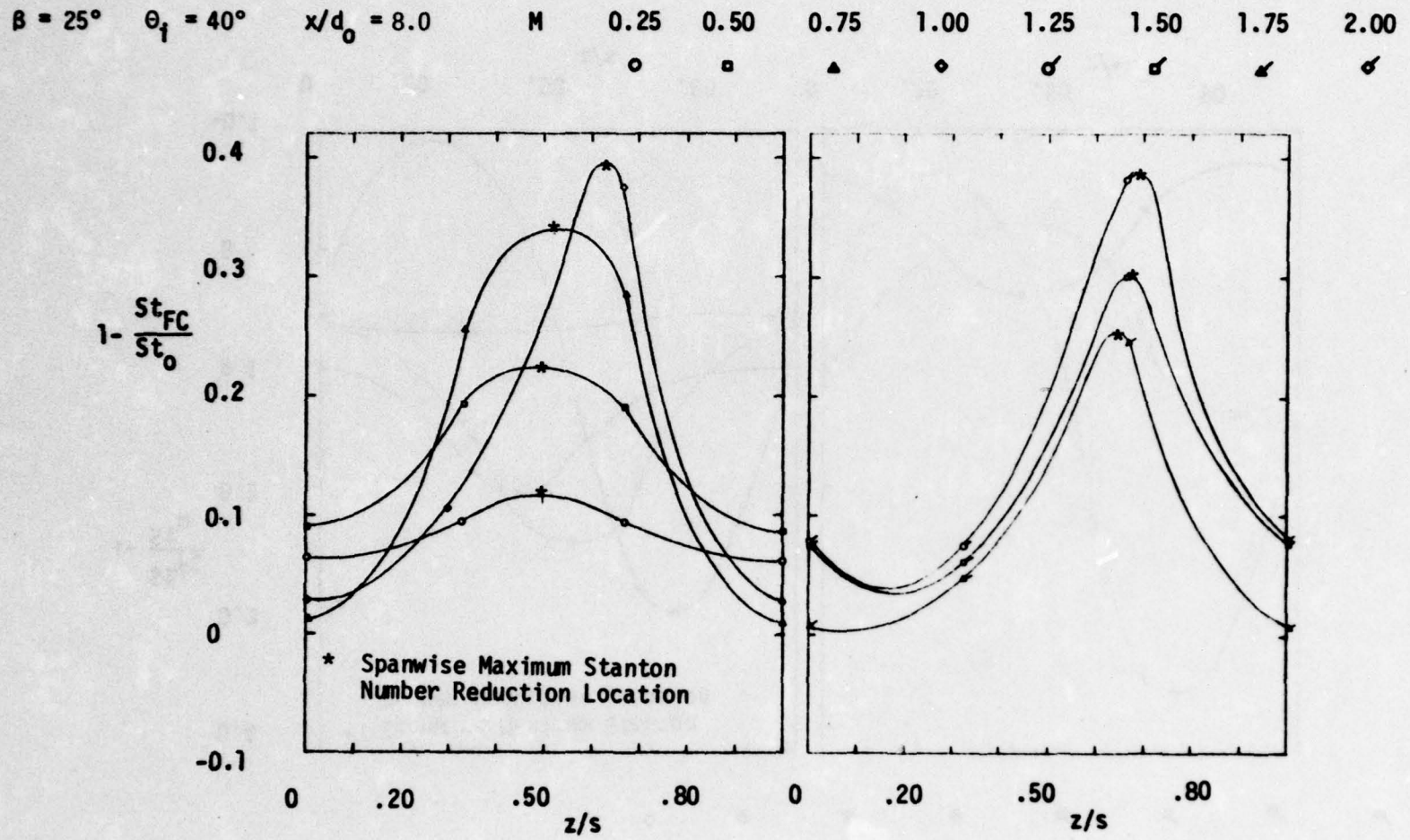

Figure A17. Spanwise Variation of the Stanton Number Reduction (β=25°, Θ_i=40°, x/d_o=8.0)

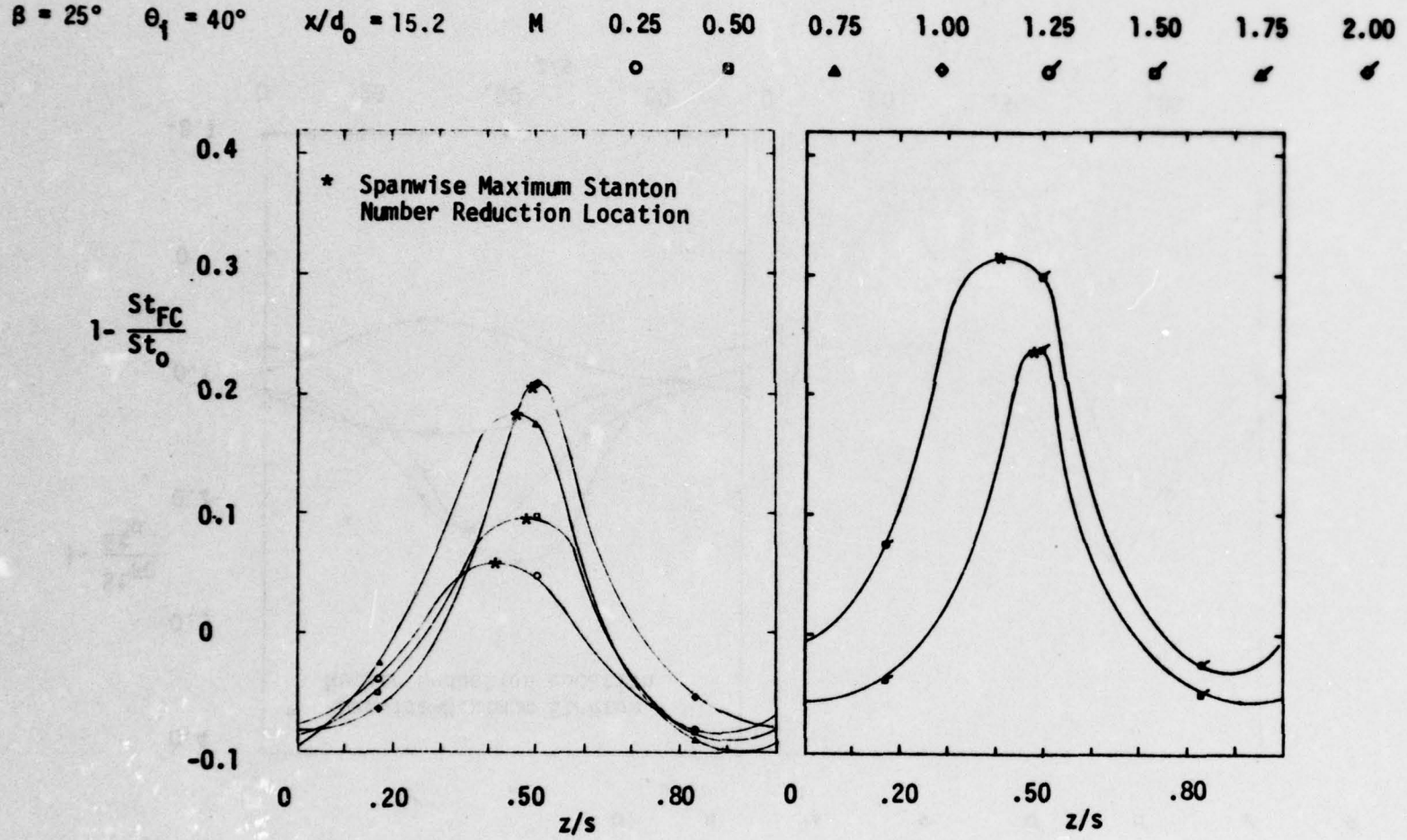

Figure A18. Spanwise Variation of the Stanton Number Reduction (β=25°, θ_i=40°, x/d_o=15.2)

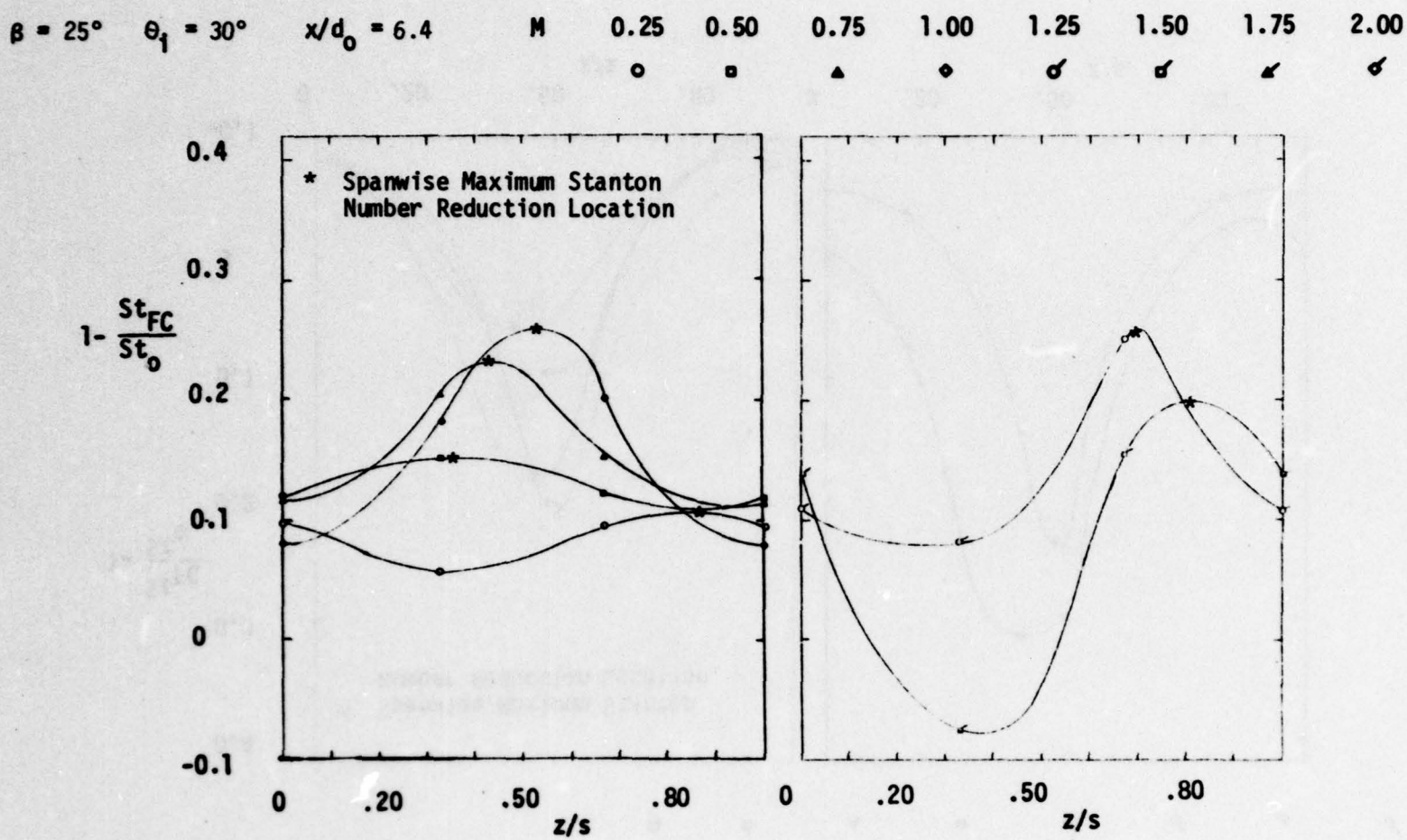

Figure A19. Spanwise Variation of the Stanton Number Reduction (β=25°, θ_i=30°, x/d_o=6.4)

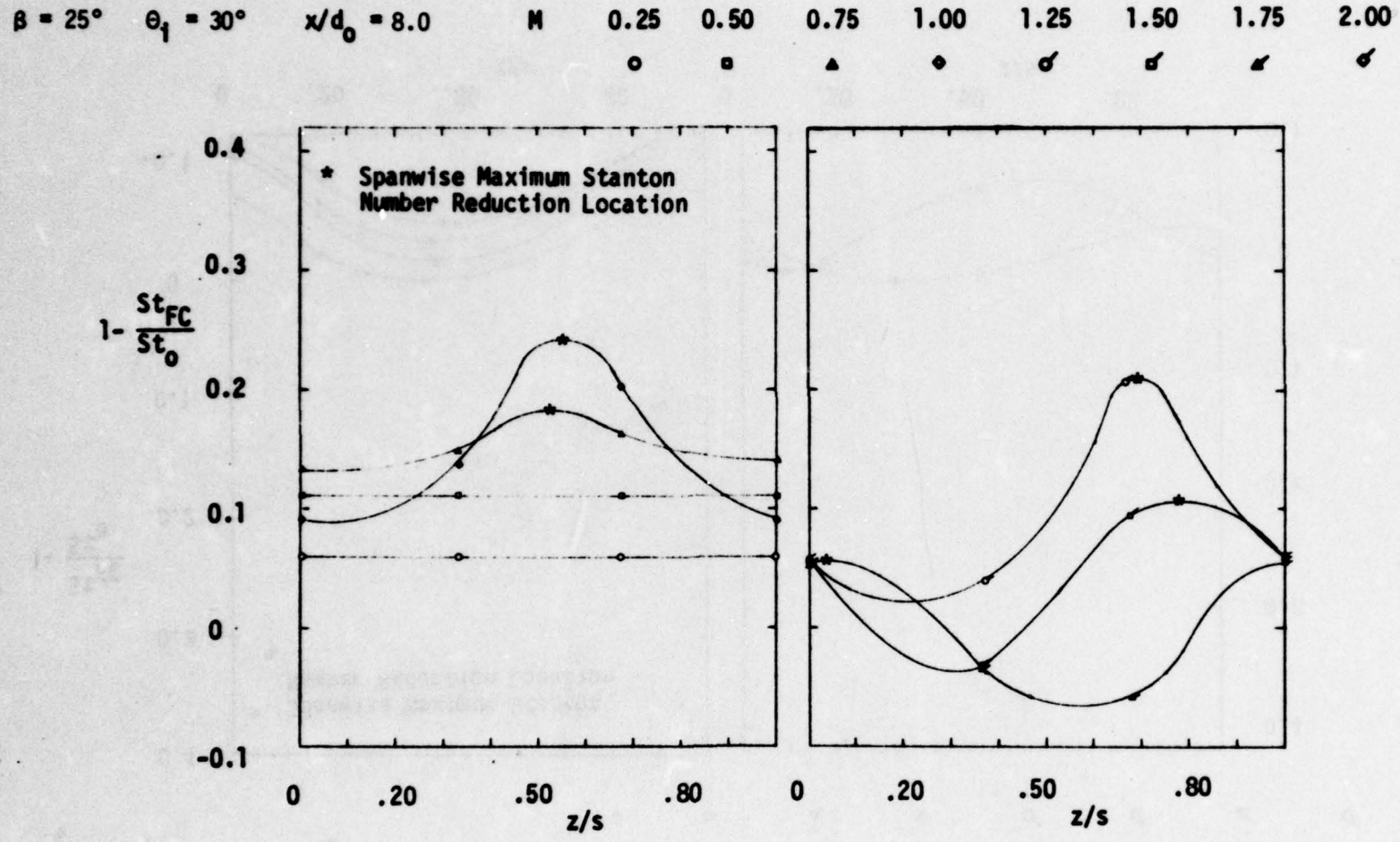

Figure A20. Spanwise Variation of the Stanton Number Reduction (β=25°, θ_i=30°, x/d_o=8.0)

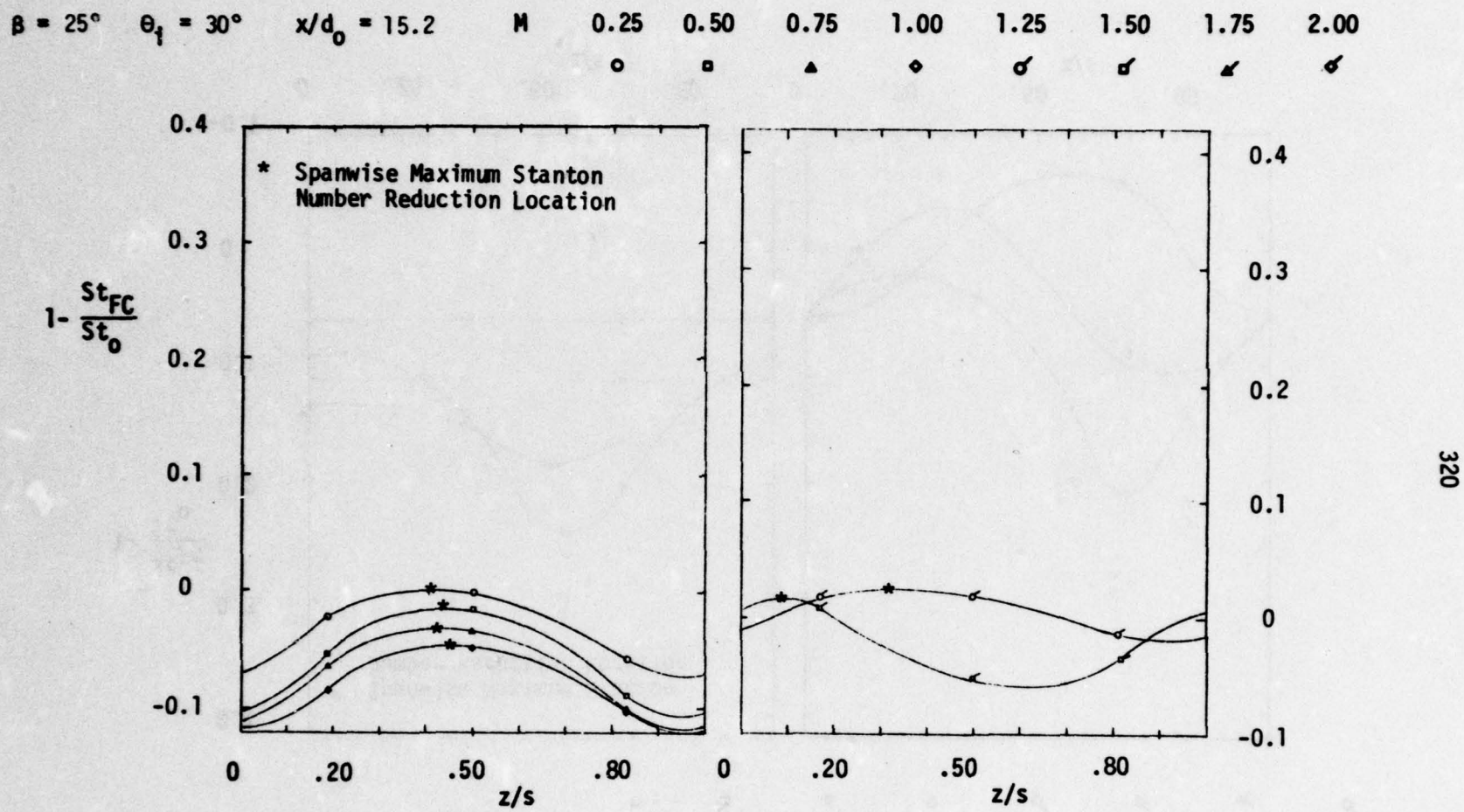

Figure A21. Spanwise Variation of the Stanton Number Reduction (β=25°, Θ_i=30°, x/d_o=15.2)

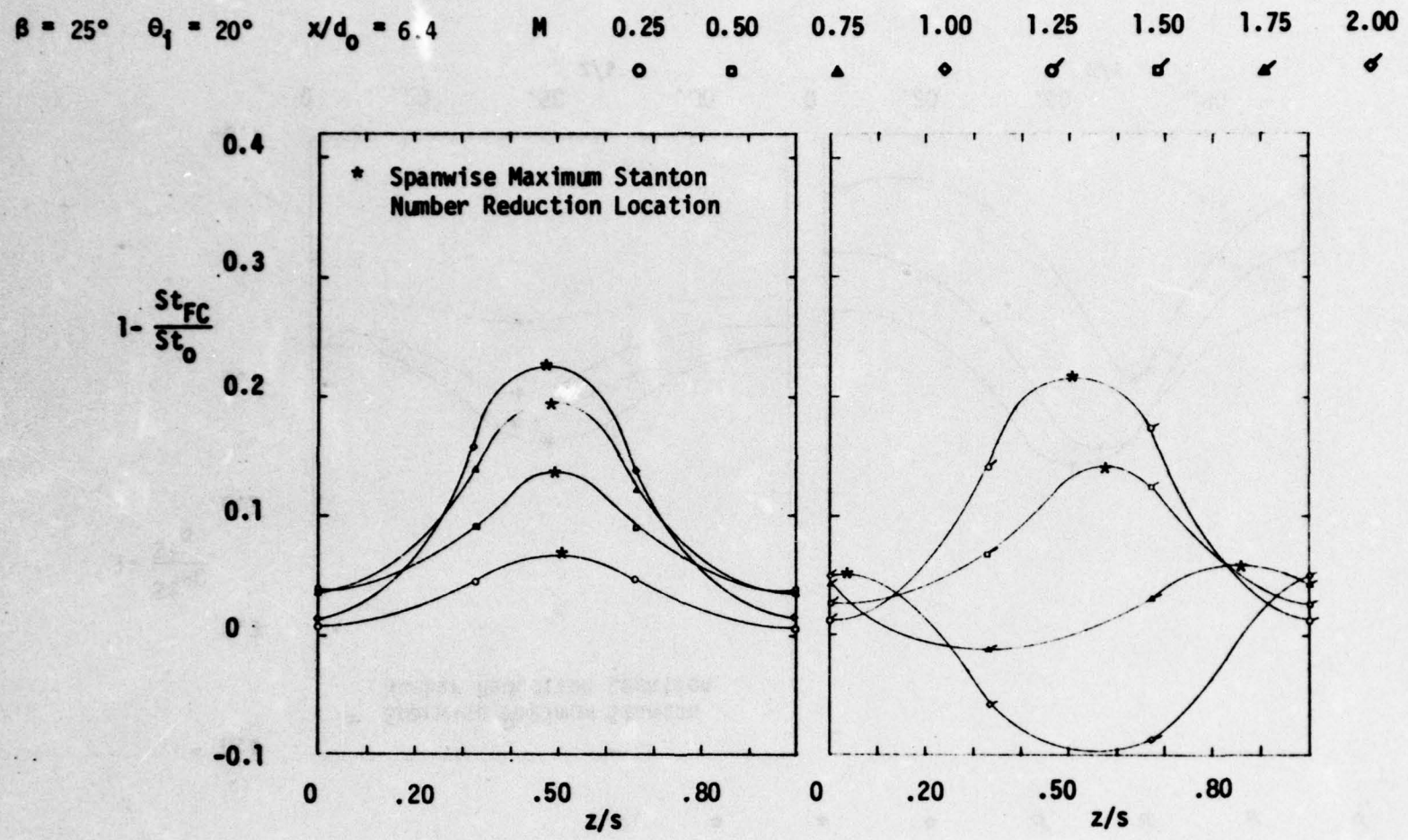

Figure A22. Spanwise Variation of the Stanton Number Reduction (β=25°, Θ_i=20°, x/d_o=6.4)

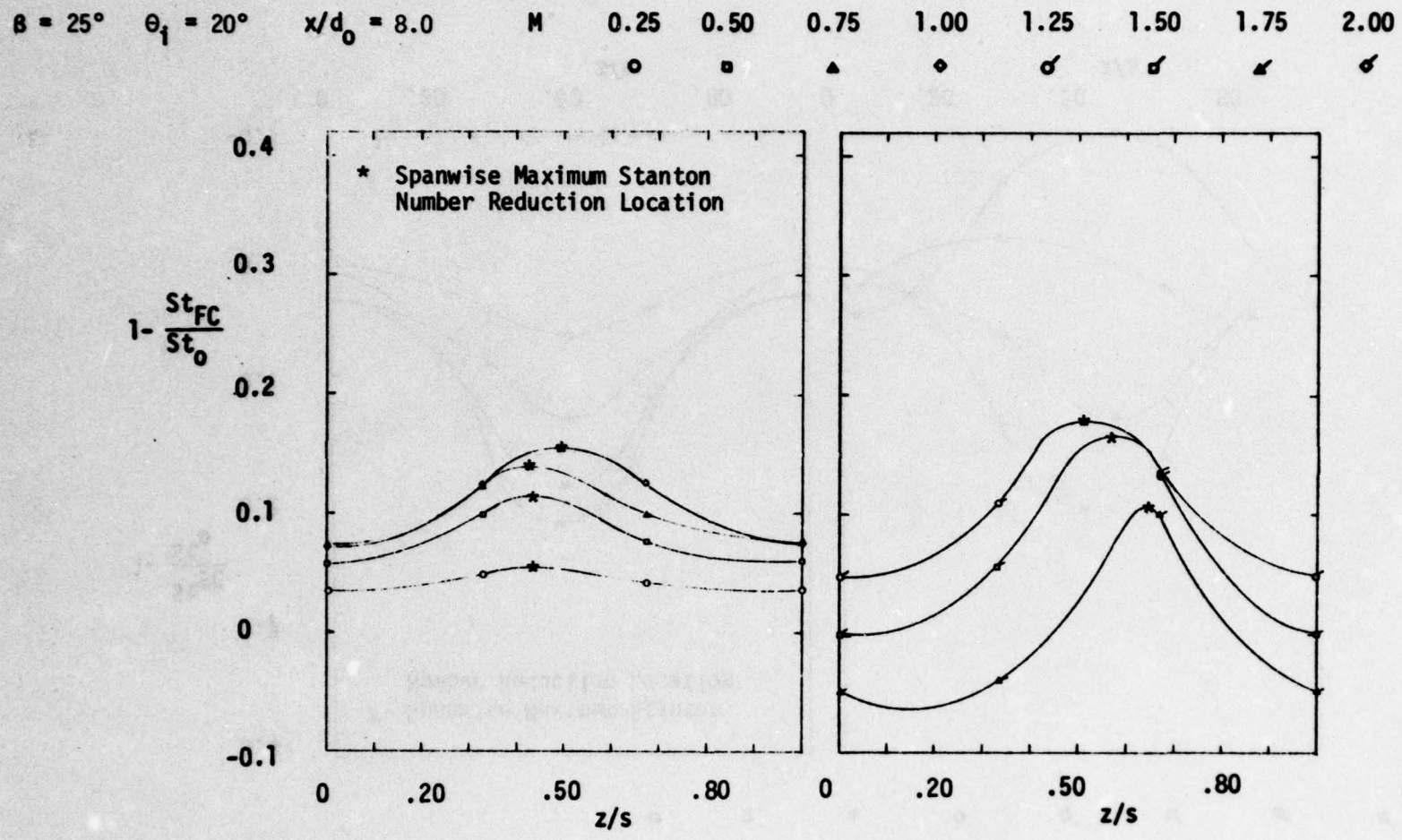

Figure A23. Spanwise Variation of the Stanton Number Reduction (β=25°, Θ_i=20°, x/d_o=8.0)

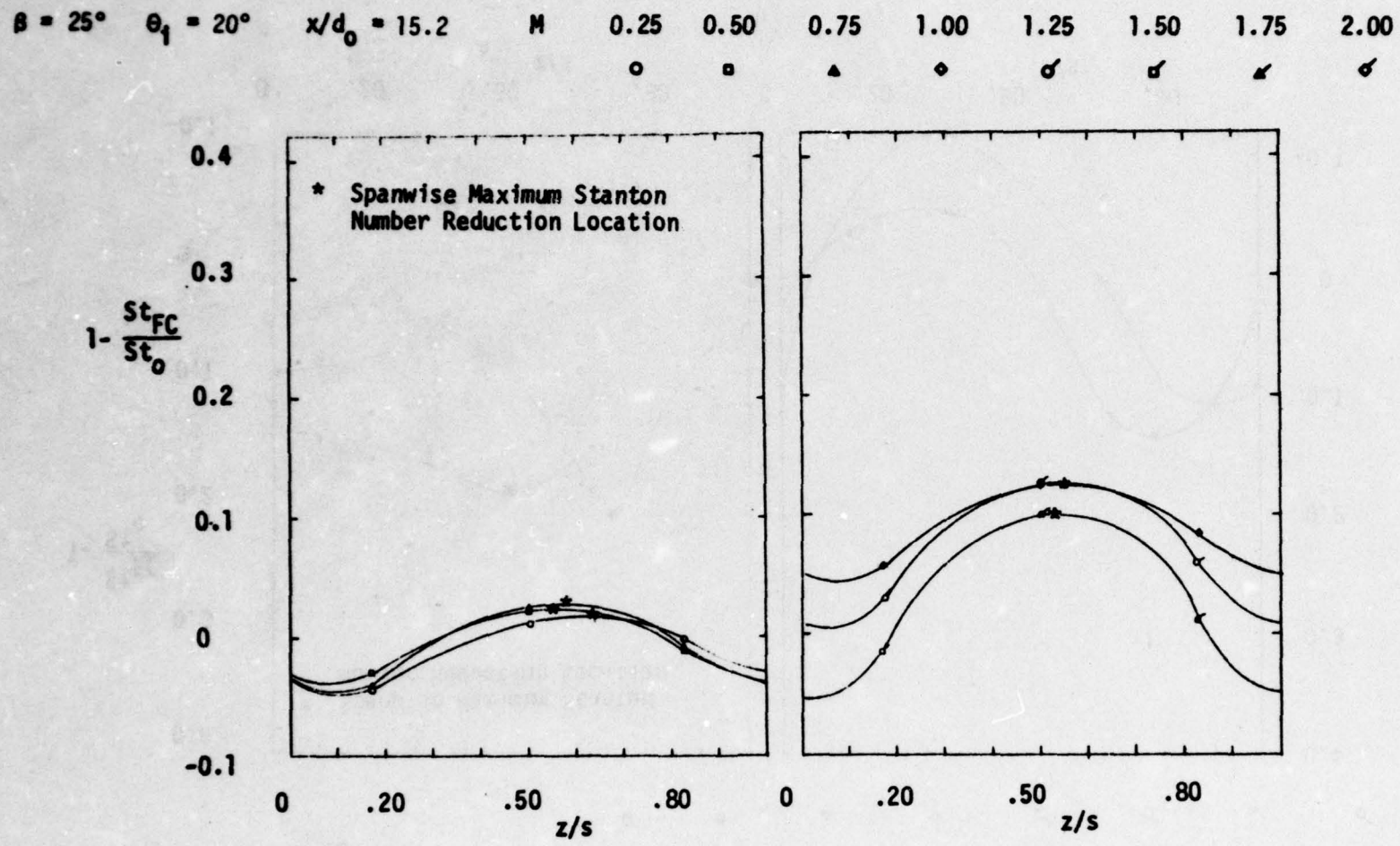

Figure A24. Spanwise Variation of the Stanton Number Reduction (β=25°, Θ_i=20°, x/d_o=15.2)

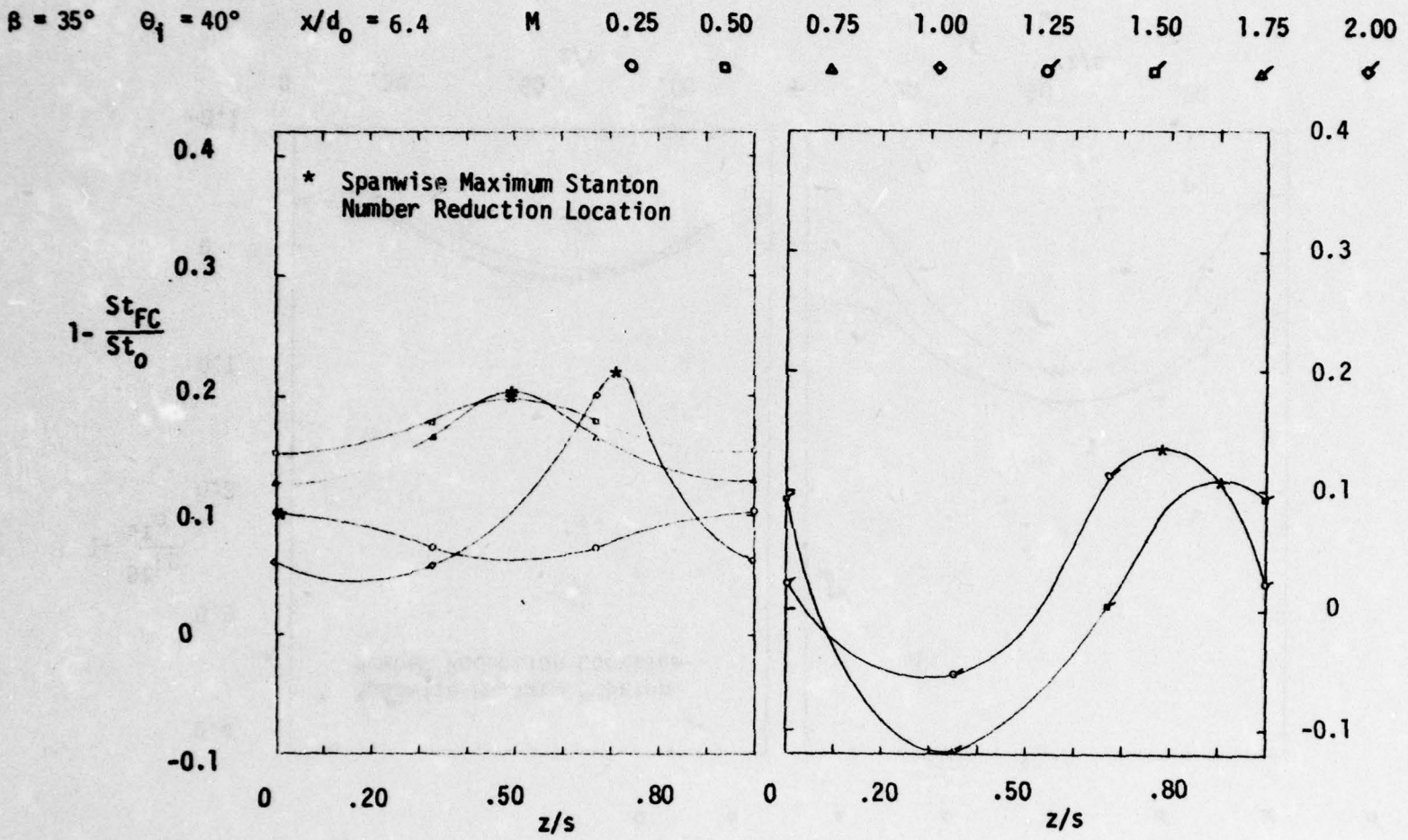

Figure A25. Spanwise Variation of the Stanton Number Reduction (β=35°, θ_i=40°, x/d_o=6.4)

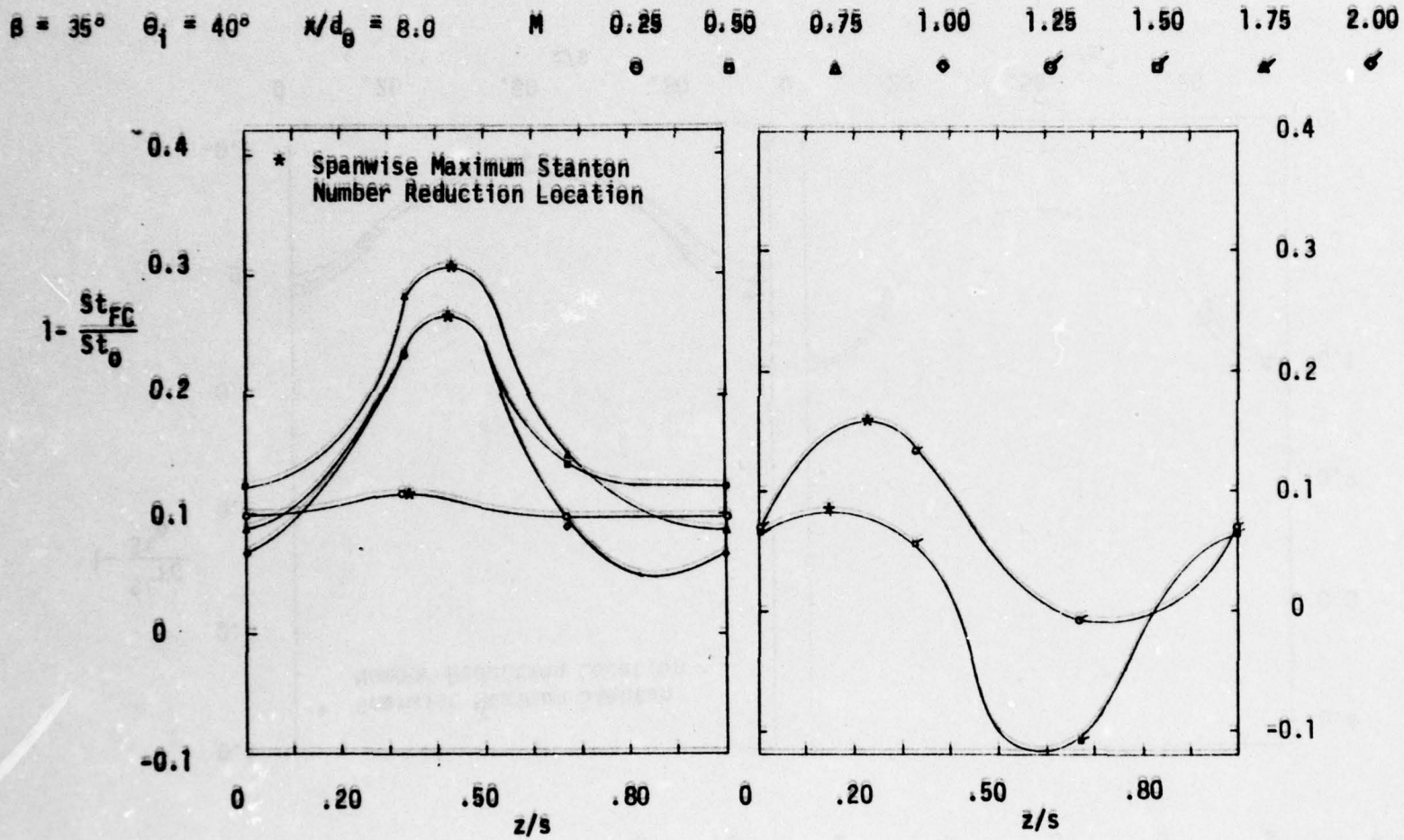

Figure A26. Spanwise Variation of the Stanton Number Reduction (β=35°, Θ_i=40°, x/d_0=8.0)

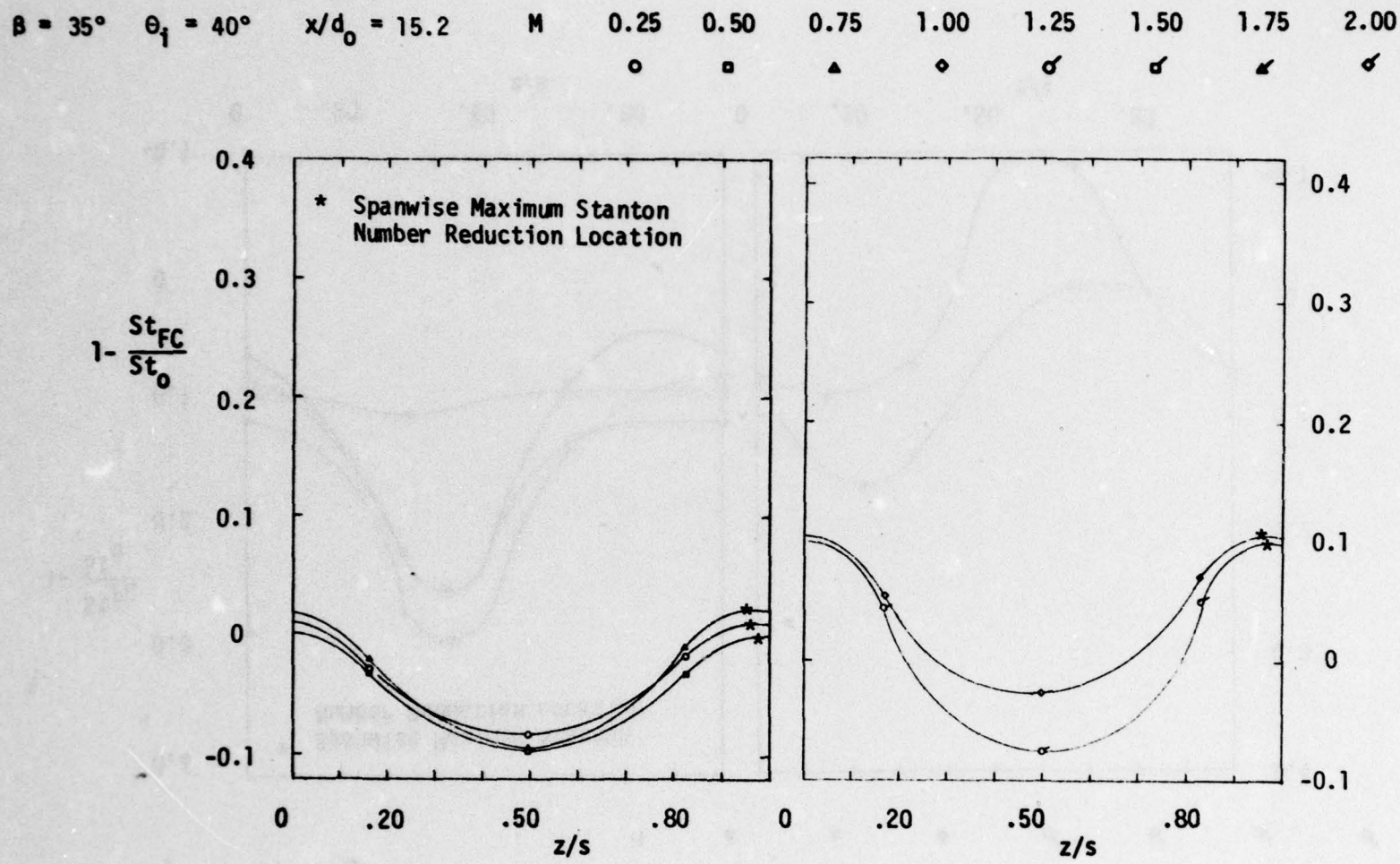

Figure A27. Spanwise Variation of the Stanton Number Reduction (β=35°, θ_i=40°, x/d_o=15.2)

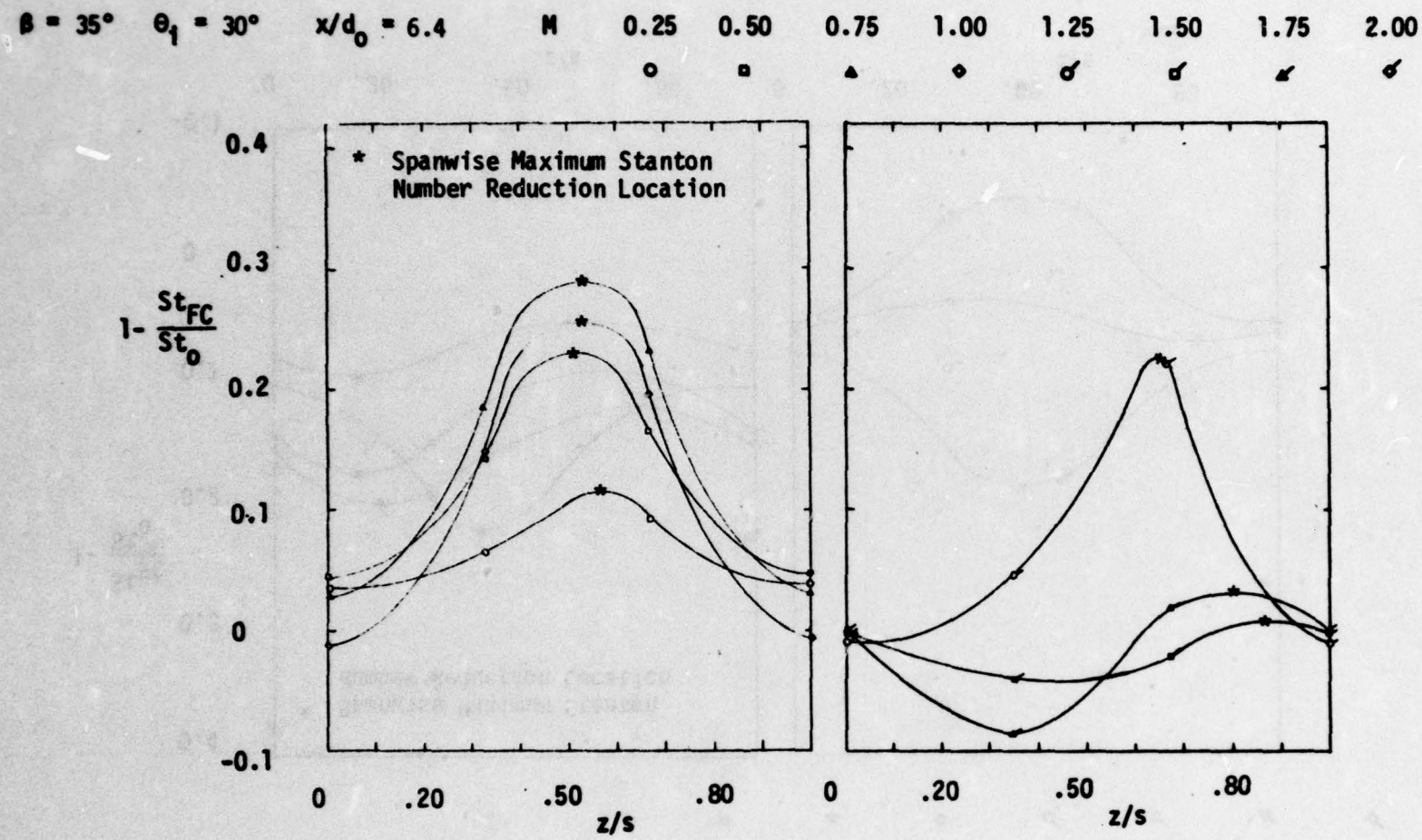

Figure A28. Spanwise Variation of the Stanton Number Reduction (β=35°, Θ_i=30°, x/d_o=6.4)

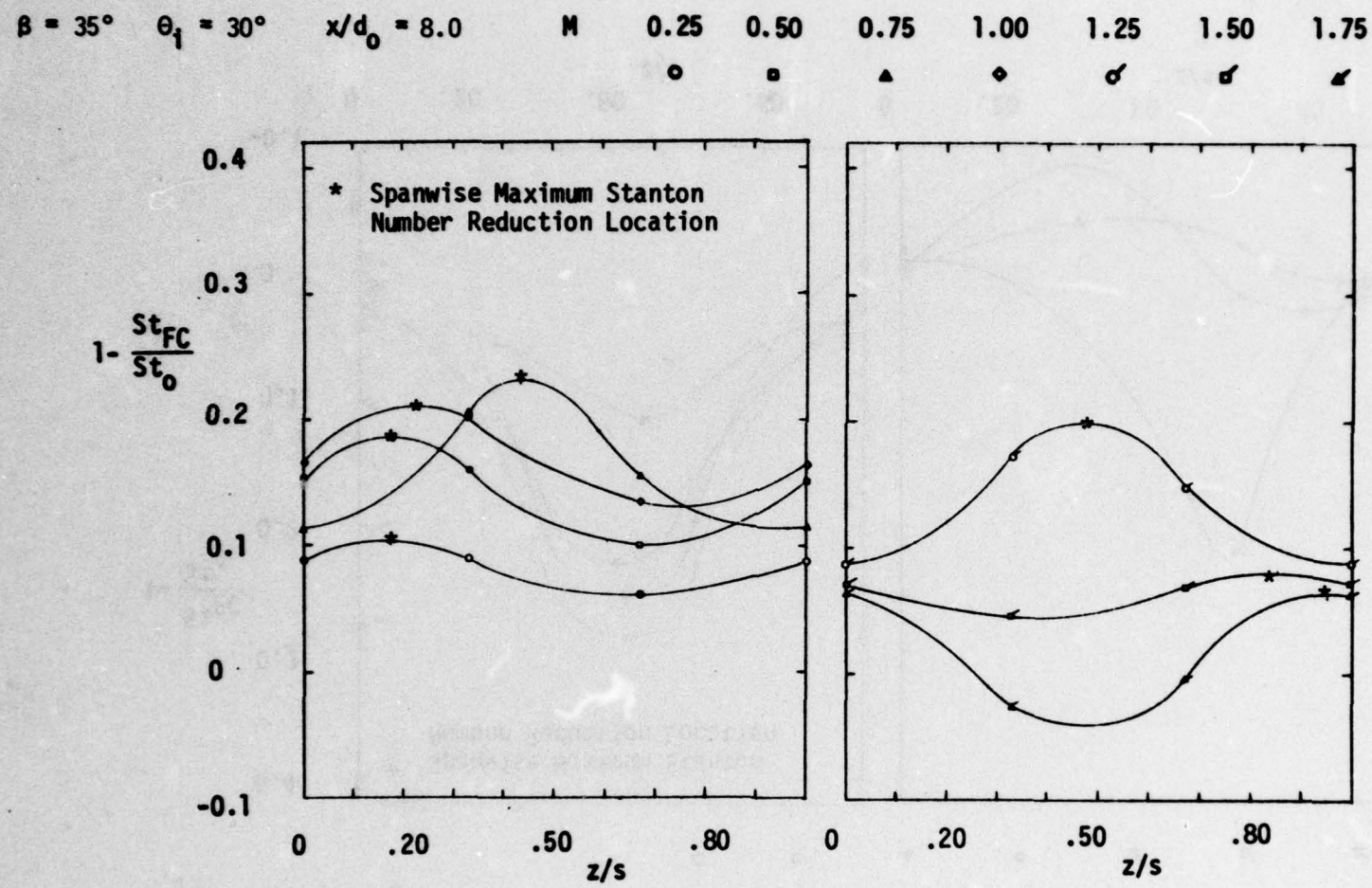

Figure A29. Spanwise Variation of the Stanton Number Reduction (β=35°, Θ_i=30°, x/d_o=8.0)

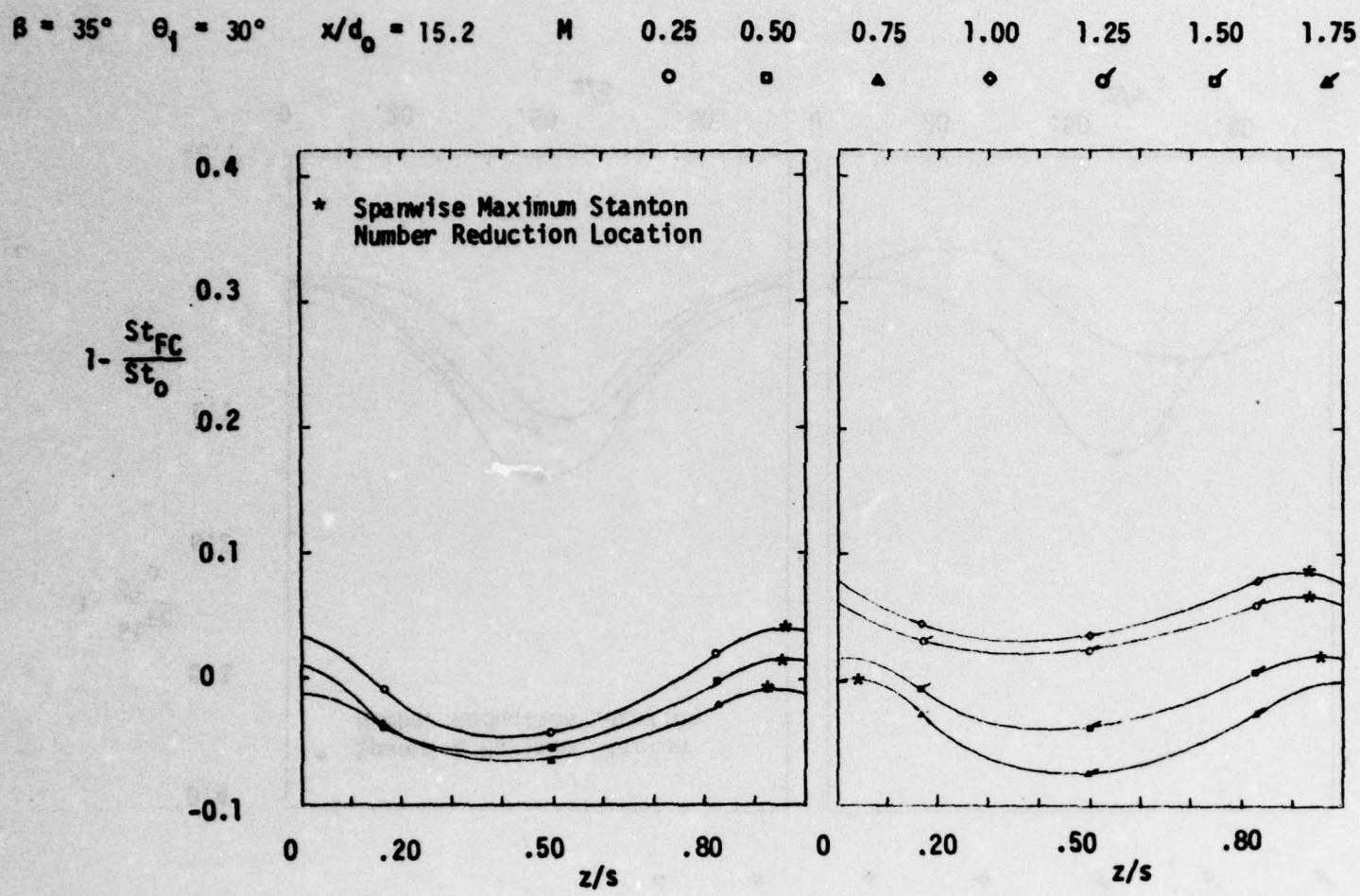

Figure A30. Spanwise Variation of the Stanton Number Reduction (β=35°, Θ_i=30°, x/d_o=15.2)

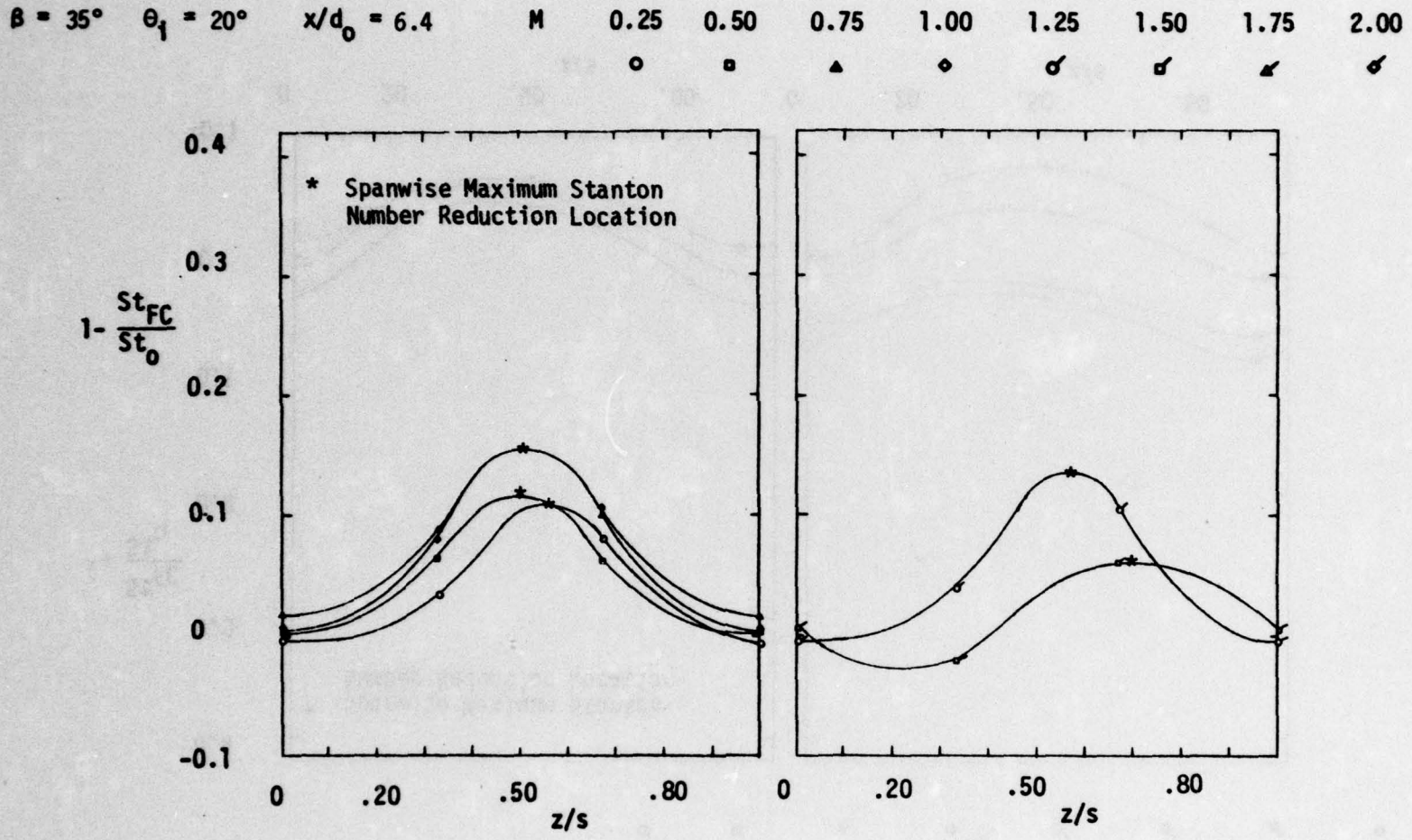

Figure A31. Spanwise Variation of the Stanton Number Reduction (β=35°, Θ_i=20°, x/d_o=6.4)

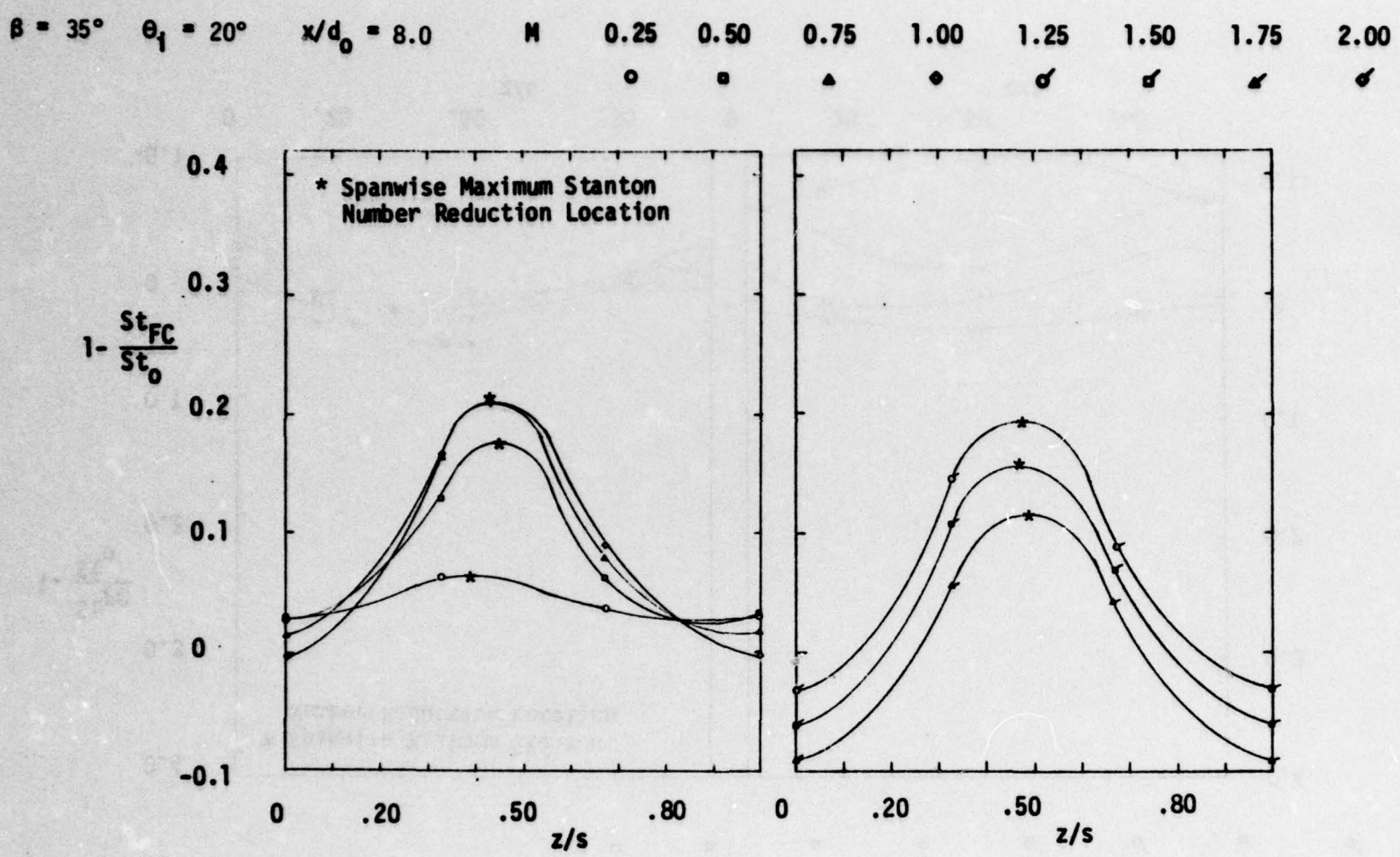

Figure A32. Spanwise Variation of the Stanton Number Reduction (β=35°, Θ_i=20°, x/d_0=8.0)

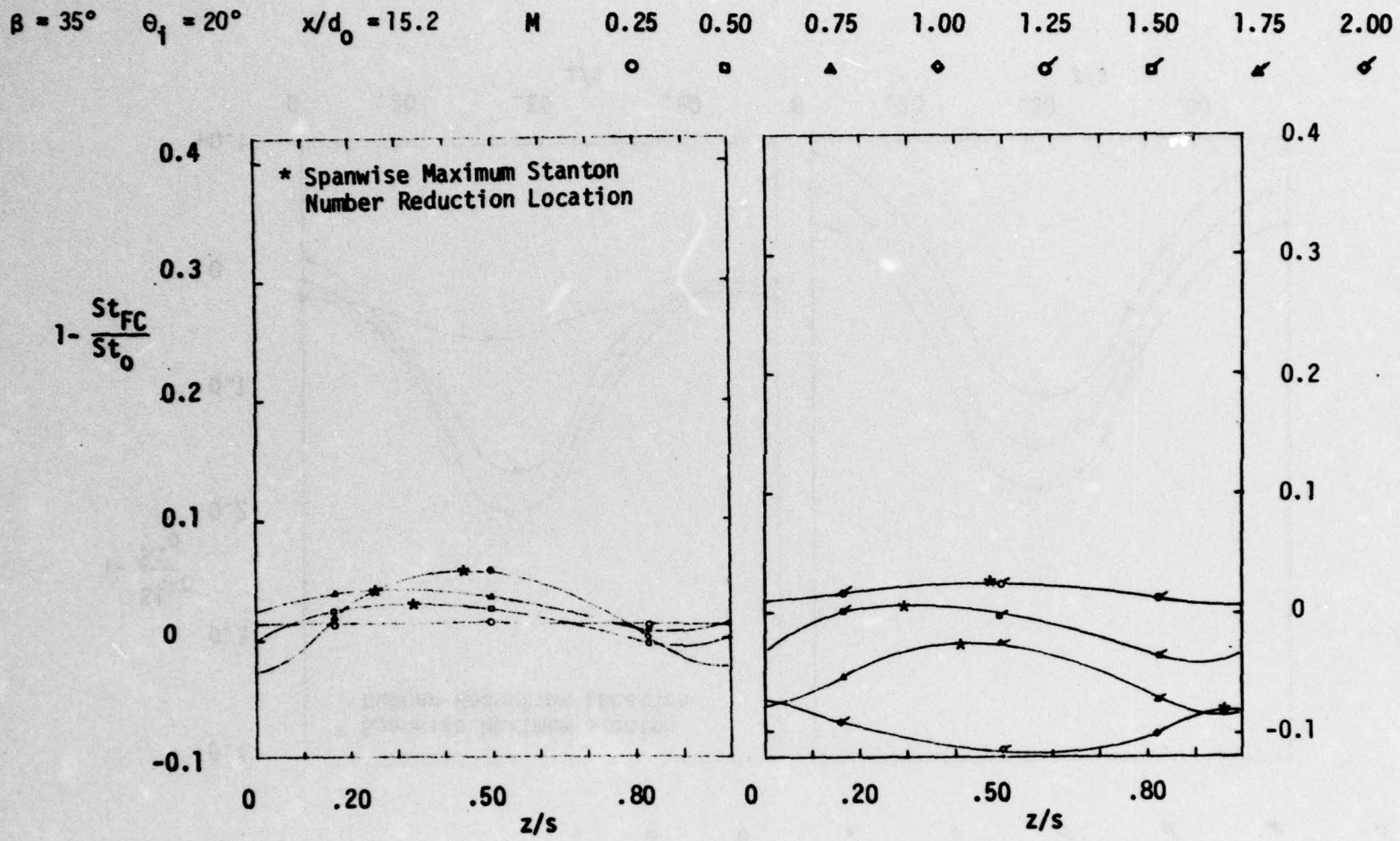

Figure A33. Spanwise Variation of the Stanton Number Reduction (β=35°, θ_i=20°, x/d_o=15.2)

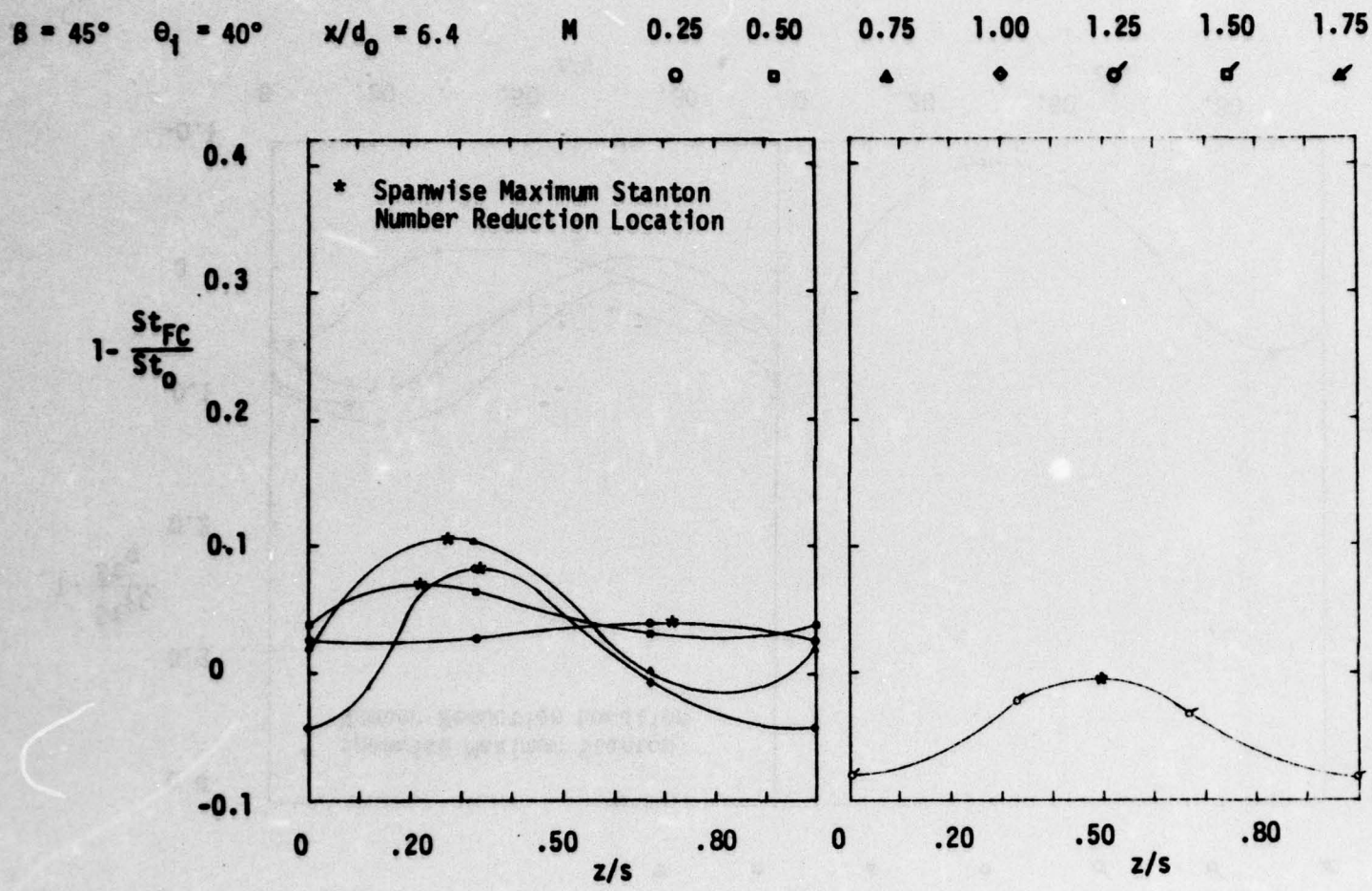

Figure A34. Spanwise Variation of the Stanton Number Reduction (β=45°, θ_i=40°, x/d_o=6.4)

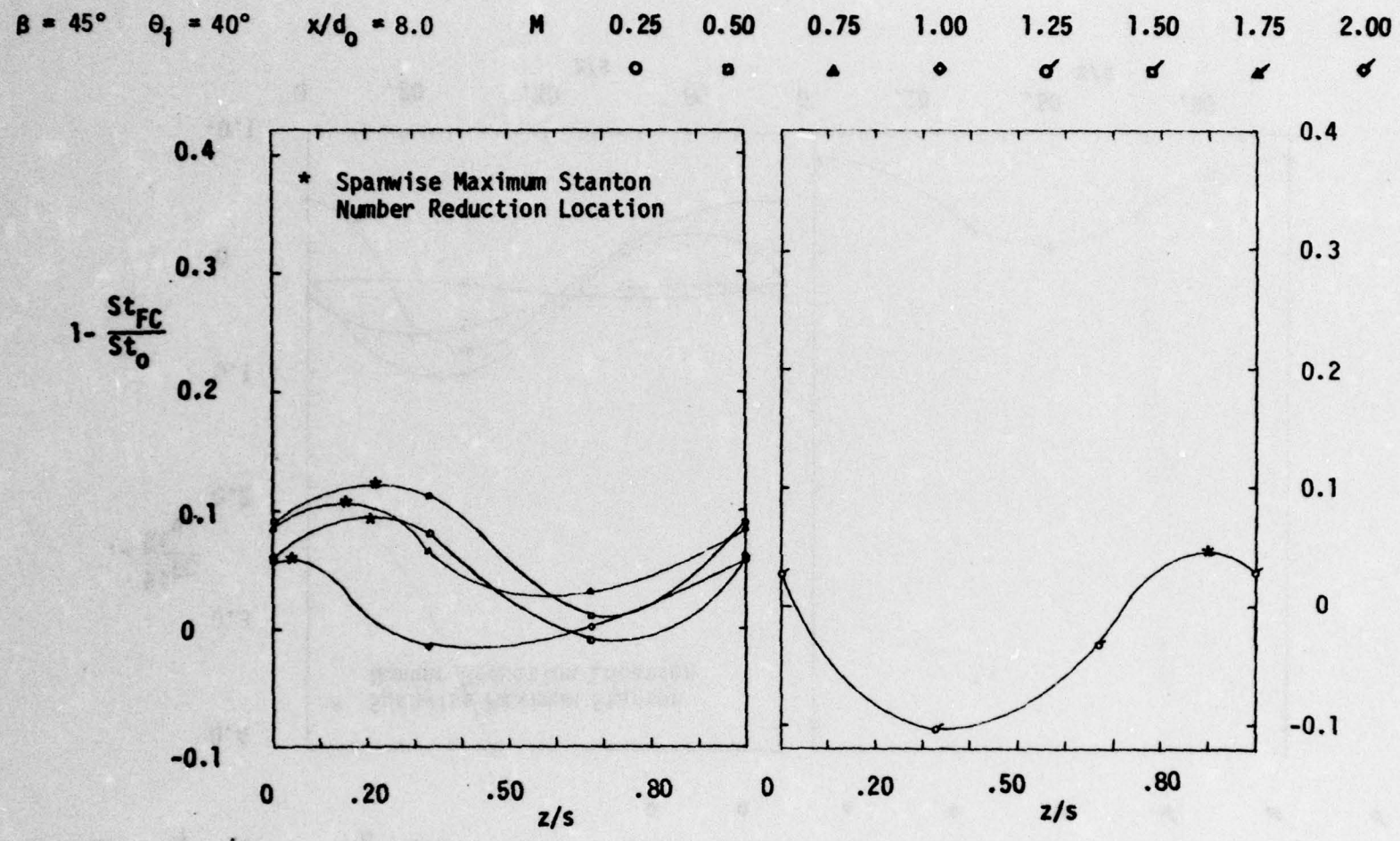

Figure A35. Spanwise Variation of the Stanton Number Reduction (β=45°, Θ_i=40°, x/d_o=8.0)

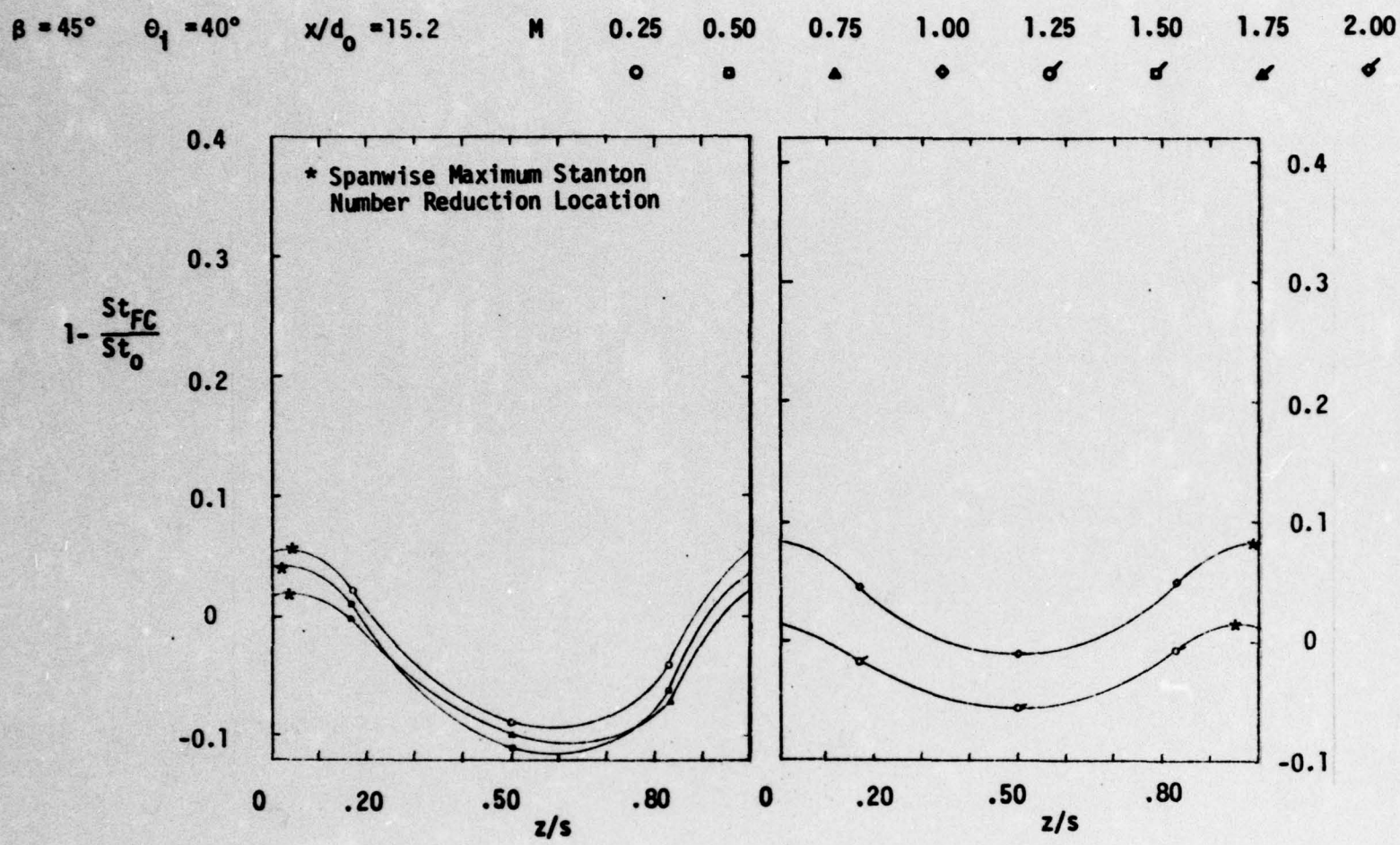

Figure A36. Spanwise Variation of the Stanton Number Reduction (β=45°, θ_i=40°, x/d_o=15.2)

TECHNICAL REPORT DISTRIBUTION LIST

Office of Naval Research
Power Branch

Defense Documentation Center (12)
Cameron Station
Alexandria, Virginia 22314

Chief of Naval Research (2)
Department of the Navy
Arlington, Virginia 22217
Attn: Mr. J.R. Patton, Jr., Code 473

Commander
Naval Air Systems Command
Department of the Navy
Washington, D.C. 20360
Attn: Code 330 (1)
Code 53673 (1)
Code 310C (1)
Technical Library, Code 604 (1)

Commander (1)
Naval Sea Systems Command
Department of the Navy
National Center #2
2521 Jefferson Davis Highway
Arlington, Virginia 20360
Attn: Code 0331

The Boeing Company (1)
Headquarters Office
P. O. Box 3707
Seattle, Washington 98124
Attn: Gas Turbine Division

Continental Aviation and Engineering Corp. (1)
12700 Kercheval Avenue
Detroit, Michigan 48215
Attn: Chief Engineer

General Electric Company (1)
Aircraft Gas Turbine Division
Cincinnati, Ohio 45215
Attn: Manager of Engineering

Commanding Officer (1)
U.S. Army Research Office
Box CM, Duke Station
Durham, North Carolina 27706
Attn: ORDOR-PC

Director (1)
National Aeronautics & Space Administration
Headquarters
Washington, D.C. 20546
Attn: Division Research Information

Director (1)
National Bureau of Standards
Gaithersburg, Maryland 20760

Office of The Assistant Secretary (1)
of Defense (R&D)
Room 3E1065 - The Pentagon
Washington, D.C. 20301
Attn: Technical Library

Aerojet-General Corporation (1)
P. O. Box 296
Azusa, California 91702
Attn: Librarian

AiResearch Manufacturing Company (1)
9851 Sepulveda Boulevard
Los Angeles, California 90045
Attn: Chief Engineer

General Motors Corporation (1)
Allison Division
Indianapolis, Indiana 46206
Attn: Director of Engineering

General Electric Company (1)
Engineering Department
Turbine Division
Schenectady, New York 12305

General Electric Company (1)
Aircraft Turbine Department
West Lynn, Massachusetts 01905

AVCO Corporation (1)
Lycoming Spencer Division
652 Oliver Street
Williamsport, Pennsylvania 17701

National Aeronautics & Space (2)
Administration
Lewis Research Center
21000 Brookpark Road
Cleveland, Ohio 44135

United Aircraft Corporation (1)
Pratt & Whitney Aircraft Division
East Hartford, Connecticut 06118
Attn: Chief Engineer

Solar Aircraft Company (1)
San Diego, California 92101
Attn: Chief Engineer

United Aircraft Corporation (1)
Research Laboratory
East Hartford, Connecticut 06118
Attn: Director of Research

Commander (1)
Naval Surface Weapons Center
White Oak
Silver Spring, Maryland 20910
Attn: Library

Commander (1)
Naval Weapons Center
China Lake, California 93555
Attn: Technical Library

Commander (3)
Wright Air Development Center
Wright-Patterson Air Force Base, Ohio 45433
Attn: WCLPN-1, WCACD, WCLPS-1

Director (6)
U.S. Naval Research Laboratory
4555 Overlook Avenue, S.W.
Washington, D.C. 20375
Attn: Technical Information Division

Office of Naval Research (6)
Department of the Navy
Code 102IP - ONRL Documents
Arlington, Virginia 22217

Director (1)
Office of Naval Research Branch Office
536 South Clark Street
Chicago, Illinois 60605

Officer in Charge
Naval Ship Engineering Center
Philadelphia Division
Philadelphia, Pennsylvania 19112
Attn: Code 6700 (1)
Technical Library (1)

Superintendent
U.S. Naval Postgraduate School
Monterey, California 93940
Attn: Professor Vavra (1)
Library, Code 0212 (1)

Westinghouse Electric Corporation (1)
Steam Turbine Division
Essington, Pennsylvania 19029

United Aircraft Corporation (1)
Pratt & Whitney Aircraft Division
P. O. Box 2691
West Palm Beach, Florida 33402

Varo, Incorporated (1)
402 East Cutierrez Street
Santa Barbara, California 93101
Attn: K. J. Widiner

Director (1)
Ordnance Research Laboratory
Pennsylvania State University
University Park, Pennsylvania 16802

Naval Ship Research & Development Center (1)
Annapolis Division
Annapolis, Maryland 21402
Attn: Library, Code A214

Naval Undersea Warfare Center (1)
3202 East Foothill Boulevard
Pasadena, California 91107
Attn: Technical Library

Naval Applied Science Laboratory (1)
Flushing and Washington Avenues
Brooklyn, New York 11251
Attn: Technical Library, Code 222

U.S. Naval Oceanographic Office (1)
Suitland, Maryland 20390
Attn: Library, Code 1640

Bureau of Naval Personnel (1)
Department of the Navy
Washington, D.C. 20370
Attn: Technical Library

Navy Underwater Sound Laboratory (1)
Fort Trumbull
New London, Connecticut 06320
Attn: Technical Library

U.S. Naval Weapons Laboratory (1)
Dahlgren, Virginia 22448
Attn: Technical Library

Director, Project SQUID (1)
Jet Propulsion Center
School of Mechanical Engineering
Purdue University
West Lafayette, Indiana 47907
Attn: Professor Murthy

Army Missile Command (1)
Research & Development Directorate
Redstone Arsenal, Alabama 35809
Attn: Propulsion Laboratory

Director (1)
Applied Physics Laboratory
8621 Georgia Avenue
Silver Spring, Maryland 20910
Attn: Library

Commander (1)
U.S. Air Force Systems Command
Andrews Air Force Base
Silver Hill, Maryland 20331

Commander (1)
Air Force Aero Propulsion Laboratory
Wright-Patterson Air Force Base
Dayton, Ohio 45433

Commander (1)
Air Force Rocket Propulsion Laboratory
Edwards Air Force Base, California 93523

Naval Missile Center (1)
Point Mugu, California 93041
Attn: Technical Library

Headquarters (1)
Naval Material Command
Special Projects Office
Washington, D.C. 20360
Attn: Technical Library

Commander (1)
Air Force Office of Scientific Research
1400 Wilson Boulevard
Arlington, Virginia 22209
Attn: J. F. Masi

Director of Defense Research (1)
and Engineering
Technical Library
Room 30128 - The Pentagon
Washington, D.C. 20301
Attn: Propulsion Technology

Chief of Research and Development (1)
Headquarters, Department of the Army
Washington, D.C. 20310
Attn: Dr. S. J. Magram
Physical & Engr. Division